

Editorial corner – a personal view

Block copolymer – a versatile template tool for nanomaterials

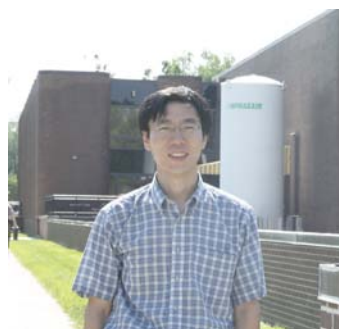
Z. Sun*

Key Laboratory of Excited State Processes, Changchun Institute of Optics, Fine Mechanics and Physics, Chinese Academy of Sciences, 3888 Eastern Nanhu Road, Changchun 130033, China

Block copolymer as a special kind of copolymers is made up of blocks of different monomers. For example, polystyrene-*b*-poly(methyl methacrylate) is usually made by first polymerizing styrene, and then subsequently polymerizing methyl methacrylate from the reactive end of the polystyrene chains. Because the different blocks are covalently bonded to each other, block copolymer can only microphase separate (or self-assemble) to form various types of ordered nanostructures ranging from 5 to 50 nm either in the bulk or solution depending on the ratio of different blocks, like hexagonal cylinder array, lamellae, and micelle nanostructures. Block copolymer provides a perfect platform for fabricating novel nanostructural materials for potential applications in advanced technologies such as nanocomposites, information storage, and bio-related nanomaterials.

Due to the microphase separation of block copolymer, the morphology of block copolymer can be tuned from particles in the matrix, hexagonal cylinder to the lamellae and then inverse phases by continuously changing the length of blocks. These nanostructures are extensively used as templates for fabrication of mesoporous nanomaterials for example mesoporous SiO₂, TiO₂ and carbon. The mesoporous materials with high surface area have many important applications in catalyst carrier and membrane separation fields. Block copolymers are also used as template to organize the functional molecules, precursors, or nanoparticles due to the chemical difference of blocks. For example, metal ions

can be loaded in one phase region; nanoparticles or nanowires can form within this phase region after reduction. On the other hand, the ordered nanostructures, especial for the vertical alignment array structure, can be directly or indirectly used as a mask for nanolithography such as Si, Ge and other semiconductor quantum dots or nanowires array. Nanostructure semiconductor and magnetic array structures are potentially possible for high efficiency information process and storage. Finally, block copolymer forms all kinds of micelles in the solution due to the solubility difference of different blocks, like spherical micelles, rodlike micelles, and vesicles. The functional units like drug molecules, fluorescent agent or magnetic agents can be co-assembled into the micelles in the solution and transferred to the target area for cure or diagnosis. Recently, block copolymer micelles have been extensively used for carrier of the drug delivery, image contrast agents, and fluorescence agents. In brief summary, block copolymer as a robust tool can be extensively using for the synthesis and fabrication of nanomaterials and biomaterials.



Dr. Zaicheng Sun
Member of International Advisory Board

*Corresponding author, e-mail: sunzc@ciomp.ac.cn
© BME-PT

A pH-, salt- and solvent-responsive carboxymethylcellulose-g-poly(sodium acrylate)/medical stone superabsorbent composite with enhanced swelling and responsive properties

W. B. Wang¹, J. X. Xu^{1,2}, A. Q. Wang^{1,*}

¹Center for Eco-material and Green Chemistry, Lanzhou Institute of Chemical Physics, Chinese Academy of Sciences, Lanzhou 730000, P.R. China

²Graduate University of the Chinese Academy of Sciences, Beijing 100049, P.R. China

Received 20 August 2010; accepted in revised form 19 November 2010

Abstract. Free-radical graft copolymerization among sodium carboxymethylcellulose (CMC), partially neutralized acrylic acid (NaA), medical stone (MS) and crosslinker *N,N'*-methylene-bis-acrylamide (MBA) was performed to prepare new carboxymethylcellulose-g-poly(sodium acrylate)/medical stone (CMC-g-PNaA/MS) superabsorbent composites. Fourier transform infrared (FTIR) spectra, thermogravimetry- differential scanning calorimetry (TG-DSC) and field emission scanning electromicroscopic (FESEM) analysis confirmed that NaA had been grafted onto CMC backbone and MS participated in polymerization, and the thermal stability and surface morphologies were improved by the addition of MS. Energy dispersive spectrometer (EDS) and elemental map (EM) analyses revealed the better distribution of MS in the CMC-g-PNaA matrix. The incorporation of 20 wt% MS clearly enhanced the water absorption by 100% (from 317 to 634 g/g). The developed composites showed enhanced swelling rate and On-Off switching swelling characteristics in various pH solutions, saline solutions and hydrophilic organic solvents, which represented interesting and reversible pH-, saline- and hydrophilic organic solvent-responsive characteristics. In addition, the composite exhibited intriguing time-dependent kinetic swelling properties in various heavy metal solutions.

Keywords: polymer composites, carboxymethylcellulose, medical stone, superabsorbent, smart-responsive swelling

1. Introduction

Organic/inorganic composite materials have unwaveringly been the subject of great interests because they frequently exhibited desired hybrid performance superior to their individual components and cost-efficient characteristics [1–4]. Among them, the composites derived from natural polysaccharides and inorganic clay minerals are especially focused by virtue of their unique commercial and environmental advantages [5], and such materials have also been honored as the material families ‘in greening the 21st century materials world’ [6].

Superabsorbents are particular 3-D network hydrophilic functional polymer materials that can absorb and conserve considerable amounts of aqueous liquids even under some pressure. Owing to the advantages over conventional absorbents (e.g. sponge, cotton, wood pulp and colloidal silica, etc.), superabsorbents have found potential application in many fields such as agriculture [7, 8], hygiene articles [9], wastewater treatment [10–13], carrier of catalyst [14] and drug delivery carrier [15, 16], etc. However, most of the practically available superabsorbents are petroleum-based synthetic polymer

*Corresponding author, e-mail: aqwang@licp.cas.cn

with severe environmental impact and high production cost [17], and so the design and development of eco-friendly superabsorbents by introducing natural raw materials have long been desired.

Thus far, many polysaccharides including starch [18, 19], cellulose [20, 21], chitosan [22, 23], alginate [24], and guar gum [25] etc. have been introduced into superabsorbent for improving the performance and environmentally friendly properties. Compared with other natural polymers, cellulose is the most potential one because it is the most abundant natural polymer with renewable, odourless, non-toxic, biodegradable and biocompatible characteristics [26]. However, cellulose is difficult to be directly modified to produce other useful materials due to its poor solubility and reactivity. Carboxymethylcellulose (CMC) is an anionic carboxymethyl ether of cellulose produced by the alkali-catalyzed reaction of cellulose with chloroacetic acid, which has been widely used as a thickening agent and stabilizing agent in industrial fields. The introduced polar carboxyl groups render the cellulose soluble, chemically reactive and strongly hydrophilic, whereas the connatural odourless, tasteless, nontoxic and biodegradable characteristics of cellulose can be retained. So, CMC is advantageous to fabricate eco-friendly polymer materials by its grafting modification [27], and its application in superabsorbent fields becomes attractive and promising. Medical stone (MS) is a special clay mineral that is different from other clays in both structure and properties. MS is an igneous rock composed of silicic acid, aluminum oxide and above 50 kinds of constant and trace elements, and so it was known as 'health-stone' [28]. The main chemical composition of MS is aluminum metasilicate including KAlSi_3O_8 , $\text{NaAlSi}_3\text{O}_8$, $\text{CaAl}_2\text{Si}_2\text{O}_8$, $\text{MgAl}_2\text{Si}_2\text{O}_8$ and $\text{FeAl}_2\text{Si}_2\text{O}_8$, etc. In such a structure, silica (SiO_2) presents regular tetrahedron with a $[\text{SiO}_4]$ configuration, and has a three-dimensional stereo-structure in which aluminum coordinates through oxo-bridging. MS has excellent porosity, multicomponent characteristic, biological activity and safety, and so it shows excellent surface activities, and has been extensively applied in food science, medicine, daily chemical industry, environmental sanitation and wastewater treatment, etc.

[29]. However, few information is available on the application of MS as an inorganic additive for the manufacture of eco-friendly superabsorbent composite materials. So, the composite of CMC, NaA and MS was expected to derive superabsorbent materials with improved network structure and swelling properties.

Based on the above background, in the current work, a series of carboxymethylcellulose-*g*-poly (sodium acrylate)/medical stone (CMC-*g*-PNaA/MS) superabsorbent composites were prepared by the combination of CMC and MS. The structure, thermal stability and morphologies of the developed composites were characterized by Fourier transform infrared spectroscopy (FTIR), thermogravimetric and differential scanning calorimetry analysis (TG-DSC), and field emission scanning electron microscopy (FESEM), energy dispersive spectrometer (EDS) and elemental map (EM) analyses. In addition, the swelling properties, and the stimuli-responsive behaviors of the composite in various medium were evaluated systematically.

2. Experimental

2.1. Materials

Sodium carboxymethylcellulose (CMC, chemically pure, 300~800 mPa·s (25°C)) was from Sinopharm Chemical Reagent Co., Ltd, China. Acrylic acid (AA, chemically pure, Shanghai Shanpu Chemical Factory, Shanghai, China) was distilled under reduced pressure before use. Medical stone (MS) micro-powder (Chinese M-Stone Development Co., Ltd, NaiMan, Inner Mongolia, China) was milled and passed through a 320-mesh screen ($<46 \mu\text{m}$) prior to use, and the main chemical composition is SiO_2 , 68.89%; Al_2O_3 , 14.06%; Fe_2O_3 , 3.61%; K_2O , 3.18%; Na_2O , 4.86%; CaO , 1.33%; MgO , 2.59%. The Cation Exchange Capacity (CEC) is 9.91 meq/100 g, the BET specific surface area is $3.915 \text{ m}^2/\text{g}$ and the average pore size is 11.943 nm. Ammonium persulfate (APS, analytical grade, Xi'an Chemical Reagent Factory, China) and *N,N*-methylene-*bis*-acrylamide (MBA, Chemically Pure, Shanghai Chemical Reagent Corp., China) was used as received. All other reagents used were of analytical grade and all solutions were prepared with distilled water.

2.2. Preparation of CMC-g-PNaA/MS superabsorbent composites

CMC (1.04 g) was dissolved in 30 ml of distilled water at 60°C in a 250 ml four-necked flask equipped with a mechanical stirrer, a thermometer, a reflux condenser and a nitrogen line to obtain a transparent solution. Afterward, 5 ml of the aqueous solution of the initiator APS (72 mg) was added dropwise to the reaction flask under continuous stirring, and kept at 60°C for 10 min to generate radicals. 7.2 g of AA was pre-neutralized using 8.0 ml of 8.5 M NaOH solution, and then crosslinker MBA (21.6 mg) and calculated amount of MS powder (0, 0.44, 0.93, 2.08, 3.57 and 5.57 g, respectively) were added under magnetic stirring to form a uniform dispersion. After cooling the reactant to 50°C, the dispersion was added to the reaction flask, and the temperature was gradually raised to 70°C and kept for 3 h to complete polymerization. Continuous purging of nitrogen was used throughout the reaction period. After being fully washed with distilled water, the obtained gel products were dried to a constant mass at 70°C, ground and passed through a 40–80 mesh sieve (180–380 μm).

2.3. Measurements of equilibrium water absorption and swelling kinetics

Dry sample (about 0.05 g) with the size of 180–380 μm was adequately contacted with excessive aqueous solution at room temperature for 4 h, until a swelling equilibrium was reached. The swollen samples were separated by a 100-mesh screen and then drained on a sieve for 10 min to remove the excess water. After weighing the swollen samples, the equilibrium water absorption of the superabsorbent was calculated using Equation (1):

$$Q_{\text{eq}} = \frac{w_s - w_d}{w_d} \quad (1)$$

where Q_{eq} [g/g] is the equilibrium water absorption calculated as grams of water per gram of sample, which are averages of three measurements; w_d and w_s are the weights of the dry sample and water-swollen sample, respectively.

Kinetic swelling behaviors of superabsorbents in each aqueous solution were measured by the following procedure: 0.05 g samples were immersed in 200 ml of aqueous solution for a set period of time. Then, the swollen gels were filtered using a

sieve, and the water absorption (Q_t) of superabsorbents at a given time (t) can be measured by weighing the swollen and dry samples, and calculated according to Equation (1). In all cases three parallel samples were used and the averages are reported in this paper.

2.4. Evaluation of pH-responsivity

The buffer solutions with various pH values were prepared by combining KH_2PO_4 , K_2HPO_4 , H_3PO_4 and NaOH solution properly and the pH values were determined by a pH meter (DELTA-320). Ionic strengths of all the buffer solutions were controlled to 0.1 M using NaCl. The equilibrium water absorption (Q_{eq}) of the composite in various pH buffer solutions was measured by a method similar to that in distilled water. The pH-reversibility of the superabsorbent composites was investigated in terms of their swelling and deswelling between pH 2.0 and 7.2 buffer solution of phosphate. Typically, the sample particle (0.05 g, 180–380 μm) was placed in a 100 mesh sieve and adequately contacted with pH 2.0 buffer solution, 154 mmol/l LiCl, NaCl or KCl solutions and distilled water until reaching equilibrium. Then, the swollen samples were soaked in pH 7.2 buffer solutions, distilled water, and methanol or ethanol for set time intervals. Finally, the swollen samples were filtered, weighed and then calculated the water absorption at a given moment according to the mass change of samples before and after swelling. The consecutive time interval is 15 min for each cycle, and the same procedure was repeated for four cycles. After every measurement, each solution was renewed.

2.5. Determination of network parameter M_c

The swelling properties of the superabsorbent depend on the crosslinking density, which can be reflected by the average molar mass among the crosslinks, M_c . M_c value is reversibly proportional to crosslinking density and can be calculated by a previously developed method [30, 31]. Typically, M_c can be expressed as Equation (2) according to Flory-Huggins theory [32]:

$$M_c = Q^{5/3} \cdot \frac{D_2 V_1}{0.5 - X_1} \quad (2)$$

where Q represents the equilibrium water absorption of the superabsorbent; D_2 denotes the density

of superabsorbent; V_1 denotes the molar volume of the solvent used for swelling studies and X_1 is the Flory-Huggins interaction parameter between solvent and superabsorbent. Because it is difficult to determine X_1 by experiment, the linear relationship between X_1 and C (the volume fractions of methanol in methanol/water mixture) was established to determine X_1 value (Equation (3)):

$$X_1 = K_1 C + K_2 \quad (3)$$

After simplified above equations, it was concluded that the relations among each parameter follows Equation (4):

$$D_2 V_1 Q^{5/3}_{\text{methanol-water}} = M_c (0.5 - K_1 C) \quad (4)$$

The plots of $D_2 V_1 Q^{5/3}_{\text{methanol-water}}$ against C give a set of straight lines, and the M_c can be calculated according to the slope of the resulting lines for each superabsorbent.

2.6. Characterizations

FTIR spectra were recorded on a Nicolet NEXUS FTIR spectrometer in 4000–400 cm^{-1} region using KBr pellets. The composite sample after swelling in various heavy metal solutions was fully washed and dried before FTIR determination. The surface morphologies, energy dispersive spectrometer (EDS) and elemental map (EM) of the samples were examined using a JSM-6701F Field Emission Scanning Electron Microscope (JEOL) after coating the

sample with gold film. Thermogravimetric (TG) and Differential scanning calorimetry (DSC) analyses of samples was studied on a Perkin-Elmer TGA-7 thermogravimetric analyzer (Perkin-Elmer Cetus Instruments, Norwalk, CT), with a temperature range of 25–700°C at a heating rate of 10 °C/min using dry nitrogen purge at a flow rate of 50 ml/min. The samples were dried at 100°C for 4 h to remove the absorbed water before determining TG-DSC curves.

3. Results and discussion

3.1. FTIR spectra analysis

As shown in Figure 1, the characteristic absorption bands of CMC at 1061, 1118 and 1162 cm^{-1} (stretching vibration of C–OH groups) were obviously weakened after reaction and shifted to 1056, 1111 and 1169 cm^{-1} for CMC-g-PNaA. The new bands at 1714 cm^{-1} (C=O stretching of –COOH groups), 1568 cm^{-1} (asymmetrical stretching vibration of –COO[−] groups), 1454 and 1409 cm^{-1} (symmetrical stretching vibration of –COO[−] groups) appeared in the spectrum of CMC-g-PNaA (Figure 1b). This result indicates that NaA monomers were grafted onto CMC backbone. Compared with the spectrum of CMC-g-PNaA, the –C=O stretching of –COOH groups at 1714 cm^{-1} shifted to 1715 cm^{-1} , and the asymmetrical stretching of –COO[−] groups at 1568 cm^{-1} shifted to 1572 cm^{-1} after forming composite. The stretching vibration of (Si)O–H at

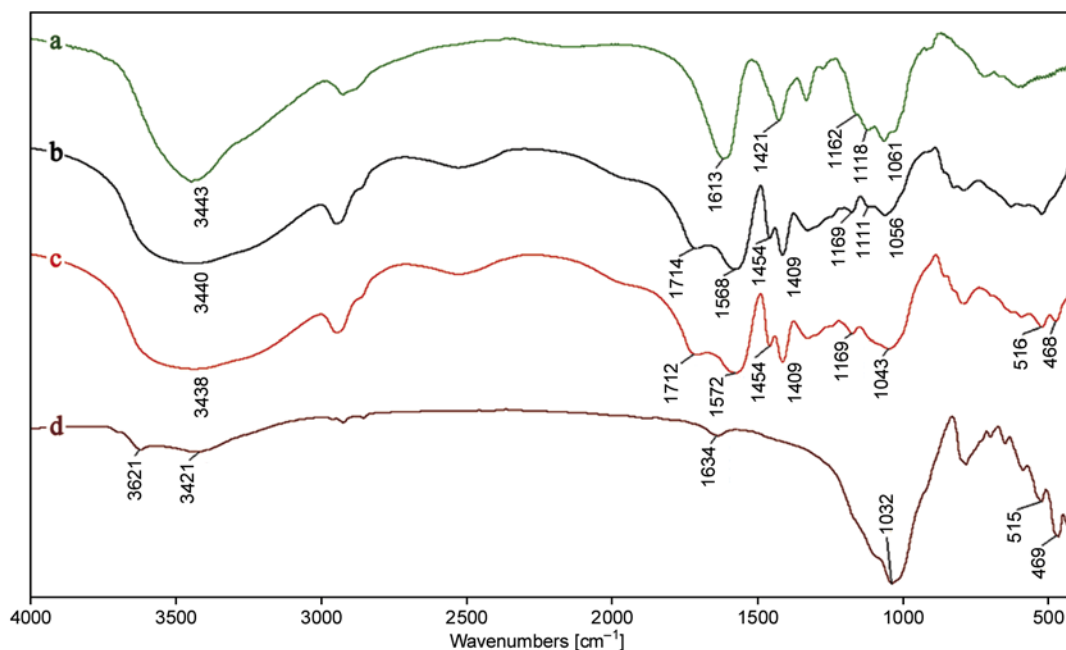


Figure 1. FTIR spectra of (a) CMC, (b) CMC-g-PNaA, (c) CMC-g-PNaA/MS (20 wt%), and (d) MS

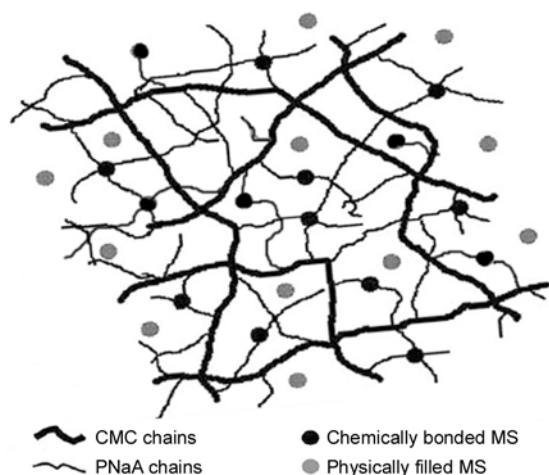


Figure 2. Schematic representation of the CMC-g-PNaA/MS superabsorbent composite

3621 cm^{-1} can almost not be observed in the spectrum of CMC-g-PNaA/MS (Figure 1c, d). The Si–O stretching vibration of MS at 1032 cm^{-1} shifted to 1043 cm^{-1} after forming composite, but its intensity was obviously weakened. The Si–O bending vibration at 468 cm^{-1} can be observed in the spectrum of CMC-g-PNaA/MS with weakened intensity. This information gives direct evidence that MS participated in the graft copolymerization reaction through its active silanol groups [33–35]. Moreover, a schematic structure illustration of the CMC-g-PNaA/MS superabsorbent composite is presented in Figure 2, the MS existed in the polymer matrix can be classified as two kinds: chemically bonding and physically filling [35].

3.2. TG-DSC analyses

Figure 3 showed the TG-DSC curves of CMC-g-PNaA hydrogel and CMC-g-PNaA/MS (20 wt%) composite. It is obvious that introduction of MS exhibited great influence on the thermal behaviors of the superabsorbents. The weight loss about 6.4 wt% below 251°C for CMC-g-PNaA (corresponding to an endothermic step at 248°C) and about 4.9 wt% below 254.7°C for CMC-g-PNaA/MS (corresponding to an endothermic step at 253°C) can be ascribed to the removal of water absorbed, the dehydration of saccharide rings in the chain of CMC [36]. The successive weight loss about 20.4 wt% ($251\text{--}432^\circ\text{C}$) for CMC-g-PNaA and about 17.3 wt% ($255\text{--}436^\circ\text{C}$) for CMC-g-PNaA/MS can be attributed to the breaking of C–O–C bonds in CMC chains (corresponding to the

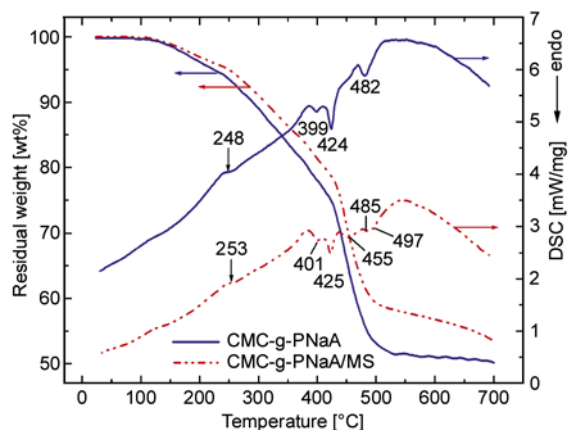


Figure 3. TG-DSC curves of CMC-g-PNaA and CMC-g-PNaA/MS (20 wt%)

endothermic peaks at 399°C for CMC-g-PNaA and 401°C for CMC-g-PNaA/MS) and the elimination of water molecule derived from the two neighboring carboxylic groups of the grafted PNaA chains due to the formation of anhydride (corresponding to the endothermic peak at 424°C for CMC-g-PNaA and 425°C for CMC-g-PNaA/MS) [37]. However, the endothermic peak of CMC-g-PNaA/MS at 425°C is obviously weaker than that of CMC-g-PNaA, and the new endothermic peak at 455°C also appeared in the DSC curve of CMC-g-PNaA/MS. This indicates that the thermal decomposition process in this region was relieved by introducing MS. The weight losses about 20.1 wt% from 432 to 502°C for CMC-g-PNaA (corresponding to a sharp endothermic peak at 482°C) and about 19.1 wt% from 436 to 504°C for CMC-g-PNaA/MS (corresponding to the continuous endothermic peak from 485 to 497°C) are due to the breakage of main-chain scission and the destruction of crosslinked network structure. Compared with the sharp endothermic peak of CMC-g-PNaA, the appearance of continuous endothermic peak in the DSC curve of CMC-g-PNaA/MS reveals that the thermal decomposition of the superabsorbent was delayed after incorporating MS. As described above, CMC-g-PNaA/MS composite exhibited slower weight-loss and thermal decomposition rate as well as lesser total weight loss than CMC-g-PNaA, which indicated the incorporation of MS improved the thermal stability of superabsorbent.

3.3. FESEM, EDS and EM analyses

Figure 4 showed the FESEM micrographs of CMC-g-PNaA, MS and CMC-g-PNaA/MS (20 and 40 wt%)

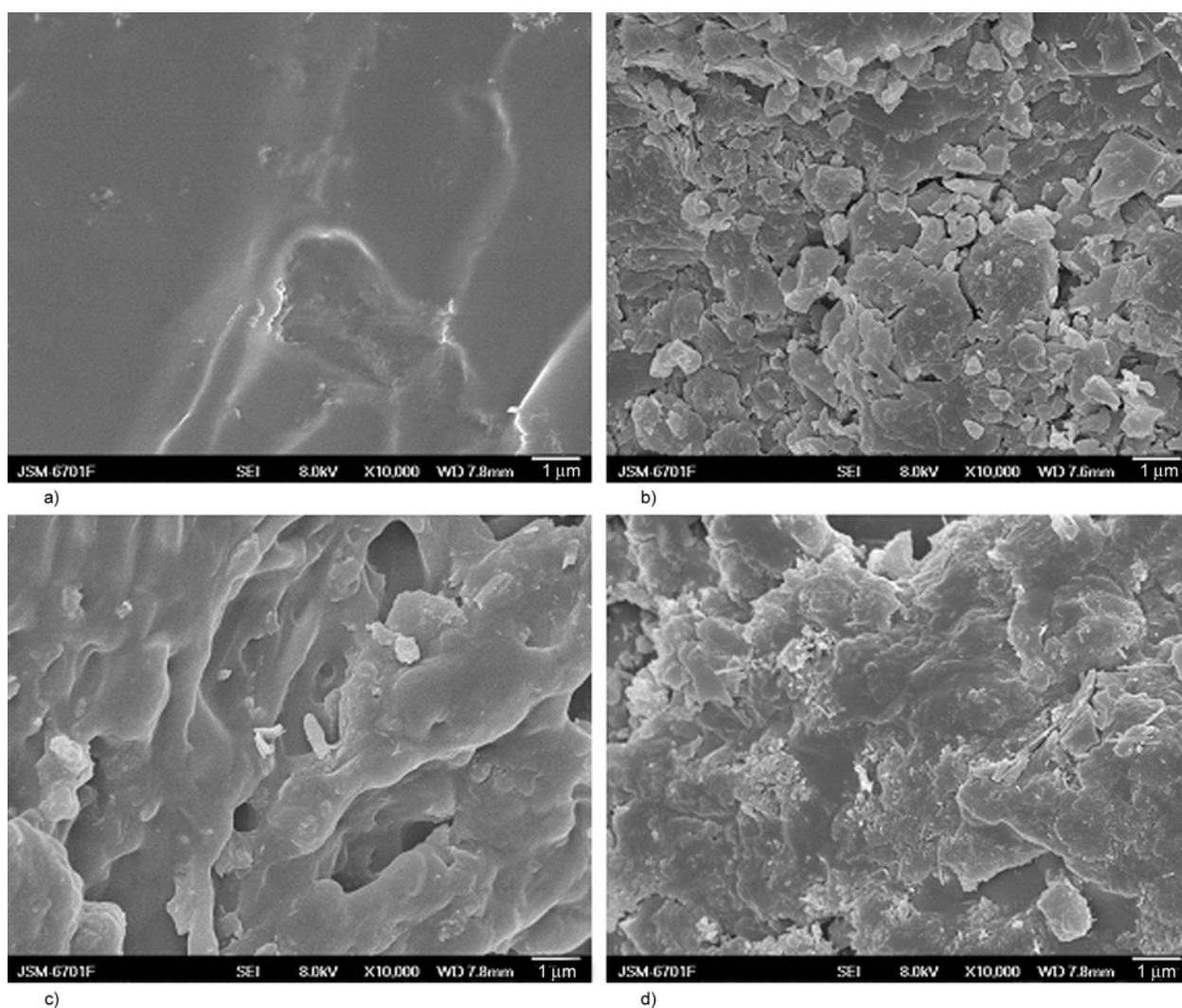


Figure 4. FESEM micrographs of (a) CMC-g-PNaA, (b) MS, (c) CMC-g-PNaA/MS (20 wt%), and (d) CMC-g-PNaA/MS (40 wt%)

superabsorbent composite. As can be seen, CMC-g-PNaA only has a smooth and dense morphology (Figure 4a), and MS shows a correspondingly coarse and sheet surface morphology (Figure 4b). After compounding MS with CMC-g-PNaA, the surface roughness of the superabsorbent was obviously increased and some pores and gap can be observed (Figure 4c), and the surface roughness of CMC-g-PNaA/MS increased with increasing the content of MS (Figure 4d), which implies that introduction of MS contributes to improve the surface morphology of the resultant composite. In addition, this observation gives a direct revelation that MS was uniformly dispersed and almost embedded within the polymer matrix without the flocculation of MS particles, and formed a homogeneous combination of MS with the matrix network.

Figure 5 shows the EDS spectrograms of CMC-g-PNaA, MS and CMC-g-PNaA/MS (20 and 40 wt%), corresponding to the surface of samples shown in Figure 4a–4d). As can be seen, only the characteristic peaks of C, O and Na elements can be observed in the EDS spectrogram of CMC-g-PNaA. After forming CMC-g-PNaA/MS composites, the Si, Al, K, Ca, Fe, Na and Mg elements ascribed to MS (Figure 5b) can also be observed, indicating that MS was distributed in the polymer matrix. For further proving this, the elemental maps (EM) for each sample were examined and are shown in Figure 6. It can be noticed that the characteristic O, Si, Al, K, Ca, Fe, Na and Mg elements of MS clearly appeared in the elemental map of the composites, and these elements showed equal distribution in the CMC-g-PNaA matrix. This result is consistent with the

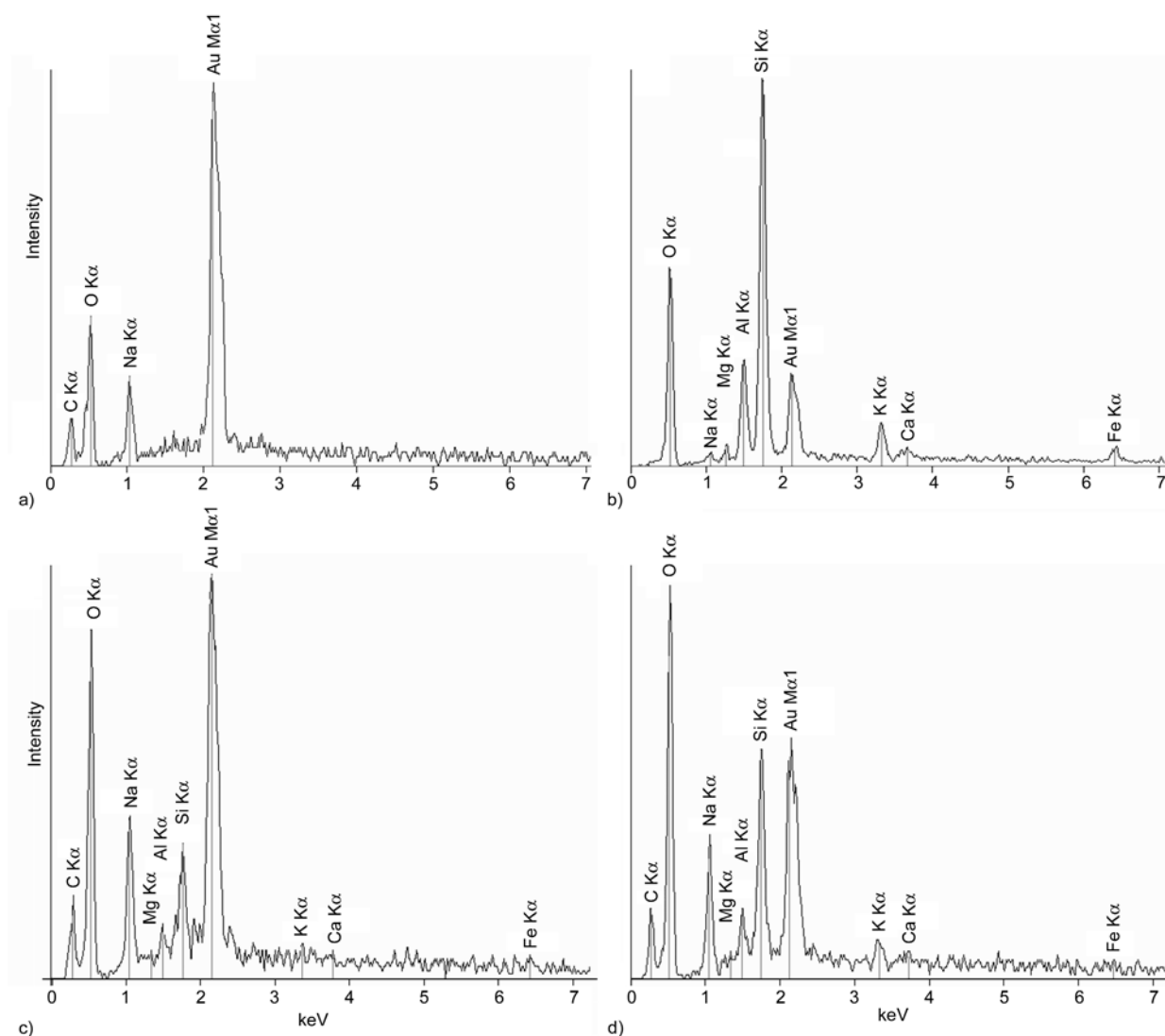


Figure 5. EDS curves of (a) CMC-g-PNaA, (b) MS, (c) CMC-g-PNaA/MS (20 wt%) and (d) CMC-g-PNaA/MS (40 wt%)

FESEM observations and EDS results, and reveals the uniform composite of CMC-g-PNaA matrix with MS.

3.4. Effects of MS content on M_c and water absorption

As shown in Figure 7, the M_c of the superabsorbent composite firstly increased and then decreased with increasing the content of MS. A similar tendency can be observed for the water absorption curves of the superabsorbents. The water absorption sharply increased with increasing the content of MS until a maximum absorption (634 g/g in distilled water and 60 g/g in 0.9 wt% NaCl solution) was achieved at 20 wt% MS, and then decreased with further increasing MS content. In comparison with the MS-free superabsorbent hydrogel, the water absorption of

the composite increased by 99% after incorporating 20 wt% of MS. This observation indicates that the water absorption of the superabsorbent is mainly dependent on the crosslinking density. The obvious enhancement of water absorption can be attributed to the following reasons: (1) MS may participate in polymerization reaction and act as additional crosslinker. As a result, the polymer network structure was improved and the network void for holding was regularly formed, and the water absorption capacity of the superabsorbent was improved [35, 38]; (2) MS can ionize and release lots of metal cations in contact with water [29], which increased the concentration of electrolyte in interior gel network and enhanced the osmotic pressure difference between gel network and swelling media, and so the water absorption can be enhanced; (3) ionization of

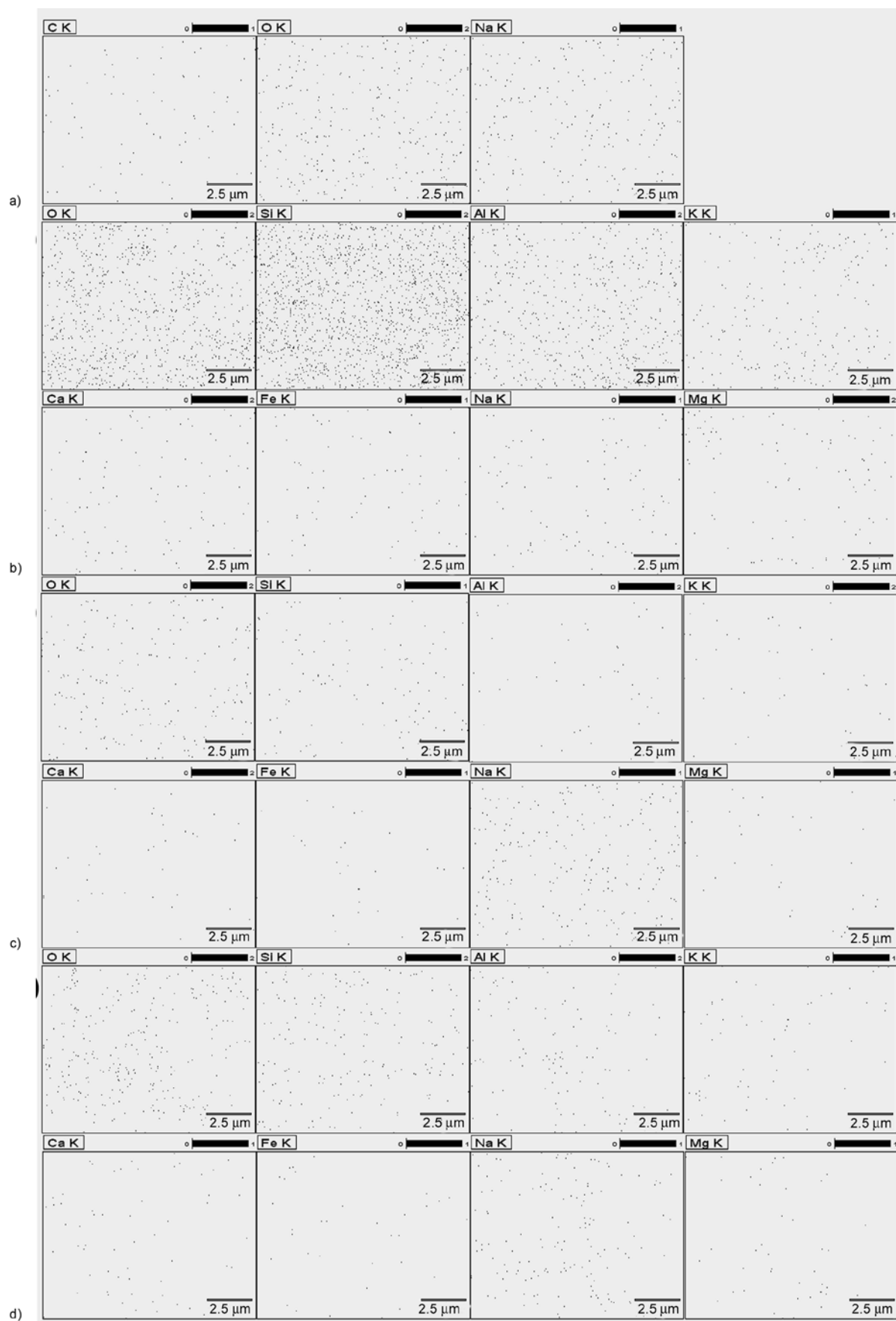


Figure 6. Element area profiles of (a) CMC-g-PNaA, (b) MS, (c) CMC-g-PNaA/MS (20 wt%) and (d) CMC-g-PNaA/MS (40 wt%) at the magnification of 10 000 \times . The small dots denote the distribution of each element in the polymeric matrix

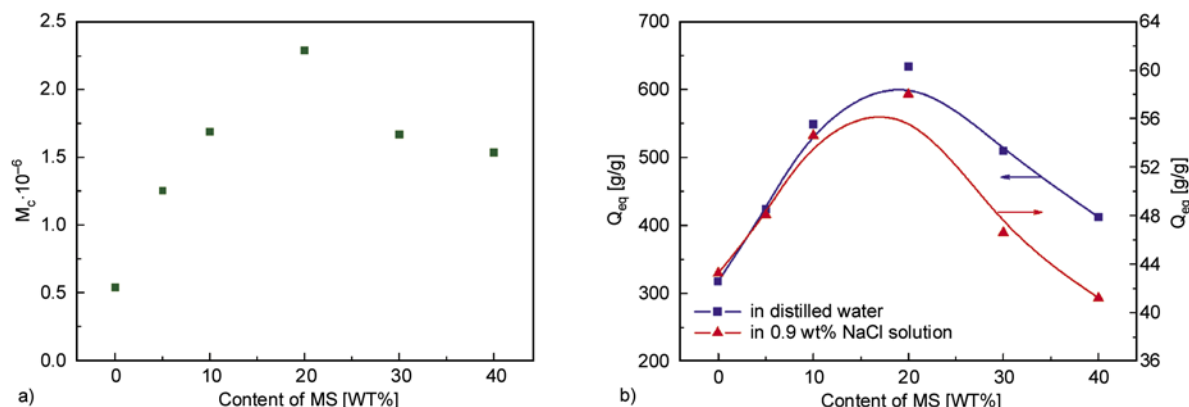


Figure 7. Effects of MS content on M_c (a) and water absorption (b)

MS may generate $[-SiO]^-$ groups [29], which can repulse with the negatively charged graft polymer chains and facilitate to the expansion of gel network, and thus contribute to improve the water absorption. However, the excessive addition of MS induced a decrease of water absorption. Because the excessive MS particles may physically fill in the polymer network, which may plug up the network voids for holding water and decrease the hydrophilicity of the composite. For this reason, the water absorption decreased with the increase of the MS content above 20 wt%. It deserves to be mentioned that the water absorption of the composite is till higher than the hydrogel without MS even the content of MS reached 40 wt%, which is extremely favorable to reduce the production cost.

3.5. Swelling kinetics in distilled water

Kinetic swelling curves of the superabsorbents in distilled water were depicted in Figure 8. It can be noticed that the water absorption sharply increased

with prolonging contact time at initial stage (<1200 s), and then the increasing trend becomes flatter until swelling equilibrium was reached (about 1800 s). In this section, Schott's pseudo second order kinetics model was used to evaluate the swelling kinetics of the superabsorbents (Equation (5)) [39]:

$$\frac{t}{Q_t} = \frac{1}{K_{is}} + \frac{1}{Q_\infty}t \quad (5)$$

where Q_t is the water absorption at a set swelling time t [s]; Q_∞ is the theoretical equilibrium water absorption [g/g]; K_{is} is the initial swelling rate constant [g/(g·s)]. As shown in Figure 8b), the plots of t/Q_t against t showed straight lines with better linear correlation coefficient, indicating that the kinetic swelling behaviors of the superabsorbents follow the pseudo second order model. The values of K_{is} , Q_∞ and swelling rate constant $K_s (= K_{is}/Q_{eq}^2, [g/(g·s)])$ can be determined by fitting experimental data using Equation (5) and calculated by the slope and intercept of the straight lines (Table 1). According

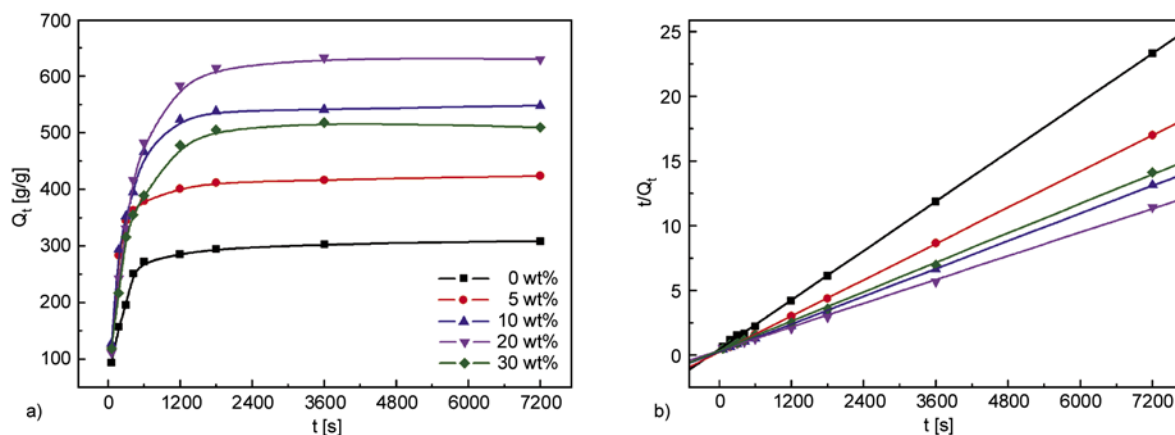


Figure 8. Swelling kinetic curves of the superabsorbents in distilled water (a) and the plots of t/Q_t against t for each superabsorbent (b)

Table 1. Swelling kinetic parameters for CMC-g-PNaA/MS composites with various amounts of MS

Samples	Q_{eq} [g/g]	Q_{∞} [g/g]	K_{is} [g/(g·s)]	$K_s \cdot 10^{-5}$ [g/(g·s)]	R
CMC-g-PNaA	318	315	2.2783	2.2530	0.9999
CMC-g-PNaA/MS (5 wt%)	424	429	4.6092	2.5639	0.9999
CMC-g-PNaA/MS (10 wt%)	549	562	3.8069	1.2631	0.9998
CMC-g-PNaA/MS (20 wt%)	633	648	2.8820	0.7193	0.9995
CMC-g-PNaA/MS (30 wt%)	514	529	2.8636	1.0839	0.9995

*Initial swelling rate constant K_{is} ; **Swelling rate constant $K_s = K_{is}/Q_{eq}^2$

to the resultant data, it can be concluded that the initial swelling rate of the superabsorbents decreased in the order of CMC-g-PNaA/MS (5 wt%) > CMC-g-PNaA/MS (10 wt%) > CMC-g-PNaA/MS (20 wt%) > CMC-g-PNaA/MS (30 wt%) > CMC-g-PNaA. This result reveals that incorporation of MS also enhanced the initial water absorption rate of the superabsorbents besides water absorption capability. It can also be noticed that the swelling rate constant (K_s) in the whole swelling process follow the order of CMC-g-PNaA/MS (5 wt%) > CMC-g-PNaA > CMC-g-PNaA/MS (10 wt%) > CMC-g-PNaA/MS (30 wt%) > CMC-g-PNaA/MS (20 wt%), indicating the moderate introduction of MS (5 wt%) is favorable to improve the swelling rate. However, the change trend of K_s is not consistent with that of K_{is} . This is because that the water absorption (Q_{eq}) of the superabsorbent composites with 10, 20 and 30 wt% of MS is higher than CMC-g-PNaA hydrogel. This means that the polymer chains need to move greater distance for reaching the swelling equilibrium, so the time of reaching equilibrium for CMC-g-PNaA/MS (10, 20 and 30 wt%) is relatively longer than that of CMC-g-PNaA.

3.6. pH-responsive characteristics

It can be noticed from Figure 9 that the water absorption of the composite is almost zero at pH 2.0 for both CMC-g-PNaA hydrogel and CMC-g-PNaA/MS composite, but the water absorption rapidly increased with enhancing the pH of external solution, and almost keep constant in the pH range of 6–12. The water absorption follows the order of CMC-g-PNaA/MS (20 wt%) > CMC-g-PNaA/MS (10 wt%) > CMC-g-PNaA/MS (30 wt%) > CMC-g-PNaA at pH 7.2. In acidic medium, the $-\text{COO}^-$ groups on the polymer chain converted to $-\text{COOH}$ groups. For one thing, the electrostatic repulsion among negatively charged $-\text{COO}^-$ groups decreased and the expansion of polymer network was restricted; for another, the increase of number of $-\text{COOH}$

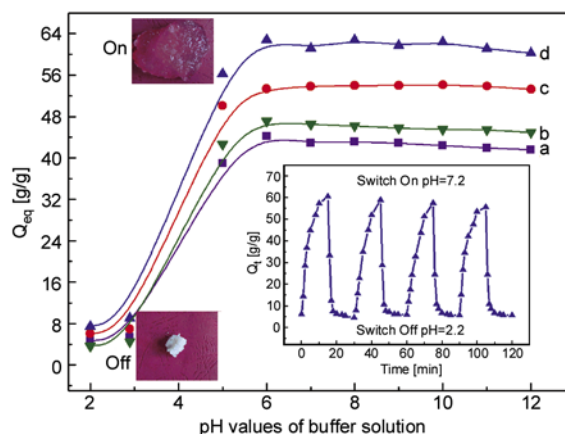


Figure 9. Variation of swelling ratio for (a) CMC-g-PNaA, (b) CMC-g-PNaA/MS (30 wt%), (c) CMC-g-PNaA/MS (10 wt%) and (d) CMC-g-PNaA/MS (20 wt%) superabsorbents at the buffer solution with various pHs. The inset is the On-Off switching behavior as reversible pulsatile swelling (pH = 7.2) and deswelling (pH = 2.0) of CMC-g-PNaA/MS (20 wt%) composite. The time interval between pH changes is 15 min.

groups strengthened the intramolecular and intermolecular hydrogen bonding interaction and enhanced the physical crosslinking degree. Thus, the polymer network swells little at low pH. For evaluating the reversibility of pH-responsivity, the swelling-deswelling cycles were evaluated between the buffer solutions of pH 2.0 (Off) and 7.2 (On). It can be obviously observed that the composite shrunken at pH 2.0 can recover to relatively higher swelling ratio at pH 7.2. After four swelling-deswelling periods between pH 2.0 and 7.2, the intriguing On-Off switchable and reversible swelling effect was observed. This implies that the pH-responsivity of the superabsorbent composite is highly reversible and the introduction of MS effectively enhanced the responsivity of the superabsorbent.

3.7. Salt-responsive characteristics

Figure 10 depicts the circular swelling-deswelling behaviors of the superabsorbent composite between distilled water and 154 mmol/l of LiCl, NaCl and

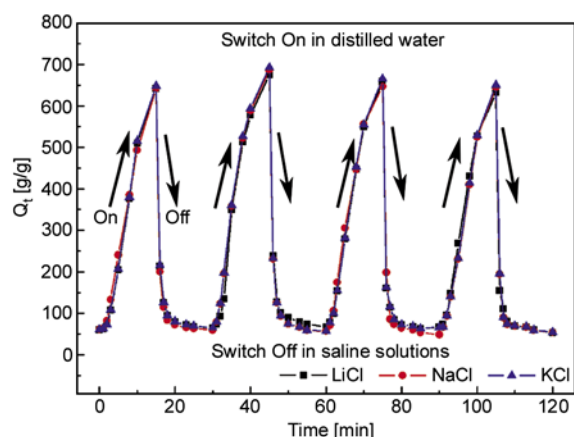


Figure 10. The reversible On-Off switching swelling behaviors of the composite between distilled and 154 mmol/l of LiCl, NaCl and KCl solutions

KCl solutions. As can be seen, the water-swollen superabsorbent composite can shrink and loss the absorbed water when it was contacted with salt solutions, but the shrunken gel can rapidly recovered in distilled water. The switching salt stimuli-responsive characteristics were observed. As well known, the osmotic pressure difference between internal gel network and external swelling media acts as the driving force for the swelling of superabsorbent; it decreases with adding polyelectrolyte to the solution. Also, the ultimate screen effects of cations on negative charges of polymer chains increased with increasing polyelectrolyte in the solution. These factors induced the deswelling of the composite. After four circles of swelling (On)-deswelling (Off), the superabsorbent still keeps excellent responsive properties, indicating the swelling of the superabsorbent is switched and reversible.

3.8. Hydrophilic organic solvents-responsive characteristics

The phase transitions of hydrogels have aroused attention since the collapse of polyacrylamide hydrogels in aqueous solution of acetone was observed [40]. The unique phase transition behavior of superabsorbent to organic solvents endows it with stimuli-responsive characteristics. Figure 11 represents the swelling (On)-deswelling (Off) cyclic curves of the superabsorbent composite between distilled water (On) and methanol or ethanol (Off). It was noticed that the composite exhibited higher water absorption in distilled water, but the absorbed water was sharply lost when it was fully contacted with

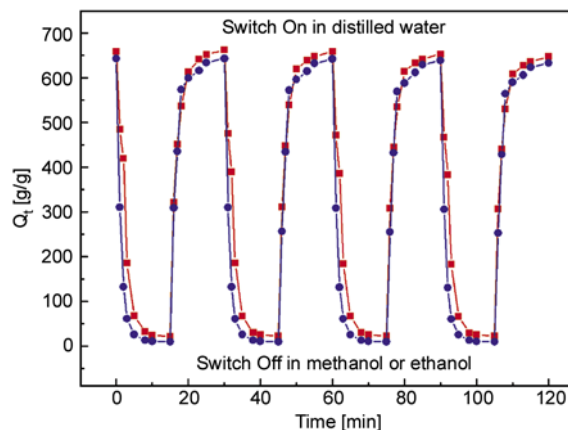


Figure 11. The reversible On-Off swelling behaviors of the composite between distilled water and methanol or ethanol

hydrophilic organic solvent. The great shrinkage of the water absorption in hydrophilic organic solvents can be attributed to the decrease of the solubility parameter and dielectric constant as well as the interaction between the polar groups of organic solvent and the ionic groups in the polymer [41]. The solubility parameter of water is $23.4 \text{ (cal/cm}^3)^{1/2}$, but the value of methanol and ethanol is only 14.5 and 12.7 $(\text{cal/cm}^3)^{1/2}$. The great decrease of solubility parameter caused the rapid shrinkage of water absorption [42]. Likewise, the dielectric constant of water is 78.54, but the dielectric constant of methanol and ethanol is only 32.63 and 24.3. As described previously [41], the dielectric constant of the solution directly affects the ionization degree of ionic groups, and the larger the dielectric constant of the solution, the bigger the osmotic pressure of the gel. Thus, the sharp decrease of dielectric constant from hydrophilic organic solvents to water certainly causes the reduction of water absorption. In addition, the polarity of water is larger than methanol and ethanol. The lower polarity of ethanol and methanol is responsible for the easier collapse of composite network in contrast to water [43]. These indicate that the collapse of the composite is a result of the total depletion of water due to the competitive extraction of water from the solvated polymeric network. It can also be observed from Figure 11 that the shrunken gel can rapidly recovered when it was immersed in distilled water, and no obvious slack after four On-Off cycles. This indicates that the hydrophilic organic solvent-responsive properties of the composite are switching and reversible.

3.9. Time-dependent characteristics in heavy-metal solutions

Effects of heavy metal saline solutions on kinetic swelling behaviors of the composite were evaluated in NiCl_2 , CuCl_2 and ZnCl_2 solutions at the concentration of 2, 5 and 10 mmol/l (Figure 12). An intriguing time-dependent swelling behavior was observed for the composite in each saline solution. The water absorption of the composite increased with prolonging contact time, reached a maximum absorption (127, 63 and 40 g/g for 2, 5 and 10 mmol/l of Ni^{2+} ; 126, 65 and 39 g/g for 2, 5 and 10 mmol/l of Cu^{2+} ; and 130, 70 and 41 g/g for 2, 5 and 10 mmol/l of Zn^{2+} , respectively) with further prolonging contact time and then decreased until the swelling almost disappeared. Also, the required time of reaching the maximum absorption was reduced with increasing the concentration of saline solution (12, 8 and 5 min for 2, 5 and 10 mmol/l of each saline solution, respectively). The time-dependent swelling effect can be attributed to the following reasons depicted in Figure 13. The superabsorbent composite contains numerous $-\text{COOH}$ and $-\text{COO}^-$ functional groups, which can complex with heavy metal cations to form an additional ionic crosslinking [12, 44]. So the effective crosslinking degree of composite network increased with prolonging the contact time. Also, the complex of $-\text{COO}^-$ with heavy metal cations would decrease electrostatic repulsion among negatively charged polymer chains and reduce the expansion degree of the hydrogel network. As a result, the absorbed water would be expelled out from the network void and the swollen hydrogel tends to shrink. After reaching the maximum swelling, the swollen composite network gradually collapsed and the initially absorbed water was squeezed out of the network under this action. For proving the complex action, the FTIR spectra of the composite after swelling in 5 mmol/l NiCl_2 , CuCl_2 and ZnCl_2 solutions for 0.5, 5, 10, 30 and 120 min were determined and are shown in Figure 14. As can be seen, the characteristic absorption bands of $-\text{COO}^-$ groups at 1572 cm^{-1} (Figure 1c) shifted to 1571 (Ni^{2+} , 0.5 min), 1568 (Ni^{2+} , 5 min), 1561 (Ni^{2+} , 10 min), 1558 (Ni^{2+} , 30 min) and 1556 cm^{-1} (Ni^{2+} , 120 min); to 1570 (Cu^{2+} , 0.5 min), 1569 (Cu^{2+} , 5 min), 1563 (Cu^{2+} , 10 min), 1560 (Cu^{2+} , 30 min) and 1557 cm^{-1} (Cu^{2+} , 120 min); to 1571

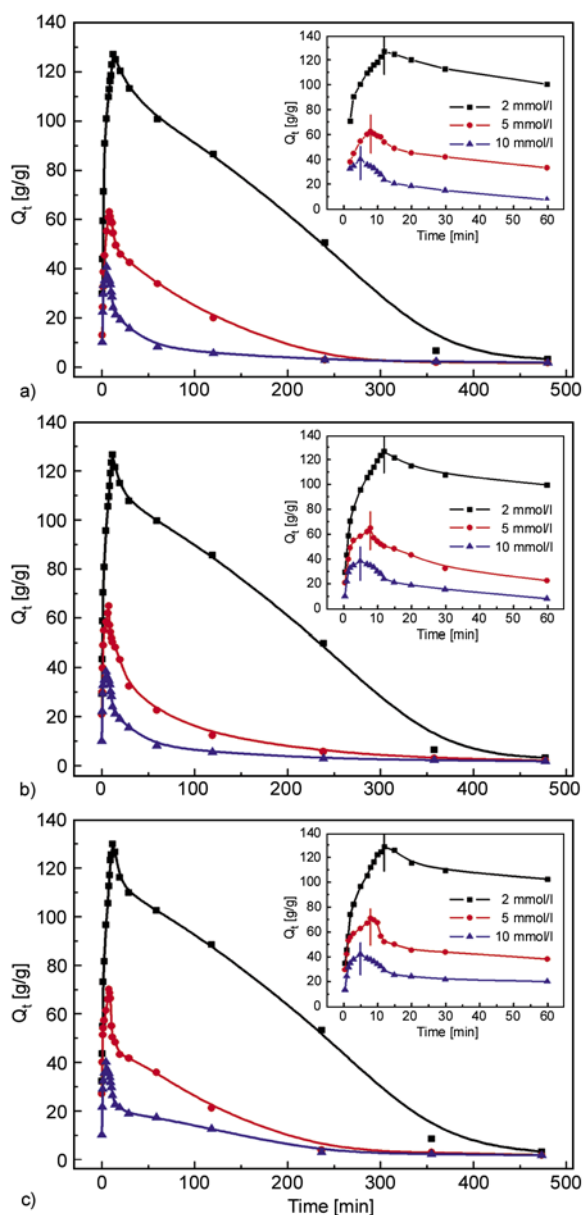


Figure 12. Kinetic swelling curves of CMC-g-PNaA/MS (20 wt%) in 2, 5 and 10 mmol/l of (a) NiCl_2 , (b) CuCl_2 and (c) ZnCl_2 solutions. The insets are the enlargement of the curves ranged from 0–60 min.

(Zn^{2+} , 5 min), 1570 (Zn^{2+} , 10 min), 1568 (Zn^{2+} , 30 min) and 1563 cm^{-1} (Zn^{2+} , 120 min) after swelling in heavy metal saline solutions for different interval, respectively. The shift of absorption band to low wavenumber indicates that Ni^{2+} , Cu^{2+} and Zn^{2+} ions were complexed with $-\text{COO}^-$ groups [44] and the additional crosslinking in hydrophilic network was formed, and so the swollen gel network tends to deswell.

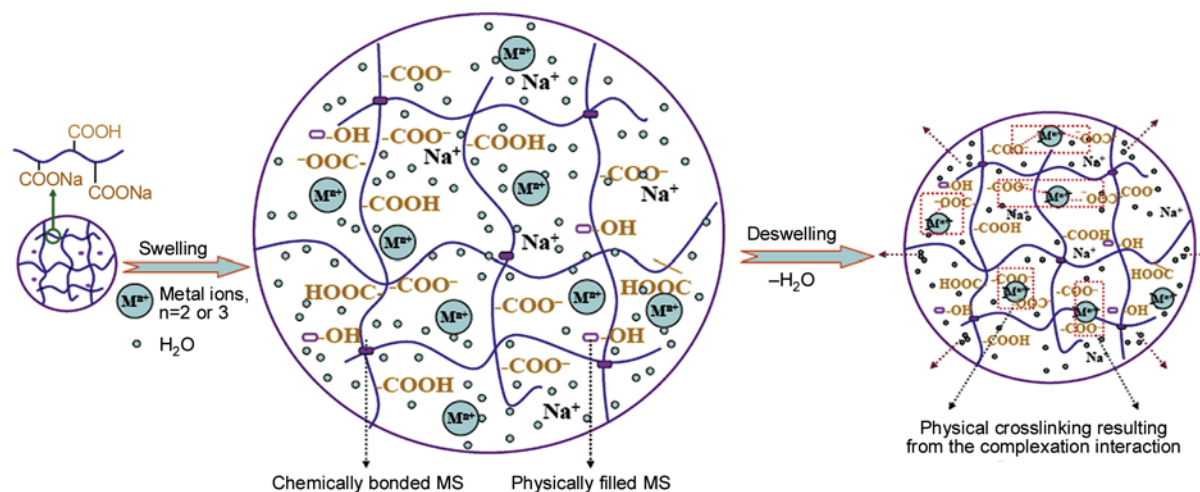


Figure 13. Proposed mechanism for the swelling–deswelling of the composite in heavy metal solutions

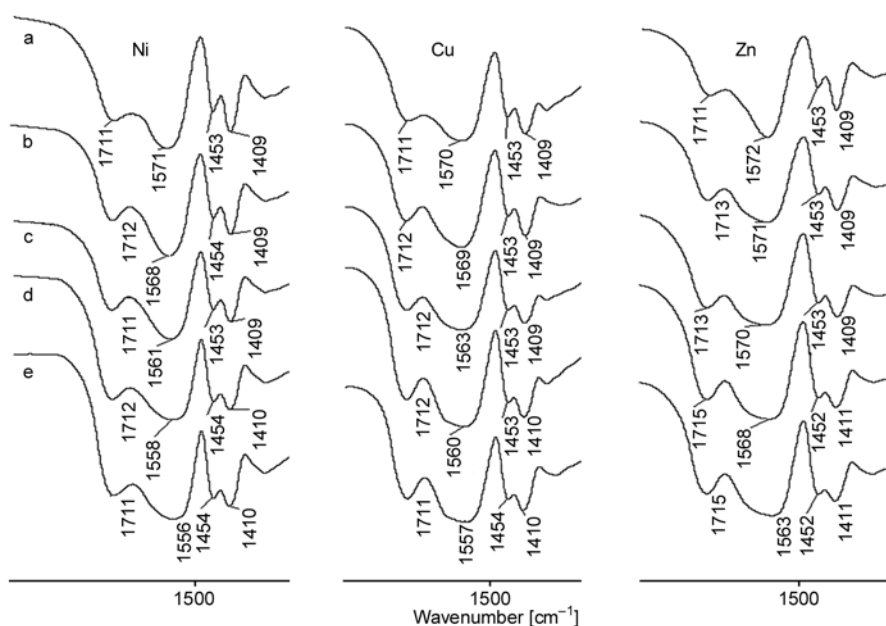


Figure 14. FTIR spectra of the superabsorbent composite after swelling in 5 mmol/l $NiCl_2$, $CuCl_2$ and $ZnCl_2$ solutions for (a) 0.5 min, (b) 5 min, (c) 10 min, (d) 30 min, (e) 120 min

4. Conclusions

For developing new kinds of superabsorbent composites with improved structure, properties and environmentally friendly characteristics, reducing the excessive consumption of petroleum resource and minimizing the pollution from the industrial polymers, a series of cellulose-based superabsorbent composites containing MS were prepared by free-radical graft copolymerization technique. FTIR analysis revealed that the NaA monomers had been grafted onto the macromolecular chains of CMC, and MS participated in the polymer reaction and combined with the network by chemically crosslinking and physically filling models. MS led

to a better dispersion in the CMC-*g*-PNaA matrix as shown by EDS and EM analyses. The incorporation of MS and the formation of composite structure clearly improved the surface morphologies, thermal stability, swelling capabilities, and swelling rate of the developed composite. The superabsorbent composite exhibited excellent switching swelling-deswelling behaviors between pH 2.0 and 7.2 buffer solution, between distilled water and 154 mmol/l LiCl, NaCl and KCl solutions, between distilled water and hydrophilic organic solvents, and the obvious pH-responsive, saline-responsive and hydrophilic organic solvent-responsive properties were presented. In addition, the intriguing time-

dependent swelling behaviors were observed in various heavy metal saline solutions, which are caused by the strong complexation action between hydrophilic $-\text{COO}^-$ groups and heavy metal ions. As described above, the superabsorbent composite based on renewable, low-cost and biodegradable natural CMC and abundant MS exhibited improved swelling properties, excellent pH-responsive, salt-reversible, hydrophilic organic solvent-reversible properties and intriguing time-dependent swelling behavior, which can be used as potential candidate for water-manageable materials or drug delivery system.

Acknowledgements

The authors thank for jointly supporting by the National Natural Science Foundation of China (No. 20877077) and 1863rd Project of the Ministry of Science and Technology, P. R. China (No. 2006AA100215).

References

- [1] Paul D. R., Robeson L. M.: Polymer nanotechnology: Nanocomposites. *Polymer*, **49**, 3187–3204 (2008). DOI: [10.1016/j.polymer.2008.04.017](https://doi.org/10.1016/j.polymer.2008.04.017)
- [2] Utracki L. A., Sepehr M., Boccaleri E.: Synthetic, layered nanoparticles for polymeric nanocomposites (PNCs). *Polymers for Advanced Technologies*, **18**, 1–37 (2007). DOI: [10.1002/pat.852](https://doi.org/10.1002/pat.852)
- [3] Dalaran M., Emik S., Güçlü G., İyim T. B., Özgümüş S.: Removal of acidic dye from aqueous solutions using poly(DMAEMA–AMPS–HEMA) terpolymer/MMT nanocomposite hydrogels. *Polymer Bulletin*, **63**, 159–171 (2009). DOI: [10.1007/s00289-009-0077-4](https://doi.org/10.1007/s00289-009-0077-4)
- [4] Zhang J. P., Wang A. Q.: Synergistic effects of Na^+ -montmorillonite and multi-walled carbon nanotubes on mechanical properties of chitosan film. *Express Polymer Letters*, **3**, 302–308 (2009). DOI: [10.3144/expresspolymlett.2009.38](https://doi.org/10.3144/expresspolymlett.2009.38)
- [5] Šimkovic I.: What could be greener than composites made from polysaccharides? *Carbohydrate Polymers*, **74**, 759–762 (2008). DOI: [10.1016/j.carbpol.2008.07.009](https://doi.org/10.1016/j.carbpol.2008.07.009)
- [6] Ray S. S., Bousmina M.: Biodegradable polymers and their layered silicate nanocomposites: In greening the 21st century materials world. *Progress in Materials Science*, **50**, 962–1079 (2005). DOI: [10.1016/j.pmatsci.2005.05.002](https://doi.org/10.1016/j.pmatsci.2005.05.002)
- [7] Teodorescu M., Lungu A., Stanescu P. O., Neamtu C.: Preparation and properties of novel slow-release NPK agrochemical formulations based on poly(acrylic acid) hydrogels and liquid fertilizers. *Industrial and Engineering Chemistry Research*, **48**, 6527–6534 (2009). DOI: [10.1021/ie900254b](https://doi.org/10.1021/ie900254b)
- [8] Mahdavinia G. R., Mousavi S. B., Karimi F., Marandi G. B., Garabaghi H., Shahabvand S.: Synthesis of porous poly(acrylamide) hydrogels using calcium carbonate and its application for slow release of potassium nitrate. *Express Polymer Letters*, **3**, 279–285 (2009). DOI: [10.3144/expresspolymlett.2009.35](https://doi.org/10.3144/expresspolymlett.2009.35)
- [9] Das A., Kothari V. K., Makhija S., Avyaya K.: Development of high-absorbent light-weight sanitary napkin. *Journal of Applied Polymer Science*, **107**, 1466–1470 (2008). DOI: [10.1002/app.26936](https://doi.org/10.1002/app.26936)
- [10] Güçlü G., Al E., Emik S., İyim T. B., Özgümüş S., Özyürek M.: Removal of Cu^{2+} and Pb^{2+} ions from aqueous solutions by starch-graft-acrylic acid/montmorillonite superabsorbent nanocomposite hydrogels. *Polymer Bulletin*, **65**, 333–346 (2010). DOI: [10.1007/s00289-009-0217-x](https://doi.org/10.1007/s00289-009-0217-x)
- [11] Guilherme M. R., Reis A. V., Paulino A. T., Fajardo A. R., Muniz E. C., Tambourgi E. B.: Superabsorbent hydrogel based on modified polysaccharide for removal of Pb^{2+} and Cu^{2+} from water with excellent performance. *Journal of Applied Polymer Science*, **105**, 2903–2909 (2007). DOI: [10.1002/app.26287](https://doi.org/10.1002/app.26287)
- [12] Tang Q., Sun X., Li Q., Wu J., Lin J.: Synthesis of polyacrylate/polyethylene glycol interpenetrating network hydrogel and its sorption of heavy-metal ions. *Science and Technology of Advanced Materials*, **10**, 015002/1–015002/7 (2009). DOI: [10.1088/1468-6996/10/1/015002](https://doi.org/10.1088/1468-6996/10/1/015002)
- [13] Kaşgöz H., Durmus A.: Dye removal by a novel hydrogel-clay nanocomposite with enhanced swelling properties. *Polymers for Advanced Technologies*, **19**, 838–845 (2008). DOI: [10.1002/pat.1045](https://doi.org/10.1002/pat.1045)
- [14] Tang Q., Lin J., Wu Z., Wu J., Huang M., Yang Y.: Preparation and photocatalytic degradability of TiO_2 /polyacrylamide composite. *European Polymer Journal*, **43**, 2214–2220 (2007). DOI: [10.1016/j.eurpolymj.2007.01.054](https://doi.org/10.1016/j.eurpolymj.2007.01.054)
- [15] Sadeghi M., Hosseinzadeh H.: Synthesis of starch-poly(sodium acrylate-co-acrylamide) superabsorbent hydrogel with salt and pH-responsiveness properties as a drug delivery system. *Journal of Bioactive and Compatible Polymers*, **23**, 381–404 (2008). DOI: [10.1177/0883911508093504](https://doi.org/10.1177/0883911508093504)

- [16] Pourjavadi A., Barzegar S.: Synthesis and evaluation of pH and thermosensitive pectin-based superabsorbent hydrogel for oral drug delivery systems. *Starch-Stärke*, **61**, 161–172 (2009).
DOI: [10.1002/star.200800063](https://doi.org/10.1002/star.200800063)
- [17] Kiatkamjornwong S., Mongkolsawat K., Sonsuk M.: Synthesis and property characterization of cassava starch grafted poly[acrylamide-co-(maleic acid)] superabsorbent via γ -irradiation. *Polymer*, **43**, 3915–3924 (2002).
DOI: [10.1016/S0032-3861\(02\)00224-0](https://doi.org/10.1016/S0032-3861(02)00224-0)
- [18] Nakason C., Wohmang T., Kaesaman A., Kiatkamjornwong S.: Preparation of cassava starch-graft-polyacrylamide superabsorbents and associated composites by reactive blending. *Carbohydrate Polymers*, **81**, 348–357 (2010).
DOI: [10.1016/j.carbpol.2010.02.030](https://doi.org/10.1016/j.carbpol.2010.02.030)
- [19] Al E., Güçlü G., Banu İyimT., Emik S., Özgümüş S.: Synthesis and properties of starch-graft-acrylic acid/Nanmontmorillonite superabsorbent nanocomposite hydrogels. *Journal of Applied Polymer Science*, **109**, 16–22 (2008).
DOI: [10.1002/app.27968](https://doi.org/10.1002/app.27968)
- [20] Demitri C., Sole R. D., Scalera F., Sannino A., Vasapollo G., Maffezzoli A., Ambrosio L., Nicolais L.: Novel superabsorbent cellulose-based hydrogels crosslinked with citric acid. *Journal of Applied Polymer Science*, **110**, 2453–2460 (2008).
DOI: [10.1002/app.28660](https://doi.org/10.1002/app.28660)
- [21] Pourjavadi A., Amini-Fazl M. S., Ayyari M.: Optimization of synthetic conditions CMC-g-poly(acrylic acid)/Celite composite superabsorbent by Taguchi method and determination of its absorbency under load. *Express Polymer Letters*, **1**, 488–494 (2007).
DOI: [10.3144/expresspolymlett.2007.69](https://doi.org/10.3144/expresspolymlett.2007.69)
- [22] Mahdavinia G. R., Pourjavadi A., Hosseinzadeh H., Zohuriaan M. J.: Modified chitosan 4. Superabsorbent hydrogels from poly(acrylic acid-co-acrylamide) grafted chitosan with salt- and pH-responsiveness properties. *European Polymer Journal*, **40**, 1399–1407 (2004).
DOI: [10.1016/j.eurpolymj.2004.01.039](https://doi.org/10.1016/j.eurpolymj.2004.01.039)
- [23] Chen Y., Liu Y-F., Tan H-M., Jiang J-X.: Synthesis and characterization of a novel superabsorbent polymer of *N,O*-carboxymethyl chitosan graft copolymerized with vinyl monomers. *Carbohydrate Polymers*, **75**, 287–292 (2009).
DOI: [10.1016/j.carbpol.2008.07.022](https://doi.org/10.1016/j.carbpol.2008.07.022)
- [24] Pourjavadi A., Ghasemzadeh H., Soleyman R.: Synthesis, characterization, and swelling behavior of alginate-g-poly(sodium acrylate)/kaolin superabsorbent hydrogel composites. *Journal of Applied Polymer Science*, **105**, 2631–2639 (2007).
DOI: [10.1002/app.26345](https://doi.org/10.1002/app.26345)
- [25] Wang W. B., Zhang J. P., Wang A. Q.: Preparation and swelling properties of superabsorbent nanocomposites based on natural guar gum and organo-vermiculite. *Applied Clay Science*, **46**, 21–26 (2009).
DOI: [10.1016/j.clay.2009.07.001](https://doi.org/10.1016/j.clay.2009.07.001)
- [26] Kim J., Yun S., Ounaies Z.: Discovery of cellulose as a smart material. *Macromolecules*, **39**, 4202–4206 (2006).
DOI: [10.1021/ma060261e](https://doi.org/10.1021/ma060261e)
- [27] Pourjavadi A., Zohuriaan-Mehr M. J., Ghasempoori S. N., Hossienzadeh H.: Modified CMC. V. Synthesis and super-swelling behavior of hydrolyzed CMC-g-PAN hydrogel. *Journal of Applied Polymer Science*, **103**, 877–883 (2007).
DOI: [10.1002/app.25224](https://doi.org/10.1002/app.25224)
- [28] Yang Z. L.: Health stone- An introduction on medical stone (in Chinese). *Information on Traditional Chinese Medicine*, **4**, 31 (1986).
- [29] Li J., Zhang P-Y., Gao Y., Song X-G., Dong J-H.: Overview of Maifanshi: Its physi-chemical properties and nutritious function in drinking water. *Environmental Science and Technology (China)*, **31**, 63–66 (2008).
- [30] Li G. Q., Lin J. M., Wu J. H.: Determination of crosslinkage density and its influence on water absorbency for superabsorbents (in Chinese). *Journal of Huaqiao University (National Science)*, **21**, 264–267 (2000).
- [31] Li X., Xu S. M., Wang J. D., Chen X. Z., Feng S.: Structure and characterization of amphoteric semi-IPN hydrogel based on cationic starch. *Carbohydrate Polymers*, **75**, 688–693 (2009).
DOI: [10.1016/j.carbpol.2008.09.009](https://doi.org/10.1016/j.carbpol.2008.09.009)
- [32] Flory P. J.: Principles of polymer chemistry. Cornell University Press, New York (1953).
- [33] Li A., Wang A. Q., Chen J. M.: Studies on poly(acrylic acid)/attapulgit superabsorbent composite. I. Synthesis and characterization. *Journal of Applied Polymer Science*, **92**, 1596–1603 (2004).
DOI: [10.1002/app.20104](https://doi.org/10.1002/app.20104)
- [34] Wu J. H., Lin J. M., Li G. Q., Wei C. R.: Influence of the COOH and COONa groups and crosslink density of poly(acrylic acid)/montmorillonite superabsorbent composite on water absorbency. *Polymer International*, **50**, 1050–1053 (2001).
DOI: [10.1002/pi.728](https://doi.org/10.1002/pi.728)
- [35] Wu J. H., Wei Y. L., Lin J. M., Lin S. B.: Study on starch-graft-acrylamide/mineral powder superabsorbent composite. *Polymer*, **44**, 6513–6520 (2003).
DOI: [10.1016/S0032-3861\(03\)00728-6](https://doi.org/10.1016/S0032-3861(03)00728-6)
- [36] Yang F., Li G., He Y-G., Ren F-X., Wang G-X.: Synthesis, characterization, and applied properties of carboxymethyl cellulose and polyacrylamide graft copolymer. *Carbohydrate Polymers*, **78**, 95–99 (2009).
DOI: [10.1016/j.carbpol.2009.04.004](https://doi.org/10.1016/j.carbpol.2009.04.004)

- [37] Huang Y. H., Lu J., Xiao C. B.: Thermal and mechanical properties of cationic guar gum/poly(acrylic acid) hydrogel membranes. *Polymer Degradation and Stability*, **92**, 1072–1081 (2007).
DOI: [10.1016/j.polymdegradstab.2007.02.011](https://doi.org/10.1016/j.polymdegradstab.2007.02.011)
- [38] Pourjavadi A., Hosseinzadeh H., Sadeghi M.: Synthesis, characterization and swelling behavior of gelatin-g-poly(sodium acrylate)/kaolin superabsorbent hydrogel composites. *Journal of Composite Materials*, **41**, 2057–2069 (2007).
DOI: [10.1177/0021998307074125](https://doi.org/10.1177/0021998307074125)
- [39] Schott H.: Swelling kinetics of polymers. *Journal of Macromolecular Science Part B: Physics*, **31**, 1–9 (1992).
DOI: [10.1080/00222349208215453](https://doi.org/10.1080/00222349208215453)
- [40] Tanaka T.: Collapse of gels and the critical endpoint. *Physical Review Letters*, **40**, 820–823 (1978).
DOI: [10.1103/PhysRevLett.40.820](https://doi.org/10.1103/PhysRevLett.40.820)
- [41] Liu Y., Xie J.-J., Zhu M.-F., Zhang X.-Y.: A study of the synthesis and properties of AM/AMPS copolymer as superabsorbent. *Macromolecular Materials and Engineering*, **289**, 1074–1078 (2004).
DOI: [10.1002/mame.200400154](https://doi.org/10.1002/mame.200400154)
- [42] Kabiri K., Zohuriaan-Mehr M. J., Mirzadeh H., Kheirabadi M. J.: Solvent-, ion- and pH-specific swelling of poly(2-acrylamido-2-methylpropane sulfonic acid) superabsorbing gels. *Journal of Polymer Research*, **17**, 203–212 (2010).
DOI: [10.1007/s10965-009-9306-7](https://doi.org/10.1007/s10965-009-9306-7)
- [43] Zhang J. P., Liu Y., Wang A. Q.: Study on superabsorbent composite XXV. Synthesis, characterization, and swelling behaviors of poly(acrylic acid-co-N-acryloylmorpholine)/attapulgit superabsorbent composites. *Polymer Composites*, **31**, 691–699 (2010).
DOI: [10.1002/pc.20845](https://doi.org/10.1002/pc.20845)
- [44] Zhang J. P., Chen H., Li P., Wang A. Q.: Study on superabsorbent composite, 14. Preparation of poly(acrylic acid)/organo-attapulgit composite hydrogels and swelling behaviors in aqueous electrolyte solution. *Macromolecular Materials and Engineering*, **291**, 1529–1538 (2006).
DOI: [10.1002/mame.200600317](https://doi.org/10.1002/mame.200600317)

Synthesis and application of solar cells of poly (3-decylthiophene)/N/titanium dioxide hybrid

J. C. Zhang^{*2}, X. Zheng¹, M. Chen¹, X. Y. Yang², W. L. Cao^{1,2}

¹Institute of Modern Catalysis, Beijing University of Chemical Technology, State Key Laboratory of Chemical Resource Engineering, Beijing 100029, China

²Institute of Science and Technology, Haikou 571126, China

Received 6 September 2010; accepted in revised form 23 November 2010

Abstract. An organic-inorganic nanocomposite material of poly (3-decylthiophene) and titanium dioxide doped with N (P3DT/N/TiO₂) were synthesized. Structures were characterized using X-ray diffraction (XRD), infrared spectroscopy (IR), transmission electron microscopy (TEM), and X-ray photoelectron spectroscopy (XPS). Optical and electrochemical properties were determined using UV-visible spectroscopy, fluorescence spectroscopy, and cyclic voltammetry. These tests indicated that P3DT/N/TiO₂ was a new p-n semiconductor photoelectric material, and the solar cell prepared with P3DT/N/TiO₂ performed well.

Keywords: polymer composites, P3DT/N/TiO₂ nanocomposite material, p-n semiconductor, photoelectric properties, solar cells

1. Introduction

Conducting polymers with highly-extended π -electron systems in their main chains have attracted much interest [1–4]. Polymers and metal oxides have been studied for many years for their independent electrical, optical, and mechanical properties [5]. Composites of these polymers with inorganic matter, combining the different properties of components, are considered remarkable advanced materials [6].

Polythiophene (PT) was widely studied as donor material in organic solar cells [7, 8]. Sharma *et al.* [9] studied the optical and photoelectrical properties of liquid state photoelectrochemical cells (PECs) based on photoactive electrodes made of poly (phenyl azo methane thiophene) (PPAT) and a composite film of nano-crystalline titanium dioxide (nc-TiO₂) and PPAT, and found that the composite film was better than PPAT by itself. Visy *et al.* [10] pre-

pared Poly (3-octyl-thiophene) (POT) and ferrous oxalate composite in order to get a better material. Suresh *et al.* [11] applied poly (3-phenyl hydrazone thiophene) (PPHT) and titanium dioxide composite in solar cells and obtained some improved results. Huisman *et al.* [12] replaced the titanium dioxide layer of solar cells with a PT/titanium dioxide composite layer and obtained solar cells that clearly show that area enlargement is beneficial to the conversion efficiency. However, there is no paper on poly (3-alkylthiophene) (P3AT) and doping inorganic nanocomposites. P3AT has good solubility, processability, stability, and electrical activity, and is convenient for mass production. The regular structure of P3AT can be obtained easily, and therefore P3AT was considered as one of the best donor materials. In this paper, the synthesis of P3DT/N/TiO₂ nanocomposite materials was introduced in detail. Chemical interactions in the material were found by

*Corresponding author, e-mail: zhangjc1@mail.buct.edu.cn

© BME-PT

X-ray diffraction, IR spectroscopy, and X-ray photoelectron spectroscopy. Ultraviolet–visible and luminescence measurements indicated that these P3DT/N/TiO₂ nanocomposites have excellent photoelectric properties. Electrochemical results indicated that the band gap of the nanocomposite hybrid was lower than that of the components.

2. Experimental section

2.1. Materials

3-Decylthiophene (Aldrich), FeCl₃ (Aldrich) and TiCl₄ (Aldrich) was used without further purification. FTO (Fluorine Tin Oxides) was commercially available. LiClO₄ was obtained from LiClO₄·3H₂O (Aldrich).

2.2. Synthesis of P3DT/N/TiO₂ nanocomposites

The conducting poly (3-decylthiophene) was synthesized with Fe (III) as catalyst and 3-decylthiophene monomer as material according to Ref. [13]. 3-decylthiophene monomer and chloroform were added to a 100 ml flask and ultrasonically dispersed for 15 min. The temperature of system was controlled at 0°C. FeCl₃ was dissolved in chloroform, and added dropwise to the flask. The reaction mixture was stirred under high-purity nitrogen for 8 h. The product was slowly added to methanol, precipitated, filtered and subjected to Soxhlet extraction with methanol for 20 h. The P3DT was then dried under vacuum at room temperature. P3DT (0.01 g) was dissolved in chloroform (2 ml) and dropped evenly on a clean quartz glass and ITO (Indium Tin Oxides) conductive glass. Red-brown P3DT films were obtained on vacuum drying the glasses.

Nano-N/TiO₂ was prepared with TiCl₄ as material according to Ref. [14]. Surfactant polyethylene glycol (PEG 800) was added to 0.3 mol/l of TiCl₄, followed by stirring vigorously at ambient temperature. The pH of the solution was adjusted to 5–6 by dripping ammonia. The sol was filtered and washed with ammonia until no presence of Cl⁻, and then transferred into a PTFE autoclave (100 ml) and maintained at 240°C for 12 h. Then the sol was washed by ethanol until no water existed. The obtained alcogel was dried at room temperature, and calcined at 500°C for 1 h to give the nano-N/TiO₂. N/TiO₂ (0.01 g) was suspended in isopropyl alcohol (2 ml) and dropped evenly on clean quartz

glasses and ITO. White N/TiO₂ films were obtained after drying in vacuum.

About 0.01 g of P3DT was dissolved in 2 ml of chloroform, and 0.05 g of N/TiO₂ was added. The mixture was ultrasonic shocked for 3 h at 40°C to get a uniform liquid. P3DT/N/TiO₂ nanocomposite powder was obtained by vacuum drying at room temperature. The uniform mixture liquid obtained above was dropped evenly on a clean quartz glass and ITO conductive glass. The red-brown P3DT/N/TiO₂ nanocomposite films were prepared by the vacuum drying method.

2.3. Preparation of dye-sensitized solar cell

The prepared TiCl₄ sol-gel was dropped on the FTO substrate and spun on a uniform plastic machine at a rate of 3000 r/min for 20 seconds. The prepared anatase TiO₂ powder of particle size about 14 nm was dropped on the sol-gel coated FTO substrate, and suffered spinning by the machine at a rate of 3000 r/min for 20 seconds. After being sintered at 450°C for 30 min, a good film was produced. H₂PtCl₆ was evenly dropped on another FTO substrate and burnt at 380°C for 30 min before the Pt electrode was obtained. The anode was sensitized by P3DT and P3DT/N/TiO₂ chloroform solution, and then packaged by the prepared Pt electrode, followed by the addition of electrolyte.

2.4. Structural characterization

X-ray diffraction (XRD) measurements were performed using a Shimadzu HR6000X (Cu target X tube, voltage 40.0 kV, current 30.0 mA, scan angle 3–80°). Infrared spectroscopy (IR) spectra were recorded in the range of 400–4000 cm⁻¹ by a prestige-21IR spectrophotometer with KBr pellet. Transmission electron microscope (TEM) measurements were performed using a HITACHI-800 transmission electron microscope. X-ray photoelectron spectroscopy (XPS) analyses were conducted by an ESCALAB 250 in which the electronic binding energy of the samples were measured.

2.5. Performance characterization

UV–visible spectra were measured using a Hitachi U-3010 spectrophotometer (Scan range: 200–800 nm). The excitation and emission spectra measurements were performed on a Hitachi F-7000 spectrofluorophotometer equipped with a 150 W xenon

lamp as the excitation source. The spectra were recorded with monochromator slit width of 1.5 nm on both the excitation and emission sides. Cyclic voltammetry (CV) measurements were carried out with a Potentiostat/Galvanostat (EG&G PAR Model 283). The counterelectrode was platinum and the reference electrode was non-aqueous Ag/Ag⁺. The CV curves were recorded in acetonitrile with 0.01 mol/l LiClO₄ as electrolyte at a scan rate of 50 mV/S. Before using, the solution was insufflated with N₂ for 30 min.

Current-voltage (I-V) measurements were taken in air at room temperature (298 K) using a Keithley 236 high current source power meter under white-light illumination from a 1000 W Xenon lamp. The light intensity was about 100 mW/cm² on the sample surfaces as measured by a photodetector. To measure the decay, we recorded the short circuit current and open circuit voltage as a function of the illumination time.

3. Results and discussion

3.1. XRD characterization of TiO₂, N/TiO₂, P3DT and P3DT/N/TiO₂

The XRD patterns of TiO₂, N/TiO₂, P3DT and P3DT/N/TiO₂ are presented in Figure 1. In XRD patterns of TiO₂ and N/TiO₂, the peaks at 25.32, 37.88, 48.08, 53.80, 55.04 and 62.80° are assigned to the (101), (004), (200), (105), (211) and (215) lattice planes, which are attributed to the signals of the anatase phase. There is little difference in two curves, so doping elements are highly monodispersed in the TiO₂. By using the Scherrer formula, it is found that the average TiO₂ particle size is 22.22 nm while N/TiO₂ is 13.69 nm. In the XRD pattern of P3DT, the ‘hill’ at 15–28° is associated with the amorphous phase, while the reflections at around 5, 10, 15.07° and 21.72° can reflect crystalline structure. The reflection at 21.72° is attributed to the interchain distance between π -stacking oxidized chains. The Bragg equation gives 0.35 nm for this distance. The reflections at 5, 10, and 15.07° Bragg angles confirm the layered structure of P3DT as having a dominant first-order reflection at $2\theta = 5^\circ$ and a lamellar interlayer spacing of 1.81 nm [10]. The diffraction peak of P3DT is quite narrow, which shows the high degree of crystallization, plane structure, and the high regularity of P3DT segments. For the P3DT/N/TiO₂ nanocomposite, the XRD pattern

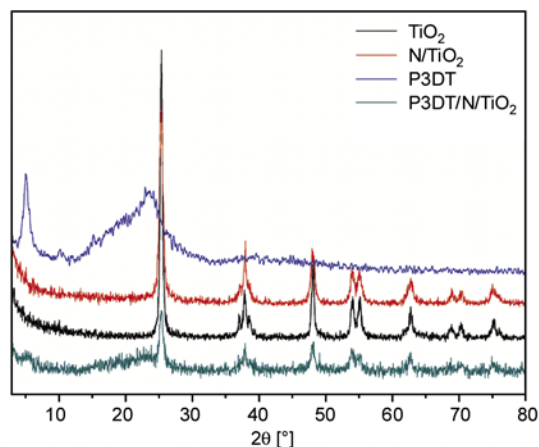


Figure 1. XRD patterns of TiO₂, N/TiO₂, P3DT and P3DT/N/TiO₂

mainly shows the strong N/TiO₂ peaks. The characteristic P3DT broad peak can not be seen on the XRD pattern of P3DT/N/TiO₂ nanocomposite. The XRD pattern of the nanocomposite has higher background intensity, lower diffraction peak intensity, decreased interplanar spacing, and reduced sharpness of the peak profiles than N/TiO₂, confirming the chemical interaction between P3DT and nano-N/TiO₂.

3.2. IR results of N/TiO₂, P3DT and P3DT/N/TiO₂

The FT-IR spectra are shown in Figure 2. In the spectrum of N/TiO₂, the Ti–O–Ti bond absorption is at about 497 cm⁻¹ [15]. In the spectrum of P3DT, there is a low-intensity peak at 3056 cm⁻¹ that can be attributed to the thiophene ring C–H stretching vibration, which is corresponding to the out-of-plane bending of the thiophene ring C–H at 830 and 720 cm⁻¹. The bands at 2921 and 2853 cm⁻¹ belong

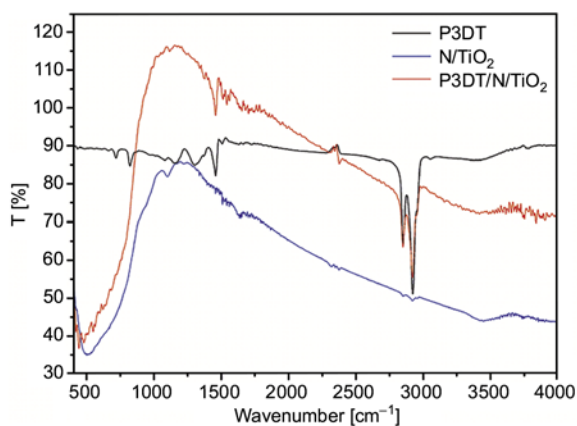


Figure 2. FT-IR spectras of N/TiO₂, P3DT and P3DT/N/TiO₂

to the C–H of CH₂ or CH₃ symmetric and asymmetric stretching, which are corresponding to the asymmetric and symmetric deformations at 1305 and 1459 cm⁻¹. The bands at 1499 and 665 cm⁻¹ correspond to the symmetric vibration of the C=C and the asymmetric vibration of the C–S, respectively. Bands coming from both N/TiO₂ and P3DT are observed in the spectrum of P3DT/N/TiO₂ nanocomposite, whereas the bands originating from N/TiO₂ and P3DT are located at low wavenumbers. In addition, several new peaks appear at 3840, 3745, 580, 476, and 418 cm⁻¹.

3.3. TEM measurements of nano-N/TiO₂

Figure 3 demonstrates the TEM results of nano-N/TiO₂. It can be seen that the particle size is between 13–15 nm, the result is basically the same with the Scherrer formula. The particles have good dispersibility and clear mesh structure. This is attributed to the use of alcohol exchange in the preparation of powder to eliminate the liquid surface tension and reduce the agglomeration of particles during the burning process; thereby high

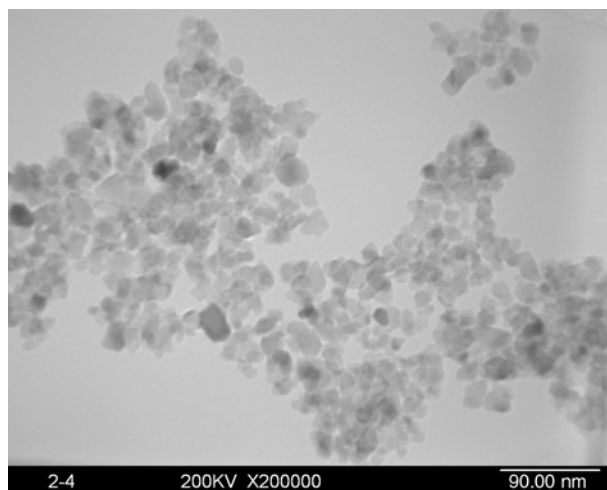


Figure 3. TEM pattern of nano-N/TiO₂

surface area, small particle size, and good dispersion of nano-particles can be obtained.

3.4. XPS characterization of N/TiO₂, P3DT and P3DT/N/TiO₂

The high-resolution XPS spectra are shown in Figure 4a–4d. In the P3DT/N/TiO₂ sample (Figure 4a), the XPS spectrum shows C, O, S, Ti and N peaks.

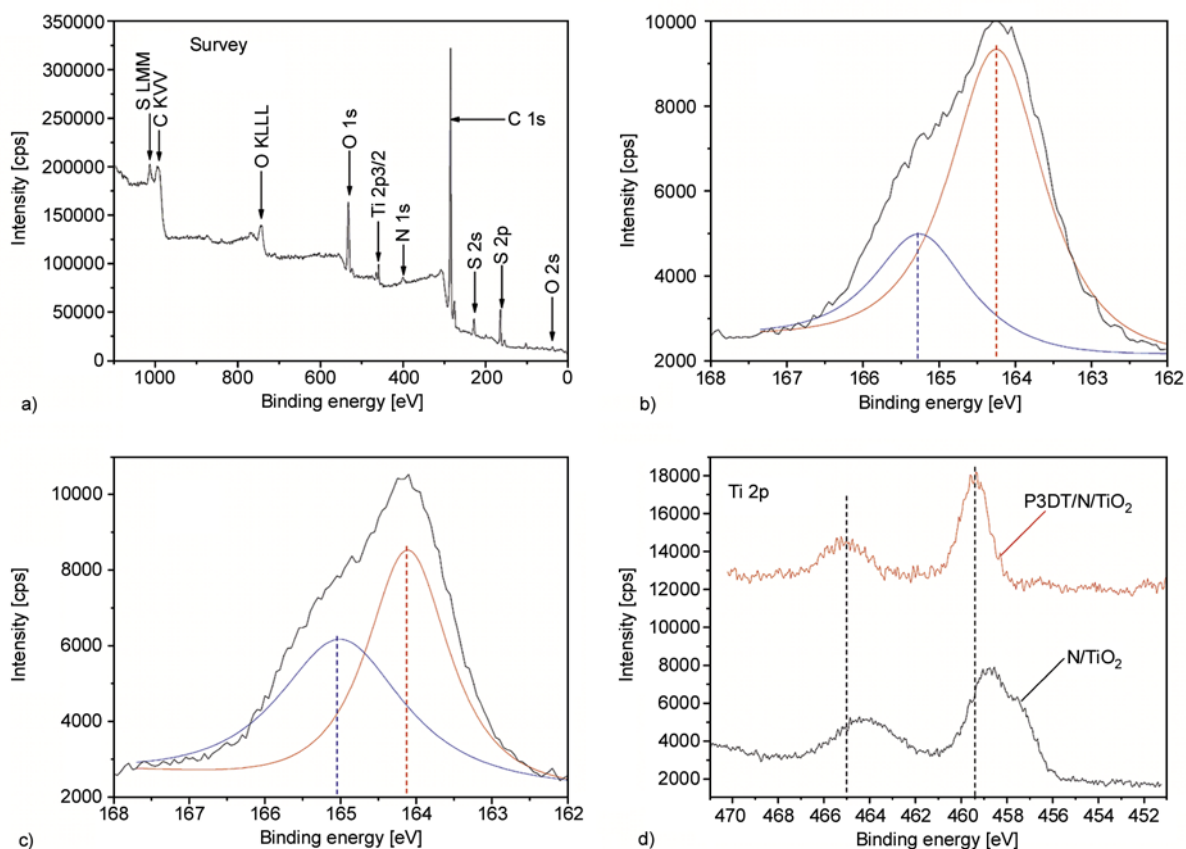


Figure 4. XPS spectras of P3DT/N/TiO₂ (a), the sulfur peaks in P3DT (b), the sulfur peaks in P3DT/N/TiO₂ (c) and Ti 2p peaks (d)

Figure 4b shows the sulfur peaks in P3DT. Two sulfur peaks (S 2p_{3/2}) are found, one with a binding energy of 164.3 eV for neutral thiophene units in the polymer chain and the other with a binding energy of 165.3 eV for oxidized thiophene units [16]. Figure 4c shows the sulfur peaks in P3DT/N/TiO₂. There are also two sulfur peaks (S 2p_{3/2}), one with a binding energy of 164.1 eV for neutral thiophene units in the polymer chain and the other with a binding energy of 165.1 eV for oxidized thiophene units, indicating that the S atom of P3DT will interact with some other atom except the C atom of P3DT after composite reaction. Figure 4d shows the displacement of Ti 2p peaks after composite reaction. The binding energy became larger, indicating that there were electrons gained and lost during the complex process and N/TiO₂ combined with P3DT at the Ti position. Comparing Figure 4b with Figure 4c, we find the sulfur peaks are displaced after composite formation, and P3DT combined with N/TiO₂ at the sulfur position.

3.5. UV–Vis spectra of N/TiO₂, P3DT and P3DT/N/TiO₂

The UV–Vis spectra of the N/TiO₂ film, P3DT film and P3DT/N/TiO₂ nanocomposite film are presented in Figure 5. The spectrum of N/TiO₂ shows the fundamental absorption of UV light ranging from 250 to 420 nm by the Ti–O bond. The UV–Vis spectrum of P3DT with maximum adsorption at a wavelength of about 457 nm for the $\pi \rightarrow \pi^*$ transition indicates the formation of the big π conjugate structure along the main chain [17, 18]. From the spectrum of P3DT/N/TiO₂ nanocomposite film, it

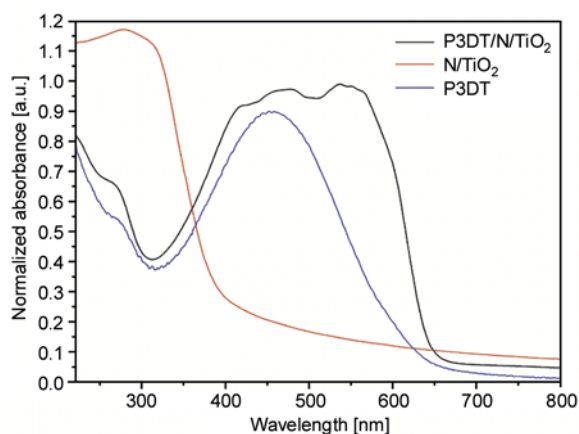


Figure 5. UV–Vis spectras of N/TiO₂, P3DT and P3DT/N/TiO₂

can be seen that there are two absorption bands with maximum wavelengths of 270 and 500 nm in the ultraviolet region and visible light region, respectively. Comparing with the spectra of N/TiO₂ and P3DT, we find the P3DT/N/TiO₂ nanocomposite film absorbs much more UV–Vis light. It is reasonable to believe that the P3DT/N/TiO₂ nanocomposite will perform better in semiconductors than P3DT and N/TiO₂.

3.6. Fluorescence spectra of N/TiO₂, P3DT, and P3DT/N/TiO₂

The fluorescence spectra of the N/TiO₂ film, P3DT film and P3DT/N/TiO₂ nanocomposite film are shown in Figure 6. Two emission peaks can be seen with the maximum emission at 386 and 454 nm in the fluorescence spectrum of N/TiO₂. There is an emission peak with the maximum emission at 630 nm in the spectrum of P3DT. The fluorescence spectrum of the P3DT/N/TiO₂ nanocomposite film is totally different from that of either P3DT or N/TiO₂. It exhibits new optical property for the new chemical interaction between P3DT and N/TiO₂ with three emission peaks at 350, 483, and 726 nm. It proves that P3DT/N/TiO₂ is a new compound.

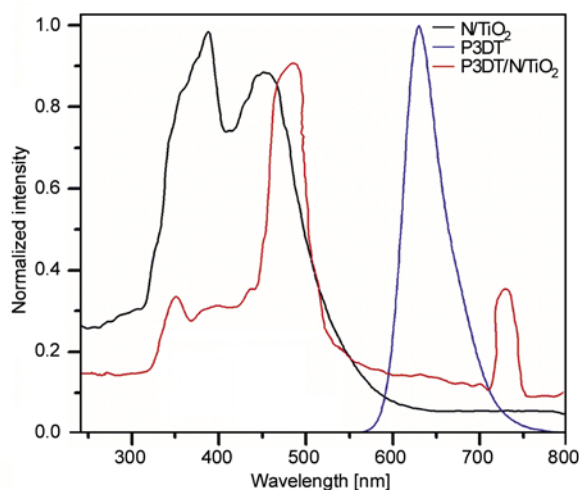


Figure 6. Fluorescence spectras of N/TiO₂, P3DT and P3DT/N/TiO₂

3.7. Cyclic voltammetry

Figure 7a–7d. show the cyclic voltammetry results of the TiO₂ film, N/TiO₂ film, P3DT solid film and P3DT/N/TiO₂ nanocomposite film. The oxidation potentials and redox of electrode and the bandgap E_g are listed in Table 1.

Table 1. The frontline molecular orbital and energy gap of TiO₂, N/TiO₂, P3DT and P3DT/N/TiO₂ nanocomposite

Sample	Φ_{ox} [eV]	Φ_{red} [eV]	E_{HOMO} [eV]	E_{LUMO} [eV]	E_g [eV]
TiO ₂	2.14	-1.01	-6.58	-3.43	3.15
N/TiO ₂	2.14	-0.75	-6.58	-3.69	2.89
P3DT	0.51	-0.62	-4.95	-3.82	1.13
P3DT/N/TiO ₂	0.30	-0.67	-4.74	-3.77	0.97

Using the Equations (1) and (2) [19, 20]:

$$E_{HOMO} \text{ (or } E_{LUMO}) = E_0 + eV_{ox} \text{ (or } eV_{red}) \quad (1)$$

$$E_g = E_{LUMO} - E_{HOMO} \quad (2)$$

E_{HOMO} is the electrode potential of the highest occupied molecular orbital; E_0 is the standard electrode potential of Ag/Ag⁺ electrodes, and its value is -4.4 eV. Φ_{ox} is the oxidation potential of electrode (as opposed to Ag/Ag⁺ electrodes). E_{LUMO} is the electrode potential of the lowest unoccupied molecular orbital; Φ_{red} is the redox potential of electrode (as opposed to Ag/Ag⁺ electrodes).

The initial oxidation/reduction potential can be seen in Figure 7. Table 1. shows that N/TiO₂ has lower

bandgap E_g than TiO₂ and the bandgap E_g of P3DT/N/TiO₂ is 0.97 eV which is lower than that of P3DT. The results indicate that the P3DT/N/TiO₂ nanocomposite is a new promising p-n type composite material.

3.8. Results of solar cells performance test

Figure 8. displays the photovoltaic performance of solar cells sensitized respectively by P3DT and P3DT/N/TiO₂ chloroform solutions, and Table 2

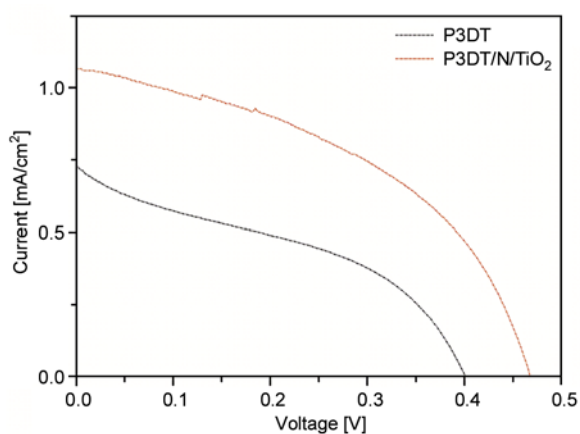
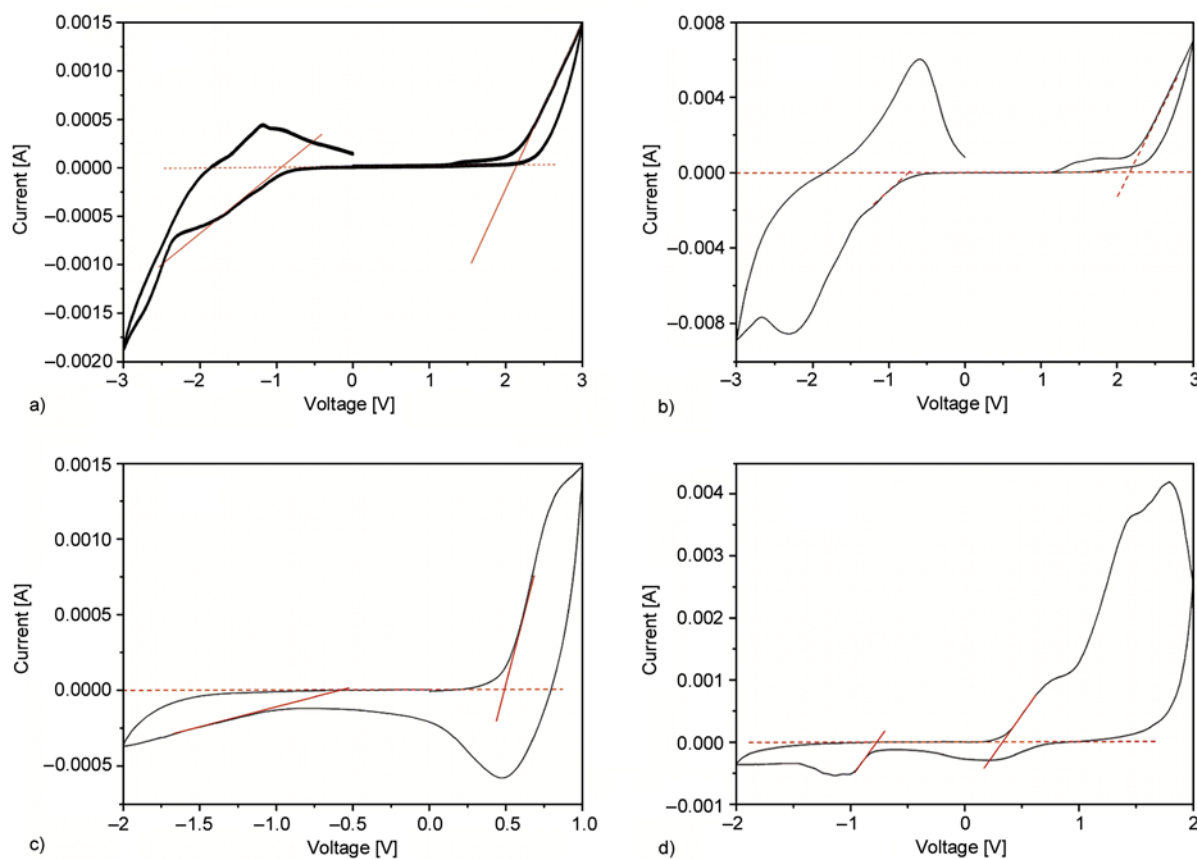
**Figure 8.** Photovoltaic performance of solar cells sensitized respectively by P3DT and P3DT/N/TiO₂**Figure 7.** Cyclic voltammograms of TiO₂ (a), N/TiO₂ (b), P3DT (c) and P3DT/N/TiO₂ (d)

Table 2. The parameters of dye-sensitized solar cells

Cells	V_{oc} [V]	J_{sc} [mA·cm ⁻²]	P_{max} [mW]	η [%]	FF
P3DT	0.401	0.733	0.0172	0.115	0.390
P3DT/N/TiO ₂	0.467	1.060	0.0450	0.225	0.455

lists the parameters of dye-sensitized solar cells. Under standard global AM1.5 G (100 mW/cm²) solar condition, the P3DT-sensitized solar cell gave a short-circuit current (J_{SC}) of 0.733 mA/cm² and an open-circuit voltage (V_{OC}) of 0.401 V, corresponding to an overall conversion efficiency (η) of 0.115%. The P3DT/N/TiO₂-sensitized solar cell gave a short-circuit current (J_{SC}) of 1.06 mA/cm² and an open-circuit voltage (V_{OC}) of 0.467 V, corresponding to an overall conversion efficiency (η) of 0.225%. The overall conversion efficiency enhancement of P3DT/N/TiO₂ relative to P3DT can be related to the chemical interaction between P3DT and N/TiO₂ in the nanocomposite.

4. Conclusion

A new Ti-S bond and new optical properties can be found in P3DT/N/TiO₂ by IR, XPS, UV and PL tests. CV tests show that P3DT/N/TiO₂ has the smallest bandgap E_g of 0.97 eV and is a kind of p-n semiconductor composite material of good performance. Solar cell performance tests indicate that the P3DT/N/TiO₂-sensitized solar cell is better than the P3DT-sensitized solar cell. All these show that P3DT/N/TiO₂ is a new kind of p-n material of good photoelectric performance.

Acknowledgements

The work was supported by the Key Planned Science and Technology Project of Hainan Province (ZDXM 20100062), and the National High Technology Research and Development Program of Hainan under Grant NO. 509013, and the National High Technology Research and Development Program of China (863 Program) under Grant NO. 2006AA03z412, and the Scientific Research Project of Hainan Education Department under Grant No.Hj 2010-52, and the Scientific Research Foundation of Graduate School of Beijing University of Chemical and Technology (No. 09Si005).

References

- [1] McCullough R. D.: The chemistry of conducting polythiophenes. *Advanced Materials*, **10**, 93–116 (1998). DOI: [10.1002/\(SICI\)1521-4095\(199801\)10:2<93::AID-ADMA93>3.0.CO;2-F](https://doi.org/10.1002/(SICI)1521-4095(199801)10:2<93::AID-ADMA93>3.0.CO;2-F)
- [2] Tiwari A., Singh V.: Synthesis and characterization of electrical conducting chitosan-graft-polyaniline. *Express Polymer Letters*, **1**, 308–317 (2007). DOI: [10.3144/expresspolymlett.2007.44](https://doi.org/10.3144/expresspolymlett.2007.44)
- [3] Çakmak O., Baştürkmen M., Kısakürek D. O.: Synthesis and characterization of conducting and non-conducting polymers of sodium 2,4,6-trichlorophenolate by microwave initiation. *Polymer*, **45**, 5451–5458 (2004). DOI: [10.1016/j.polymer.2004.06.049](https://doi.org/10.1016/j.polymer.2004.06.049)
- [4] Lawandy S. N., Halim S. F., Darwish N. A.: Structure aggregation of carbon black in ethylene-propylene diene polymer. *Express Polymer Letters*, **3**, 152-158 (2009). DOI: [10.3144/expresspolymlett.2009.20](https://doi.org/10.3144/expresspolymlett.2009.20)
- [5] Smestad G. P., Spiekermann S., Kowalik J., Grant C. D., Schwartzberg A. M., Zhang J., Tolbert L. M., Moons E.: A technique to compare polythiophene solid-state dye sensitized TiO₂ solar cells to liquid junction devices. *Solar Energy Materials and Solar Cells*, **76**, 85–105 (2003). DOI: [10.1016/S0927-0248\(02\)00252-0](https://doi.org/10.1016/S0927-0248(02)00252-0)
- [6] Vorotyntsev M. A., Vasilyeva S.: Metallocene-containing conjugated polymers. *Advances in Colloid and Interface Science*, **139**, 97–149 (2008). DOI: [10.1016/j.cis.2008.01.006](https://doi.org/10.1016/j.cis.2008.01.006)
- [7] Kim J. Y., Kim S. H., Lee H. H., Lee K., Ma W., Gong X., Heeger A. J.: New architecture for high-efficiency polymer photovoltaic cells using solution-based titanium oxide as an optical spacer. *Advanced Materials*, **18**, 572–576 (2006). DOI: [10.1002/adma.200501825](https://doi.org/10.1002/adma.200501825)
- [8] Kim J. Y., Lee K., Coates N. E., Moses D., Nguyen T-Q., Dante M., Heeger A. J.: Efficient tandem polymer solar cells fabricated by all-solution processing. *Science*, **317**, 222–225 (2007). DOI: [10.1126/science.1141711](https://doi.org/10.1126/science.1141711)
- [9] Sharma G. D., Suresh P., Sharma S. K., Roy M. S.: Photovoltaic properties of liquid-state photoelectrochemical cells based on PPAT and a composite film of PPAT and nanocrystalline titanium dioxide. *Synthetic Metals*, **158**, 509–515 (2008). DOI: [10.1016/j.synthmet.2008.03.026](https://doi.org/10.1016/j.synthmet.2008.03.026)
- [10] Visy Cs., Bencsik G., Németh Z., Vértés A.: Synthesis and characterization of chemically and electrochemically prepared conducting polymer/iron oxalate composites. *Electrochimica Acta*, **53**, 3942–3947 (2008). DOI: [10.1016/j.electacta.2007.07.060](https://doi.org/10.1016/j.electacta.2007.07.060)

- [11] Sharma G. D., Suresh P., Sharma S. K., Roy M. S.: Optical and electrical properties of hybrid photovoltaic devices from poly (3-phenyl hydrazone thiophene) (PPHT) and TiO₂ blend films. *Solar Energy Materials and Solar Cells*, **92**, 61–70 (2008). DOI: [10.1016/j.solmat.2007.08.009](https://doi.org/10.1016/j.solmat.2007.08.009)
- [12] Huisman C. L., Goossens A., Schoonman J.: Preparation of a nanostructured composite of titanium dioxide and polythiophene: A new route towards 3D heterojunction solar cells. *Synthetic Metals*, **138**, 237–241 (2003). DOI: [10.1016/S0379-6779\(02\)01310-3](https://doi.org/10.1016/S0379-6779(02)01310-3)
- [13] Han Z. Y., Zhang J. C., Yang X. Y., Zhu H., Cao W. L.: Synthesis and photoelectric property of poly (3-octylthiophene)/zinc oxide complexes. *Solar Energy Materials and Solar Cells*, **94**, 194–200 (2010). DOI: [10.1016/j.solmat.2009.09.001](https://doi.org/10.1016/j.solmat.2009.09.001)
- [14] Han Z. Y., Zhang J. C., Yang X. Y., Zhu H., Cao W. L.: Synthesis and photoelectric property of poly (3-octylthiophene)/titanium dioxide nano-composite material. *Journal of Materials Science: Materials in Electronics*, **21**, 6, 554–561 (2010). DOI: [10.1007/s10854-009-9956-6](https://doi.org/10.1007/s10854-009-9956-6)
- [15] Xu J-C., Liu W-M., Li H-L.: Titanium dioxide doped polyaniline. *Materials Science and Engineering: C*, **25**, 444–447 (2005). DOI: [10.1016/j.msec.2004.11.003](https://doi.org/10.1016/j.msec.2004.11.003)
- [16] Kang E. T., Neoh K. G., Tan K. L.: Surface modifications of poly(3-alkylthiophene) films by graft copolymerization. *Macromolecules*, **25**, 6842–6848 (1992). DOI: [10.1021/ma00051a019](https://doi.org/10.1021/ma00051a019)
- [17] Janáky Cs., Visy Cs.: Synthesis and characterization of poly(3-octylthiophene)/ γ -Fe₂O₃ nanocomposite – A promising combination of superparamagnetic–thermoelectric–conducting properties. *Synthetic Metals*, **158**, 1009–1014 (2008). DOI: [10.1016/j.synthmet.2008.07.014](https://doi.org/10.1016/j.synthmet.2008.07.014)
- [18] Trznadel M., Zagórska M., Lapkowski M., Louarn G., Lefrant S., Pron A.: UV–VIS–NIR and Raman spectroelectrochemistry of regioregular poly(3-octylthiophene): Comparison with its non-regioregular analogue. *Journal of the Chemical Society, Faraday Transactions*, **92**, 1387–1393 (1996). DOI: [10.1039/FT9969201387](https://doi.org/10.1039/FT9969201387)
- [19] Shi C. J., Yao Y., Yang Y., Pei Q. B.: Regioregular copolymers of 3-alkoxythiophene and their photovoltaic application. *Journal of the American Chemical Society*, **128**, 8980–8986 (2006). DOI: [10.1021/ja061664x](https://doi.org/10.1021/ja061664x)
- [20] Hwang S-W., Chen Y.: Synthesis and electrochemical and optical properties of novel poly(aryl ether)s with isolated carbazole and p-quaterphenyl chromophores. *Macromolecules*, **34**, 2981–2986 (2001). DOI: [10.1021/ma001855z](https://doi.org/10.1021/ma001855z)

Water-responsive shape memory hybrid: Design concept and demonstration

K. Fan¹, W. M. Huang^{2*}, C. C. Wang², Z. Ding², Y. Zhao², H. Purnawali², K. C. Liew², L. X. Zheng²

¹Hwa Chong Institution, 661 Bukit Timah Road, 269734 Singapore

²School of Mechanical and Aerospace Engineering, Nanyang Technological University, 50 Nanyang Avenue, 639798 Singapore

Received 9 September 2010; accepted in revised form 23 November 2010

Abstract. Shape memory materials are featured by their ability to recover their original shapes when a particular stimulus, such as heat, light, magnetic field, even moisture/water, etc. is applied. However, it is not an easy task for non-professionals to synthesize a shape memory material which can meet all the requirements of a particular application. Even for professionals, like materials researchers, it could involve tedious trial and error procedures. In this paper, the concept of water-responsive shape memory hybrid is proposed and the advantages are demonstrated by two examples. The hybrid concept is versatile and can be easily accessed by those even without much polymer/chemistry background. Moreover, the performance of such hybrids can be well-predicted. This concept can be further extended into *solvent*-responsive shape memory hybrids, which can be routinely designed and realized in a Do-It-Yourself manner by almost anyone.

Keywords: Tailor-made polymers, smart polymers, polymer composites

1. Introduction

Shape memory materials are featured by their ability to recover their original shapes when a particular stimulus is applied [1]. For shape memory alloys (SMAs), the stimuli are thus far limited to heat (including joule heating) and magnetic field only [2–4], whereas for shape memory polymers (SMPs), the stimuli are further extended to include light, chemical (including water, pH change, etc) and many others [5–8].

Shape memory materials, in particular SMAs, have been used in a wide range of engineering applications for many years [2, 3, 9]. More recently, SMPs have been attracting a lot of attention due to their great potential, in particular for biomedical applications [10–12]. As compared with SMAs [13], SMPs are lower in cost (for both material and processing),

and easier to be customized to achieve tailored properties and functions to meet the needs of a particular application [2, 11, 14–18].

Despite these advantages, the synthesis of a new SMP requires not only strong background in polymer/chemistry but also extensive trial and error procedures. Moreover, although there are a myriad number of SMPs that have been developed or still under development all over the world, till today few of these SMPs are commercially available or widely accepted in some specific fields. One of the rationales behind it is that it is relatively easy to develop a new SMP, but as a new material, it requires tremendous effort and time to conduct various tests in order to ensure its reliability/stability for any real engineering applications [19–21]. For instance, long term stability of materials, such as SMP stents [22],

*Corresponding author, e-mail: mwmhuang@ntu.edu.sg

within a liquid environment is a major concern in the biomedical applications.

From the application point of view, the ideal solution is to use the materials that have been traditionally used in the industry, so that devices made of these materials are not only compatible (in every aspect) to both the fabrication processes and the working environment but also meets the particular requirements. Furthermore, its performance can also be well-predicted even in the early design stage.

In this paper, a hybrid concept was demonstrated to achieve water-driven shape recovery, i.e., water-responsive shape memory hybrid was designed and produced. This concept is generic and easily accessible to those even without much chemistry/polymer knowledge.

It should also be pointed out that the focus of this paper is twofold, one is for proof of concept and the other is for demonstrating the convenience and versatility in the design and fabrication of such shape memory materials in a Do-It-Yourself manner.

2. Mechanism and concept

Unlike SMAs, in which the reversible martensitic transformation is the driving mechanism behind the shape memory phenomenon [2], the shape memory effect in polymers is the result of a two-segment system [1]. As illustrated in Figure 1a, a SMP normally includes an elastic segment, which is always elastic within the temperature range of our interest, and a transition segment, which is able to dramatically alter its stiffness when a particular stimulus, which might be heat, light or water etc., is applied. At the presence of the right stimulus, the transition segment becomes soft, so that the polymer can be easily stretched, while the elastic segment is also deformed accordingly (Figure 1b). Upon removal of the stimulus, the transition segment becomes hard again and thus, the deformation of the elastic

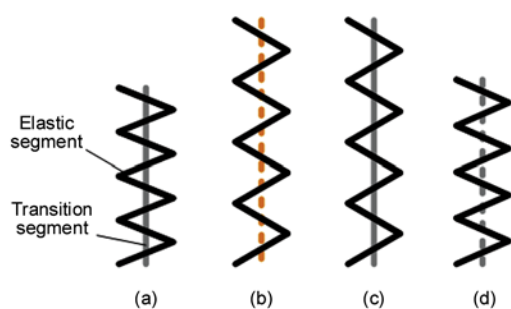


Figure 1. Illustration of the shape memory effect: normal state (a), deformed state (b), preserved state (c), recovered state (d)

segment is largely preserved (Figure 1c). The polymer can virtually maintain this temporary shape (stretched shape) forever. Only the presence of a stimulus (either the same stimulus as previously used for fixing the temporary shape or a different one) that causes the softening of the transition segment can trigger the release of the stored elastic energy in the elastic segment. Consequently, the polymer recovers its original shape (Figure 1d).

This mechanism for the shape memory effect in polymers can also be applied into hybrids, resulting in the avoidance of the difficulties in the syntheses of polymers, which require not only strong background knowledge and extensive experience in polymer/chemistry but also tremendous efforts in trial and error procedures. Fundamentally, such a hybrid is a kind of composite, consisting of matrix (the elastic segment) and inclusion (the transition segment), similar to the mixtures reported in [23]. By selecting the right materials for the matrix and inclusion, together with the right processing technique, we can minimize the chemical interaction between the elastic segment and transition segment as much as possible, so that the properties and behaviors of the resulted materials can be well predicted from the very beginning.

Water (or moisture)-responsive SMP has been realized in a couple of polymer systems [24, 25]. Because of the strong interaction between the elastic and transition segments in these polymers, it is difficult to predict their properties (such as the transition/shape recovery temperature and stiffness) and behaviors (e.g. the recovery stress and recoverable strain). Individual characterization of their respective properties/behaviors after synthesis is required. As such, tailoring a shape memory material to meet the requirements of a particular application, which is possible in theory, is in fact a tedious and costly process in practice.

In the next section, based on the concept of shape memory hybrid discussed above, we demonstrate two simple approaches to achieve water-responsive shape memory hybrids, in which the chemical interaction between the elastic and transition segments is largely avoided.

3. Fabrication and demonstration

As discussed above, the chemical interaction between the elastic and transition segments in shape memory

hybrids should be minimized or totally avoided (if possible), so that the properties and behaviors of the resulted hybrids can be well predicted from the very beginning. This can be achieved in two ways. One is to select the material components (for the elastic matrix and the transition inclusion) which do not have any possible chemical reaction at all, while the other is to select a processing technique to avoid or minimize such chemical reaction.

Here, two examples of the preparation of water-responsive shape memory hybrids using two different approaches are presented. To achieve the water-responsive function in the simplest way, a solid material that can dissolve in the water is used as the transition inclusion. This material should be adequately strong and be in the powder/micro particle form for easy and good dispersion within the elastic matrix. Many non-organic crystals, such as cupric sulphate and sodium acetate, are water-soluble. They are good candidates, at least for demonstration purpose at this stage. Whereas for the elastic matrix, the material should be elastic and stable throughout the entire working processes.

Depending on the material properties of the elastic matrix and transition inclusion, different processing procedures can be applied to fabricate a shape memory hybrid.

3.1. Polymer sponge/cupric sulphate pentahydrate hybrid

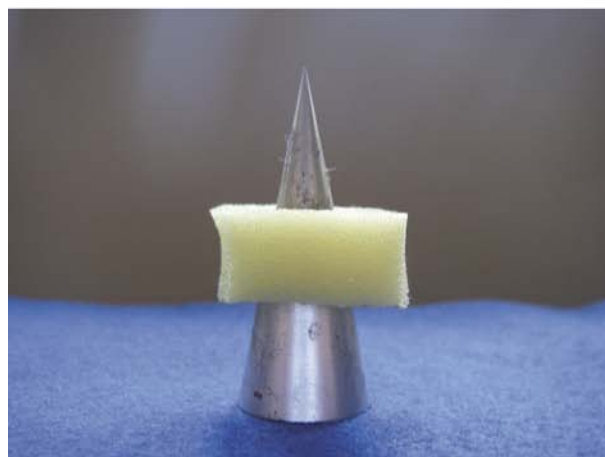
Cupric sulphate pentahydrate bought from Sigma-Aldrich, was used as the transition inclusion. The elastic matrix was a polymer sponge, which was selected mainly because it can be significantly compressed. An aluminum cone (base diameter: 2 cm; height: 5 cm) was pushed through the sponge (2.8 cm long \times 2.5 cm wide \times 1.3 cm thick) along its thickness, as shown in Figure 2a and b. Figure 2c shows a small through-thickness crack after the removal of the cone, indicating that a permanent deformation, although limited, did occur.

The water-responsive feature was demonstrated by means of showing the closure of a large hole inside the sponge upon immersing into room temperature water (about 22°C).

The experiment was done in two steps. The details of the first step are as follows.



a)



b)



c)

Figure 2. Polymer sponge with a sharp end aluminum cone punched through. Top view (a), side view (b), after removal of aluminum cone (c).

1. A saturated solution of cupric sulfate was prepared in a ratio of 20 g cupric sulfate pentahydrate per 100 ml of water.
2. The solution was heated to 100°C to accelerate the dissolution process.

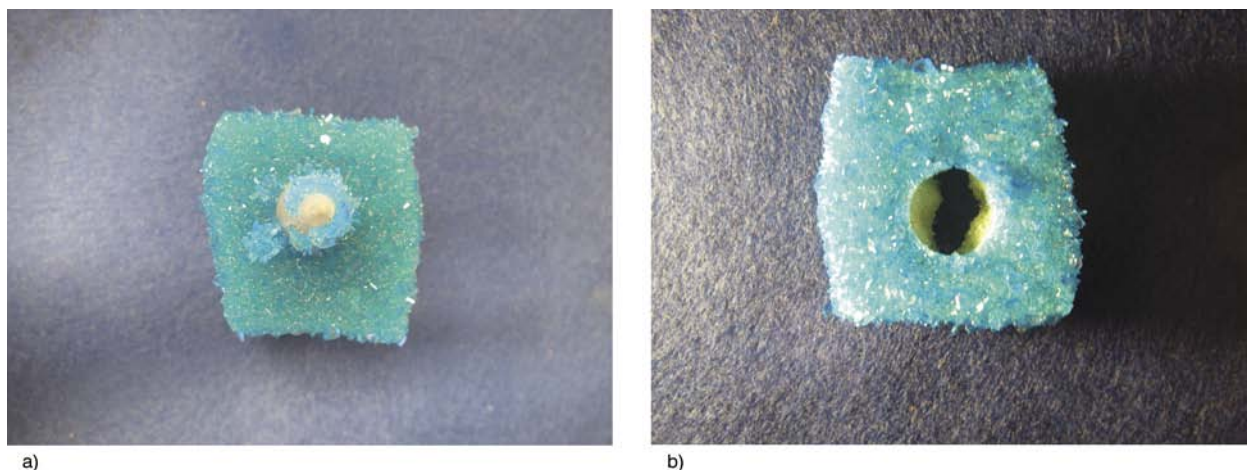


Figure 3. Sponge with aluminum cone after crystallization of cupric sulphate pentahydrate (a) and after removal of aluminum cone (b)

3. The cone was inserted into the sponge (Figure 2b).
4. The cone and sponge were immersed into the saturated cupric sulfate solution.
5. The sponge was squeezed so as to absorb as much saturated cupric sulfate solution as possible.
6. The cone and the sponge were left in the saturated solution for 24 hours.
7. The cone and the sponge were removed from the solution (Figure 3a).
8. The cone was removed from the sponge.

It can be seen from Figure 3b that the hole is virtually well preserved. For a better comparison, Figure 4 reveals different parts of the sponge with/without cupric sulfate pentahydrate crystals. The

part with cupric sulfate pentahydrate crystals is solid and stiff, while the part without the crystals is porous, soft and elastic.

Figure 5 shows the cyclic uniaxial compression testing results of both the original sponge and the sponge/cupric sulfate pentahydrate hybrid. It can be seen that the stiffness of sponge/cupric sulfate pentahydrate hybrid is significantly higher, which indicates that after crystallization, cupric sulfate pentahydrate is strong enough to retain the shape of the deformed sponge, i.e., shape recovery is largely prevented so that the hole can be largely maintained.

It can also be noticed that remarkable residual strain occurs in the original sponge upon loaded to about 12.5% compressive strain. As such, the elasticity of

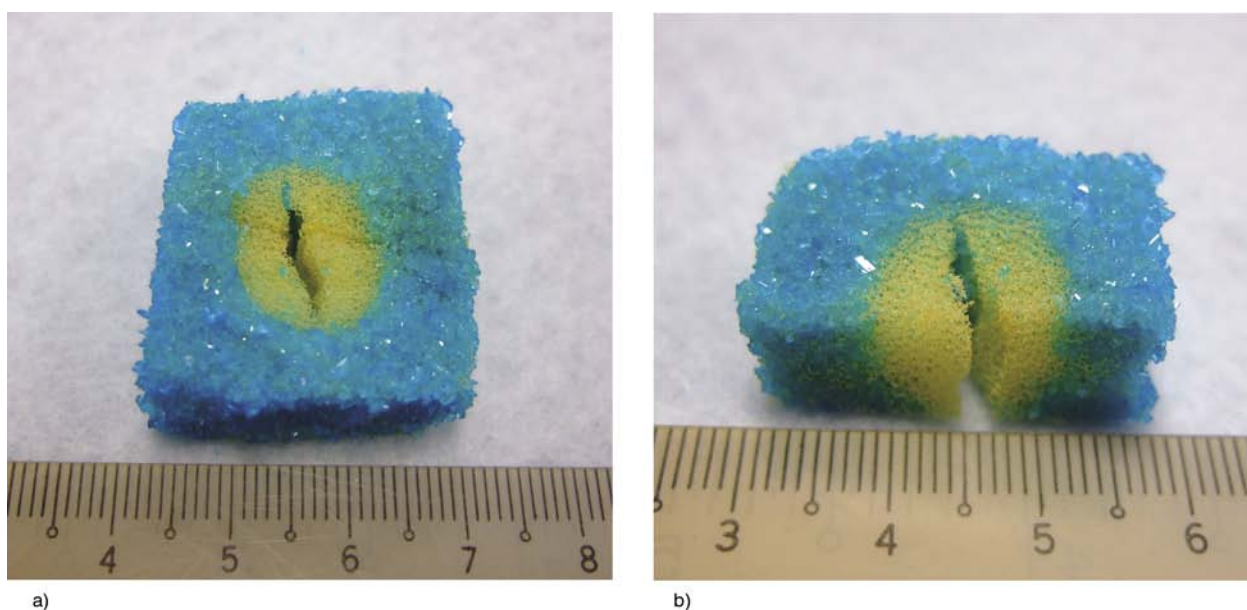


Figure 4. Comparison of parts with/without cupric sulphate pentahydrate in a sponge (a) and a sectional view (b). The unit indicated in the ruler is in cm.

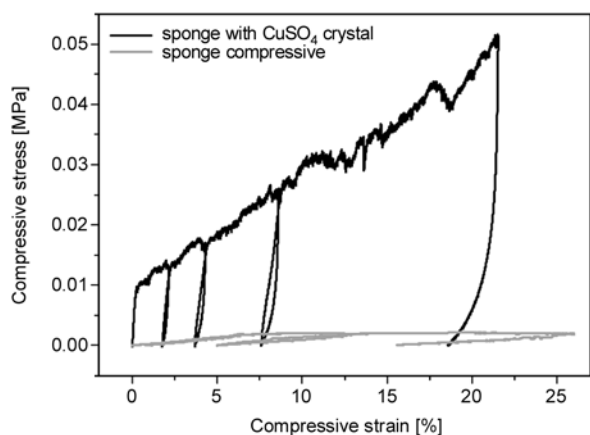


Figure 5. Stress vs. strain curves of sponge and sponge with cupric sulphate pentahydrate (CuSO_4) in cyclic uniaxial compression tests

the sponge is limited. This is consistent with the observed residual crack after penetration shown in Figure 2c.

In the second step, the sponge (Figure 3b) was immersed into room temperature water. Figure 6 presents the snapshots of the recovery (hole clo-

sure) sequence. As cupric sulfate pentahydrate gradually dissolved in the water, the color of the sponge changed from dark blue back to its original color, and the hole closed gradually due to the release of the elastic energy stored in the pre-deformed sponge. After about 6 minutes, the hole was largely closed.

3.2. Silicone/sodium acetate trihydrate hybrid

Silicone has become a widely used material for a variety of applications, mainly due to its excellent biocompatibility and elasticity. Sylgard[®]184 silicone elastomer (from Dow Corning) was used as the elastic matrix, and sodium acetate trihydrate (from Sigma-Aldrich) as the transition inclusion in this part of study. The as-received silicone came in two parts, i.e., liquid silicone base and curing agent. After mixing in a ratio of 10:1, curing can be done either at room temperature or at high temperatures (for a shorter curing time). The cured silicone is transparent, rubber-like and mechanically/chemically stable from -40 to 270°C .

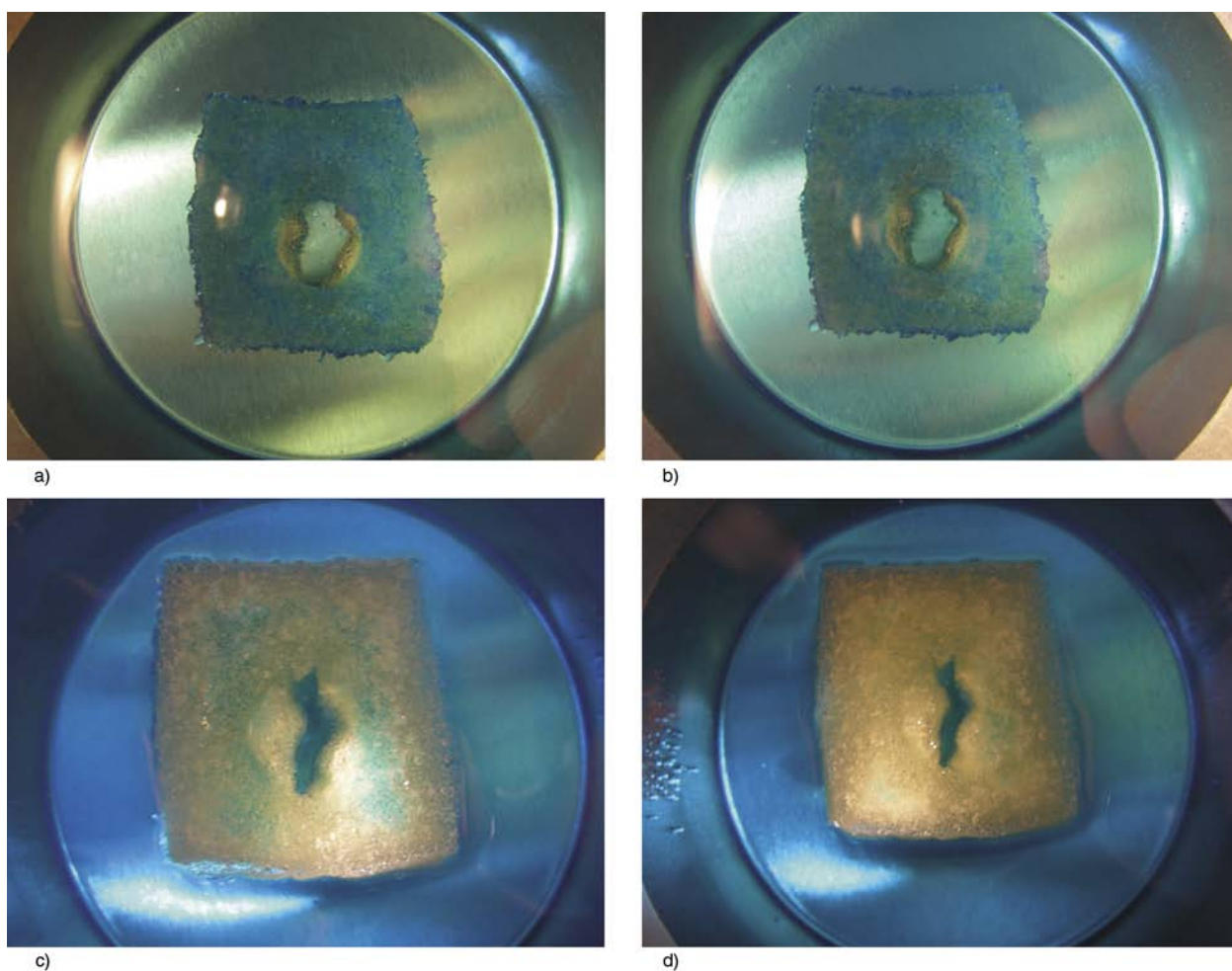


Figure 6. Shape recovery (hole closure) of sponge/cupric sulphate pentahydrate hybrid upon immersing into room temperature water (a–d)

Different from cupric sulfate pentahydrate, upon heating sodium acetate trihydrate starts to melt at about 60°C due to the transition of sodium acetate trihydrate ($C_2H_3NaO_2 \cdot 3H_2O$) into sodium acetate anhydrous ($C_2H_3NaO_2$) and water ($3H_2O$) (sodium acetate dissolved in this $3H_2O$) (refer to Figure 7). At above 85°C, a full liquid state is reached. Hence, sodium acetate liquid can be mixed with liquid silicone base at above 85°C. After cooling back to room temperature, curing agent can be added in for solidifying the silicone. As an alternative, at room temperature sodium acetate trihydrate can be ground into tiny powders and the powders can then be mixed directly into the silicone. In our experiment, the latter was followed as this approach is more

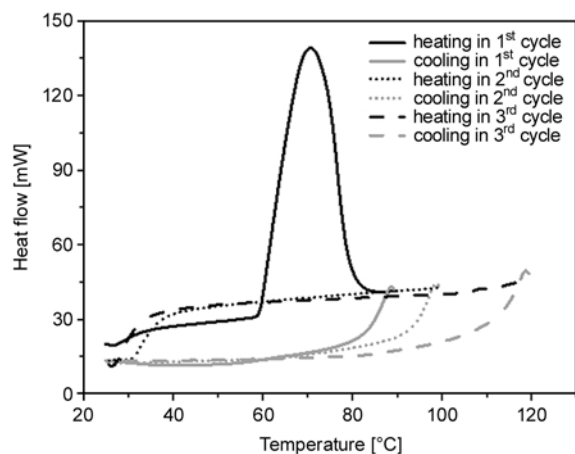


Figure 7. Result of differential scanning calorimeter test of sodium acetate trihydrate

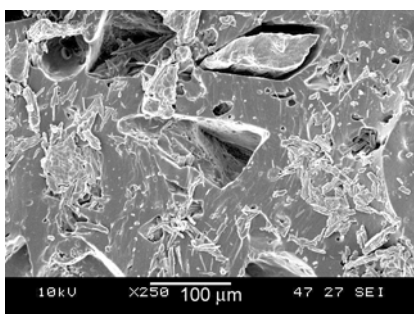


Figure 8. Typical SEM image showing the dispersion of sodium acetate trihydrate (at 50 vol%) within silicone

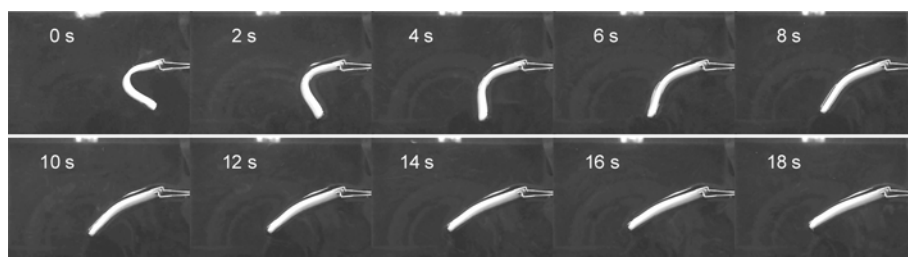


Figure 9. Shape recovery of a strip hybrid (60 vol% of sodium acetate trihydrate) upon immersing into 72.5°C water

convenient. Figure 8 is a typical SEM image, which reveals the dispersion of sodium acetate trihydrate within silicone matrix. It can be seen clearly that tiny sodium acetate trihydrate crystals actually have a tendency towards forming aggregates. A closer look reveals that these aggregates are not fully isolated from each other but connected by some separate crystals.

In order to program the silicone/sodium acetate trihydrate hybrid into a temporary shape, a piece of this hybrid sample (strip shape, with 60 vol% of sodium acetate trihydrate) was heated to above the melting temperature of sodium acetate trihydrate and then bent into a U-shape. After cooling back to room temperature, sodium acetate trihydrate re-crystallized. Hence, apart from a slight elastic recovery, the deformed shape was largely preserved (becoming V-shape) after the constraint was removed. Thermally induced shape recovery (i.e., the thermo-responsive shape memory effect) was examined by immersing the distorted hybrid sample into hot water. As revealed in Figure 9, the sample recovered its original flat strip shape in 18 s in 72.5°C water.

To verify the water-responsive feature, a hybrid ring (with 50 vol% of sodium acetate trihydrate) was prepared (refer to Figure 10, original). The ring was heated to above the melting temperature of sodium acetate trihydrate and deformed into a Y-shape. After cooling back to room temperature, the deformed shape was mainly retained. Subsequently, the deformed ring was immersed into room temperature water. Figure 10 reveals the sequence that the ring gradually recovered its original shape after 50 hours of immersion.

3.3. Discussion

Two approaches have been demonstrated to fabricate water-responsive shape memory hybrids. In the first approach, the temporary shape was achieved by means of re-crystallization of the inclusion

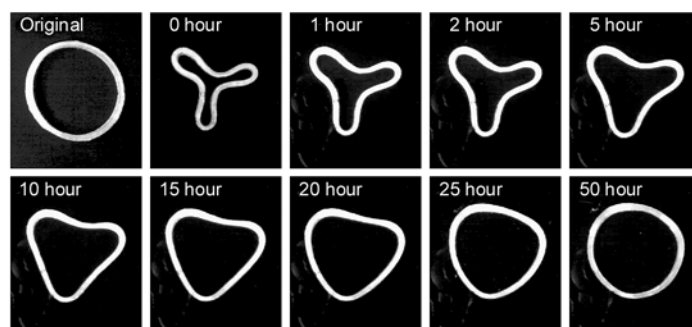


Figure 10. Shape recovery of a hybrid ring (50 vol% of sodium acetate trihydrate) upon immersing into room temperature water

material inside the deformed porous matrix. As the porous matrix is a cured polymer, the possible chemical interaction between the inclusion and matrix is minimized. In the second approach, the temporary shape was achieved by heating the hybrid to the melting temperature of the inclusion, deforming the hybrid and then followed by cooling it back to the room temperature. As we can see, by selecting a proper processing procedure, we can limit, if not totally avoid, the possible chemical interaction between the matrix and the inclusion.

Depending on the type of the inclusion, the porosity of the matrix, the shape of inclusion (closed cell or open cell), and/or the permeability of the matrix, the speed of shape recovery can be controlled.

As compared with the traditional approaches to fabricate water-responsive shape memory polymers (e.g., [25]), the proposed hybrid concept is more convenient and versatile. For instance, the types of inclusion materials are not limited. Hence, medicine can even be used as the inclusion for drug-release [26, 27]. Retractable eluting shape memory stent, which can release drug gradually and eventually shrink its size for easy removal, could be a potential application area.

After the materials for the matrix and inclusion are selected, one can easily predict the properties and behaviors of the resulted hybrid, i.e., the hybrid can be designed following a standard approach as in the design of a conventional composite material. This is another major advantage of this hybrid concept.

This concept can be easily extended into solvent-responsive shape memory hybrids [28], in which a particular chemical is the stimulus to trigger the shape recovery or other means of mechanical action. Consequently, targeted drug release can be more

conveniently (or even routinely) realized. Once the hybrid senses a particular chemical from the surrounding environment, it releases the drug automatically [29, 30].

4. Conclusions

In this paper, the concept of water-responsive shape memory hybrid is proposed. The advantages are demonstrated by the two examples. As we can see, the hybrid concept is versatile and can be easily accessed by those even without much polymer/chemistry background. Moreover, the performance of the resulted hybrid can be well-predicted in the early design stage. This concept can also be further extended into *solvent*-responsive shape memory hybrids, which can be routinely realized in a Do-It-Yourself manner by almost anyone.

References

- [1] Huang W. M., Ding Z., Wang C. C., Wei J., Zhao Y., Purnawali H.: Shape memory materials. *Materials Today*, **13**, 54–61 (2010). DOI: [10.1016/S1369-7021\(10\)70128-0](https://doi.org/10.1016/S1369-7021(10)70128-0)
- [2] Otsuka K., Wayman C.: *Shape memory materials*. Cambridge University Press, Cambridge (1998).
- [3] Miyazaki S., Fu Y. Q., Huang W. M.: *Thin film shape memory alloys—fundamentals and device applications*. Cambridge University Press, Cambridge (2009).
- [4] Entel P., Gruner M. E., Dannenberg A., Siewert M., Nayak S. K., Herper H. C., Buchelnikov V. D.: Fundamental aspects of magnetic shape memory alloys: Insights from ab initio and Monte Carlo studies. *Materials Science Forum*, **635**, 3–12 (2009). DOI: [10.4028/www.scientific.net/MSF.635.3](https://doi.org/10.4028/www.scientific.net/MSF.635.3)
- [5] Rousseau I. A.: Challenges of shape memory polymers: A review of the progress toward overcoming SMP's limitations. *Polymer Engineering and Science*, **48**, 2075–2089 (2008). DOI: [10.1002/pen.21213](https://doi.org/10.1002/pen.21213)

- [6] Mather P. T., Luo X., Rousseau I. A.: Shape memory polymer research. *Annual Review of Material Research*, **39**, 445–471 (2009).
DOI: [10.1146/annurev-matsci-082908-145419](https://doi.org/10.1146/annurev-matsci-082908-145419)
- [7] Huang W. M., Yang B., Zhao Y., Ding Z.: Thermo-moisture responsive polyurethane shape-memory polymer and composites: A review. *Journal of Materials Chemistry*, **20**, 3367–3381 (2010).
DOI: [10.1039/B922943D](https://doi.org/10.1039/B922943D)
- [8] Xie T.: Tunable polymer multi-shape memory effect. *Nature*, **464**, 267–270 (2010).
DOI: [10.1038/nature08863](https://doi.org/10.1038/nature08863)
- [9] Funakubo H.: *Shape memory alloys*. Gordon and Breach Science Publishers, New York (1987).
- [10] Lendlein A.: *Shape-memory polymers*. Springer, Heidelberg (2010).
DOI: [10.1007/978-3-642-12359-7](https://doi.org/10.1007/978-3-642-12359-7)
- [11] Leng J., Du S.: *Shape-memory polymers and multifunctional composites*. CRC Press, Boca Raton (2010).
- [12] Sun L., Huang W. M.: Thermo/moisture responsive shape-memory polymer for possible surgery/operation inside living cells in future. *Materials and Design*, **31**, 2684–2689 (2010).
DOI: [10.1016/j.matdes.2009.11.036](https://doi.org/10.1016/j.matdes.2009.11.036)
- [13] Huang W. M.: On the selection of shape memory alloys for actuators. *Materials and Design*, **23**, 11–19 (2002).
DOI: [10.1016/S0261-3069\(01\)00039-5](https://doi.org/10.1016/S0261-3069(01)00039-5)
- [14] Gunes S. I., Jana S. C.: Shape memory polymers and their nanocomposites: A review of science and technology of new multifunctional materials. *Journal of Nanoscience and Nanotechnology*, **8**, 1616–1637 (2008).
DOI: [10.1166/jnn.2008.038](https://doi.org/10.1166/jnn.2008.038)
- [15] Yakacki C. M., Shandas R., Safranski D., Ortega A. M., Sassaman K., Gall K.: Strong, tailored, biocompatible shape-memory polymer networks. *Advanced Functional Materials*, **18**, 2428–2435 (2008).
DOI: [10.1002/adfm.200701049](https://doi.org/10.1002/adfm.200701049)
- [16] Xie T., Xiao X., Cheng Y.-T.: Revealing triple-shape memory effect by polymer bilayers. *Macromolecular Rapid Communications*, **30**, 1823–1827 (2009).
DOI: [10.1002/marc.200900409](https://doi.org/10.1002/marc.200900409)
- [17] Xie T., Rousseau I. A.: Facile tailoring of thermal transition temperatures of epoxy shape memory polymers. *Polymer*, **50**, 1852–1856 (2009).
DOI: [10.1016/j.polymer.2009.02.035](https://doi.org/10.1016/j.polymer.2009.02.035)
- [18] Nair D. P., Cramer N. B., Scott T. F., Bowman C. N., Shandas R.: Photopolymerized thiol-ene systems as shape memory polymers. *Polymer*, **51**, 4383–4389 (2010).
DOI: [10.1016/j.polymer.2010.07.027](https://doi.org/10.1016/j.polymer.2010.07.027)
- [19] Yang B., Huang W. M., Li C., Li L.: Effects of moisture on the thermomechanical properties of a polyurethane shape memory polymer. *Polymer*, **47**, 1348–1356 (2006).
DOI: [10.1016/j.polymer.2005.12.051](https://doi.org/10.1016/j.polymer.2005.12.051)
- [20] Pretsch T., Müller W. W.: Shape memory poly(ester urethane) with improved hydrolytic stability. *Polymer Degradation and Stability*, **95**, 880–888 (2010).
DOI: [10.1016/j.polymdegradstab.2009.12.020](https://doi.org/10.1016/j.polymdegradstab.2009.12.020)
- [21] Lorenzo V., Díaz-Lantada A., Lafont P., Lorenzo-Yustos H., Fonseca C., Acosta J.: Physical ageing of a PU-based shape memory polymer: Influence on their applicability to the development of medical devices. *Materials and Design*, **30**, 2431–2434 (2009).
DOI: [10.1016/j.matdes.2008.10.023](https://doi.org/10.1016/j.matdes.2008.10.023)
- [22] Smith K. E., Parks S. S., Hyjek M. A., Downey S. E., Gall K.: The effect of the glass transition temperature on the toughness of photopolymerizable (meth)acrylate networks under physiological conditions. *Polymer*, **50**, 5112–5123 (2009).
DOI: [10.1016/j.polymer.2009.08.040](https://doi.org/10.1016/j.polymer.2009.08.040)
- [23] Weiss R. A., Izzo E., Mandelbaum S.: New design of shape memory polymers: Mixtures of an elastomeric ionomer and low molar mass fatty acids and their salts. *Macromolecules*, **41**, 2978–2980 (2008).
DOI: [10.1021/ma8001774](https://doi.org/10.1021/ma8001774)
- [24] Huang W. M., Yang B., An L., Li C., Chan Y. S.: Water-driven programmable polyurethane shape memory polymer: Demonstration and mechanism. *Applied Physics Letters*, **86**, 114105/1–114105/3 (2005).
DOI: [10.1063/1.1880448](https://doi.org/10.1063/1.1880448)
- [25] Jung Y. C., So H. H., Cho J. W.: Water-responsive shape memory polyurethane block copolymer modified with polyhedral oligomeric silsesquioxane. *Journal of Macromolecular Science Part B: Physics*, **45**, 453–461 (2006).
DOI: [10.1080/00222340600767513](https://doi.org/10.1080/00222340600767513)
- [26] Chen M.-C., Chang Y., Liu C.-T., Lai W.-Y., Peng S.-F., Hung Y.-W., Tsai H.-W., Sung H.-W.: The characteristics and *in vivo* suppression of neointimal formation with sirolimus-eluting polymeric stents. *Biomaterials*, **30**, 79–88 (2009).
DOI: [10.1016/j.biomaterials.2008.09.006](https://doi.org/10.1016/j.biomaterials.2008.09.006)
- [27] Wischke C., Lendlein A.: Shape-memory polymers as drug carriers – A multifunctional system. *Pharmaceutical Research*, **27**, 527–529 (2010).
DOI: [10.1007/s11095-010-0062-5](https://doi.org/10.1007/s11095-010-0062-5)
- [28] Du H., Zhang J.: Solvent induced shape recovery of shape memory polymer based on chemically cross-linked poly(vinyl alcohol). *Soft Matter*, **6**, 3370–3376 (2010).
DOI: [10.1039/b922220k](https://doi.org/10.1039/b922220k)
- [29] Gall K., Kreiner P., Turner D., Hulse M.: Shape-memory polymers for microelectromechanical systems. *Journal of Microelectromechanical Systems*, **13**, 472–483 (2004).
DOI: [10.1109/JMEMS.2004.828727](https://doi.org/10.1109/JMEMS.2004.828727)
- [30] Lee B. R., Baik H. J., Oh N. M., Lee E. S.: Intelligent polymeric nanocarriers responding to physical or biological signals: A new paradigm of cytosolic drug delivery for tumor treatment. *Polymers*, **2**, 86–101 (2010).
DOI: [10.3390/polym2020086](https://doi.org/10.3390/polym2020086)

Specific interactions, structure and properties in segmented polyurethane elastomers

K. Bagdi^{1,2}, K. Molnár^{1,2}, I. Sajó³, B. Pukánszky^{1,2*}

¹Laboratory of Plastics and Rubber Technology, Budapest University of Technology and Economics, H-1521 Budapest, P.O. Box 91, Hungary

²Institute of Materials Science and Environmental Chemistry, Chemical Research Center, Hungarian Academy of Sciences, H-1525 Budapest, P.O. Box 17, Hungary

³Institute of Nanochemistry and Catalysis, Chemical Research Center, Hungarian Academy of Sciences, H-1525 Budapest, P.O. Box 17, Hungary

Received 10 September 2010; accepted in revised form 30 November 2010

Abstract. Two sets of segmented polyurethane (PU) elastomers were prepared from 4,4'-methylenebis(phenyl isocyanate) (MDI), 1,4-butanediol (BD) and a polyester or a polyether polyol, respectively. The molecular mass of both polyols was 1000 g/mol. The stoichiometric ratio of isocyanate and hydroxyl groups was 1 and the polyol/total diol ratio changed from 0 to 1 in 0.1 steps. One step bulk polymerization was carried out in an internal mixer and the samples were compression molded for testing. The results proved that specific interactions determine the phase structure and properties of these materials. Crystallinity was approximately the same in the two types of polyurethanes and the amount of relaxing soft segments was also similar. The determination of interaction parameters from solvent absorption and differences in glass transition temperatures indicated stronger interaction between hard and soft segments in the polyester than in the polyether polyurethane. Larger transparency of the polyester PU indicated the formation of smaller dispersed particles of the hard phase. The larger number of smaller hard phase units led to the formation of more physical cross-links distributed more evenly in the polymer. These differences in the phase structure of the polymers resulted in stronger strain hardening tendency, larger strength and smaller deformations for the polyester than for the polyether polyurethane.

Keywords: biocompatible polymers, polyurethane elastomer, specific interactions, phase separation, physical cross-links

1. Introduction

Segmented polyurethanes (PU) are versatile materials used in many segments of life [1]. They are applied as automotive parts, in building and construction, in electrical and engineering applications, in the oil, chemical and food industry and in many other fields [1, 2]. One of their major application areas is health care, where they are used mainly as medical devices in the form of encapsulants for hollow-fiber devices, dip-molded gloves and balloons, asymmetric membranes, functional coatings, and as extruded profiles for cardiovascular catheters [3–5].

The properties of segmented polyurethanes depend on their structure, which is quite complicated. Their molecular structure is determined by the components used in the polymerization reaction and on stoichiometry, and they phase separate during the reaction forming a supermolecular structure [6–10]. Phase separation has been the subject of many studies [11, 12]. The results showed that structural units of various forms and sizes develop during polymerization [13–15]. Besides a crystalline or at least highly ordered phase, soft and hard segments form corresponding phases which are partially soluble in

*Corresponding author, e-mail: bpukanszky@mail.bme.hu

each other [16–21]. Solubility depends very much on the interaction of the components, the urethane groups are capable of forming specific interactions, H-bonds with each other, but also with the soft segments [22, 23]. Depending on preparation conditions, the final structure of the product is determined by kinetic effects, but a very large extent by interactions [24].

Polyurethanes are usually prepared from an isocyanate, a polyol and a chain extender [25]. Only a few isocyanates are used in practice, mostly the aromatic compounds 4,4'-methylenebis(phenyl isocyanate) (MDI) and toluene diisocyanate (TDI). The versatility of polyols is much larger, they may differ in chemical structure, molecular weight or functionality. Polyether and polyester polyols form probably the most important groups of this component [1, 25]. It is obvious to assume that interactions will be different in polyurethanes prepared from the two kinds of polyols, and experience supports this assumption by showing that the properties of products prepared from them differ considerably [26]. Although the effect of the structure and characteristics of the polyol on PU properties have been investigated extensively [27–30], many questions related to structure-property correlations in these materials remain open.

The goal of this communication is to discuss the possible effect of specific interactions on the structure and properties of segmented linear polyurethane elastomers. Two series of samples were prepared from a polyether and a polyester polyol with similar molecular weight. The stoichiometric ratio of isocyanate and hydroxyl groups (NCO/OH ratio) was kept constant while the –OH functional group ratio of polyol/total diol (POH/OH ratio) was changed and used as variable in the experiments. Because of the larger molecular weight of the polyol compared to butanediol, the changing of this ratio results in a relative increase on the amount of the soft phase. Changing POH/OH ratio makes possible the adjustment of properties (hardness, strength, elongation,

T_g) to specific applications. Using the entire composition range allowed us seeing the effect of interactions and changing composition on a wider scale and also drawing more comprehensive conclusions even if the practical relevance of larger POH/OH ratios is small. The structure of the polymers was characterized by various methods and an attempt was made to explain the apparently contradictory results with differences in interactions.

2. Experimental

4,4'-methylenebis(phenyl isocyanate) (MDI) was used as isocyanate and 1,4-butanediol (BD) as chain extender in both series. The polyether polyol was polytetrahydrofuran (PTHF), while the polyester was diol-end-capped poly(butanediol-adipate) (PBDA); both polyols had a molecular mass of 1000 g/mol. All the chemicals were acquired from Sigma-Aldrich Co. (USA). MDI was used as received, butanediol was distilled under vacuum at 190°C for 3 hours, and the polyols were dried at 80°C under vacuum for a day before the reaction. The stoichiometric ratio of isocyanate and hydroxyl groups (NCO/OH ratio) was 1 in all materials. The variable was the –OH functional group ratio of polyol/total diol (POH/OH ratio), which changed from 0 to 1 in 0.1 steps. One step bulk polymerization was carried out in a W50EH internal mixer (Brabender GmbH & Co., Duisburg, Germany) at 150°C, 50 rpm for 30 min. The polymer was compression molded into 1 mm plates at 200°C and 5 min using an SRA 100 (Fontijne Grotnes BV, Vlaardingen, Netherlands) machine. The molecular structure of the repeat units of the polyether and polyester polyurethane elastomers are shown in Figure 1.

The torque and temperature of mixing were recorded during polymerization. The time dependence of these quantities offers information about the kinetics of polymerization and about the molecular mass of the final product. Fourier transform attenuated total reflectance infra-red spectra (FTIR-ATR) were

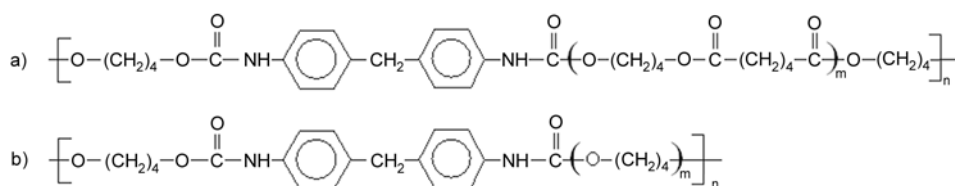


Figure 1. Molecular structure of the repeat units of the polyether and polyester polyurethane elastomers. a) polyester, b) polyether PU.

recorded on the compression molded plates in the wavelength range of 4000 and 400 cm^{-1} , using a Scimitar 2000 (Varian Inc., USA) apparatus equipped with a Specac Golden Gate ATR reflection unit and a wide band Hg-Cd-Te (MCT) detector. The original spectra were corrected before evaluation using the Advanced ATR Correction Algorithm by Thermo Scientific [31]. Specific interactions were estimated by the measurement of solvent absorption. Ethanol and n-octane were used as solvents and Flory-Huggins interaction parameters were calculated from equilibrium solvent uptake. The relaxation transitions of the various phases of the polymers were studied by differential scanning calorimetry (DSC) with a TA 4000 apparatus (Mettler Toledo, USA) equipped with a DSC 30 cell. Two heating and a cooling runs were done on 10 mg samples with a rate of 20°C/min. Dynamic mechanical spectra (DMA) were recorded on samples with 20×6×1 mm dimensions between –120 and 200°C at 2°C/min heating rate in N₂ atmosphere using a Pyris Diamond DMA apparatus (Perkin Elmer, USA). The measurements were carried out in tensile mode at 1 Hz frequency and 10 μm deformation. The structure of the samples was characterized by X-ray diffraction (XRD). XRD patterns were recorded using a PW 1830/PW 1050 equipment (Phillips, Amsterdam, Netherlands) with CuK α radiation at 40 kV and 35 mA in reflection mode. Mechanical properties were determined by tensile testing on dog-bone type specimens with 50×10×1 mm dimensions at 100 mm/min cross-head speed using an 5566 (Instron, USA) apparatus. Tensile strength and elongation-at-break were derived from recorded force vs. elongation traces, while tensile modulus was determined from the initial, linear section of the traces. Shore A hardness was determined with an S1 portable durometer (Instron, USA) on 4 mm thick samples created by the stacking of 1 mm pieces. The transparency of the compression molded plates was measured using a Spekol ultra-violet-visible (UV-VIS) (Analytic, Jena, Germany) apparatus at 500 nm wavelength.

3. Results and discussion

The results of the study will be presented in several sections. The dependence of properties on composition, i.e. on the POH/OH ratio, is shown first, followed by the characterization of structure. Specific

interactions and their possible role in structure development are presented next, while practical consequences are discussed in the final section.

3.1. Properties

The molecular weight of all polymers should be the same, since the same stoichiometry, conditions and polyols with the same molecular weight are used for their preparation. Molecular weight can be determined by gel permeation chromatography (GPC) in dilute solution, but polyurethanes are not always easy to dissolve [32–33]. Since our polymers were prepared by reactive processing, the equilibrium torque measured during the reaction offers information about the molecular weight of the polymers produced. In an earlier study we found good agreement between molecular weight determined by GPC and torque recorded in the internal mixer [33]. Equilibrium torque determined for the two series is presented in Figure 2. Considerable differences can be seen in viscosity between the polyether and polyester polyurethanes in spite of our expectations. Several reasons may explain these differences. Under the conditions of reactive processing the polyols may have different reactivity leading to different kinetics and final molecular weights. Side reactions may also occur during polymerization and in different extents. However, detailed analysis of FTIR spectra could not reveal the formation of biuret or allophanate groups resulting from such reactions in

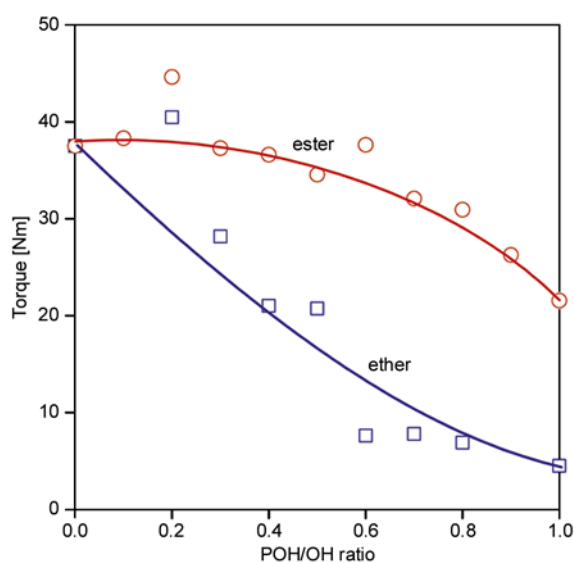


Figure 2. Effect of composition on the viscosity (equilibrium torque) measured at the end of the polymerization reaction in the mixer. Symbols: (○) polyester, (□) polyether polyol.

either of the series. Finally, we cannot exclude the role of interactions as a possible reason for the differences. The larger number of carboxyl groups in the polyester PU may interact with each other, but also with the urethane groups and increase viscosity. The decrease of viscosity with the POH/OH ratio from 0 to 1 also indicates the role of interactions.

Polyurethane elastomers are often characterized by their Shore A hardness, which changes with the relative amount of polyol and chain extender. The hardness of the two series of polymers is compared to each other in Figure 3. Polyether polyurethanes are obviously softer than polyesters and the difference is more pronounced at larger POH/OH ratios. We must assume that the phase segregated morphology differs in the two types of polymers and either the extent of phase separation or the properties of the phases change with composition. At small POH/OH ratios hard segments (MDI and the chain extender) dominate structure, but with increasing polyol content the role of the chemical structure of the polyol, interactions and their effect on phase structure become more pronounced.

The tensile strength and deformability of PU elastomers are other important characteristics determining their possible application. These properties clearly depend both on the molecular and the phase structure of the polymer. In the absence of strong interactions molecular weight determines elongation and strength, while the formation of physical

cross-links results in a considerable increase in both properties. The tensile strengths of the two series are compared to each other in Figure 4. The difference is even larger than in the previous figure. Much larger strengths and different composition dependence is observed for the polyester urethanes than for their polyether counterparts. The maximum in the composition dependence of strength for the polyester PU is a result of several factors. With increasing polyol content the amount of soft phase increases, the size of the hard phase decreases and its distribution becomes more homogeneous. A larger number of smaller physical cross-link sites increase both elongation and strength (strain hardening). Because of weaker unlike interactions a smaller number of larger hard phase units form in the polyether PU and the effect of changing composition (increasing amount of soft phase) dominate (see also section 3.2. on structure). These differences may result from dissimilar molecular structure as suggested by the change of viscosity in Figure 2 or by different interactions and phase structure. The picture is further complicated by the results presented in Figure 5, in which the elongation-at-break values of the samples are plotted against the POH/OH ratio. The larger elongation of the polyether polyurethanes gives an indirect answer and proof that the molecular weight of the polymers is more or less the same. Ultimate elongation is proportional to molecular weight since larger molecules can uncoil more. The similar magnitude of elonga-

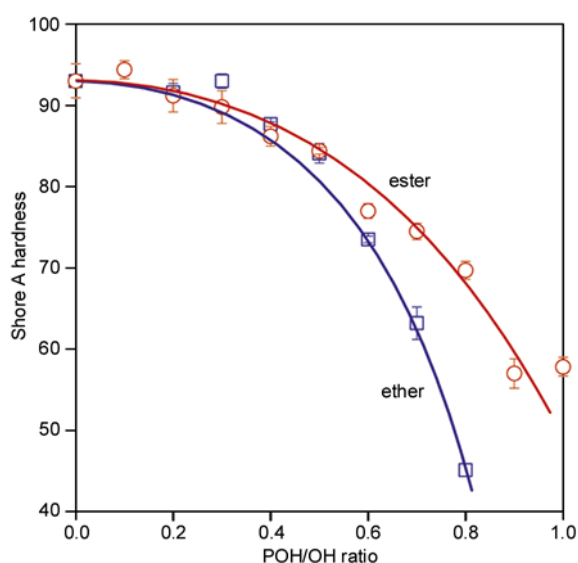


Figure 3. Changes in the Shore A hardness of segmented polyurethane elastomers with the POH/OH ratio. Symbols: (○) polyester, (□) polyether polyol.

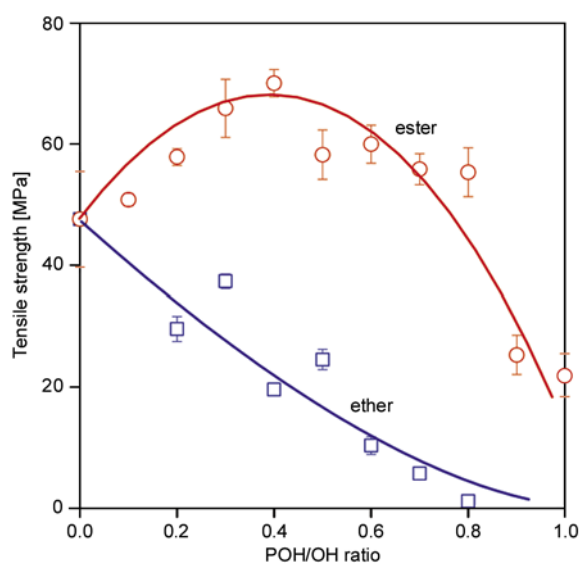


Figure 4. Composition dependence of the tensile strength of polyurethanes prepared with different polyols. Symbols: (○) polyester, (□) polyether polyol.

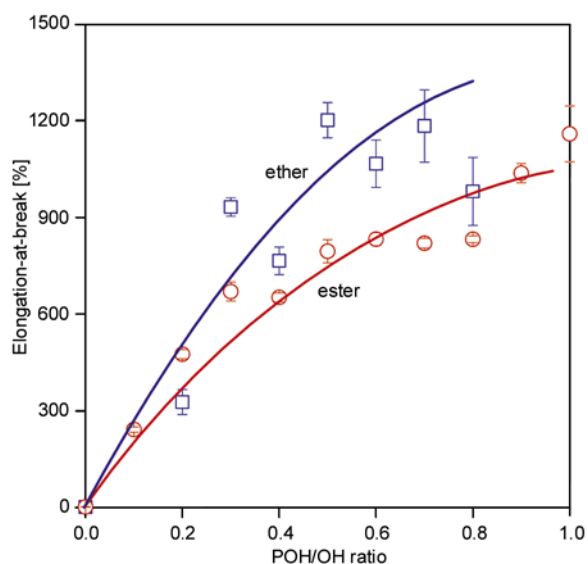


Figure 5. Ultimate elongation of polyurethane elastomers plotted against the POH/OH ratio. Symbols: (○) polyester, (□) polyether polyol.

tions in the two series indicate similar molecular weights, while the smaller actual values of the polyester urethanes points to the role of interactions and phase structure. We may assume that polyether segments can enter into weaker interaction with each other and the urethane groups, thus less soft segments dissolve in the hard phase and the molecules remain more flexible. This leads to smaller hardness and larger elongation, but smaller strength. The results presented up to now emphasize the role of interactions and phase structure, thus we analyze structure in the next section.

3.2. Structure

Hard segments are known to form an ordered, crystalline phase in PU elastomers. This crystalline phase melts at high temperature and can be detected by DSC. Crystallinity and order is small, but this phase may hinder solubility and influence properties considerably. Besides DSC, another technique to study ordered, crystalline structures is X-ray diffraction. The XRD traces of selected polyurethanes are presented in Figure 6. Two compositions were selected for comparison, one rich in hard segments at 0.2 POH/OH ratio and one at high polyol content at 0.8 POH/OH ratio, where the soft phase dominates properties. We can see that order is clearly visible at small POH/OH ratio, but the polymers are practically completely amorphous at large polyol content. Hardly any difference can be detected

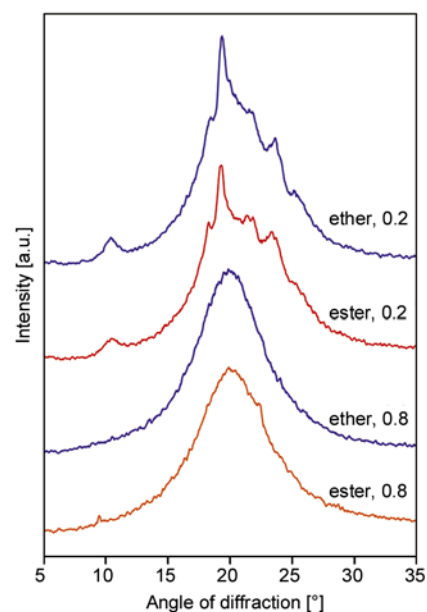


Figure 6. XRD traces of selected PU samples. Effect of composition on crystallinity. The number in the legend indicates the POH/OH ratio.

between the polyurethanes prepared with the two types of polymers, but visual evaluation might be deceiving. The ether urethane seems to be more ordered than the ester at small POH/OH ratio, while the polyester PU exhibits a very small peak at around 22.3 degree hinting at the presence of crystallinity. Unfortunately DSC traces did not confirm the presence of soft phase crystallinity, but this is not very surprising, since its amount is very small, if it is present at all. Quantitative analysis [34] of XRD spectra showed about 10% crystallinity for the polymer containing only hard segments, about 6% at a POH/OH ratio of 0.2 and almost zero above POH/OH = 0.4. This result also means that not crystallinity, but interactions, and the structure and properties of the hard phase result in the differences in strength observed in Figure 4, since the polymers are practically completely amorphous in the composition range in which the strength of the two types of polymers differs the most (POH/OH > 0.4). Thermal methods offer valuable information about the phase structure of heterophase polymers and about the mobility of the segments going through transitions. The analysis of spectra may even offer some information about the composition of the phases. The DMA spectra of the two types of PU are compared to each other in Figure 7 at the POH/OH ratio of 0.5. We can see that the relaxation transition of the soft phase can be detected easily at sub ambi-

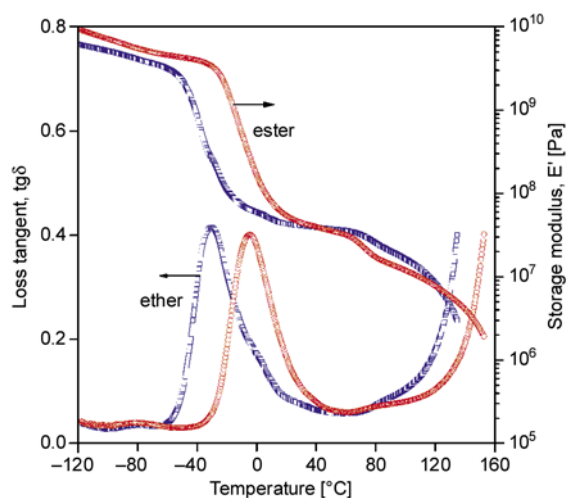


Figure 7 Comparison of the DMTA spectra of PU elastomers prepared with polyether and polyester polyols at 0.5 POH/OH ratio

ent temperatures. The soft phase of polyether urethane has lower glass transition temperature than that of the polyester PU. The detection and analysis of the hard phase is much more difficult. Hard segments are stiff and their mobility does not change much even after the transition. The transition can be detected by the change of the storage modulus, but identification is much more difficult on the $\tan\delta$ trace.

The analysis of DSC traces yields very similar results. The identification of the glass transition of the soft phase is unambiguous, while that of the hard phase is more difficult and the reliability of any quantity derived from the traces for the hard phase is much smaller. The composition dependence of the glass transition temperature of the phases determined by DSC is presented in Figure 8. and Table 1. We can see that the T_g of both phases changes with composition. The transition temperature of the soft phase decreases continuously, while that of the hard phase drops quite considerably first, then increases slightly with increasing polyol content. We must call attention here to the fact that because of the difference in the molecular weight of butanediol and the polyol the amount of soft phase increases with increasing POH/OH ratio thus leading to changes in partial solubility and in the composition of the phases. The drop in the T_g of the hard phase is a result of unlike interactions, which are stronger in the polyester than in the polyether PU. The slight increase at above the POH/OH ratio of 0.2 is probably caused by more pronounced phase

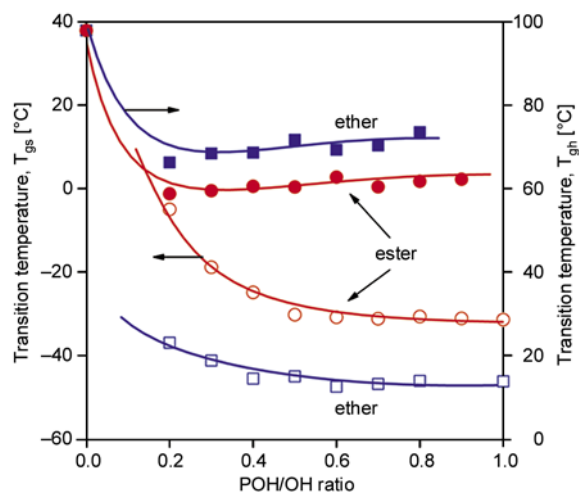


Figure 8. Changes in the glass transition temperature of the phases with composition. T_g was determined by DSC at 20°C/min heating rate. Symbols: (○, ●) polyester, (□, ■) polyether polyol.

Table 1. Glass transition temperatures of the soft and hard phases of polyether and polyester polyurethanes elastomers determined by DSC

POLI(OH)/OH	T_{gs} [°C]		T_{gh} [°C]	
	ester	ether	ester	ether
0.0	–	–	97.89	97.89
0.2	–5.00	–36.94	58.75	66.27
0.3	–18.85	–41.21	59.48	68.43
0.4	–24.88	–45.56	60.52	68.61
0.5	–30.22	–45.02	60.36	71.68
0.6	–30.84	–47.49	62.73	69.31
0.7	–31.20	–46.84	60.41	70.32
0.8	–30.68	–46.11	61.73	73.52
0.9	–31.10	–	62.22	–
1.0	–31.37	–46.21	–	–

separation with increasing soft segment content. The composition dependence of the transition temperature of the phases is similar for the two types of polymers, but the actual values are not. The T_g of the soft phase of polyester polyurethanes is larger in the entire composition range than in the polyether polymers, while the opposite is valid for the hard phase. These results indicate smaller mobility for the soft and larger for the hard segments in the polyester PU. Accordingly, we can conclude that the structural units of the polyester PU molecules enter into stronger interactions with each other than those in the polyether PU.

Further information is supplied about structure at a different scale by the dependence of light transmittance on composition (Figure 9). Large heterogeneities in a transparent matrix scatter light and

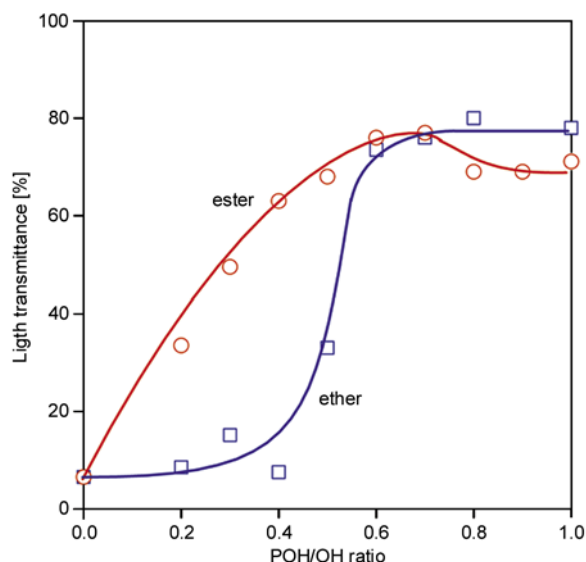


Figure 9. Effect of composition on the transparency of the polyurethane elastomers studied. Symbols: (○) polyester, (□) polyether polyol.

decrease the transparency of materials. Scattering starts for particles in the range of 20 nm and the material becomes completely opaque if the size of dispersed particles reaches several 100 nm. At small POH/OH ratios the composition dependence of transparency indicates large differences in the phase structure of the two types of polymers. The size of the dispersed phase decreases much faster in the polyester PU than in its polyether counterpart. The slight decrease of light transmittance above 0.8 polyol ratio might be related to the crystallization of the soft phase as indicated by XRD analysis (see Figure 6).

3.3. Interactions

As mentioned already, specific interactions are expected to develop between the carbonyl and ether groups of the polyol and the urethane groups, the former being stronger than the latter. Interactions may result in shifts in the corresponding vibrations in the FTIR spectra. Unfortunately the carbonyl groups of the polyester polyol absorb in the same wavelength range as the carbonyl in the urethane group. A detailed analysis of the spectra revealed only a substantial increase in the intensity of free carbonyl groups in the polyester PU as compared to the polyether polymer.

Another way to estimate interactions in a two phase polymer is the measurement of solvent absorption and the calculation of the Flory-Huggins interaction

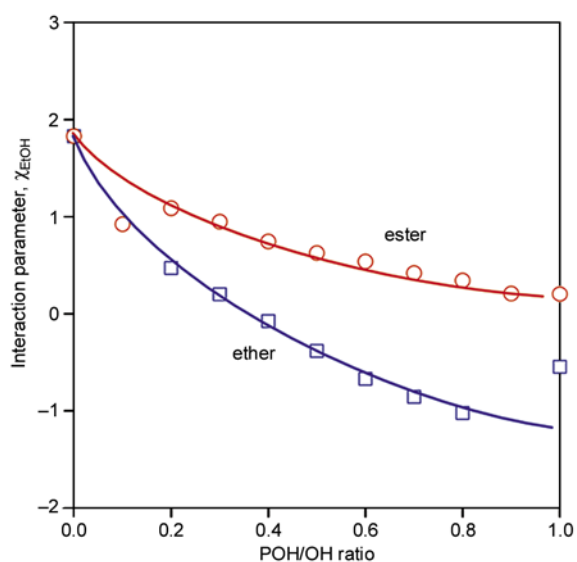


Figure 10. Flory-Huggins interaction parameter determined from ethanol absorption (χ_{EtOH}) plotted as a function of POH/OH ratio. Symbols: (○) polyester, (□) polyether polyol.

parameter from equilibrium solvent uptake. Interaction parameters determined with ethanol (χ_{EtOH}) are plotted in Figure 10 as a function of composition. We can see that larger values are measured in the polyester polyurethane than in the polyether PU indicating weaker interaction. However, in order to understand competitive interactions in such a system, we must consider the interaction of all possible components. The χ_{EtOH} values presented in Figure 10 represent the average interaction of the solvent molecules with the polymer and not the interaction between the segments of PU. Less solvent uptake indicates stronger self-interactions among the segments of the polymer leading to smaller solvent absorption and smaller interaction parameters. The results of these experiments confirm further our previous assumptions that unlike segments of the polyester PU form stronger interactions with each other than those of the polyether polymer.

Stronger interactions among the soft and hard segments should lead to smaller mobility of the soft segment and its larger partial solubility in the hard phase, as well as to decreased number of relaxing species. The number of relaxing units in a phase can be determined from the intensity of the transition, from the area or height of the $\tan\delta$ peak, or from the change in specific heat in the DSC trace. The intensity of soft phase transition is presented as a function of composition in Figure 11. The two types of

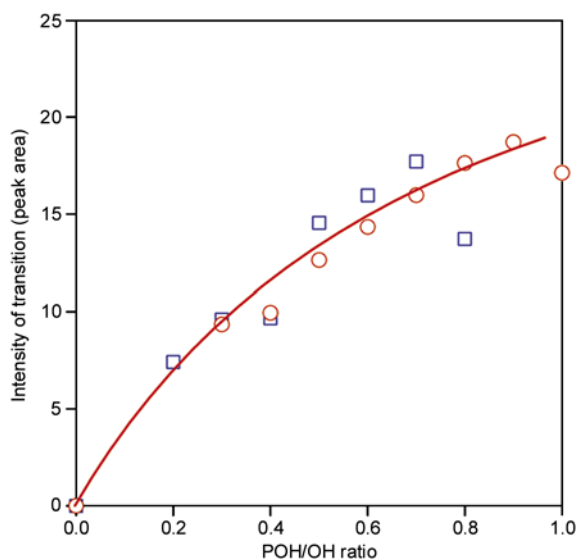


Figure 11. Effect of polyol type and composition on the amount of relaxing soft segments in polyurethane elastomers. Symbols: (○) polyester, (□) polyether polyol.

polymers obviously do not differ from each other in this respect that is rather surprising. Accepting the fact that the amount of the relaxing soft segments is approximately the same in the polyether and polyester urethanes, we must come to the conclusion that differences observed in properties must be caused by the size, number and characteristics of the hard phase.

3.4. Discussion

Results indicate that crystallinity or even order has limited importance at larger than 0.4 POH/OH ratio, but hard segments must play an important role in the determination of properties, especially in the large differences in strength observed in Figure 4. Dispersed units of the hard phase act as physical cross-links and determine the strength as well as deformability of the polymers. The difference in the density of physical cross-links, and/or their dissimilar properties are shown well by the strain hardening behavior of the polymers. Stress vs. strain traces of selected samples are presented in Figure 12. The tensile behavior of the two types of polymers differs significantly from each other. Much larger strengths are measured in the polyester polyurethanes at smaller ultimate deformations, than in the polyether samples, which can be explained with the larger number and more even distribution of physical cross-link sites. Larger hard phase units with

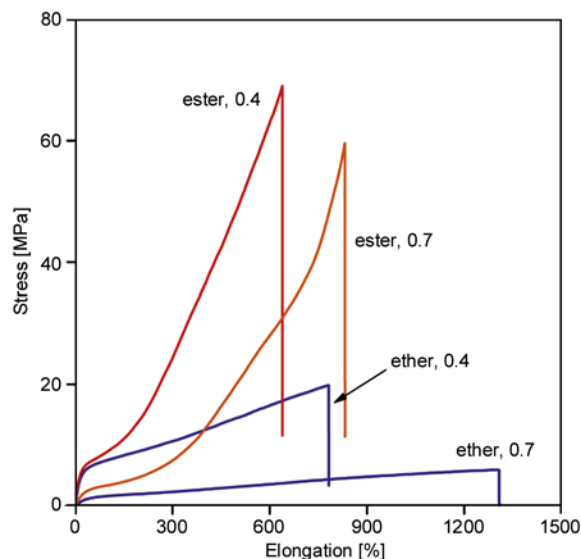


Figure 12. Stress vs. elongation traces of selected polyurethane elastomers; change in behavior with polyol type and composition. Numbers in the legend indicate POH/OH ratio.

larger distances among them must result in the larger elongation of the polyether polyurethanes, and disentanglement of the chains and/or failure of these phases occurs at considerably smaller strengths. Obviously the stronger interaction of the polyester segments with the hard phase results in stronger materials.

The effect of physical cross-links can be visualized quite well if we calculate the work of deformation, i.e. if we multiply ultimate strength (σ) with the corresponding elongation ($\Delta L/L_0$), i.e. $\sigma\Delta L/L_0$. Cross-linking increases both strength and elongation up to a certain cross-link density in elastomers, and decreases above a critical value. The number and deformability of the soft segments is another important factor determining this quantity in our PU elastomers. The work of deformation is plotted against composition in Figure 13. We can see that the correlation has a maximum in both cases. The amount of the hard phase decreases continuously with increasing polyol content and the amount of soft phase thus also the mobility of the soft segments increases at the same time. At small POH/OH ratio this leads to an increase in deformability, which together with the large number of homogeneously distributed physical cross-link sites increase the work of deformation. At very large POH/OH ratios the number of cross-links decreases leading to a decrease in this characteristics. Although the ten-

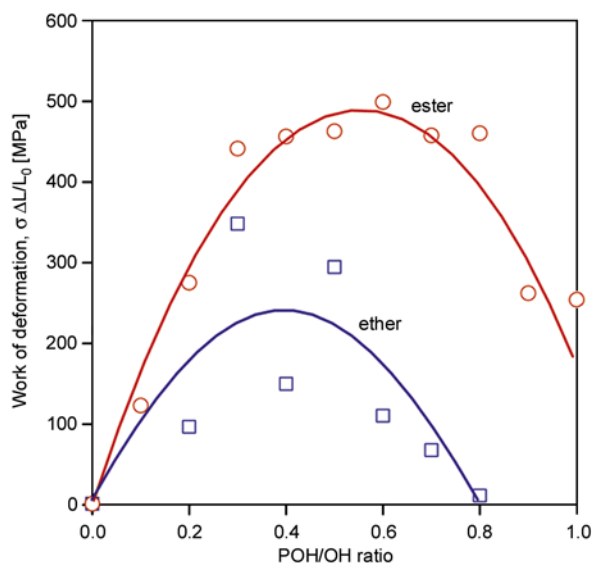


Figure 13. Work of deformation plotted against the POH/OH ratio of segmented polyurethane elastomers. Effect of polyol type on cross-link density. Symbols: (○) polyester, (□) polyether polyol.

density is the same for the two polymers, the actual values, but also the scatter of the points differ considerably. Fewer cross-links distributed less homogeneously in the polyether polyurethane lead to smaller values and to a less unambiguous correlation. The strain hardening tendency of the polymers and additional analysis of mechanical properties clearly prove the role of interactions in the determination of the properties of segmented linear polyurethane elastomers.

4. Conclusions

The comparison of two sets of polyurethane elastomers prepared with a polyester and a polyether polyol of the same molecular weight proved that specific interactions determine the phase structure and properties of these materials. Crystallinity was approximately the same in the two types of polyurethanes and the amount of relaxing soft segments was also similar. The determination of interaction parameters from solvent absorption and differences in glass transition temperatures indicated stronger interaction between hard and soft segments in the polyester than in the polyether polyurethane. Larger transparency of the polyester PU indicated the formation of smaller dispersed particles of the hard phase. The larger number of smaller hard phase units led to the formation of more physical cross-links distributed more evenly in the polymer. These

differences in the phase structure of the polymers resulted in stronger strain hardening tendency, larger strength and smaller deformations for the polyester than for the polyether polyurethane.

Acknowledgements

The authors are indebted to Judith Mihály and Gábor Keresztury for their help in the recording and evaluation of FTIR-ATR spectra. The project was partially financed by the National Scientific Research Fund of Hungary (OTKA Grant No. K 68748) and by the New Hungary Development Plan (Project ID: TÁMOP-4.2.1/B-09/1/KMR-2010-0002); their support is highly appreciated. This work is connected to the scientific program of the 'Development of quality-oriented and harmonized R+D+I strategy and functional model at BME' project.

References

- [1] Randall D., Lee S.: The polyurethanes book. Wiley, New York (2003).
- [2] Seymour R. B., Kauffman G. B.: Polyurethanes: A class of modern versatile materials. *Journal of Chemical Education*, **69**, 909–910 (1992). DOI: [10.1021/ed069p909](https://doi.org/10.1021/ed069p909)
- [3] Zdrahala R. J., Zdrahala I. J.: Biomedical applications of polyurethanes: A review of past promises, present realities, and a vibrant future. *Journal of Biomaterials Applications*, **14**, 67–90 (1999). DOI: [10.1177/088532829901400104](https://doi.org/10.1177/088532829901400104)
- [4] Lamba N. M. K., Woodhouse K. A., Cooper S. L.: Polyurethanes in biomedical applications. CRC Press, Boca Raton (1997).
- [5] Bártolo P., Bidanda B.: Bio-materials and prototyping applications in medicine. Springer, New York (2008).
- [6] Rausch K. W., Sayigh A. A. R.: Structure property relationships in polyurethane elastomers prepared by one-step reaction. *Industrial and Engineering Chemistry Product Research and Development*, **4**, 92–98 (1965). DOI: [10.1021/i360014a008](https://doi.org/10.1021/i360014a008)
- [7] Kojio K., Nakashima S., Furukawa M.: Microphase-separated structure and mechanical properties of norbornane diisocyanate-based polyurethanes. *Polymer*, **48**, 997–1004 (2007). DOI: [10.1016/j.polymer.2006.12.057](https://doi.org/10.1016/j.polymer.2006.12.057)
- [8] Velankar S., Cooper S. L.: Microphase separation and rheological properties of polyurethane melts. 1. Effect of block length. *Macromolecules*, **31**, 9181–9192 (1998). DOI: [10.1021/ma9811472](https://doi.org/10.1021/ma9811472)
- [9] Velankar S., Cooper S. L.: Microphase separation and rheological properties of polyurethane melts. 2. Effect of block incompatibility on the microstructure. *Macromolecules*, **33**, 382–394 (2000). DOI: [10.1021/ma990817g](https://doi.org/10.1021/ma990817g)

- [10] Velankar S., Cooper S. L.: Microphase separation and rheological properties of polyurethane melts. 3. Effect of block incompatibility on the viscoelastic properties. *Macromolecules*, **33**, 395–403 (2000). DOI: [10.1021/ma9908189](https://doi.org/10.1021/ma9908189)
- [11] Furukawa M., Mitsui Y., Fukumaru T., Kojio K.: Microphase-separated structure and mechanical properties of novel polyurethane elastomers prepared with ether based diisocyanate. *Polymer*, **46**, 10817–10822 (2005). DOI: [10.1016/j.polymer.2005.09.009](https://doi.org/10.1016/j.polymer.2005.09.009)
- [12] Pompe G., Pohlers A., Pötschke P., Pionteck J.: Influence of processing conditions on the multiphase structure of segmented polyurethane. *Polymer*, **39**, 5147–5153 (1998). DOI: [10.1016/S0032-3861\(97\)10350-0](https://doi.org/10.1016/S0032-3861(97)10350-0)
- [13] Tocha E., Janik H., Debowski H., Vancso G. J.: Morphology of polyurethanes revisited by complementary AFM and TEM. *Journal of Macromolecular Science Part B: Physics*, **41**, 1291–1304 (2002). DOI: [10.1081/MB-120013098](https://doi.org/10.1081/MB-120013098)
- [14] Król P., Pilch-Pitera B.: Phase structure and thermal stability of crosslinked polyurethane elastomers based on well-defined prepolymers. *Journal of Applied Polymer Science*, **104**, 1464–1474 (2007). DOI: [10.1002/app.25011](https://doi.org/10.1002/app.25011)
- [15] Garrett J. T., Xu R., Cho J., Runt J.: Phase separation of diamine chain-extended poly(urethane) copolymers: FTIR spectroscopy and phase transitions. *Polymer*, **44**, 2711–2719 (2003). DOI: [10.1016/S0032-3861\(03\)00165-4](https://doi.org/10.1016/S0032-3861(03)00165-4)
- [16] Li Y., Kang W., Stoffer J. O., Chu B.: Effect of hard-segment flexibility on phase separation of segmented polyurethanes. *Macromolecules*, **27**, 612–614 (1994). DOI: [10.1021/ma00080a043](https://doi.org/10.1021/ma00080a043)
- [17] Chu B., Gao T., Li Y., Wang J., Desper C. R., Byrne C. A.: Microphase separation kinetics in segmented polyurethanes: Effects of soft segment length and structure. *Macromolecules*, **25**, 5724–5729 (1992). DOI: [10.1021/ma00047a025](https://doi.org/10.1021/ma00047a025)
- [18] Miller J. A., Lin S. B., Hwang K. K. S., Wu K. S., Gibson P. E., Cooper S. L.: Properties of polyether-polyurethane block copolymers: Effects of hard segment length distribution. *Macromolecules*, **18**, 32–44 (1985). DOI: [10.1021/ma00143a005](https://doi.org/10.1021/ma00143a005)
- [19] Saiani A., Daunch W. A., Verbeke H., Leenslag J.-W., Higgins J. S.: Origin of multiple melting endotherms in a high hard block content polyurethane. 1. Thermodynamic investigation. *Macromolecules*, **34**, 9059–9068 (2001). DOI: [10.1021/ma0105993](https://doi.org/10.1021/ma0105993)
- [20] Saiani A., Rochas C., Eeckhaut G., Daunch W. A., Leenslag J.-W., Higgins J. S.: Origin of multiple melting endotherms in a high hard block content polyurethane. 2. Structural investigation. *Macromolecules*, **37**, 1411–1421 (2004). DOI: [10.1021/ma034604+](https://doi.org/10.1021/ma034604+)
- [21] Saiani A., Novak A., Rodier L., Eeckhaut G., Leenslag J.-W., Higgins J. S.: Origin of multiple melting endotherms in a high hard block content polyurethane: Effect of annealing temperature. *Macromolecules*, **40**, 7255–7262 (2007). DOI: [10.1021/ma070332p](https://doi.org/10.1021/ma070332p)
- [22] Yilgör E., Burgaz E., Yurtsever E., Yilgör I.: Comparison of hydrogen bonding in polydimethylsiloxane and polyether based urethane and urea copolymers. *Polymer*, **41**, 849–857 (2000). DOI: [10.1016/S0032-3861\(99\)00245-1](https://doi.org/10.1016/S0032-3861(99)00245-1)
- [23] Liu J., Ma D., Li Z.: FTIR studies on the compatibility of hard–soft segments for polyurethane–imide copolymers with different soft segments. *European Polymer Journal*, **38**, 661–665 (2002). DOI: [10.1016/S0014-3057\(01\)00247-6](https://doi.org/10.1016/S0014-3057(01)00247-6)
- [24] Król P.: Synthesis methods, chemical structures and phase structures of linear polyurethanes. Properties and applications of linear polyurethanes in polyurethane elastomers, copolymers and ionomers. *Progress in Materials Science*, **52**, 915–1015 (2007). DOI: [10.1016/j.pmatsci.2006.11.001](https://doi.org/10.1016/j.pmatsci.2006.11.001)
- [25] Macosko C.W.: RIM, Fundamentals of reaction injection molding. Hanser, Munich (1989).
- [26] Crawford D. M., Bass R. G., Haas T. W.: Strain effects on thermal transitions and mechanical properties of thermoplastic polyurethane elastomers. *Thermochimica Acta*, **323**, 53–63 (1998). DOI: [10.1016/S0040-6031\(98\)00541-3](https://doi.org/10.1016/S0040-6031(98)00541-3)
- [27] Sonnenschein M. F., Lysenko Z., Brune D. A., Wendt B. L., Schrock A. K.: Enhancing polyurethane properties via soft segment crystallization. *Polymer*, **46**, 10158–10166 (2005). DOI: [10.1016/j.polymer.2005.08.006](https://doi.org/10.1016/j.polymer.2005.08.006)
- [28] Eceiza A., de la Caba K., Kortaberria G., Gabilondo N., Marieta C., Corcuera M. A., Mondragon I.: Influence of molecular weight and chemical structure of soft segment in reaction kinetics of polycarbonate diols with 4,4'-diphenylmethane diisocyanate. *European Polymer Journal*, **41**, 3051–3059 (2005). DOI: [10.1016/j.eurpolymj.2005.06.022](https://doi.org/10.1016/j.eurpolymj.2005.06.022)
- [29] Hernandez R., Weksler J., Padsalgikar A., Choi T., Angelo E., Lin J. S., Xu L.-C., Siedlecki C. A., Runt J.: A comparison of phase organization of model segmented polyurethanes with different intersegment compatibilities. *Macromolecules*, **41**, 9767–9776 (2008). DOI: [10.1021/ma8014454](https://doi.org/10.1021/ma8014454)
- [30] Rueda-Larraz L., d'Arlas F. B., Tercjak A., Ribes A., Mondragon I., Eceiza A.: Synthesis and microstructure–mechanical property relationships of segmented polyurethanes based on a PCL–PTHF–PCL block copolymer as soft segment. *European Polymer Journal*, **45**, 2096–2109 (2009). DOI: [10.1016/j.eurpolymj.2009.03.013](https://doi.org/10.1016/j.eurpolymj.2009.03.013)

- [31] Stangret J., Kamienska-Piotrowicz E., Laskowska K.: FT-IR studies of molecular interactions in formamide–methanol mixtures. *Vibrational Spectroscopy*, **44**, 324–330 (2007).
DOI: [10.1016/j.vibspec.2007.02.003](https://doi.org/10.1016/j.vibspec.2007.02.003)
- [32] Ojha U., Kulkarni P., Faust R.: Syntheses and characterization of novel biostable polyisobutylene based thermoplastic polyurethanes. *Polymer*, **50**, 3448–3457 (2009).
DOI: [10.1016/j.polymer.2009.05.025](https://doi.org/10.1016/j.polymer.2009.05.025)
- [33] Pukánszky B. Jr., Bagdi K., Tóvölgyi Z., Varga J., Botz L., Hudak S., Dóczy T., Pukánszky B.: Nanophase separation in segmented polyurethane elastomers: Effect of specific interactions on structure and properties. *European Polymer Journal*, **44**, 2431–2438 (2008).
DOI: [10.1016/j.eurpolymj.2008.06.008](https://doi.org/10.1016/j.eurpolymj.2008.06.008)
- [34] Brückner S.: Estimation of the background in powder diffraction patterns through a robust smoothing procedure. *Journal of Applied Crystallography*, **33**, 977–979 (2000).
DOI: [10.1107/S0021889800003617](https://doi.org/10.1107/S0021889800003617)

Effect of surfactant alkyl chain length on the dispersion, and thermal and dynamic mechanical properties of LDPE/organo-LDH composites

N. Muksing¹, R. Magaraphan¹, S. Coiai^{2*}, E. Passaglia²

¹Polymer Processing and Polymer Nanomaterials Research Unit, Center for Petroleum, Petrochemicals and Advanced Materials, The Petroleum and Petrochemical College, Chulalongkorn University, Bangkok 10330, Thailand

²CNR-ICCOM UOS Pisa, c/o Department of Chemistry and Industrial Chemistry, University of Pisa, Via Risorgimento 35, 56126 Pisa, Italy

Received 10 September 2010; accepted in revised form 4 December 2010

Abstract. Low density polyethylene/layered double hydroxide (LDH) composites were prepared via melt compounding using different kinds of organo-LDHs and polyethylene-grafted maleic anhydride as the compatibilizer. The organo-LDHs were successfully prepared by converting a commercial MgAl-carbonate LDH into a MgAl-nitrate LDH, which was later modified by anion exchange with linear and branched sodium alkyl sulfates having different alkyl chain lengths ($n_c = 6, 12$ and 20). It was observed that, depending on the size of the surfactant alkyl chain, different degrees of polymer chain intercalation were achieved, which is a function of the interlayer distance of the organo-LDHs, of the packing level of the alkyl chains, and of the different interaction levels between the surfactant and the polymer chains. In particular, when the number of carbon atoms of the surfactant alkyl chain is larger than 12, the intercalation of polymer chains in the interlayer space and depression of the formation of large aggregates of organo-LDH platelets are favored. A remarkable improvement of the thermal-oxidative degradation was evidenced for all of the composites; whereas only a slight increase of the crystallization temperature and no significant changes of both melting temperature and degree of crystallinity were achieved. By thermodynamic mechanical analysis, it was evidenced that a softening of the matrix is may be due to the plasticizing effect of the surfactant.

Keywords: polymer composites, organo-LDHs, morphological features, thermal properties

1. Introduction

Layered double hydroxides (LDHs), commonly known as hydrotalcite-like compounds or anionic clays, are a class of host-guest materials whose general formula is $[M_{1-x}^{2+}M_x^{3+}(\text{OH})_2]^{x+}A_{x/n}^{n-} \cdot m\text{H}_2\text{O}$, where M^{2+} is a divalent metal ion (i.e. Mg^{2+} , Zn^{2+} , etc.), M^{3+} is a trivalent metal ion (i.e. Al^{3+} , Cr^{3+} , etc.), A is an anion with valency n (i.e. CO_3^{2-} , Cl^- , NO_3^- , etc.) or an organic anion, m is the number of moles of water per formula weight of compound, and x is a stoichiometric coefficient, generally rang-

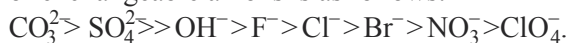
ing between 0.2 and 0.4, which determines the layer charge density and the anion exchange capacity [1–3].

LDHs are structurally similar to the mineral brucite $[\text{Mg}(\text{OH})_2]$ with a fraction of the M^{2+} ions being replaced by M^{3+} ions. Such replacement results in a net positive charge on the octahedral layers, which is balanced by the anions located in the interlayer region where the hydration water molecules are also present [3, 4].

*Corresponding author, e-mail: serena.coiai@ns.dcci.unipi.it

Owing to their highly tunable and unique anion exchange properties, LDHs are being considered as new emerging layered host materials that can be tailored to accommodate a wide range of guest molecules to create novel solids with desirable physical and chemical properties controlled by host–guest and guest–guest interactions [5]. As layered hosts, LDHs have been used in many potential applications, such as catalysts, ceramic precursors, ion exchangers, absorbents, medicine stabilizers, and for controlled release of anions [6–13]. Very recently, their potential as nanofillers for preparing polymer nanocomposites has received considerable attention from both academic and industrial points of view. In contrast to more conventional layered silicates (i.e. MMT), LDHs possess certain inherent advantages; for example, being mostly of synthetic origin, their composition and properties can be modulated by simply changing the type and the molar ratio of the metal ion pairs during the preparation. In addition, the unique positive charge of LDH crystal layers provides a greater flexibility in selecting the most suitable organic modifiers. However, the hydrophilic nature, the strong interlayer electrostatic interactions, and the small intergallery space (around 0.28 nm) make them incompatible with hydrophobic polymers. For this reason, it is necessary to modify the LDH surface, usually with organic anions [14], in order to minimize the attractive forces between the layers, and to increase the interlayer distance and hydrophobicity of LDH, aiming to obtain a good dispersion in polymer matrices.

There are several methods reported in the literature for preparing organo-modified LDHs, i.e. anion-exchange of a precursor LDH, regeneration, thermal reaction, direct synthesis by coprecipitation, and the more recent one-step synthesis method [15–17]. Among all of the methods described, anion exchange is one of the more commonly used and several anionic species, such as phosphates, carboxylates, sulfonates, and sulfates, have been used [18]. Actually, the exchange reaction is controlled by the selectivity of the layered host for the different anions, and in a previous work by Miyata *et al.* [19], it was demonstrated that the selectivity scale of exchangeable anions is as follows:



LDHs containing ClO_4^- , NO_3^- , or even Cl^- are generally used as precursors for up taking long-chain

organic anions owing to their large anion-exchanging capacity.

LDH-based polymer nanocomposites have been extensively investigated with a large number of polymers, including, epoxy resins [20], polyamide [21], poly(ethylene terephthalate) [22], poly(vinyl alcohol) [23], poly(lactic acid) [24], poly(ϵ -caprolactone) [25], polypropylene [26–30], and polyethylene [15, 31–40]. Much attention has been focused on preparing LDH polyethylene (PE)-based nanocomposites due to the good balance between processability, mechanical properties, and chemical resistance of this thermoplastic polymer, very suitable for packaging and engineering applications. In particular, LDH PE-based nanocomposites were prepared by solution intercalation [31–34] and melting processes [35–40]. Costa and coworkers [35, 39] first reported the preparation of intercalated/flocculated LDPE/(dodecyl benzene sulphonate, DBS)-LDH nanocomposites using a melt intercalation process. A complex morphological feature of dispersed LDH particles was observed, with the particles mostly located in the form of thin platelets and agglomerates. Rheological studies of these nanocomposites evidenced a significant change of the linear viscoelastic response in the low frequency region with respect to the matrix due to the formation of a network-like structure via the interaction between the LDH particles and the polymer chains, even if the morphological analysis by X-ray diffraction (XRD) and transmission electron microscopy (TEM) did not give evidence of homogeneous dispersion and perfect exfoliation of DBS-LDH particles. Nonetheless, both thermal stability and fire resistance properties were significantly enhanced [36], most likely due to the barrier effect of LDH layers on the oxygen diffusion, thus preserving PE chain segments from thermal oxidation. Similar results were also achieved in the case of LLDPE/dodecyl sulphate (DS)-LDH nanocomposites [37] and PE/stearate-LDH nanocomposites [38].

Even though it has been demonstrated that the organic modification of LDH is sufficient to achieve the intercalation of PE chains between the layers [41], the use of a compatibilizer, such as a polyethylene functionalized with maleic anhydride groups (PEMAH), is necessary to improve the interactions between the polymer and the LDH and to favor the formation of composites with a stable morphology.

Costa *et al.* [39] prepared PE/LDH composites using an unmodified PE and a PE functionalized with MAH, both as the matrix; in particular, it was investigated how the chemical compatibility of the polymer matrix with LDH influences the morphology of the composites and the rheological properties. The scanning electron microscopy (SEM) analysis evidenced that platelets were well coated by the functionalized polymer, while the formation of structural associations, or clusters, was associated with the presence of the unmodified PE. A different behavior of rheological parameters vs. temperature, due to a deviation from the liquid-like low frequency toward a pseudo solid-like flow, was also observed in the presence of the functionalized PE, originating from the differences between the polymer-particle and particle-particle chemical interactions [42].

In the framework of a study of the role of interfacial effects/interactions in the preparation of nanocomposites, we report results about the morphology and properties of LDPE/organo-LDH composites prepared by changing the type of anion used for modifying the LDH. LDH-CO₃ was first converted to LDH-NO₃ for facilitating the organo-modification by anion exchange. Then, three different organo-LDHs were prepared with linear and branched alkyl sulfates having different alkyl chain lengths ($n_c = 6, 12$ and 20 , which is the number of carbon atoms of the main alkyl chain), and the products were characterized by XRD, Fourier transform infrared spectroscopy (FTIR), SEM, and thermogravimetry (TGA). Finally, LDPE composites were prepared by melt processing with all of the organo-LDHs and using a PEMAH as compatibilizer of the system. The morphology, and thermal and thermo-mechani-

cal properties of such materials were investigated in order to evaluate the effect of the dispersion of LDH platelets in the polymer matrix on the final properties.

2. Experimental part

2.1. Materials

Low-density polyethylene (LDPE, Riblene FL34), with a density of 0.924 g/cm³ and a melt flow index of 2.1 g/10 min (190°C, 2.16 kg) was purchased from Polimeri Europa S.p.A (Mantova, Italy). Polyethylene, functionalized with maleic anhydride (PEMAH) UL EP Compoline[®] by Auserpolimeri S.r.l. (Lucca, Italy), having a melt flow index of 2.5 g/10 min (190°C, 2.16 kg) and an amount of maleic anhydride grafted groups of 0.5 to 1.0 wt%, was used as the compatibilizer. MgAl hydroxy carbonate, PURAL MG63HT (LDH-CO₃), having the following molecular formula, Mg_{0.66}Al_{0.34}(OH)₂(CO₃)_{0.17}·0.62H₂O as previously determined [28], was kindly supplied by Sasol GmbH (Hamburg, Germany). 2-ethylhexyl sulphate, dodecyl sulphate, and eicosyl sulfate were purchased from Aldrich Chemical Company (Steinheim, Germany). The chemical structures are shown in Figure 1.

2.2. Synthesis of Mg/Al LDH-NO₃ and organo-LDHs

The Mg/Al layered double hydroxide, labeled as LDH-CO₃, was used as the precursor. The nitrate form, with the formula

[Mg_{0.66}Al_{0.34}(OH)₂](NO₃)_{0.34}·0.44H₂O], labeled as LDH-NO₃, was obtained by titration at room temperature of the LDH-CO₃ dispersed in a 1M NaNO₃ aqueous solution (mass/volume = 2 g/100 ml) with

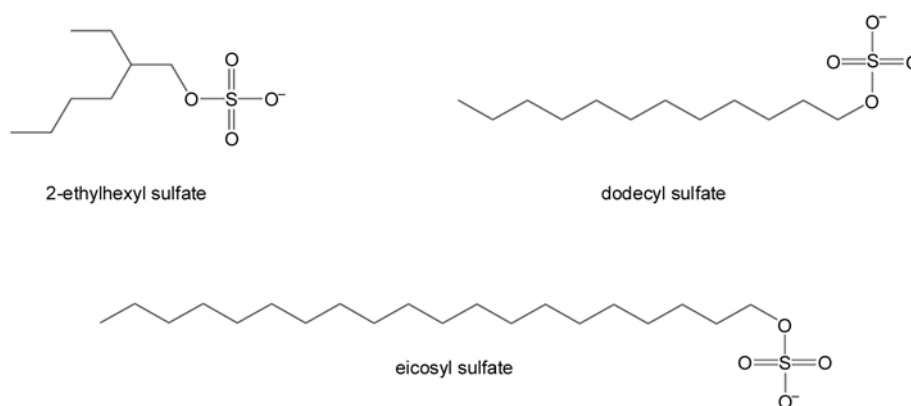


Figure 1. Chemical structure of anionic surfactant guest molecules used for preparing the organo-LDHs

a 1M HNO₃. After titration, the white solid was washed several times with CO₂-free deionized water and dried overnight at 60°C in a vacuum oven [43]. The calculated anion-exchange capacity (AEC) of the LDH-NO₃ was 3.81 mmol of NO₃⁻/g, calculated as follows: AEC = $x/M_w \cdot 10^3$ (mequiv/g), where M_w and x are the molecular weight and the layer charge per octahedral unit, respectively [44, 45]. The organo-LDHs were synthesized via anion-exchange reaction. Firstly, for each organo-LDH, an amount of surfactant corresponding to 1.5 times the AEC of the LDH-NO₃ was dissolved in 100 ml of CO₂-free deionized water and heated at 70°C until a clear solution was obtained. The pH of the solution was maintained at 10 by using 1M NaOH solution. Secondly, 1 g of the LDH-NO₃ was added to the surfactant solution, followed by ultrasound treatment for 15 min. The mixture was magnetically stirred for 24 h at 70°C in nitrogen atmosphere. Then the resulting organo-LDHs were first separated by centrifugation at 6000×g for 10 min, washed several times with CO₂-free deionized water until pH = 7, and finally dried at 60°C under N₂ atmosphere till constant weight. The organo-LDHs were labeled as LDH-C6, LDH-C12, and LDH-C20 having 2-ethylhexyl sulfate, dodecyl sulfate, and eicosyl sulfate, respectively, as interlayer anions.

2.3. Preparation of LDPE/organo-LDH composites

LDPE composites with different organo-LDHs were prepared in an internal batch mixer (Plastograph PL2100, Brabender, Duisburg, Germany) 30 ml chamber at 180°C using a screw speed of 80 rpm. In the first step, LDPE and PEMA_H were melt blended in the mixing chamber for 4 min until achieving a constant torque value, then the desired amount and type of organo-LDH was added and compounded for 16 min. The amount of clay was fixed at 2.5 wt% with respect to the polymer matrix in the case of LDH-C6 and LDH-C12, and 1.5 wt% for LDH-20, whereas the PEMA_H compatibilizer was added in the same amount as the organo-LDH. In the case of the LDH-C12, a second composite was prepared by adding 5 wt% LDH-C12 with respect to the total amount of polymers to obtain LDPE/LDH-C12_5%. The exact formulation for each composite is given in Table 2.

Table 1. Reflections of the <00l> series, interlayer spacing values, and chemical formulae of the LDH-CO₃, LDH-NO₃, and organo-LDHs modified with various types of alkyl sulfate surfactants

Sample	No. of carbon alkyl chain length (n _c)	Reflections of the <00l> series [°]			Arrangement in the interlayer LDH	B ^a (FWHM, rad.)	Chemical formulae ^b
		<003>	<006>	<009>			
LDH-CO ₃	–	9.9 (0.89)	23.4 (0.38)	34.6 (0.26)	–	0.24	Mg _{0.66} Al _{0.34} (OH) ₂ (CO ₃) _{0.17} ·0.62H ₂ O
LDH-NO ₃	–	9.9 (0.89)	19.9 (0.45)	34.6 (0.26)	–	0.25	Mg _{0.66} Al _{0.34} (OH) ₂ (NO ₃) _{0.34} ·0.44H ₂ O
LDH-C6	6	4.2 (2.12)	8.5 (1.04)	12.6 (0.74)	monolayer	0.52	Mg _{0.66} Al _{0.34} (OH) ₂ (CO ₃) _{0.092} (C ₈ H ₁₇ SO ₄) _{0.157} ·0.48H ₂ O
LDH-C12	12	3.6 (2.42)	7.3 (1.22)	10.9 (0.81)	monolayer	0.38	Mg _{0.66} Al _{0.34} (OH) ₂ (CO ₃) _{0.101} (C ₁₂ H ₂₅ SO ₄) _{0.139} ·0.52H ₂ O
LDH-C20	20	2.7 (3.25)	5.5 (1.61)	8.3 (1.07)	monolayer	0.42	Mg _{0.66} Al _{0.34} (OH) ₂ (CO ₃) _{0.062} (C ₂₀ H ₄₁ SO ₄) _{0.216} ·0.65H ₂ O

^aB is the full-width at half-maxima (FWHM, rad.) obtained from XRD results.

^bThe chemical formulae of the LDH-CO₃, LDH-NO₃, and organo-LDHs were determined by combining the results of ICP-OES, elemental analysis, and TGA analysis.

Table 2. Composition of LDPE/organo-LDH composites and their thermal properties

Composites (LDPE/PEMAH/Organo-LDH composition)	T _{10%} [°C]	T _{50%} [°C]	T _{max} [°C]	ΔT _{max} [°C]	T _{c, peak} [°C]	T _{m, peak} [°C]	ΔH _m [J/g]	χ _c ^a	Residue ^b [%]
LDPE (100)	376.0	414.6	434.2	–	85.6	108.8	132.2	45.1	0.31
LDPE/PEMAH (97.5/2.5)	380.0	417.6	431.5	–	84.9	112.3	130.5	44.5	0.48
LDPE/LDH-C6 (97.5/2.5/2.5)	371.8	443.0	464.2	32.7	86.4	110.3	126.1	44.1	1.35
LDPE/LDH-C12 (97.5/2.5/2.5)	370.7	433.3	452.1	20.6	84.4	112.2	125.6	44.0	1.09
LDPE/LDH-C20 (98.5/1.5/1.5)	384.9	440.4	456.8	25.3	86.9	109.6	130.7	45.3	0.68
LDPE/LDH-C12_5% (95/5/5)	367.8	434.7	457.0	25.5	84.5	110.0	119.7	43.0	2.13

^aCalculated as follows: $\chi_c = \Delta H_m / (1 - x) \Delta H_m^0 \cdot 100$, where ΔH_m is the experimental melting enthalpy, $(1 - x)$ is the polyethylene fraction by weight in the composite, and ΔH_m^0 is the melting enthalpy of infinite polyethylene crystal (293 J/g).

^bResidue at 900°C obtained from TGA analysis.

2.4. Characterizations

X-ray diffraction (XRD) patterns of LDH-CO₃, LDH-NO₃, organo-LDHs, and their LDPE composites were recorded by using a Kristalloflex 810, (Siemens, Karlsruhe, Germany) diffractometer (CuK_α radiation, $\lambda = 0.15406$ nm) in the 2θ region of 1.5 to 40° at the scanning rate of 0.016°/min. The crystallite size of LDHs was calculated using the Scherrer Equation (1):

$$L = \frac{\lambda \cdot \kappa}{B \cdot \cos\theta} \quad (1)$$

where L [nm] is the thickness of the crystallite in the direction perpendicular to the plane metal hydroxide sheet in LDH materials, κ is a factor between 0.87 and 1.00, B is the full-width at half-maxima (FWHM, rad) and θ is the scattering angle [°].

Fourier transform infrared (FT-IR) spectra of the LDH-CO₃, LDH-NO₃, and organo-LDHs were recorded over the wavenumber range 450 to 4000 cm⁻¹ using a spectrophotometer (Model 1760-X, PerkinElmer, Waltham, Massachusetts, USA). The spectra were obtained by mixing the sample with potassium bromide powder.

The thermogravimetric analysis (TGA) of the LDH-CO₃, LDH-NO₃, organo-LDHs, and LDPE composites was performed (Model TGA/SDTA 851^e, Mettler-Toledo GmbH, Schwerzenbach, Switzerland). Samples (~10 mg) were placed in alumina sample pans and runs were carried out at the standard rate of 10°C/min from 25 to 900°C under air flow (60 ml/min).

The Mg/Al ratios of the LDH-NO₃ and organo-LDHs were determined by inductively coupled plasma atomic emission spectrometry (ICP-OES) (Varian Vista MPX, Varian, Palo Alto, California, USA) using a Varian Vista MPX spectrometer, as

previously reported [28]. For this analysis samples were dissolved in a nitric acid solution. In this way it was determined the stoichiometric coefficient x of the LDH general formula $[M_{1-x}^{2+}Al_x^{3+}(OH)_2]^{x+}A_{x/n}^{n-} \cdot mH_2O$. Carbon, hydrogen, and sulfur elemental analyses of the organo-LDHs were determined by a CHNS elementary analyzer (TruSpec[®], LECO Corporation, St Joseph, Michigan, USA). The analyses yielded the following results:

LDH-C6: 55.98% C, 7.52% H, 5.46% S;

LDH-C12: 54.72% C, 7.11% H, 5.15% S;

LDH-C20: 56.59% C, 7.51% H, 5.80% S.

Accordingly, the intercalation amount of alkyl sulfate surfactants into the LDH interlayers was calculated. Finally, the moles of water per formula weight of compound, m , were estimated by the first step of degradation of the TGA. The chemical formulae of the organo-LDHs, calculated by combining all these information are given in Table 1.

The morphological features of the LDH-CO₃, LDH-NO₃, and organo-LDHs were studied using a scanning electron microscope (FE-SEM) (S-4800, Hitachi High-Technologies Corporation, Ibaraki-ken, Japan). The powdered samples were first spread on a sample button using conducting cement, while the composite samples were dipped and fractured in liquid nitrogen before putting them on the sample button. Then, all of the samples were sputtered with platinum before viewing under the electron microscope operating at 3 kV.

The transmission electron microscopy (TEM) (Zeiss EM 900 microscope, Carl Zeiss, Oberkochen, Germany) was performed operating at an acceleration voltage of 80 kV. Ultrathin sections (about 50 nm thick) of compression-moulded plaques were prepared by a cryoultramicrotome (Leica EM FSC,

Leica Mikrosystems GmbH, Vienna, Austria) equipped with a diamond knife, keeping the samples at -145°C .

Differential scanning calorimetry (DSC) measurements were carried out on 5–10 mg samples by using a calorimeter equipped with a CCA7 liquid nitrogen cooling device (DSC7, PerkinElmer, Waltham, Massachusetts, USA). The melting/crystallization behaviour of LDPE, LDPE/PEMAH blends and organo-LDH composites was investigated in the temperature range from -30 to 200°C at the scanning rate of $20^{\circ}\text{C}/\text{min}$ under nitrogen flow. Indium ($T_m = 156.95^{\circ}\text{C}$; $\Delta H_m = 28.49 \text{ J}/^{\circ}\text{C}$) and zinc ($T_m = 419.50^{\circ}\text{C}$) were used as calibration standards. The crystallinity degree from DSC was calculated according to the Equation (2):

$$x_c = \frac{\Delta H_m}{(1 - x) \cdot \Delta H_m^0} \cdot 100 \quad (2)$$

where ΔH_m is the experimental melting enthalpy, $(1 - x)$ is the polyethylene fraction by weight in the composite and ΔH_m^0 is the melting enthalpy of an infinite polyethylene crystal (293 J/g).

The thermo-mechanical properties of materials were investigated by dynamic mechanical thermal analysis (DMTA) (DMA7e, PerkinElmer, Waltham, Massachusetts, USA) in three-point bending geometry. Thermograms were obtained at a heating rate of $5^{\circ}\text{C}/\text{min}$ and 1 Hz frequency in the temperature range of -150 to 50°C .

Specimens of the composites for XRD, TEM and DMTA ($2 \times 1 \times 0.2 \text{ cm}$) analyses were prepared at 190°C by using a laboratory hot-press (Carver 3851-0, Carver[®], Wabash, Indiana, USA).

3. Results and discussion

3.1. Preparation and characterization of the organo-LDH particles

To facilitate the exchange process with organic surfactants, the LDH carbonate form (LDH-CO_3) was converted into nitrate (LDH-NO_3) following the method described by Miyata [19]. The XRD pattern of the LDH-NO_3 evidences the shift of all diffraction maxima to lower angles and, in particular, the (003) basal reflection from $2\theta = 11.7^{\circ}$ to $2\theta = 9.9^{\circ}$, corresponding to an enlargement of the basal spacing (d_{003}) from 0.76 to 0.89 nm (Figure 2a). Moreover, the FTIR spectrum of the LDH-NO_3 (Figure 2b) shows peaks at 1384 and 839 cm^{-1} , due to the ν_3 and ν_2 vibration modes, respectively, of the NO_3^- [43], in addition to adsorption peaks at 670 and 550 cm^{-1} (Al–OH and Mg–OH translation modes), and a broad adsorption peak at 3459 cm^{-1} , associated with the –OH stretching [46].

The XRD patterns of the organo-LDHs modified with anionic surfactants having alkyl chains of different lengths, two linear and one branched, are shown in Figure 3a. For all of the samples, it was clear that there was a further shift toward lower angles of the (003) basal reflection with the increasing number of carbon atoms of the surfactant alkyl chain (n_c), which is consistent with an enlargement of the interlayer distance from 0.89 to 2.12 , 2.42 and 3.25 nm for $n_c = 6$, 12 and 20 , respectively (Table 1). Moreover, higher order reflection peaks (00*l*), due to the formation of well-ordered guest intercalated LDH layers, are shown in the XRD patterns. Nonetheless, even if the anion exchange was carried out under nitrogen atmosphere to prevent

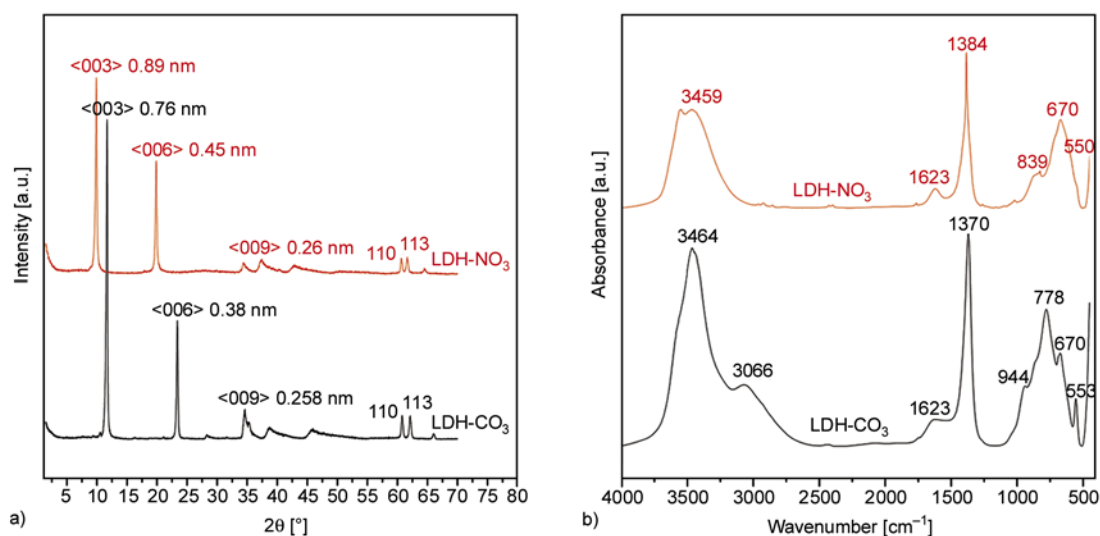


Figure 2. XRD patterns (a) and FTIR spectra (b) of LDH-NO_3 and LDH-CO_3

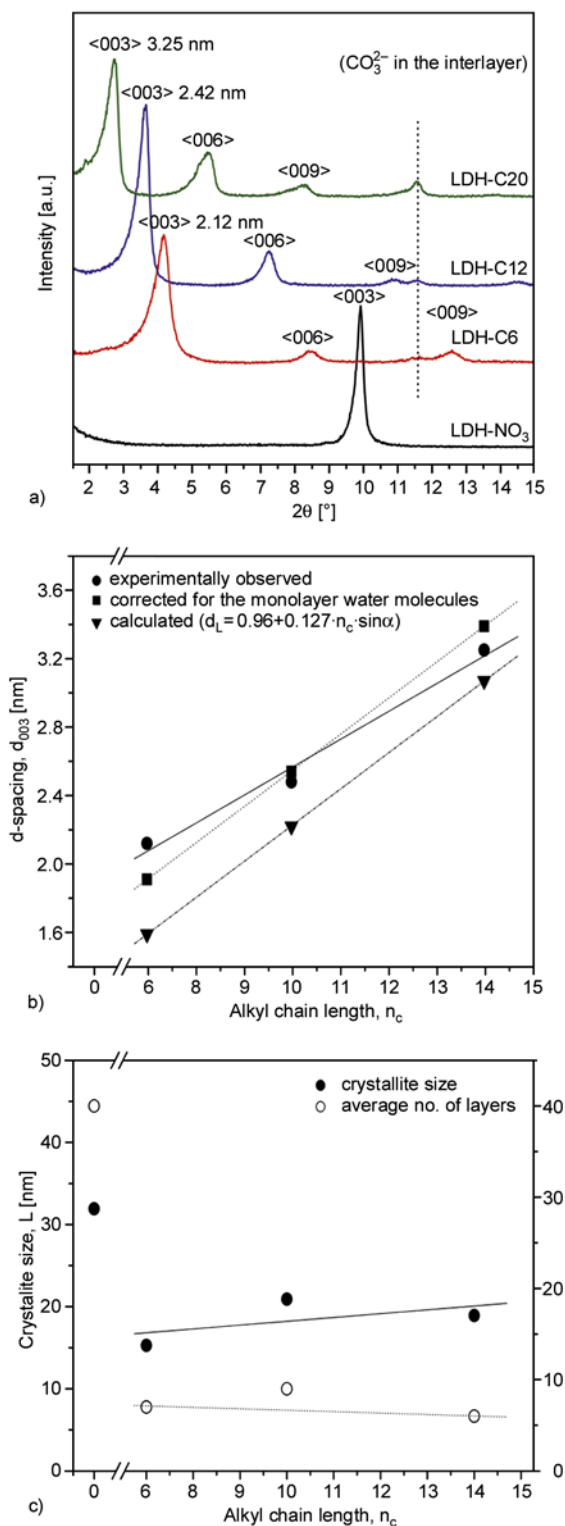


Figure 3. Effect of alkyl chain length (n_c) of sulfate surfactants on: (a) XRD patterns of organo-LDHs, (b) d -spacing and alkyl chain arrangement between the LDH layers, and (c) average crystallite size

carbonate contamination, a weak peak at $2\theta \approx 11.5^\circ$ (0.77 nm), related to the co-intercalation of carbonate anions, still exists for all of the samples. A per-

pendicular orientation of surfactants in organo-LDHs has been observed in previous studies [47–49]. Indeed, due to the small equivalent area of LDHs, the surfactants form generally mono- or bimolecular films instead of lying flat on the interlamellar surfaces. Based on these investigations, which were carried out for a wide range of LDHs and surfactants, the relation for predicting the interlayer distance in the case of primary alkyl sulfates with monolayer or bilayer arrangement of the surfactant in the interlayer space is given by Equations (3) and (4), respectively [48–51]:

$$\text{monolayers: } d_L [\text{nm}] = 0.96 + 0.127 \cdot n_c \cdot \sin \alpha \quad (3)$$

$$\text{bilayers: } d_L [\text{nm}] = 1.42 + 0.254 \cdot n_c \cdot \sin \alpha \quad (4)$$

where d_L is the basal spacing in nm, n_c is the number of carbon atoms in the alkyl chain of the surfactant, and α is the tilt angle of the alkyl chain from the normal of the metal hydroxide sheet. In particular, it has been demonstrated that in the case of alkyl sulfate anions the value of the α angle is 56° [47–49, 52, 53]; moreover, a layer of adsorbed water molecules is generally present in between the hydrocarbon chain end of the surfactant and the metal hydroxide layer [47, 48, 51, 52] which takes up about 0.3 – 0.5 nm. In particular, a value of 0.32 nm for the adsorbed layer of water molecules was reported in the case of LDH modified with dodecyl benzene sulfonate anions. According to these results, the experimental interlayer distances of organo-LDHs were compared with predicting values estimated by considering a monolayer arrangement of the alkyl sulfate ions between the layers of LDHs (Figure 3b). The calculated d_L values were corrected by considering an adsorbed layer of water molecules of 0.32 nm. The linear relationship existing between the d_L values and the number of carbon atoms of the surfactant alkyl chains (Figure 3b) is consistent with the hypothesis of a monolayer arrangement of all surfactants between the LDH layers. A close similarity between experimental and calculated values was obtained in the case of LDH-C12, whereas for both LDH-C6 and LDH-C20, small differences were observed which could be due to a different tilt angle of the surfactant alkyl chains and/or a different amount of the water adsorbed layer with respect to those considered for the valuation. In particular, for the case of LDH-C6 the ethyl

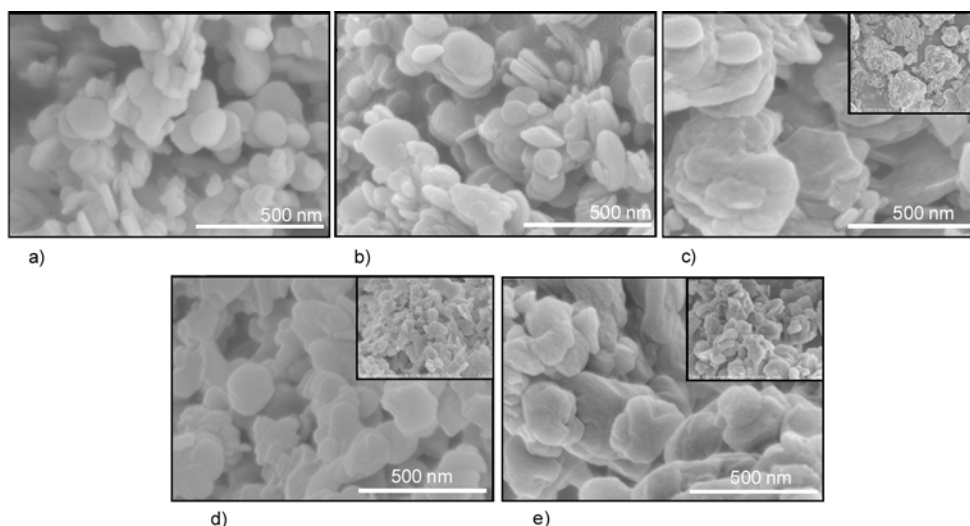


Figure 4. SEM micrographs of (a) LDH-CO₃, (b) LDH-NO₃, (c) LDH-C₆, (d) LDH-C₁₂ and (e) LDH-C₂₀ at low and high magnifications

branched chain of the surfactant could induce steric hindrance, thus changing the interlayer orientation to a higher tilt angle. By analyzing the XRD patterns (Figure 3c), it appears that both the average crystallite size and the average number of metal hydroxide layers of the organo-LDHs (calculated from the ratio of the average crystallite size and the *d*-spacing) decrease with respect to the LDH-NO₃, and there is no linear relation with *n_c*.

The morphological features of LDH-CO₃, LDH-NO₃, and organo-LDHs are presented in Figure 4a–e. The high magnification SEM micrograph of the LDH-CO₃ (Figure 4a) reveals a stacking of hexagonal plate-like particles with a highly anisometric nature, where the lateral dimension varies from 100 to 200 nm and the thickness is less than 100 nm. After the exchange of carbonate with nitrate anions, the particle morphology is substantially unchanged (Figure 4b), whereas the nitrate exchange with the organic surfactants leads to clear variation.

In particular, for the smallest surfactant alkyl chain (*n_c* = 6, Figure 4c), the stacking structure of the plate-like particles seems to be partially lost. Actually, the particles appear in aggregated form (see the inset picture) with a size of \square 500 nm and a rougher surface than the unmodified particles. The irregular particle morphology in our case may come from the ethyl-branched structure of the surfactant probably hindering the ordering of the LDH layers, as similarly observed [52]. Most likely, the stacks tend to connect to each other, probably via hydrophobic interactions [54]. When *n_c* is increased

to 12 (Figure 4d), well-stacked hexagonal particles reappear, whereas for *n_c* equal to 20 (Figure 4e), the particle morphology is somewhat changed as compared to the others. Indeed, the LDH-C₂₀ particles arrange themselves in a non-uniform stacking of irregular hexagonal plate-like particles. Also, there appears to be an uneven surface and unshaped edges, probably as a consequence of the excess of anionic surfactants draped over the outer particle surfaces [52, 54, 55].

The successful exchange of these surfactants into the LDH layers was also confirmed by the FTIR spectra (Figure 5). The organo-LDHs show absorption peaks at 1220 and 1065 cm⁻¹, corresponding to symmetric and asymmetric S=O vibration of the

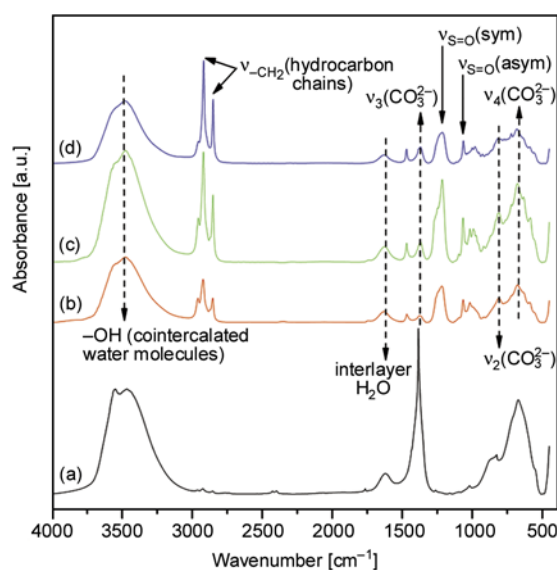


Figure 5. FTIR spectra of (a) LDH-NO₃, (b) LDH-C₆, (c) LDH-C₁₂ and (d) LDH-C₂₀

sulfate group, as well as absorption peaks at 2850–2965 cm^{-1} , which are due to the $-\text{CH}_2$ stretching of the hydrocarbon chains [37, 56]. The appearance of broad characteristic peaks of CO_3^{2-} ions at 1370 (ν_3), 820 (ν_2), and 680 cm^{-1} (ν_4), suggests there are a few carbonate ions remaining between the layers, in agreement with XRD results [3, 37]. The presence of interlayer water molecules in the organo-LDHs was evidenced by the shoulder absorption band at 1632 cm^{-1} , due to the H_2O bending vibration.

The TGA/DTG curves of the LDH-NO_3 and the organo-LDHs are shown in Figure 6. It can be seen that the LDH-NO_3 exhibits a two step decomposition process. The first weight loss step, up to 300°C, is attributed to the loss of adsorbed and interlayer water molecules (~9%), whereas the second weight loss step, between 300 and 750°C (~37%), corresponds to the loss of the interlayer nitrate ions and to the dehydroxylation of the metal hydroxide layers [57]. The thermal decomposition behavior of all of the organo-LDHs mainly takes place in four steps. The first decomposition step, up to 180°C (~10%), corresponds to the loss of the surface water molecules and crystallization water located in the

interlayer region. This step shifts to lower temperatures as compared to the unmodified LDH; this shift is due to the fact that the interaction between the interlayer water molecules and the hydroxide layers was greatly reduced by the incorporation of surfactant molecules [36]. In the temperature range of 180 to 800°C, there is a combination of three degradation steps (accounting for about 50% of the sample mass loss) which are due to the degradation of the samples up to the formation of metal oxides. This combinatorial degradation stage and the related exothermic effect involve more processes: the decomposition of intercalated alkyl sulfate surfactants (180 to 260°C) [36], the loss of some interlayer carbonate ions interfering with partial dehydroxylation of the layered LDH (260 to 500°C), and then the complete dehydroxylation process of the layered LDH. Among the organo-LDHs, LDH-C20 exhibits a maximum thermal stability, most likely due to the higher stability of the eicosyl sulfate compared to the other surfactants.

Moreover, as expected, the smallest amount of residue at 900°C was obtained for this sample which

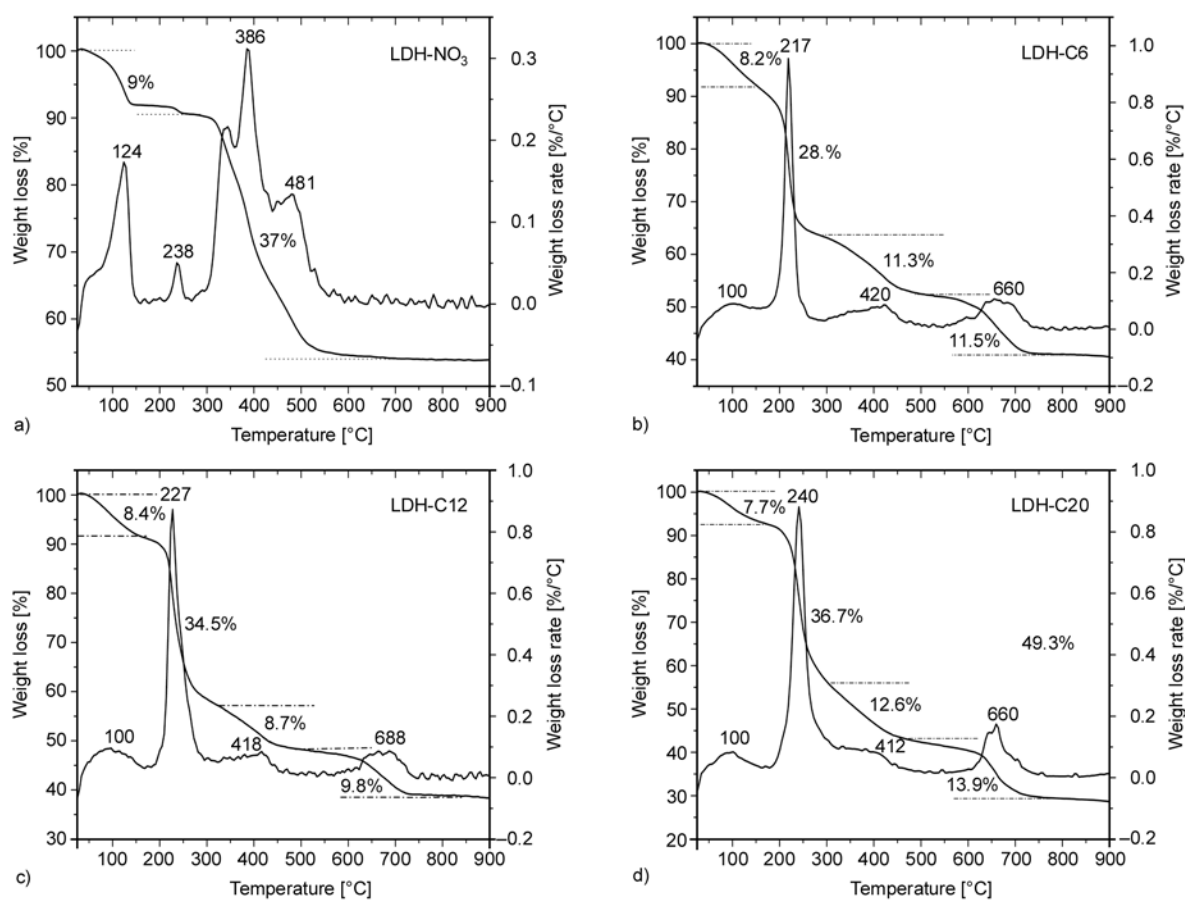


Figure 6. TGA/DTG curves of (a) LDH-NO_3 , (b) LDH-C6 , (c) LDH-C12 and (d) LDH-C20

contains the surfactant with the highest molecular weight.

3.2. Preparation and characterization of the LDPE/organo-LDH composites

After the addition of the organo-LDH to the molten matrix, no significant changes in the torque-versus-time plot were observed for any of the samples (Figure 7a). Generally, in the case of organo-clays, it is reported that fracturing of clay particles into smaller aggregates, and delamination lead to a gradual increase of the melt viscosity, thus determining a torque raise [58]. In our case, the unchanged torque behavior could be due to the plasticizing effect of the high surfactant amount present in the organo-LDHs, which could suppress any effect of reinforcement.

The XRD patterns of the composites in the range $2\theta = 1.5$ to 10° are shown in Figure 7b. In the case of the LDPE/LDH-C6 sample, a (003) basal reflection at $2\theta = 3.9^\circ$ (2.3 nm), very close to the value of pure LDH-C6, was observed, thus suggesting that the LDH-C6 was probably not dispersed in the LDPE matrix. On the other hand, in the case of the LDPE/LDH-C12 and LDPE/LDH-C20 composites, (003) basal reflections of low intensity at $2\theta = 3.18^\circ$ (2.8 nm) and $2\theta = 2.28^\circ$ (3.9 nm), respectively, were observed. For these two samples, the polymer chains were intercalated, and it cannot be excluded that a partially exfoliated/intercalated mixed morphology, as well as small or disordered stacks of platelets, was formed. Moreover, it was observed that the higher order basal reflection (i.e. $\langle 006 \rangle$ and $\langle 009 \rangle$) distinctly reduced or disappeared, further evidenc-

ing that the well-ordered structure of the metal hydroxide layers was at least partially destroyed [59]. These results are in agreement with the values of Flory-Huggins interaction parameters between the LDPE and organo-LDHs. Actually, the interaction between the LDPE and organo-LDHs can be estimated according to the method reported in the literature and based on the determination of solubility parameters using the molar attraction constants of the functional groups derived from the Hoy's table [60, 61]. In particular, the solubility parameters of LDPE and organo-LDHs can be calculated according to the following Equation (5):

$$\delta = \frac{\rho \sum F_i}{M} \quad (5)$$

where δ is the solubility parameter of the species, $\sum F_i$ is the sum of the molar attraction constants of all the groups in the repeating unit of the species, M is the molecular weight of the repeating unit, and ρ is the density of the species. The solubility parameters for LDPE and LDH-C6, LDH-C12 and LDH-C20 are 18.0, 16.3, 16.9 and 17.1 $\text{J}^{1/2} \cdot \text{cm}^{-3/2}$. Hence, the Flory-Huggins interaction parameter (χ_{AB}) between two components (A and B) can be calculated as shown in Equation (6):

$$(\delta_A - \delta_B)^2 = \frac{\chi_{AB} RT}{V_r} \quad (6)$$

where R is the gas constant, T is the temperature and V_r is a reference volume (which can be considered to be $100 \text{ cm}^3 \cdot \text{mol}^{-1}$). In particular, the χ_{AB} value for LDPE and LDH-20 (0.03) is smaller than for LDPE and LDH-12 (0.05) and LDPE and LDH-6

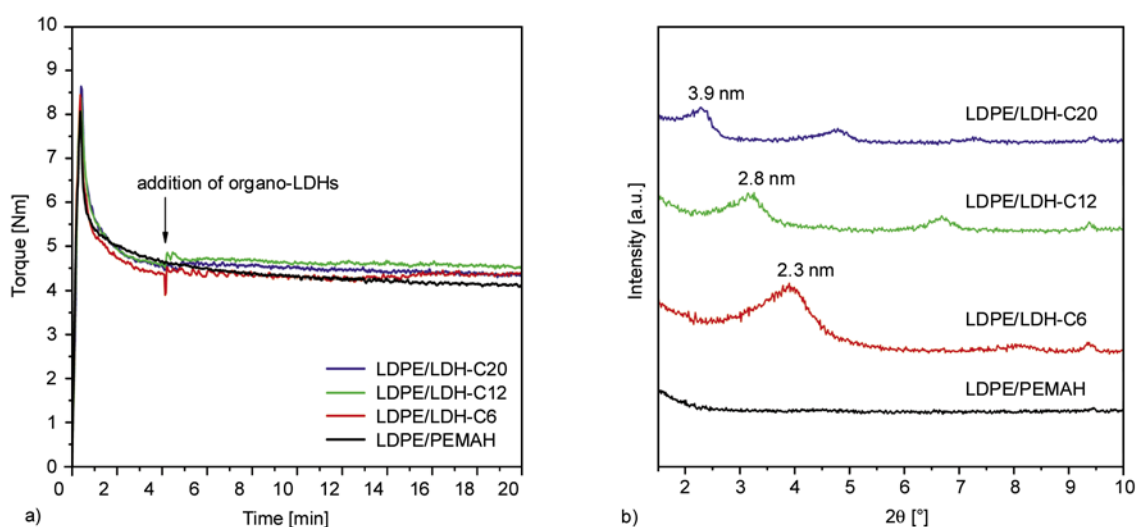


Figure 7. Torque vs. time plot during melt mixing (a) and XRD patterns (b) of the LDPE/organo-LDH composites

(0.12), thus indicating an interaction more thermodynamically favorable, even if in all the three cases the values are rather low.

To have a clearer overview of the dispersion of the LDH platelets, SEM images were acquired on the fractured surfaces of the samples (Figure 8a–c). In the case of the LDPE/LDH-C6 composite (Fig-

ure 8a), both low and high magnification SEM images evidenced the presence of aggregates of LDH-C6 platelets of 2 to 3 μm , whereas, in the case of composites containing LDH-C12 (Figure 8b) and LDH-C20 (Figure 8c), the aggregates have lower dimensions (see high magnification images; particles pointed to by arrows) and the LDH particles

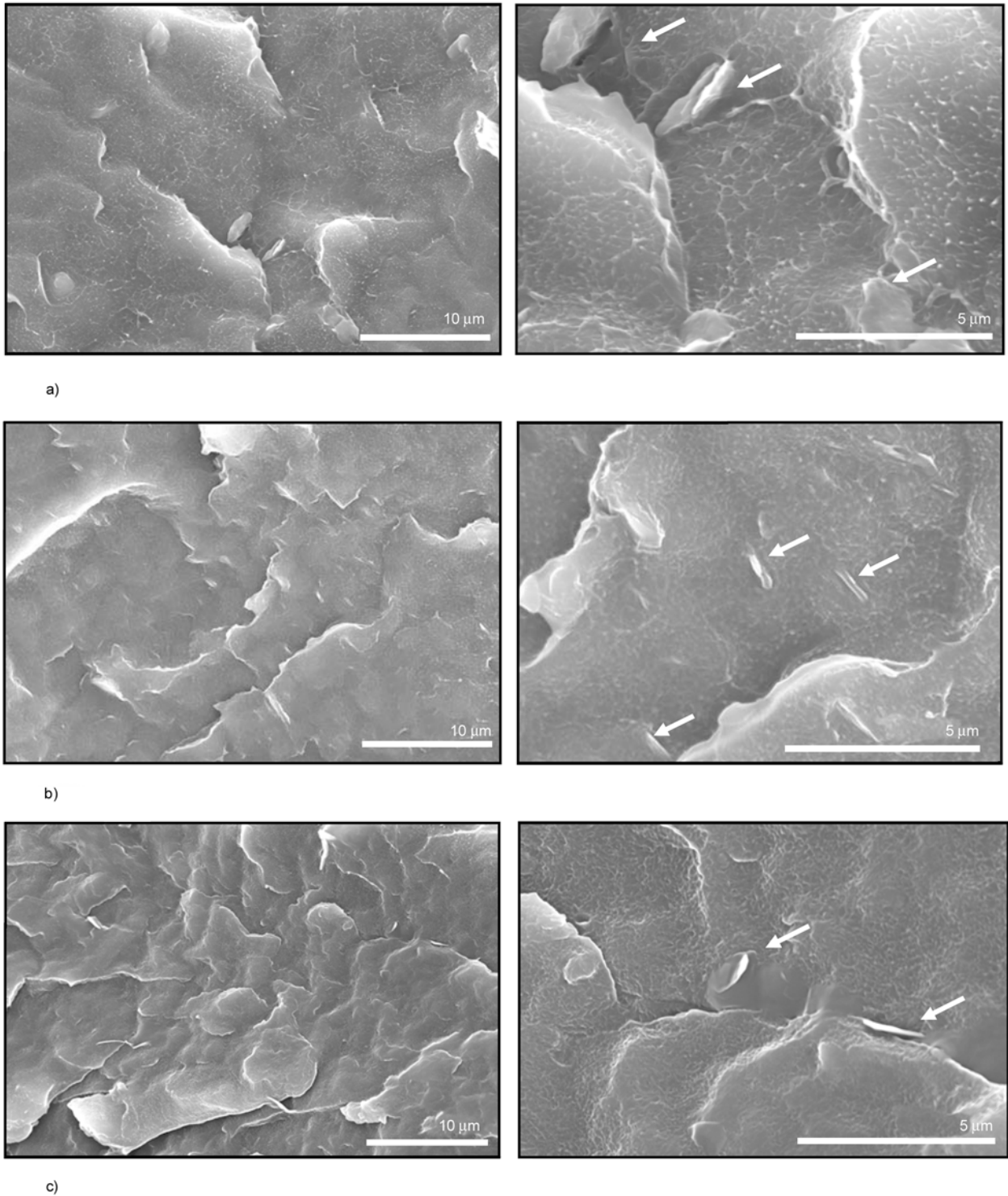


Figure 8. SEM micrographs of the composites: (a) LDPE/LDH-C6; (b) LDPE/LDH-C12; and (c) LDPE/LDH-C20, at low (3000 \times , left) and high (10000 \times , right) magnifications

seem to be better dispersed in the matrix. Moreover, no voids were observed between the intercalated particles and the matrix at the failure surface, which indicates that a strong interaction exists between them. Therefore, it seems that the dispersed platelets were well coated by the LDPE, probably thanks to the presence of PEMAH chains, which should promote favorable interactions with the LDH surface. By combining the XRD and SEM results, it appears that the extent of the organo-LDH dispersion in the LDPE depends ‘primarily’ on the interlayer distance of the organo-LDHs and, therefore, on the chain length of the anionic modifiers and their assembly between the LDH layers. Moreover, the favorable interactions between the organo-LDHs and the polymer matrix promote intercalation, dispersion and adhesion. Actually, the increase of the *d*-spacing and, therefore the formation of intercalated structures, was preferentially observed when the number of carbon atoms of the surfactant alkyl chain is equal to or larger than 12. To deeply investigate the morphology of the LDPE/LDH-C12 sample, TEM images were acquired (Figure 9). As already indicated by SEM analysis, micrometric particles of different dimensions up to more than 10 μm , may be formed by assembling of intercalated tactoids, were observed into the matrix. Furthermore, neither submicrometer tactoids nor single lamellae were detected. On the basis of these results, it can be reasonably supposed that during melt processing, polymer

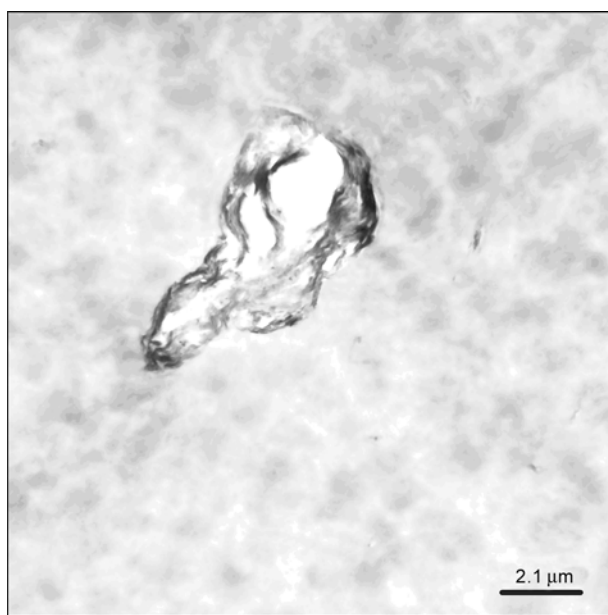


Figure 9. TEM image of the LDPE/LDH-C12 sample

chains preferentially intercalate between the LDH sheets of the organo-LDHs having the highest *d*-spacing values (LDH-C12 and LDH-C20), likely also as a consequence of better interactions between the long chain surfactants and the PE; but intercalation was not sufficient to obtain high degrees of delamination and dispersion of platelets.

Generally, the properties of nanocomposites prepared with organo-clays are improved or depressed when the amount of filler is increased. In order to investigate this aspect, LDH-C12 was selected for preparing an additional organo-LDH/LDPE composite with 5 wt% of organo-LDH with respect to the polymers (LDPE/LDH-C12_5%). The XRD pattern of this new sample evidenced a broad diffraction peak at $2\theta = 3.4^\circ$ ($d_{003} = 2.7 \text{ nm}$), slightly more shifted toward the (003) reflection of the pristine LDH-C12 with respect to the reflection detected in the case of the 2.5 wt% composite (Figure 10a).

This result could be a consequence of the presence of non-intercalated LDH-C12 platelets. Actually, low and high magnification SEM images (Figure 10b) evidenced the presence of numerous aggregates with a size of about 2 to 5 μm , most likely made of several interconnected LDH platelets. It seems that these big particles are kept together by strong face-face interactions between adjacent LDH platelets (indicated by the circle) or between individual layers.

The TGA and DTG curves of the LDPE, LDPE/PEMAH, and organo-LDH composites are shown in Figure 11. The temperatures corresponding to 10 and 50% of weight loss ($T_{10\%}$ and $T_{50\%}$), the temperature at the maximum rate of weight loss (T_{max}), and the residue obtained at 900°C are reported in Table 2. A two-step decomposition is apparent for the composites: the first step, in the temperature range of 200 to 405°C (\square 25% weight loss), involves the dehydration of metal hydroxide layers, thermal degradation of the organic modifiers, and volatilization of the thermo-oxidative products of LDPE [33]; the second step, in the temperature range of 405 to 600°C (\square 70–75% weight loss), is ascribed to the decomposition of polyethylene chains and the volatilization of the residual polymer [62]. It can be observed that the initial degradation (i.e. at 10% weight loss of composites) is faster, compared to the pure matrix, which is due to the earlier degrada-

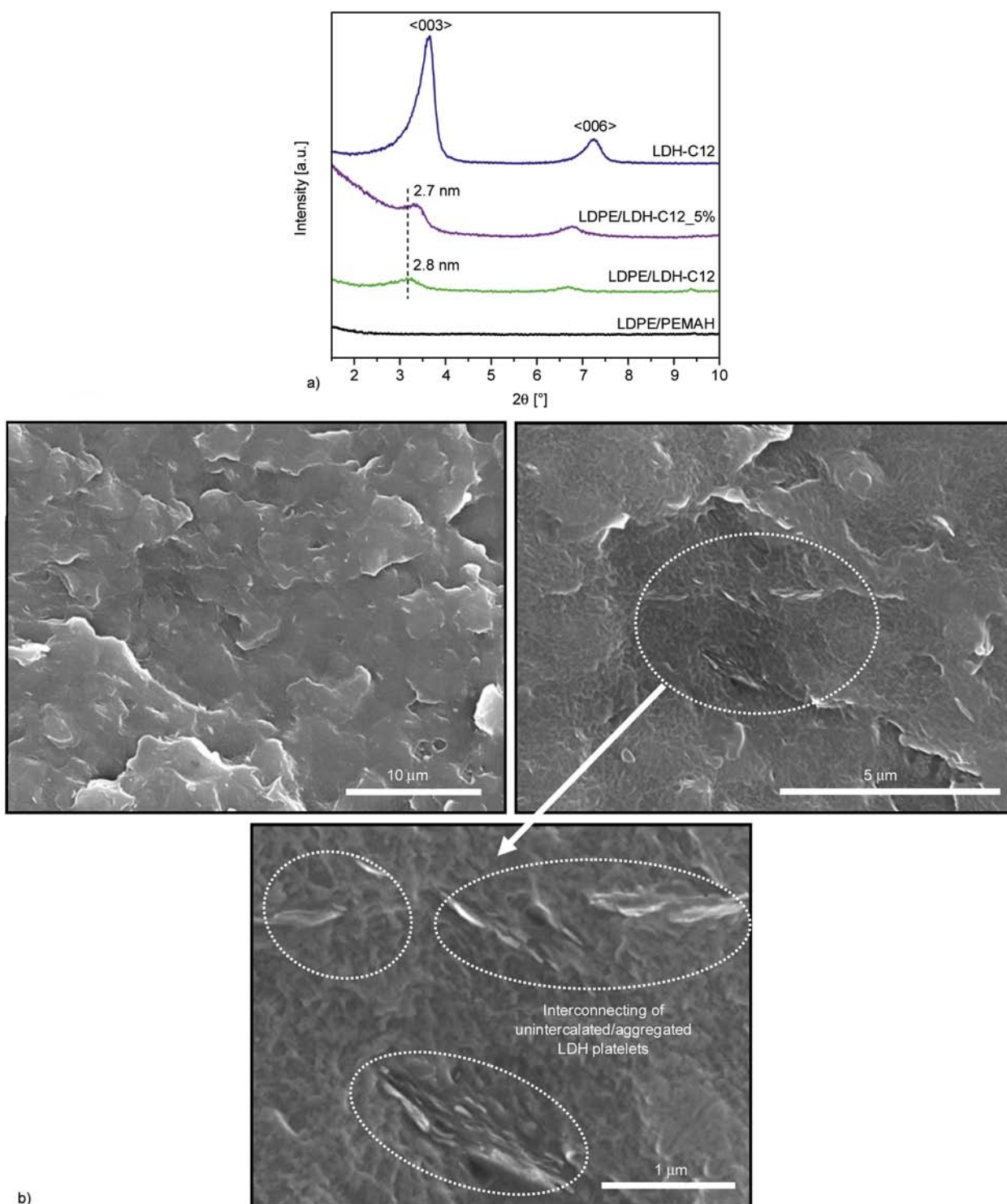


Figure 10. Comparison of the XRD patterns of LDPE/LDH-C12 and the LDPE/LDH-C12_5% composites (a) and low and high magnification SEM images of the LDPE/LDH-C12_5% composite (b)

tion of the organic modifiers [34, 37]. However, the layers produced by the fast degradation of the organo-LDHs are very advantageous for promoting the charring process, thus enhancing the thermal stability of the polymer materials. This remarkable enhancement of thermal properties is characterized

by a shift of the TGA and DTG curves (Figure 11b) toward higher temperatures, after 25% weight loss, and the temperature at the maximum rate of weight loss (T_{max}) is increased by about 20 to 33°C with respect to the pure matrix, suggesting a generally slower degradation process. Among these compos-

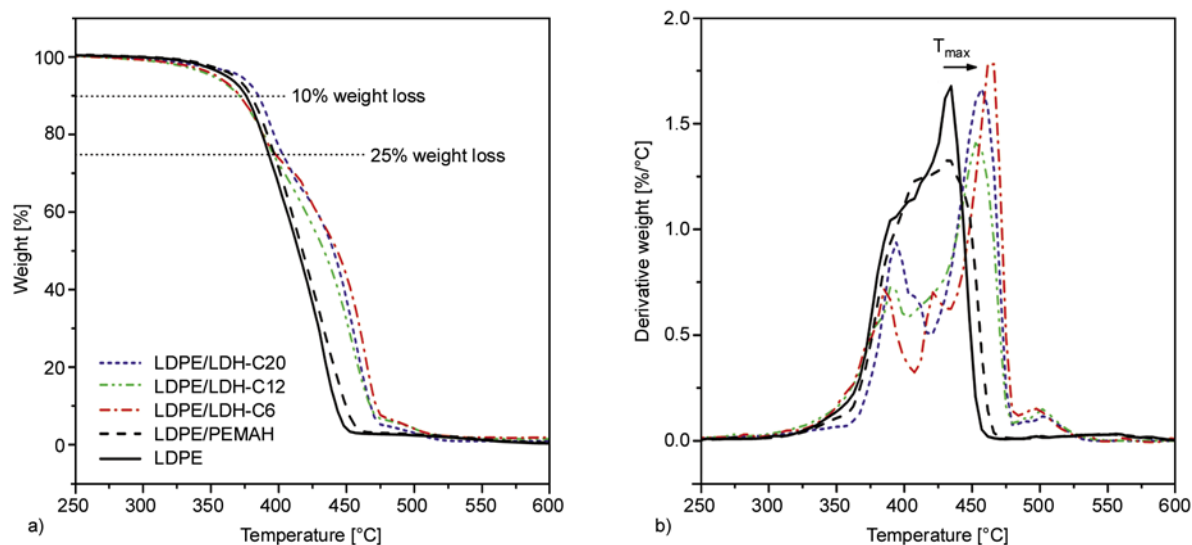


Figure 11. TGA (a) and DTG (b) thermograms of the LDPE/organo-LDH composites

ites, the LDPE/LDH-C6 sample has the highest degradation temperature, even though the XRD and SEM analyses evidenced a poor dispersion degree. However, the degradation temperature of the LDPE/LDH-C20 is nearly the same as that of the LDPE/LDH-C6, even if a lower amount of clay was added to the LDPE/LDH-C20 sample (1.5 wt% with respect to the LDPE/PEMAH blend). This infers that LDH platelets in the bulk polymer promote the charring process and enhance the flame retardant properties of the LDPE [36, 37, 63].

The residue left after combustion of LDPE and LDPE/PEMAH blend is nearly zero as the hydrocarbon chains are converted into gaseous products. If we assume that by heating up the composites to 900°C under air both the polymers and the organic part of organo-LDHs are completely burnt, the amount of TGA residue could be deduced from the organo-LDH formulae. Actually, by considering the formation of metal oxides, the residue is proportional to the amount of organo-LDH added to the polymer blends.

The melting (T_m) and crystallization (T_c) peak temperatures, as well as the melting enthalpy (ΔH_m) and degree of crystallinity (χ_c), were determined by DSC measurements (Table 2).

Most of the samples show an increase of T_c , especially in the case of LDPE/LDH-C20, and a slight decrease of T_m with respect to the LDPE/PEMAH blend. The increase of T_c is probably due to the heterogeneous nucleation activity of the dispersed LDH platelets; actually, just a small amount of the

LDH platelets could accelerate the crystallization process of LDPE. However, the degree of crystallinity seems unchanged and independent of the type of composite. By comparing the two LDPE composites prepared with different concentrations of LDH-C12, it can be observed that there was no significant influence of the amount of organo-LDH on the crystallization and melting behavior of LDPE. Instead, a slight decrease of degree of crystallinity (χ_c , Table 2) is observed; this decrease is probably due to the suppression effect of the aggregated-LDH, which hinders the growth of the LDPE crystallites.

The storage modulus (E'), loss modulus (E'') and loss tangent ($\tan\delta$) behavior vs. temperature of composites prepared with the different types of organo-LDHs are shown in Figure 12a–c.

Generally, LDPE exhibits three relaxations (known as α , β and γ) which are associated with chain motions in the crystalline phase (α at about +50°C), chain motions of branched structures in the amorphous matrix (the β -relaxation, at about –20°C, is absent in entirely linear polyethylene), and the motion of the amorphous polyethylene which is caused by small local short-range segmental motions involving three to five CH₂ chain segments (γ at about –125°C) [64, 65]. It can be observed from Figure 12a that the E' of all of the samples decreases slowly until –50°C; then a sharp drop appears, which is related to the β -relaxation process. The E' of the composites is higher than that of the LDPE/PEMAH matrix in the low temperature region

(Table 3), except in the case of the LDPE/LDH-C20 sample.

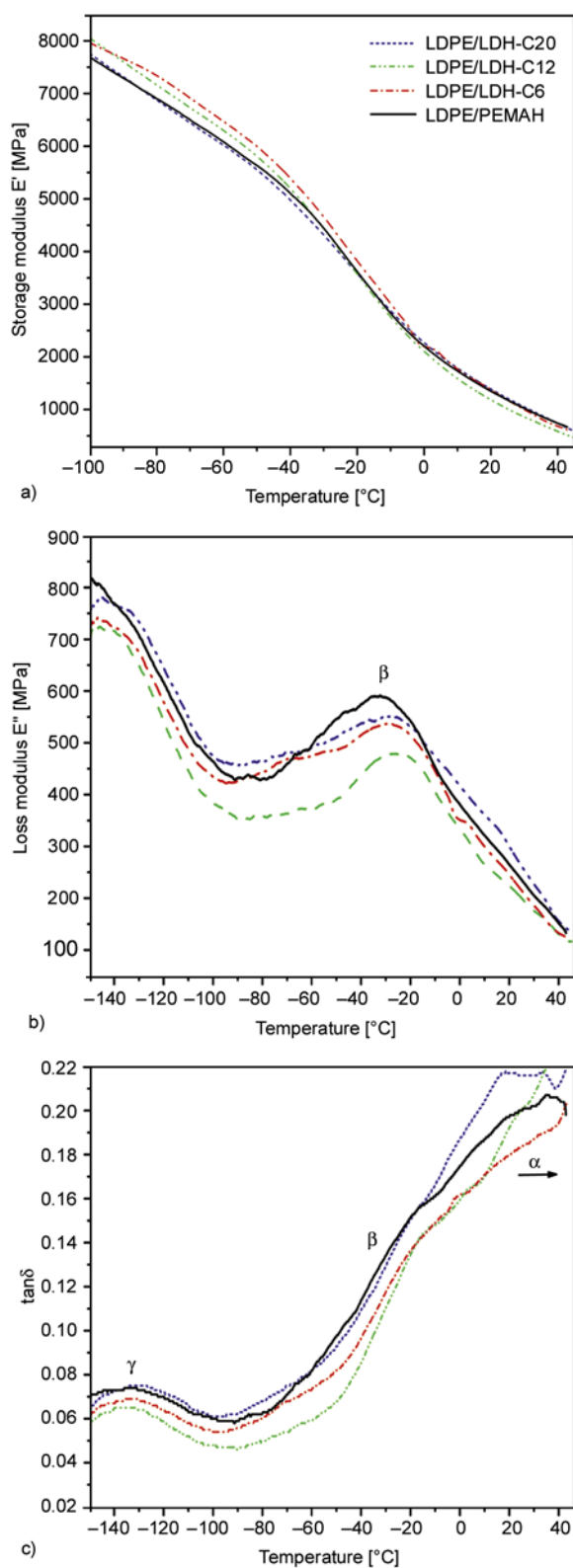


Figure 12. Dynamic (a) storage modulus, (b) loss modulus, and (c) loss tangent of the pure matrix and the LDPE/organo-LDH composites

In a previous work, it was found that LDPE/organo-LDH nanocomposites, prepared in a twin screw extruder, had a lower storage modulus with respect to the polymer matrix [41], not evidencing reinforcement, but rather a softening of the matrix. It was assumed that this effect could be a consequence of the low stiffness of the organo-LDH particles [66–68], even if it was not excluded that the free surfactant and surfactant molecules loosely bound to the outer surface of the LDH particles could increase the mobility of the polymer chains at the polymer-filler interfacial region, thus acting as plasticizers [68]. On the basis of the results collected here, it can be assumed that higher values of E' are probably obtained when the organo-LDH dispersion is poor. Actually, the highest E' was achieved for the LDPE/LDH-C6 sample, which has the worst dispersion morphology, as evidenced by the XRD and SEM characterizations. Nonetheless, it cannot be excluded that, independently of morphology, the surfactant chain could act as a plasticizer, increasing the mobility of the polymer chains at the polymer-filler interfacial region; the longer the alkyl chain, the higher the extent of the surfactant-polymer interaction as demonstrated by the calculation of interaction parameters, and greater the efficiency of the surfactant as plasticizer. This means that the different lengths of the surfactant alkyl chain play a fundamental role, not only related to the dispersion/morphology aspects, but also to the interactions at the interface, thus very much affecting the final properties.

The β -relaxation is assumed here to be the glass transition temperature (T_g) of the composite. Indeed, it is reported that both the γ - and β -relaxations are quoted to have the properties of the glass-rubber transition. In particular, when the alkyldiene content is low, the γ -peak is more prominent, whereas β -relaxation is the dominant mechanism at high alkyldiene content. It has been also shown that the higher the amorphous fraction, the more intense is the β -relaxation, which may be classified as T_g [64, 65]. It appears from Figure 12b–c that the peak position related to the β -relaxation of the composites shifts to higher temperatures compared to that of the LDPE.

Generally the state of dispersion of clay platelets in polymer nanocomposite systems is determined by dynamic oscillatory shear measurements. Actually,

Table 3. Dynamic storage modulus and peak temperature of β and γ relaxations for the pure matrix and the LDPE/organo-LDH composites

Composites	Storage modulus, E' , [MPa]			Relaxations peak temperature [°C]	
	-100°C	-80°C	-60°C	β	γ
LDPE/PEMAH	7704.8	6911.1	6108.8	-33.6	-133.5
LDPE/LDH-C6 (2.5 wt%)	7997.7	7353.6	6479.8	-27.6	-132.2
LDPE/LDH-C12 (2.5 wt%)	8075.8	7163.6	6304.1	-25.6	-133.0
LDPE/LDH-C20 (1.5 wt%)	7782.9	6911.1	6030.8	-27.1	-129.2
LDPE/LDH-C12_5% (5.0 wt%)	8238.9	7477.6	6712.0	-27.8	-132.0

the storage (G') and loss moduli (G'') of the nanocomposites increases monotonically with the clay loading at all frequencies, but beyond a threshold volume fraction, the individual layers and tactoids are not able to rotate freely, and thus incomplete relaxation occurred when subjected to the shear. This incomplete relaxation due to the physical jamming or to the formation of a percolated three dimensional network leads to the presence of the pseudo-solid-like behavior observed in both intercalated and exfoliated nanocomposites [69, 70]. It is suggested that the strong interaction between the polymer and the clay platelets restricts the mobility and alters the relaxation processes of the polymer, leading to the low-frequency plateau in the shear moduli and non-Newtonian viscosity behavior with clay loading at the low-shear rate [71]. These measurements also showed that $\tan\delta$ (G''/G') is dependent on polymer-clay interaction; in particular, $\tan\delta > 3$ for non-associated, $1 < \tan\delta < 3$ for weakly associated, and $\tan\delta < 1$ for strongly associated dispersed particles [72]. Hyun *et al.* [73] also evidenced that the clay content affects the $\tan\delta$ value: at low clay content $\tan\delta$ is greater than 1, while at high clay content $\tan\delta$ becomes less than 1. In our case, the height of the $\tan\delta$ peak of the composites (Figure 12c) decreases with respect to the matrix, moving from the composite prepared by adding LDH-C20 to LDH-C12 and to LDH-C6. The $\tan\delta$ values for the β -relaxation (-40°C) are for all the samples much smaller than 1: LDPE/PEMAH = 0.114, LDH-C6 = 0.097, LDH-C12 = 0.088 and to LDH-C20 = 0.110. This suggests the presence of strongly associated dispersed platelets, which supports the formation of intercalated composites, as shown by XRD results and confirmed by the large rigid aggregates evidenced by SEM images. It can be also observed that $\tan\delta$ curves after room temperature seem to move to higher temperature, which is correlated to the α -relaxation region. Most likely the polymer-clay

interactions not only restricted the molecular motion in the amorphous phase, but also confined the segmental relaxation in the crystalline phase [64]. A similar behavior was observed on other systems such as EVA/EPDM/DS-LDH nanocomposites [67] and PBT nanocomposites [68].

By increasing the LDH concentration of the composites (LDPE/LDH-C12_5% vs. LDPE/LDH-C12) a higher E' value was observed throughout the entire temperature range (Table 3), thus suggesting that the addition of the LDH enhanced the stiffness of the composite. The temperature dependence of the storage modulus enhancement factor, defined as $E'_{real} = E'_{composite}/E'_{pure\ matrix}$, in the case of the LDPE/LDH-C12 (2.5 wt%) and LDPE/LDH-C12_5% (5 wt%) composites, is shown in Figure 13.

By increasing the amount of LDH-C12, the relative storage modulus is increased. This may contribute to the fact that some volume of the composite is occupied by LDH particles, for which the storage modulus is much greater than for the pure polymer.

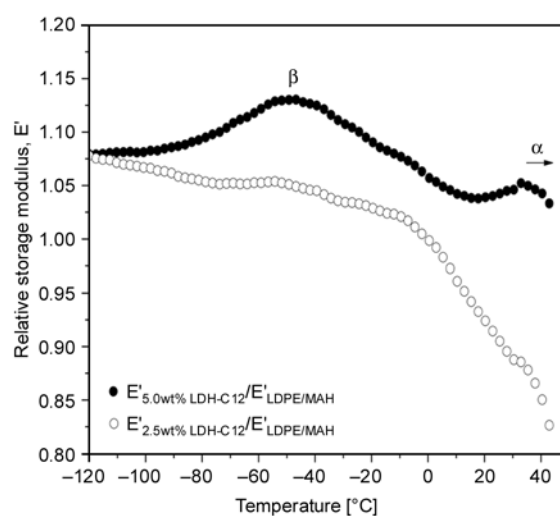


Figure 13. Temperature dependence of relative storage modulus ($E'_{composite}/E'_{pure\ matrix}$) for the 2.5 and 5 wt% LDH-C12 composites.

In that case, two distinct peaks appear at -46 and 33°C , which are related to the setting up of the chain motion in the amorphous (β -relaxation) and crystalline (α -relaxation) phases, respectively. In the case of the LDPE/LDH-C12 (2.5 wt%) sample, the relative modulus curve is nearly constant from the beginning until -10°C , and afterward it suddenly drops. The observed glass transition temperature (T_g) of the LDPE/LDH-C12_5% (5 wt%) sample slightly decreases compared to that of LDPE/LDH-C12, but it is much higher than that of the pure matrix (see Table 3). Moreover, as already been suggested about the $\tan\delta$ value for higher clay loading, the composite with 5 wt% LDH-C12 shows the strongly associated dispersed clay platelets with $\tan\delta$ less than 1 (0.087).

4. Conclusions

LDPE/organo-LDH composites were prepared via melt-compounding using PEMAH as the compatibilizer. Pristine LDH- CO_3 was modified with various alkyl chain length sulfates ($n_c = 6, 12$ and 20) by a two step anion exchange methodology. The XRD analysis demonstrated that intercalated LDPE/organo-LDH composites were obtained by melt mixing, depending on the chain length of the anionic modifiers. In particular, intercalated structures were achieved when the number of carbon atoms of the surfactant alkyl chain was equal to or larger than 12. Moreover, the TGA analysis showed that the composites exhibited a remarkable enhancement of thermal properties, in which the decomposition temperature is 20 to 33°C higher than that of the pure matrix. The DSC results showed an increase of the crystallization temperature, due mainly to nucleation effects, whereas, neither significant changes of the melting temperature nor of the degree of crystallinity were observed. On the other hand, the mechanical properties, and in particular the storage modulus data, were affected by the morphology and by the physical properties of the surfactants at the interface. Generally, a reinforcing effect was observed by using LDH modified by surfactants having short alkyl chains (C6), providing larger aggregates owing to a sort of physical crosslinking effect induced by the strong interactions between the functionalized polymer and the layered clay. The significant increase of the β -relaxation peak temperature related to the glass transition tempera-

ture (T_g) of the composites may be explained by the stronger interactions between the polymer and the layered filler, which restricted the mobility of the polymer chains. By increasing the chain length of the LDH modifier, a softening of the composite was observed due to a plasticizing effect of the surfactant, which also promoted effective interactions between the matrix and the nanofiller, thus providing a better morphology. This means that the alkyl chain length of the surfactant could play a fundamental role, not only related to the dispersion/morphology aspects, but also to the interactions at the interface, very much affecting the final properties.

Acknowledgements

The research was funded by the Department of Chemistry and Industrial Chemistry, University of Pisa, the National Project PRIN prot. 200898KCKY, and the Royal Golden Jubilee Ph.D. Program (RGJ). The authors express their appreciation to Prof. Francesco Ciardelli for the helpful discussion and support. Dr. Lucia Conzatti (CNR-ISMAR UOS Genova, Genova, Italy) is gratefully acknowledged for her cooperation about TEM analysis.

References

- [1] Brown G., Gastuche M. C.: Mixed magnesium-aluminum hydroxides. II. Structure and structural chemistry of synthetic hydroxycarbonates and related minerals and compounds-II. *Clay Minerals*, **7**, 193–201 (1967).
- [2] Miyata S., Kumara T.: Synthesis of new hydrotalcite-like compounds and their physico-chemical properties. *Chemistry Letters*, **2**, 843–848 (1973). DOI: [10.1246/cl.1973.843](https://doi.org/10.1246/cl.1973.843)
- [3] Cavani F., Trifirò F., Vaccari A.: Hydrotalcite-type anionic clays: Preparation, properties and applications. *Catalysis Today*, **11**, 173–301 (1991). DOI: [10.1016/0920-5861\(91\)80068-K](https://doi.org/10.1016/0920-5861(91)80068-K)
- [4] Reichle W. T.: Synthesis of anionic clay minerals (mixed metal hydroxides, hydrotalcite). *Solid State Ionics*, **22**, 135–141 (1986). DOI: [10.1016/0167-2738\(86\)90067-6](https://doi.org/10.1016/0167-2738(86)90067-6)
- [5] Auerbach S. M., Carrado K., Dutta P. K.: *Handbook of layered materials*. Marcel Dekker, New York (2004).
- [6] Constantino V. R. L., Pinnavaia T. J.: Basic properties of $\text{Mg}_{1-x}\text{Al}_x^{3+}$ layered double hydroxides intercalated by carbonate, hydroxide, chloride, and sulfate anions. *Inorganic Chemistry*, **34**, 883–892 (1995). DOI: [10.1021/ic00108a020](https://doi.org/10.1021/ic00108a020)
- [7] del Arco M., Malet P., Trujillano R., Rives V.: Synthesis and characterization of hydrotalcites containing Ni(II) and Fe(III) and their calcination products. *Chemistry of Materials*, **11**, 624–633 (1999). DOI: [10.1021/cm980492z](https://doi.org/10.1021/cm980492z)

- [8] Xu Z. P., Zeng H. C.: Thermal evolution of cobalt hydroxides: A comparative study of their various structural phases. *Journal of Materials Chemistry*, **8**, 2499–2506 (1998).
DOI: [10.1039/A804767G](https://doi.org/10.1039/A804767G)
- [9] Hermosín M. C., Pavlovic J., Ulibarri M. A., Cornejo J.: Hydrotalcite as sorbent for trinitrophenol: Sorption capacity and mechanism. *Water Research*, **30**, 171–177 (1996).
DOI: [10.1016/0043-1354\(95\)00088-3](https://doi.org/10.1016/0043-1354(95)00088-3)
- [10] Qian M., Zeng H. C.: Synthesis and characterization of Mg–Co catalytic oxide materials for low-temperature N₂O decomposition. *Journal of Materials Chemistry*, **7**, 493–499 (1997).
DOI: [10.1039/A607627K](https://doi.org/10.1039/A607627K)
- [11] Ambroggi V., Fardella G., Grandolini G., Perioli L.: Intercalation compounds of hydrotalcite-like anionic clays with antiinflammatory agents – I. Intercalation and in vitro release of ibuprofen. *International Journal of Pharmaceutics*, **220**, 23–32 (2001).
DOI: [10.1016/S0378-5173\(01\)00629-9](https://doi.org/10.1016/S0378-5173(01)00629-9)
- [12] Guo X., Xu S., Zhao L., Lu W., Zhang F., Evans D. G., Duan X.: One-step hydrothermal crystallization of a layered double hydroxide/alumina bilayer film on aluminum and its corrosion resistance properties. *Langmuir*, **25**, 9894–9897 (2009).
DOI: [10.1021/la901012w](https://doi.org/10.1021/la901012w)
- [13] Luan L., Li W., Liu S., Sun D.: Phase behavior of mixtures of positively charged colloidal platelets and non-adsorbing polymer. *Langmuir*, **25**, 6349–6356 (2009).
DOI: [10.1021/la804023b](https://doi.org/10.1021/la804023b)
- [14] Crepaldi E. L., Pavan P. C., Valim J. B.: Anion exchange in layered double hydroxides by surfactant salt formation. *Journal of Materials Chemistry*, **10**, 1337–1343 (2000).
DOI: [10.1039/A909436I](https://doi.org/10.1039/A909436I)
- [15] Costa F. R., Saphiannikova M., Wagenknecht U., Heinrich G.: Layered double hydroxide based polymer nanocomposites. *Advances in Polymer Science*, **210**, 101–168 (2008).
DOI: [10.1007/12_2007_123](https://doi.org/10.1007/12_2007_123)
- [16] Ciardelli F., Coiai S., Passaglia E., Pucci A., Ruggeri G.: Nanocomposites based on polyolefins and functional thermoplastic materials. *Polymer International*, **57**, 805–836 (2008).
DOI: [10.1002/pi.2415](https://doi.org/10.1002/pi.2415)
- [17] Wang D-Y., Costa F. R., Vyalikh A., Leuteritz A., Scheler U., Jehnichen D., Wagenknecht U., Haussler L., Heinrich G.: One-step synthesis of organic LDH and its comparison with regeneration and anion exchange method. *Chemistry of Materials*, **21**, 4490–4497 (2009).
DOI: [10.1021/cm901238a](https://doi.org/10.1021/cm901238a)
- [18] Newman S. P., Jones W.: Synthesis, characterization and applications of layered double hydroxides containing organic guests. *New Journal of Chemistry*, **22**, 105–115 (1998).
DOI: [10.1039/A708319J](https://doi.org/10.1039/A708319J)
- [19] Miyata S.: Anion-exchange properties of hydrotalcite-like compounds. *Clays and Clay Minerals*, **31**, 305–311 (1983).
DOI: [10.1346/CCMN.1983.0310409](https://doi.org/10.1346/CCMN.1983.0310409)
- [20] Hsueh H-B., Chen C-Y.: Preparation and properties of LDHs/epoxy nanocomposites. *Polymer*, **44**, 5275–5283 (2003).
DOI: [10.1016/S0032-3861\(03\)00579-2](https://doi.org/10.1016/S0032-3861(03)00579-2)
- [21] Hsueh H-B., Chen C-Y.: Preparation and properties of LDHs/polyimide nanocomposites. *Polymer*, **44**, 1151–1161 (2003).
DOI: [10.1016/S0032-3861\(02\)00887-X](https://doi.org/10.1016/S0032-3861(02)00887-X)
- [22] Lee W. D., Im S. S., Lim H-M., Kim K-J.: Preparation and properties of layered double hydroxide/poly(ethylene terephthalate) nanocomposites by direct melt compounding. *Polymer*, **47**, 1364–1371 (2006).
DOI: [10.1016/j.polymer.2005.12.056](https://doi.org/10.1016/j.polymer.2005.12.056)
- [23] Messersmith P. B., Stupp S. I.: High-temperature chemical and microstructural transformations of a nanocomposite organoceramic. *Chemistry of Materials*, **7**, 454–460 (1995).
DOI: [10.1021/cm00051a004](https://doi.org/10.1021/cm00051a004)
- [24] Wang D-Y., Leuteritz A., Wang Y-Z., Wagenknecht U., Heinrich G.: Preparation and burning behaviors of flame retarding biodegradable poly(lactic acid) nanocomposite based on zinc aluminum layered double hydroxide. *Polymer Degradation and Stability*, **95**, 2474–2480 (2010).
DOI: [10.1016/j.polymdegradstab.2010.08.007](https://doi.org/10.1016/j.polymdegradstab.2010.08.007)
- [25] Costantino U., Bugatti V., Gorrasi G., Montanari F., Nocchetti M., Tammaro L., Vittoria V.: New polymeric composites based on poly(ϵ -caprolactone) and layered double hydroxides containing antimicrobial species. *Applied Materials and Interfaces*, **1**, 668–677 (2009).
DOI: [10.1021/am8001988](https://doi.org/10.1021/am8001988)
- [26] Ding P., Qu B.: Synthesis of exfoliated PP/LDH nanocomposites via melt-intercalation: Structure, thermal properties, and photo-oxidative behavior in comparison with PP/MMT nanocomposites. *Polymer Engineering and Science*, **46**, 1153–1159 (2006).
DOI: [10.1002/pen.20568](https://doi.org/10.1002/pen.20568)
- [27] Kuppinger J., Göschel U., Reeksting B., Vorster O.: Maleic anhydride grafted polypropylene-layered hydrotalcite master batch and resultant nanocomposites prepared by melt processing: Structure characterization and mechanical properties. *Journal of Polymer Engineering*, **27**, 339–356 (2007).
- [28] Coiai S., Passaglia E., Hermann A., Augier S., Pratelli D., Streller R. C.: The influence of the compatibilizer on the morphology and thermal properties of polypropylene-layered double hydroxide composites. *Polymer Composites*, **31**, 744–754 (2010).
DOI: [10.1002/pc.20857](https://doi.org/10.1002/pc.20857)

- [29] Wang D.-Y., Das A., Costa F. R., Leuteritz A., Wang Y.-Z., Wagenknecht U., Heinrich G.: Synthesis of organo cobalt–aluminum layered double hydroxide via a novel single-step self-assembling method and its use as flame retardant nanofiller in PP. *Langmuir*, **26**, 14162–14169 (2010).
DOI: [10.1021/la102449m](https://doi.org/10.1021/la102449m)
- [30] Wang D.-Y., Das A., Leuteritz A., Boldt R., Häußler L., Wagenknecht U., Heinrich G.: Thermal degradation behaviors of a novel nanocomposite based on polypropylene and Co-Al layered double hydroxide. *Polymer Degradation and Stability*, **96**, 285–290 (2011).
DOI: [10.1016/j.polymdegradstab.2010.03.003](https://doi.org/10.1016/j.polymdegradstab.2010.03.003)
- [31] Chen W., Qu B.: Structural characteristics and thermal properties of PE-g-MA/MgAl-LDH exfoliation nanocomposites synthesized by solution intercalation. *Chemistry of Materials*, **15**, 3208–3213 (2003).
DOI: [10.1021/cm030044h](https://doi.org/10.1021/cm030044h)
- [32] Chen W., Qu B.: LLDPE/ZnAl LDH-exfoliated nanocomposites: Effects of nanolayers on thermal and mechanical properties. *Journal of Materials Chemistry*, **14**, 1705–1710 (2004).
DOI: [10.1039/B401790K](https://doi.org/10.1039/B401790K)
- [33] Chen W., Feng L., Qu B.: Preparation of nanocomposites by exfoliation of ZnAl layered double hydroxides in nonpolar LLDPE solution. *Chemistry of Materials*, **16**, 368–370 (2004).
DOI: [10.1021/cm0303484](https://doi.org/10.1021/cm0303484)
- [34] Qiu L., Chen W., Qu B.: Morphology and thermal stabilization mechanism of LLDPE/MMT and LLDPE/LDH nanocomposites. *Polymer*, **47**, 922–930 (2006).
DOI: [10.1016/j.polymer.2005.12.017](https://doi.org/10.1016/j.polymer.2005.12.017)
- [35] Costa F. R., Abdel-Goad M., Wagenknecht U., Heinrich G.: Nanocomposites based on polyethylene and Mg–Al layered double hydroxide. I. Synthesis and characterization. *Polymer*, **46**, 4447–4453 (2005).
DOI: [10.1016/j.polymer.2005.02.027](https://doi.org/10.1016/j.polymer.2005.02.027)
- [36] Costa F. R., Wagenknecht U., Heinrich G.: LDPE/Mg–Al layered double hydroxide nanocomposite: Thermal and flammability properties. *Polymer Degradation and Stability*, **92**, 1813–1823 (2007).
DOI: [10.1016/j.polymdegradstab.2007.07.009](https://doi.org/10.1016/j.polymdegradstab.2007.07.009)
- [37] Du L., Qu B.: Structural characterization and thermal oxidation properties of LLDPE/MgAl-LDH nanocomposites. *Journal of Materials Chemistry*, **16**, 1549–1554 (2006).
DOI: [10.1039/B514319E](https://doi.org/10.1039/B514319E)
- [38] Costantino U., Gallipoli A., Nocchetti M., Camino G., Bellucci F., Frache A.: New nanocomposites constituted of polyethylene and organically modified ZnAl-hydrotalcites. *Polymer Degradation and Stability*, **90**, 586–590 (2005).
DOI: [10.1016/j.polymdegradstab.2005.05.019](https://doi.org/10.1016/j.polymdegradstab.2005.05.019)
- [39] Costa F. R., Wagenknecht U., Jehnichen D., Goad M. A., Heinrich G.: Nanocomposites based on polyethylene and Mg–Al layered double hydroxide. Part II. Rheological characterization. *Polymer*, **47**, 1649–1660 (2006).
DOI: [10.1016/j.polymer.2005.12.011](https://doi.org/10.1016/j.polymer.2005.12.011)
- [40] Manzi-Nshuti C., Hossenlopp J. M., Wilkie C. A.: Comparative study on the flammability of polyethylene modified with commercial fire retardants and a zinc aluminum oleate layered double hydroxide. *Polymer Degradation and Stability*, **94**, 782–788 (2009).
DOI: [10.1016/j.polymdegradstab.2009.02.004](https://doi.org/10.1016/j.polymdegradstab.2009.02.004)
- [41] Coiai S., Scatto M., Conzatti L., Azzurri F., Andreotti L., Salmini E., Stagnaro P., Zanolin A., Cicogna F., Passaglia E.: Optimization of organo-layered double hydroxide dispersion in LDPE-based nanocomposites. *Polymer for Advanced Technologies*, in press (2011).
DOI: [10.1002/pat.1759](https://doi.org/10.1002/pat.1759)
- [42] Costa F. R., Satapathy B. K., Wagenknecht U., Weidisch R., Heinrich G.: Morphology and fracture behaviour of polyethylene/Mg–Al layered double hydroxide (LDH) nanocomposites. *European Polymer Journal*, **42**, 2140–2152 (2006).
DOI: [10.1016/j.eurpolymj.2006.04.005](https://doi.org/10.1016/j.eurpolymj.2006.04.005)
- [43] Tammara L., Tortora M., Vittoria V., Costantino U., Marmottini F.: Methods of preparation of novel composites of poly(ϵ -caprolactone) and a modified Mg/Al hydrotalcite. *Journal of Polymer Science Part A: Polymer Chemistry*, **43**, 2281–2290 (2005).
DOI: [10.1002/pola.20701](https://doi.org/10.1002/pola.20701)
- [44] Zammarano M., Bellayer S., Gilman J. W., Franceschi M., Beyer F. L., Harris R. H., Meriani S.: Delamination of organo-modified layered double hydroxides in polyamide 6 by melt processing. *Polymer*, **47**, 652–662 (2006).
DOI: [10.1016/j.polymer.2005.11.080](https://doi.org/10.1016/j.polymer.2005.11.080)
- [45] Zammarano M., Franceschi M., Bellayer S., Gilman J. W., Meriani S.: Preparation and flame resistance properties of revolutionary self-extinguishing epoxy nanocomposites based on layered double hydroxides. *Polymer*, **46**, 9314–9328 (2005).
DOI: [10.1016/j.polymer.2005.07.050](https://doi.org/10.1016/j.polymer.2005.07.050)
- [46] Velu S., Ramkumar V., Narayanan V., Swamy C. S.: Effect of interlayer anions on the physicochemical properties of zinc–aluminium hydrotalcite-like compounds. *Journal of Materials Science*, **32**, 957–964 (1997).
DOI: [10.1023/A:1018561918863](https://doi.org/10.1023/A:1018561918863)
- [47] Kopka H., Beneke K., Lagaly G.: Anionic surfactants between double metal hydroxide layers. *Journal of Colloid and Interface Science*, **123**, 427–436 (1988).
DOI: [10.1016/0021-9797\(88\)90263-9](https://doi.org/10.1016/0021-9797(88)90263-9)

- [48] Meyn M., Beneke K., Lagaly G.: Anion-exchange reactions of layered double hydroxides. *Inorganic Chemistry*, **29**, 5201–5207 (1990).
DOI: [10.1021/ic00351a013](https://doi.org/10.1021/ic00351a013)
- [49] Meyn M., Beneke K., Lagaly G.: Anion-exchange reactions of hydroxy double salts. *Inorganic Chemistry*, **32**, 1209–1215 (1993).
DOI: [10.1021/ic00059a030](https://doi.org/10.1021/ic00059a030)
- [50] You Y., Zhao H., Vance G. F.: Surfactant-enhanced adsorption of organic compounds by layered double hydroxides. *Colloids and Surfaces A: Physicochemical and Engineering Aspects*, **205**, 161–172 (2002).
DOI: [10.1016/S0927-7757\(01\)01137-2](https://doi.org/10.1016/S0927-7757(01)01137-2)
- [51] Carlino S.: The intercalation of carboxylic acids into layered double hydroxides: A critical evaluation and review of the different methods. *Solid State Ionics*, **98**, 73–84 (1997).
DOI: [10.1016/S0167-2738\(96\)00619-4](https://doi.org/10.1016/S0167-2738(96)00619-4)
- [52] Costa F. R., Leuteritz A., Wagenknecht U.: Intercalation of Mg–Al layered double hydroxide by anionic surfactants: Preparation and characterization. *Applied Clay Science*, **38**, 153–164 (2008).
DOI: [10.1016/j.clay.2007.03.006](https://doi.org/10.1016/j.clay.2007.03.006)
- [53] Costa F. R., Leuteritz A., Wagenknecht U., Auf der Landwehr M., Jehnichen D., Haussler L., Heinrich G.: Alkyl sulfonate modified LDH: Effect of alkyl chain length on intercalation behavior, particle morphology and thermal stability. *Applied Clay Science*, **44**, 7–14 (2009).
DOI: [10.1016/j.clay.2008.12.020](https://doi.org/10.1016/j.clay.2008.12.020)
- [54] Lagaly G., Beneke K.: Intercalation and exchange reactions of clay minerals and non-clay layer compounds. *Colloid and Polymer Science*, **269**, 1198–1211 (1991).
DOI: [10.1007/BF00652529](https://doi.org/10.1007/BF00652529)
- [55] Pavan P. C., Crepaldi E. L., Gomes G. D., Valim J. B.: Adsorption of sodium dodecylsulfate on a hydrotalcite-like compound. Effect of temperature, pH and ionic strength. *Colloids and Surfaces A: Physicochemical and Engineering Aspects*, **154**, 399–410 (1999).
DOI: [10.1016/S0927-7757\(98\)00847-4](https://doi.org/10.1016/S0927-7757(98)00847-4)
- [56] Aramendia M. A., Borau V., Jiménez C., Luque J. M., Marinas J. M., Ruiz J. R., Urbano F. J.: Epoxidation of limonene over hydrotalcite-like compounds with hydrogen peroxide in the presence of nitriles. *Applied Catalysis A: General*, **216**, 257–265 (2001).
DOI: [10.1016/S0926-860X\(01\)00570-1](https://doi.org/10.1016/S0926-860X(01)00570-1)
- [57] Kanazaki E.: Effect of atomic ratio Mg/Al in layers of Mg and Al layered double hydroxide on thermal stability of hydrotalcite-like layered structure BY means of in situ high temperature powder X-Ray diffraction. *Materials Research Bulletin*, **33**, 773–778 (1998).
DOI: [10.1016/S0025-5408\(98\)00021-X](https://doi.org/10.1016/S0025-5408(98)00021-X)
- [58] Durmus A., Kasgoz A., Macosko C. W.: Linear low density polyethylene (LLDPE)/clay nanocomposites. Part I: Structural characterization and quantifying clay dispersion by melt rheology. *Polymer*, **48**, 4492–4502 (2007).
DOI: [10.1016/j.polymer.2007.05.074](https://doi.org/10.1016/j.polymer.2007.05.074)
- [59] Vaia R. A., Liu W.: X-ray powder diffraction of polymer/layered silicate nanocomposites: Model and practice. *Journal of Polymer Science Part B: Polymer Physics*, **40**, 1590–1600 (2002).
DOI: [10.1002/polb.10214](https://doi.org/10.1002/polb.10214)
- [60] van Krevelen D. W., te Nijenhuis K.: *Properties of polymers*. Elsevier, Amsterdam (2009).
- [61] Lim S-K., Hong E-P., Song Y-H., Park B. J., Jin H., Chin I-J.: Preparation and interaction characteristics of exfoliated ABS/organoclay nanocomposite. *Polymer Engineering and Science*, **50**, 504–512 (2010).
DOI: [10.1002/pen.21551](https://doi.org/10.1002/pen.21551)
- [62] Kashiwagi T., Gilman J. W., Nyden M. R., Lomakin S. M.: New intumescent polymeric materials polymer combustion and new flame retardants. in ‘Fire retardancy of polymers. The use of intumescence’ (eds: Le Bras M., Bourbigot S., Camino G.). *The Royal Society of Chemistry, Cambridge*, 175–202 (1998).
- [63] Tang Y., Hu Y., Song L., Zong R., Gui Z., Chen Z., Fan W.: Preparation and thermal stability of polypropylene/montmorillonite nanocomposites. *Polymer Degradation and Stability*, **82**, 127–131 (2003).
DOI: [10.1016/S0141-3910\(03\)00173-3](https://doi.org/10.1016/S0141-3910(03)00173-3)
- [64] Hoffman J. D., Williams G., Passaglia E.: Analysis of the α , β , and γ relaxations in polychlorotrifluoroethylene and polyethylene: Dielectric and mechanical properties. *Journal of Polymer Science Part C: Polymer Symposia*, **14**, 173–235 (1966).
DOI: [10.1002/polc.5070140116](https://doi.org/10.1002/polc.5070140116)
- [65] Khanna Y. P., Turi E. A., Taylor T. J., Vickroy V. V., Abbott R. F.: Dynamic mechanical relaxations in polyethylene. *Macromolecules*, **18**, 1302–1309 (1985).
DOI: [10.1021/ma00148a045](https://doi.org/10.1021/ma00148a045)
- [66] Xie Y., Yu D., Kong J., Fan X., Qiao W.: Study on morphology, crystallization behaviors of highly filled maleated polyethylene-layered silicate nanocomposites. *Journal of Applied Polymer Science*, **100**, 4004–4011 (2006).
DOI: [10.1002/app.23206](https://doi.org/10.1002/app.23206)
- [67] Kuila T., Srivastava S. K., Bhowmick A. K.: Ethylene vinyl acetate/ethylene propylene diene terpolymer-blend-layered double hydroxide nanocomposites. *Polymer Engineering and Science*, **49**, 585–591 (2009).
DOI: [10.1002/pen.21286](https://doi.org/10.1002/pen.21286)
- [68] Berti C., Fiorini M., Sisti L.: Synthesis of poly(butylene terephthalate) nanocomposites using anionic clays. *European Polymer Journal*, **45**, 70–78 (2009).
DOI: [10.1016/j.eurpolymj.2008.09.039](https://doi.org/10.1016/j.eurpolymj.2008.09.039)

- [69] Krishnamoorti R., Vaia R. A., Giannelis E. P.: Structure and dynamics of polymer-layered silicate nanocomposites. *Chemistry of Materials*, **8**, 1728–1734 (1996). DOI: [10.1021/cm960127g](https://doi.org/10.1021/cm960127g)
- [70] Ren J., Silva A. S., Krishnamoorti R.: Linear viscoelasticity of disordered polystyrene-polyisoprene block copolymer based layered-silicate nanocomposites. *Macromolecules*, **33**, 3739–3746 (2000). DOI: [10.1021/ma992091u](https://doi.org/10.1021/ma992091u)
- [71] Krishnamoorti R., Giannelis E. P.: Rheology of end-tethered polymer layered silicate nanocomposites. *Macromolecules*, **30**, 4097–4102 (1997). DOI: [10.1021/ma960550a](https://doi.org/10.1021/ma960550a)
- [72] Rohn C. L.: *Analytical polymer rheology: Structure processing property relationships*. Hanser, Munich (1995).
- [73] Hyun Y. H., Lim S. T., Choi H. J., Jhon M. S.: Rheology of poly(ethylene oxide)/organoclay nanocomposites. *Macromolecules*, **34**, 8084–8093 (2001). DOI: [10.1021/ma002191w](https://doi.org/10.1021/ma002191w)

Post-impact mechanical characterisation of E-glass/basalt woven fabric interply hybrid laminates

I. M. De Rosa, F. Marra, G. Pulci, C. Santulli*, F. Sarasini, J. Tirillò, M. Valente

Sapienza – Università di Roma, Department of Chemical Engineering Materials Environment, Via Eudossiana 18 - 00184 Rome, Italy

Received 22 September 2010; accepted in revised form 4 December 2010

Abstract. Post-impact properties of different configurations (symmetrical and non-symmetrical) of hybrid laminates including E-glass and basalt fibre composites, all with volume fraction of fibres equal to 0.38 ± 0.02 and manufactured by RTM, have been studied. With this aim, interlaminar shear strength tests and four-point flexural tests of laminates impacted with different energies (0, 7.5, 15 and 22.5 J) have been performed. Acoustic emission (AE) localisation and AE evolution with applied flexural stress was studied to support impact damage characterisation, provided by SEM and transient thermography. The results indicate that a symmetrical configuration including E-glass fibre laminate as a core for basalt fibre laminate skins presents the most favourable degradation pattern, whilst intercalation of layers may bring to further improvement of the laminate properties, but also to more extended and complex damage patterns.

Keywords: polymer composites, mechanical properties, basalt fibres, acoustic emission, post-impact degradation

1. Introduction

In recent years, natural fibres, either extracted from plants, such as jute, flax, hemp, or of mineral origin, such as basalt, are increasingly proposed as a non-toxic and more easily recyclable alternative to glass fibres as a result of stricter environmental requirements. More specifically, the higher density of basalt fibres (about 2700 kg/m^3) is widely compensated by their higher modulus, excellent heat resistance, good resistance to chemical attack and to wear and low water absorption [1]. This suggests not only the possibility to apply them as a replacement for glass fibres, which has been the object of a previous study [2], but also the idea of making hybrids, able to combine, possibly with a positive global effect, the properties of both materials. As a matter of fact, hybridisation of basalt fibres has been attempted with ceramic fibres, to provide improved hot wear resistance to friction materials [3], and

with high tensile strength fibres, such as carbon [4] and Kevlar [5]. In these cases, basalt provides a sufficient resistance, in particular to impact, even superior to that obtained by a possible substitution with glass fibres, coupled in particular with a substantial reduction in costs, with respect to carbon and Kevlar fibres. In the case of basalt/Nylon fibres hybrid laminates, low tensile modulus of Nylon is improved by adding basalt fibres, whilst nylon provides some more impact resistance [6].

In contrast, basalt hybridisation with glass fibres would imply using two fibres, which are chemically not very different: continuous basalt fibre has a not very different content in silica and alumina from glass fibres and also a comparable, if not superior, tensile strength [7]. A significant difference is their behaviour under corrosion: for basalt fibres, resistance to acids is much higher than that to alkalis, whilst for glass fibres resistance to acids is nearly

*Corresponding author, e-mail: carlo.santulli@uniroma1.it

the same as that to alkalis [8]. This can for example make the former preferable over the latter for example in the automotive industry, where extensive use of acids is made. Moreover, basalt fibres, not containing additives in a single producing process, present an additional advantage in cost. Also, a previous study aimed at the comparison and discussion of the electrical properties of composites reinforced with basalt and E-glass woven fabrics, suggested that dielectric behaviour of the two composites in the frequency range 10 kHz–1 MHz is almost identical [9].

All the above findings would indicate that the combined use of basalt and glass fibres may have some scope: broadening the application field of the final material would also possibly result in a prospective reduced cost, without affecting its properties. It is significant, however, to assess that the composite presents a sufficient impact resistance to use it for structural components.

The major mode for impact damage absorption in basalt fabrics composites appears to be fibre breakage, delamination appearing less diffuse than in E-glass fibre composites [2, 6]. Also, previous study suggested that in basalt fabrics composites and hybrids, crack propagation patterns during impact may be complex, if single layers are used in an interplay layout [5]. This damage complexity has the important consequence that it is not easy to directly find out whether the hybridisation produces a positive effect or not with respect to the original laminates, an indication which could be given e.g., by the rule of mixtures [10]. In this context, the measurement of post-impact residual strength becomes particularly important.

In this study, the different configurations, including symmetrical and asymmetrical glass/basalt laminates, are fully characterised using interlaminar shear strength tests and flexural tests. Impact damage is characterised from the study of post-impact flexural properties assisted by acoustic emission and thermography, visualising damage using scanning electron microscope (SEM) fractographs. This is carried out along the lines of two comparative studies between configurations of glass/jute fibre hybrid laminates, performed by the same research group [11–12] and in the aforementioned study about the comparison of E-glass and basalt fibre composites [2].

2. Materials and methods

The basalt (BAS 220.1270.P) and E-glass fabrics (RE 220P) were plain weave fabrics supplied by Basaltex-Flocart NV (Wevelgem, Belgium) and Mugnaini Group srl (Stiava-Massarosa, Italy), respectively. Both fabrics had the same specific surface weight (220 g/m²). The matrix used was a Bisphenol-A epoxy based vinylester resin (DION 9102) produced by Reichhold, Inc (Research Triangle Park, North Carolina, USA). The hardener and accelerator were Butanox LPT (MEKP, 2 wt.%) and NL-51P (Cobalt 2-ethylhexanoate, 1 wt.%), respectively. The laminates were manufactured by a laboratory Resin Transfer Moulding (RTM) system described in [9]. From the laminates were removed the specimens for mechanical characterization.

All hybrid configurations, listed in Table 1, were produced using fourteen fabric layers and with a similar volume fraction, equal to 0.38 ± 0.02 , so that the thickness of all the produced configurations was approximately the same. The fibre volume used was the maximum one, which allowed sufficient impregnation from the resin with the RTM system employed.

Four-point bending tests were performed in accordance with ASTM D 6272. Five specimens for each configuration type were tested, having the following dimensions: 150 mm \times 30 mm \times 3.1 mm ($L \times W \times t$). A span-to-depth ratio of 25:1 and a cross-head speed of 2.5 mm/min were used. Strain gauges were used to evaluate the flexural modulus. The specimens were loaded in tension either as received or following impact with energies of 7.5, 15 and 22.5 Joules, applied as described below. It is suggested that most part of impact damage, even with the highest energy applied, which does not result in the full penetration of the laminate, should be contained in the width of the specimen. The interlaminar shear strength was evaluated in accordance with ASTM D 2344. Ten specimens were tested for each laminate, having the following dimensions: 20 mm \times 6.2 mm \times 3.1 mm ($L \times W \times t$). A span-to-depth ratio of 4:1 and a cross-head speed of 1 mm/min were used. The mechanical characterization was performed on a Z010 universal testing machine by Zwick/Roell (Ulm, Germany) equipped with a 10 kN load cell.

Glass/basalt hybrid specimens were impacted and then subjected to post-impact four-point bending

Table 1. Hybrid laminates configurations

Configuration	Layup sequence	Basalt layers (avg. vol.% fibres)	E-glass layers (avg. vol.% fibres)
B	14B	14 (38%)	–
V	14V	–	14 (38%)
VBV	3V/8B/3V	8 (22%)	6 (16%)
BVB	3B/8V/3B	6 (16%)	8 (22%)
BVBV	(1B/1V/1B/1V/1B/1V/1B) _s	7 (19%)	7 (19%)

tests, using five samples per configuration and impact energy. Impact tests were performed on an instrumented impact tower fitted with an anti-rebound device. The impact point was located at the centre of the specimens. The impact energy was changed varying the mass of the hemispherical drop-weight striker ($\varphi = 12.7$ mm), thus keeping a constant velocity of 2.5 m/s, obtaining energies of 7.5, 15 and 22.5 J.

Post-impact flexural tests were monitored by acoustic emission until final fracture occurred using an AMSY-5 AE system by Vallen Systeme GmbH (Icking, Munich, Germany). The AE acquisition settings used throughout this experimental work were as follows: threshold = 35 dB, Rearm Time (RT) = 0.4 ms, Duration Discrimination Time (DDT) = 0.2 ms and total gain = 34 dB. This level of threshold was selected after 30 minutes recording of the background noise with the AE setup configuration actually used, and was set 6 dB above the maximum level of the recorded spurious signal from the electronic system. The PZT AE sensors used (code SE150-M by DECI, Midland, Texas, USA) were resonant at 150 kHz. The sensors were placed on the surface of the specimens at both ends to allow linear localization.

After impact, the damaged area was observed using an Avio/Hughes Probeye TVS 200 (Cinisello Balsamo, Italy) thermal video system. The heating was obtained using a 500 W lamp: a 5 s pulse was applied, positioning the lamp at approximately 200 mm from the sample, so that a maximum temperature of 35°C was obtained on the sample surface. The cooling transient period was not long enough to allow images acquisition, so that the thermograms were acquired between 2 and 5 s during heating. The emissivity was set at 0.90 when the surface illuminated was in basalt and at 0.15 when it was in glass: these values were deemed offering in both cases images with the best contrast with the background. The variations of temperature on the specimen sur-

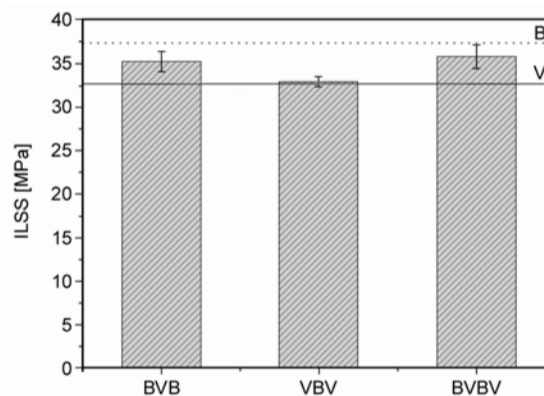
face were mainly ascribed to geometry alterations produced by impact damage, since both these composites show poor conductivity.

The microstructural characterization was carried out by scanning electron microscopy (SEM) using a Philips XL40 (Eindhoven, Netherlands). Prior to all SEM observations, the specimens were sputtered with gold to prevent charging.

3. Results

3.1. Mechanical properties

The principal purpose of adding basalt fibre laminates to E-glass fibre laminates would be getting a final laminate which, in spite of a slight weight penalty, has better mechanical properties, both as received and after impact. A previous study [2] demonstrated that non-impacted basalt fibre reinforced laminates show interlaminar shear strength and flexural properties slightly superior to those of E-glass fibre reinforced laminates. Here, in the VBV laminate, which includes the lowest number of basalt fibre layers among the three configurations, adding them does not result in an improvement of interlaminar shear strength over pure E-glass fibre reinforced laminates (Figure 1). The other two configurations, BVB and BVBV, present values of the interlaminar shear strength which are intermediate between E-glass fibre and basalt fibre reinforced laminates.

**Figure 1.** Interlaminar shear strength of the different hybrid laminates

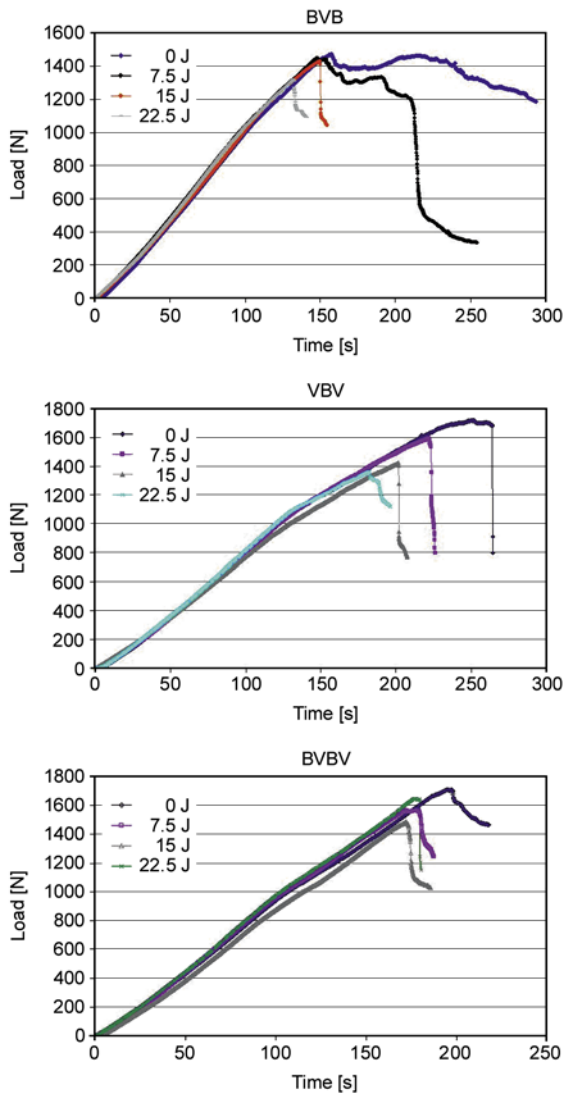


Figure 2. Typical flexural curves for hybrid laminates impacted at 0, 7.5, 15 and 22.5 J

As regards the study of degradation of flexural properties with increasing impact energies, typical flexural curves of non-impacted and impacted hybrid laminates of all configurations are shown in Figure 2. The main difference which may be observed is that BVB hybrids, when non-impacted or impacted at the lowest energy, show a more gradual failure process than the other hybrids. Impact reduces the flexural strength in a more variable way among the different configurations than it does with flexural modulus (compare Figure 3 and 4). In particular, in Table 2 all configurations are ranked from the higher to the lower flexural strength, including also the pure E-glass and basalt fibre reinforced laminates. The larger degradation of flexural strength of VBVB laminates with growing impact energy is clearly observable, whilst in general BVBV appears

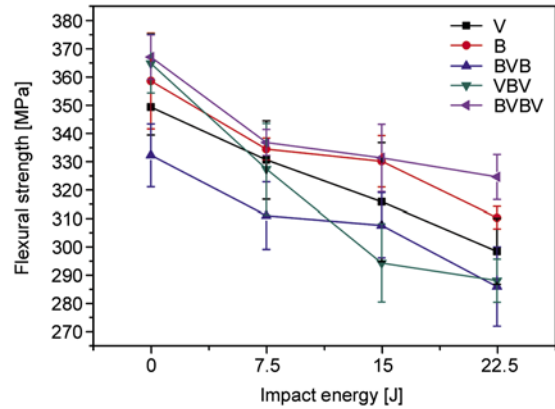


Figure 3. Post-impact flexural strength of the different laminates (compared with pure E-glass, V, and pure basalt fibre laminates, B)

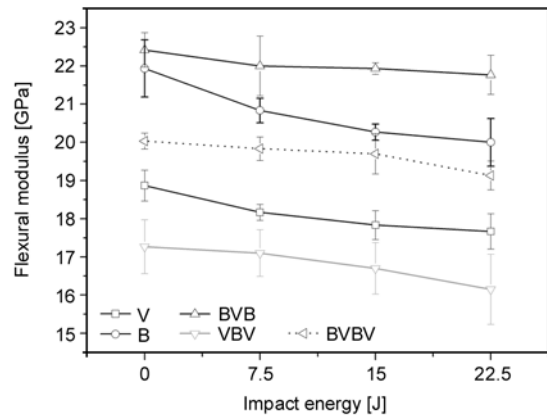


Figure 4. Post-impact flexural modulus of the different laminates (compared with pure E-glass, V, and pure basalt fibre laminates, B)

Table 2. Laminates ordered from maximum to minimum flexural strength at different impact energies

Position	0 J	7.5 J	15 J	22.5 J
1	BVBV	BVBV	BVBV	BVBV
2	VBVB	B	B	B
3	B	V	V	V
4	V	VBV	BVB	VBV
5	BVB	BVB	VBV	BVB

in all cases the best laminate configuration in this respect. As regards flexural modulus (Figure 4), BVB and VBVB laminates give at all impact energies the higher and lowest performance of all configurations, respectively: it is also to be noted that all laminates show comparable levels of degradation. The average residual flexural strength of impact damaged specimens normalized to that of undamaged ones is reported in Figure 5. This figure aims at clarifying which is the average level of degradation which is to be expected in every laminate as an

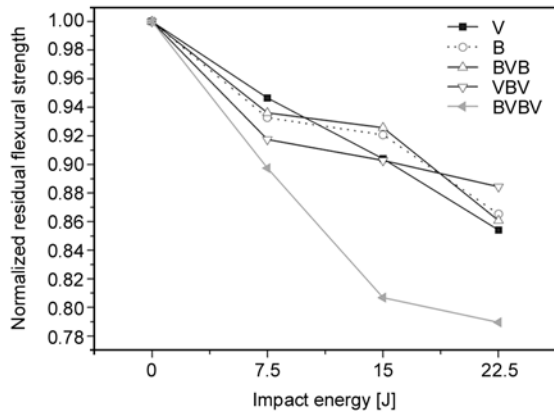


Figure 5. Normalised residual flexural strength of the different laminates (compared with pure E-glass, V, and pure basalt fibre laminates, B)

effect of impact damage with respect to the same laminate before the impact event. Here again, the lowest residual properties are shown by VBV laminates.

3.2. Acoustic emission analysis

Prior to the acoustic emission analysis, the measurement of the wave propagation speed in the laminates has been performed within an accuracy of ± 10 m/s, as allowed by the AE system on the distances involved. The values obtained are reported in Table 3. It can be noticed as the difference among values obtained for the three hybrid laminates can be considered within the statistical variability of the measurement.

As a preliminary consideration, from AE cumulative counts vs. time curves it is possible to identify an approximate load where acoustic emission activity starts. In particular, neglecting sparse low-counts events, which may take place even at very low load, acoustic emission is considered to commence when it starts to be visible from AE cumulative counts vs. time graphs, referred to the whole test, an example of which is given in Figure 6. This happens when AE counts exceed approximately 1/500 of the final cumulative counts: at this point, an AE start load is measured. This derives empirically from the maximum achievable end-of-scale of the graph on the

Table 3. Wave propagation speed of the laminates [m/s]

Laminate	Wave propagation speed [m/s]
B	3970
V	3660
BVB	3800
VBV	3840
BVBV	3780

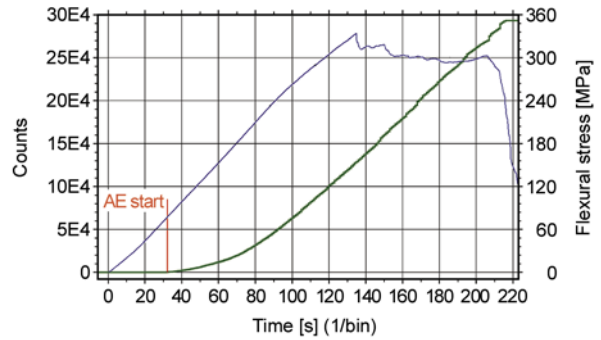


Figure 6. AE start load measured from cumulative counts vs. time curve (in green) and the corresponding flexural stress vs. time curve (in blue) (BVB hybrid laminate impacted at 7.5 Joules)

Y-axis (1654 pixels), and the fact that only a gradient of not less than three pixels starts being visible. Beyond the AE start load, AE activity during monotonic loading is likely to grow with increasing stress, although the specific characteristics of such behaviour may change considerably depending on materials properties and presence of irreversible damage. To better clarify these characteristics, the tests have been divided in five phases, according to the load levels, from 0 to 25%, 25 to 50%, 50 to 75%, and 75 to 100% of the maximum load. The fifth phase is denominated as ‘post’ and represents those AE events detected after reaching the maximum load, when the load decreases in the immediate proximity of failure. The phases are reported on a typical flexural loading curve in Figure 7.

A further analysis of AE data is performed on their location with respect to impact (if any): the centre of the impacting head corresponds to the midpoint between the edge of the two sensors (located at abscissa 15 and 135 mm, respectively), at the abscissa $x = 75$ mm. With respect to their locations, the events are divided in four classes, namely A, for those detected within the impacted length (68–81 mm),

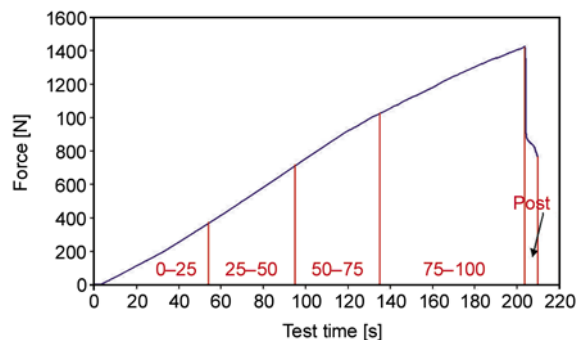


Figure 7. Load levels on a typical flexural load vs. time curve (VBV hybrid laminate impacted at 15 Joules)

B, detected in a location displaced by no more than one impacted length from either of the extremes of A (55–68 and 81–94 mm), C, detected in the remaining part of the laminate between the sensor edges (15–55 and 94–135 mm), and D, detected under the sensors and outside them (0–15 and 135–150 mm). More specifically, the localisation analysis is aimed at discerning on impacted samples between the two principal modes of impact damage. These represent the indentation mode, which is limited to the area in physical contact with the impacting head ('A' class of AE events), and the delamination mode, which has been approximated for low impact energies with a ring-shaped area extending no further than twice the impacting head diameter from the centre ('B' class of AE events). Other events detected in the bulk of the laminate between the sensors are in the 'C' class, whilst those very close to the laminate's edge, which can be supposed to be mostly unrelated with fracture events, are in the 'D' class. An example of the distribution between the four classes is reported using different colours in Figure 8. Results in Figure 9, concerning stress where acoustic emission activity starts, indicate that for non-impacted laminates, the worst performance is obtained with VBV laminates, which are supposed to be slightly less tolerant to pure flexural loading. In the laminates impacted with the lowest energy (7.5 J), acoustic emission may initiate later during loading (in particular, this happens on VBV and with lesser evidence on BVB hybrids). This is likely to suggest that the limited depth and gravity of impact damage is not yet sufficient to trigger further crack growth and delamination in the laminates, as an effect of flexural loading, rather making the material less sensitive to it.

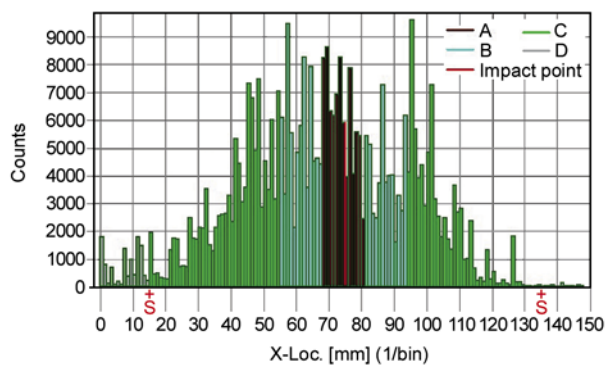


Figure 8. Partition of the events according to their location along the laminate (BVBV laminate impacted at 22.5 J) (letter S indicates sensors location)

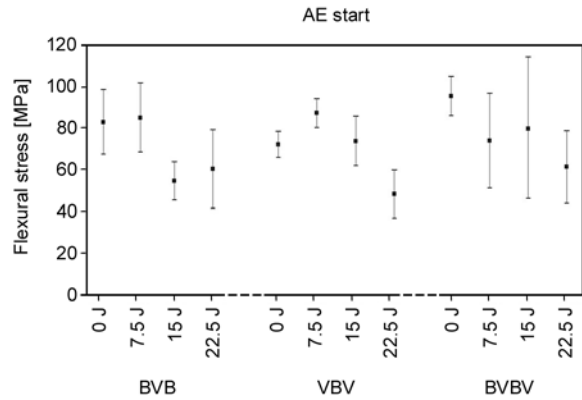


Figure 9. AE start stress [MPa] for all hybrid laminate configurations

A significant degradation of properties occurs with impact at 22.5 J for VBV laminates and both at 15 and 22.5 J on BVB laminates: here AE start is around 55 MPa, compared with 80 MPa for the non-impacted BVB laminates. A large scattering in performance is observed for BVBV laminates, which may be the result of the variable adhesion between the different interfaces between glass and basalt fibre layers in the laminates.

The results obtained from the study of the evolution of acoustic emission activity with load are reported in Figure 10. This analysis can be considered quite reliable in that the patterns of flexural load vs. time curve does not change much between hybrids (see Figure 2) (apart from some differences on BVB hybrids at 0 and 7.5 J). The main indication from Figure 9 are that the typical trend of increased AE detection with growing load is more frequently disturbed here than it was on pure E-glass or basalt laminates. In particular, it can be noticed that there is a strongly variable normalised count rate in the final part of the test when the applied stress goes beyond the quasi-elastic limit. In general, it is suggested, by comparison with what observed on pure basalt or E-glass fibre laminates in [2], that whenever the growing trend of acoustic emission is preserved (such as for example is the case for VBV laminates impacted at 15 and especially 22.5 J), damage progression which produces acoustic emission takes place preferentially in one of the two laminates. In contrast, when no clear trend is observable, it is possible that both E-glass and basalt fibre laminate forming the hybrids are damaged in a comparable way (this happen e.g., in all BVB laminates, with exception of the 22.5 J impacted ones).

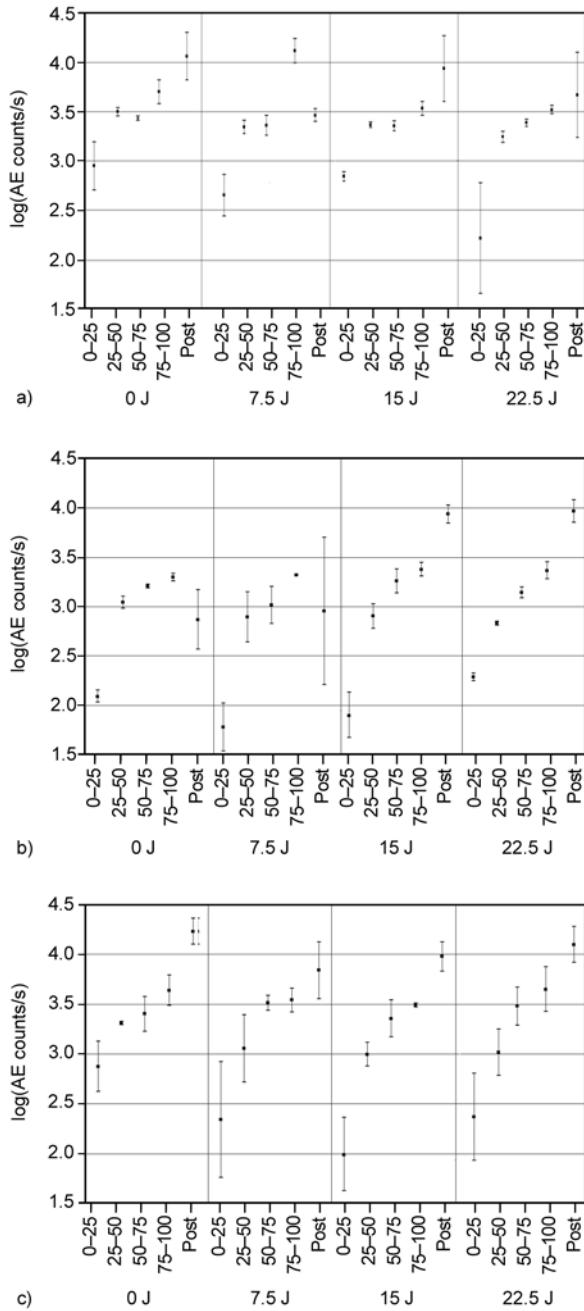


Figure 10. a) AE log (Count rate over time) vs. load for BVB hybrid laminates; b) AE log (Count rate over time) vs. load for VBV hybrid laminates; c) AE log (Count rate over time) vs. load for BVBV hybrid laminates

AE location analysis (Figure 11) indicates that there are more B-class than A-class normalised events for impacted BVB laminates, whilst the opposite is true for impacted VBV laminates: this suggests that in the former case most critical damage is in the wider delaminated area, whilst in the latter it is in the immediate vicinity of the impact centre, in a belt whose length corresponds to the impactor diameter.

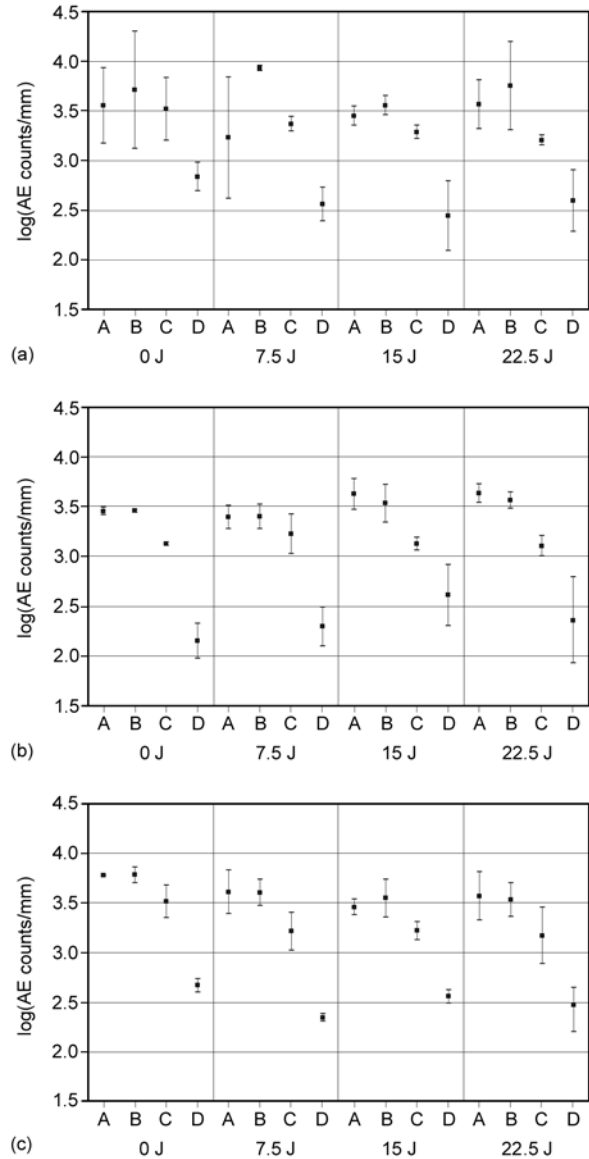


Figure 11. a) AE log (Count rate over distance) vs. X-location for BVB hybrid laminates; b) AE log (Count rate over distance) vs. X-location for VBV hybrid laminates; c) AE log (Count rate over distance) vs. X-location for BVBV hybrid laminates

For BVBV laminates, an intermediate situation between the two is revealed.

3.3. Impact damage characterisation

Impact damage characterisation was carried out on laminates which are larger than those necessarily used for post-impact flexural tests. This allowed clarifying whether damage produced by applying these impact energies was effectively contained in the width of flexural specimens. This is more often than not the case, with exceptions for the 22.5 Joules impacted laminates. In Figure 12 are represented

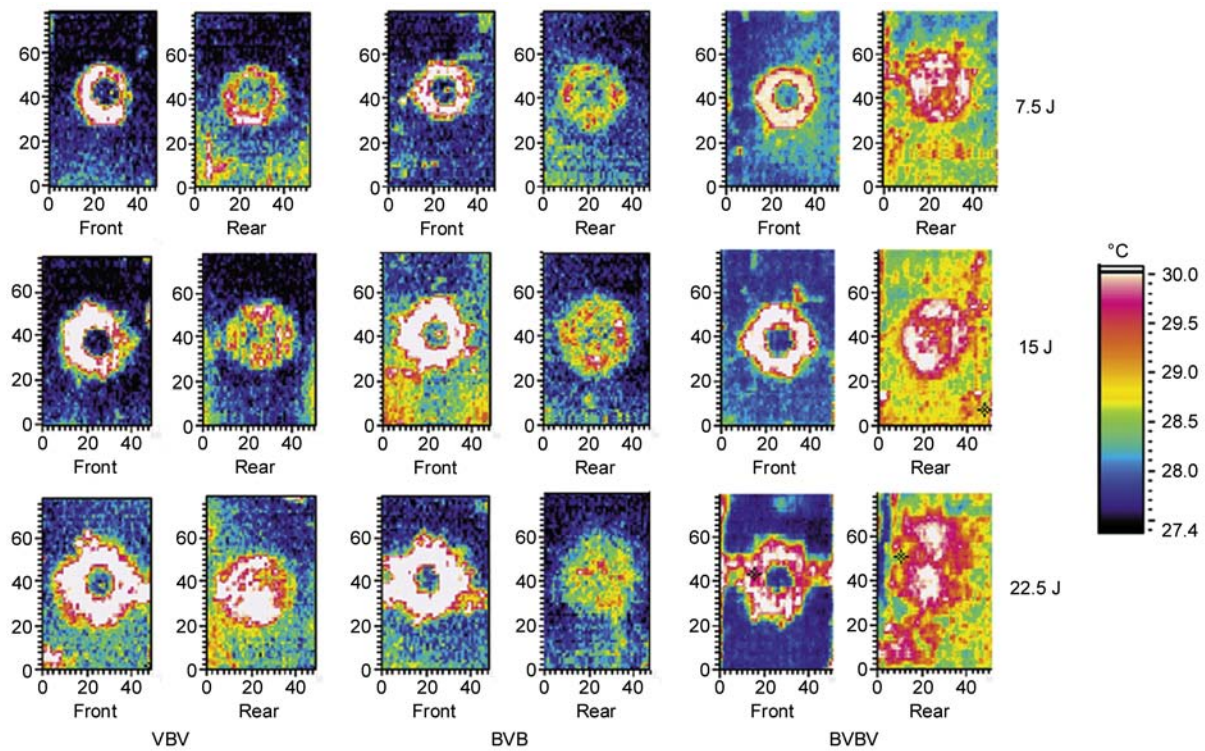


Figure 12. IR thermograms of both surfaces of the impacted laminates (dimensions are given in mm)

the impacted and non-impacted surfaces of the hybrid laminates at the different impact energies, as obtained using pulsed IR thermography: a region with dimensions 75×45 mm is shown in the images. As a general consideration, the visualisation of the impacted area was easier whenever a basalt fibre laminate is observed, due to its high emissivity. In contrast, in some cases on the glass fibre reinforced laminates the weaving structure created some disturbance to the thermographic signal. In particular, the difficulties of observing impact damage on E-glass fibre reinforced laminates using IR thermography have been recently reported in [13]. The measurements suggest that at 7.5 and 15 J the dimension of the impact damaged area for all laminates is comparable. At 22.5 J all laminates appear heavily damaged in most of their mid-section corresponding to the impact line. However, whilst BVBV laminates show a more symmetrical delamination area, clearly extending towards both edges, the other two laminates show a more unpredictable damage progression. This may occur either preferentially in the direction of one of the edges, as is the case for VBV laminates, or in other random directions, as it happens with BVB laminates. The presence of dissymmetric damage does suggest in general that stiffness

degradation consequent to impact affects in variable way the layers of the hybrid laminates, and in the case of BVBV laminate some kind of internal compensation between damage in the different layers may take place [14].

Photographs of the impact-damaged surface (those taken on the BVB laminate have been inverted for better clarity) (Figure 13) do suggest that damage appears more extended in the B-area and beyond it for VBV laminates: also, the increment of damage, passing from 15 to 22.5 J impact energy, is greater than for the other laminates. This consideration confirms by the comparison of the respective AE start stresses in Figure 9. In contrast, damage spreads around the whole of B-area for BVB and BVBV laminates, even at 15 J, going considerably beyond that for 22.5 J impact energy, especially on BVBV laminates. This substantially confirms what has been stated, dealing with AE localisation data analysis, although of course some overlapping does exist, when projecting 2-D images into 1-D AE localisation graphs. It needs also to be noted for completeness that the digital inversion of images on the BVB laminates does not provide exactly the same level of contrast between damaged and undamaged parts, as it is for the direct images, so damage on these

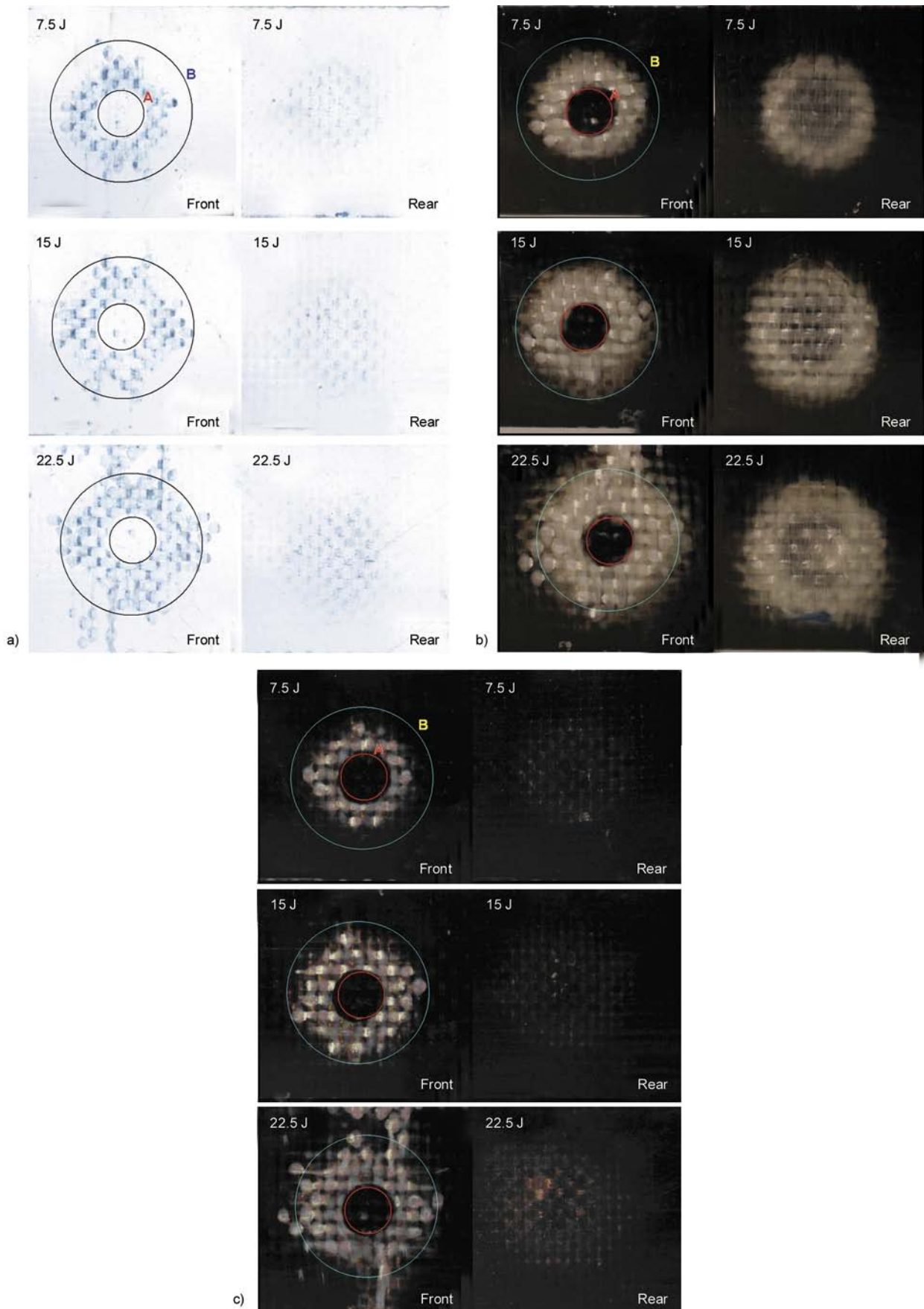


Figure 13. a) Inverted value photographs of impacted BVB laminates (A and B areas are as defined for AE localisation analysis); b) Photographs of VBV laminates (A and B areas are as defined for AE localisation analysis); c) Photographs of BVBV laminates (A and B areas are as defined for AE localisation analysis)

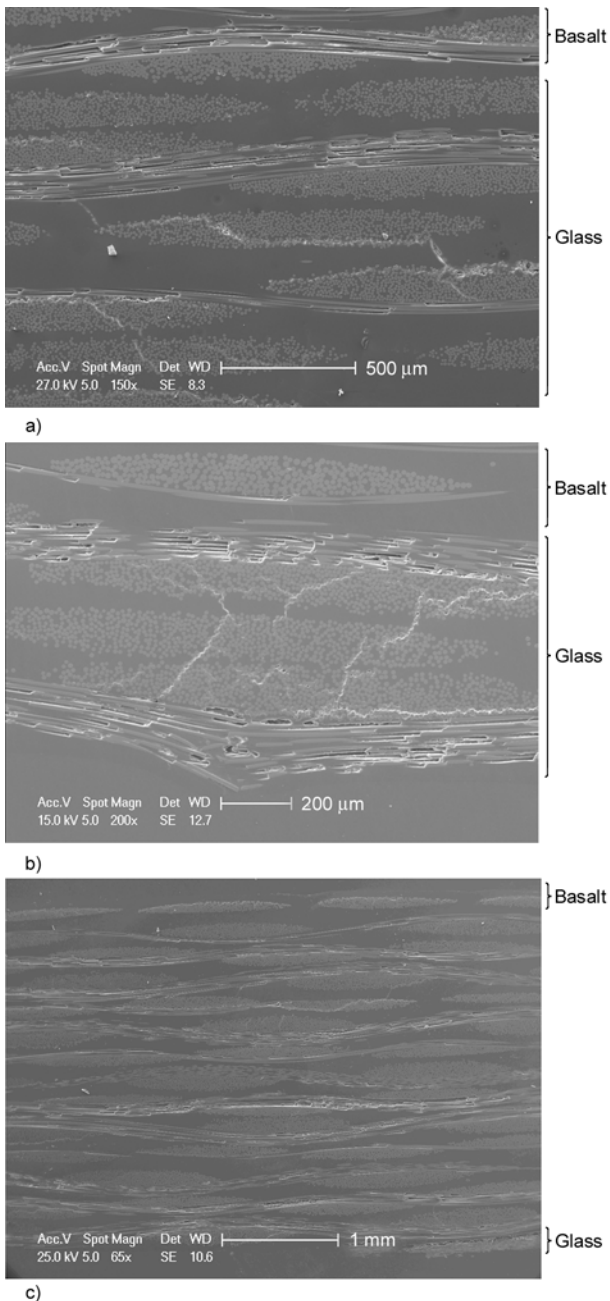


Figure 14. a) Transverse section of impacted BVB laminate (impact energy = 22.5 J); b) transverse section of impacted VBV laminate (impact energy = 22.5 J); c) transverse section of impacted BVBV laminate (impact energy = 22.5 J) (the inner layers are alternatively glass and basalt)

laminates might be slightly underestimated: however, the general sense of the statement can be confirmed.

This is substantially confirmed by SEM micrographs representing transverse sections of impacted region of all hybrid laminate configurations impacted at the highest impact energy (Figure 14). In BVB laminate most damage lies in the central glass fibre

laminates (Figure 14a), whilst in the VBV laminate it is the lowest part (again a glass fibre laminate) which appears heavily damaged. In BVBV, the general appearance shows a limited presence of damage, though sometimes extended also to the basalt fibre layers (Figure 14c). It may be suggested that the presence of basalt fibre multi-layers tend to stop crack propagation, which is not the case for glass fibre ones. Post-impact residual properties of symmetrical (such as BVB and VBV) hybrid compared with intercalated hybrid (such as BVBV) laminates has been the object of a previous work on glass/jute hybrid laminates [11]. In that case, it appeared that in the intercalated hybrid laminate crack propagation is more controllable than in the superior symmetrical hybrid laminates. Due to the different nature of basalt fibre, here the perspective appears reversed, in the sense that high stiffness of basalt would sometimes allow the development of cracks in inner layers, rather than their bare compression, as it was the case with jute. Further improvement in properties is also likely to be obtained whenever using more complex systems for intercalation, which involve the combined presence of both fibres on the same layer: this has been attempted already with carbon and basalt fibres [15]. However, post-impact behaviour may be quite complex and unpredictable, and needs to be thoroughly assessed, which has not been the case so far.

4. Conclusions

This comparative study between different hybrid configurations based on E-glass and basalt fibre reinforced laminates confirms the slight superiority of basalt fibre woven laminates over E-glass fibre ones as for post-impact performance. It suggests furthermore that a symmetrical configuration including the lower strength material (glass) as a core for the higher strength one (basalt) presents the most favourable degradation pattern. In particular, concerns about the possible sudden collapse of the core during post-impact can be, at least in principle, overlooked. The reverse situation (basalt as core) is slightly less favourable, because it does appear less suitable to stop crack propagation, especially at impact energies approaching penetration. Further improvement of the ‘as received’ mechanical properties can be possibly obtained by intercalating single layers of E-glass and basalt laminates: however,

this happens at the expense of the predictability of post-impact crack propagation. A suggestion for further work would include the investigation of intermediate structures between the one-to-one intercalated hybrids and the symmetrical ones.

References

- [1] Czigány T.: Trends in fiber reinforcements – The future belongs to basalt fiber. *Express Polymer Letters*, **1**, 59 (2007).
DOI: [10.3144/expresspolymlett.2007.11](https://doi.org/10.3144/expresspolymlett.2007.11)
- [2] De Rosa I. M., Marra F., Pulci G., Santulli C., Sarasini F., Tirillò J., Valente M.: Post-impact mechanical characterisation of glass and basalt woven fabric laminates. *Composite Structures*, in press (2011).
- [3] Öztürk B., Aslan F., Öztürk B.: Hot wear properties of ceramic and basalt fiber reinforced hybrid friction materials. *Tribology International*, **40**, 37–48 (2007).
DOI: [10.1016/j.triboint.2006.01.027](https://doi.org/10.1016/j.triboint.2006.01.027)
- [4] Artemenko S. E., Kadykova Y. A.: Polymer composite materials based on carbon, basalt, and glass fibres. *Fibre Chemistry*, **40**, 37–39 (2008).
DOI: [10.1007/s10692-008-9010-0](https://doi.org/10.1007/s10692-008-9010-0)
- [5] Wang X., Hu B., Feng Y., Liang F., Mo J., Xiong J., Qiu Y.: Low velocity impact properties of 3D woven basalt/aramid hybrid composites. *Composites Science and Technology*, **68**, 444–450 (2008).
DOI: [10.1016/j.compscitech.2007.06.016](https://doi.org/10.1016/j.compscitech.2007.06.016)
- [6] Dehkordi M. T., Nosraty H., Shokrieh M. M., Minak G., Ghelli D.: Low velocity impact properties of intraply hybrid composites based on basalt and nylon woven fabrics. *Materials and Design*, **31**, 3835–3844 (2010).
DOI: [10.1016/j.matdes.2010.03.033](https://doi.org/10.1016/j.matdes.2010.03.033)
- [7] Deák T., Czigány T.: Chemical composition and mechanical properties of basalt and glass fibers: A comparison. *Textile Research Journal*, **79**, 645–651 (2009).
DOI: [10.1177/0040517508095597](https://doi.org/10.1177/0040517508095597)
- [8] Wei B., Cao H., Song S.: Environmental resistance and mechanical performance of basalt and glass fibers. *Materials Science and Engineering A*, **527**, 4708–4715 (2010).
DOI: [10.1016/j.msea.2010.04.021](https://doi.org/10.1016/j.msea.2010.04.021)
- [9] Carmisciano S., De Rosa I. M., Sarasini F., Tamburano A., Valente M.: Basalt woven fiber reinforced vinylester composites: Flexural and electrical properties. *Materials and Design*, **32**, 337–342 (2011).
DOI: [10.1016/j.matdes.2010.06.042](https://doi.org/10.1016/j.matdes.2010.06.042)
- [10] Marom G., Fischer S., Tuler F. R., Wagner H. D.: Hybrid effects in composites: Conditions for positive or negative effects versus rule-of-mixtures behaviour. *Journal of Materials Science*, **13**, 1419–1426 (1978).
DOI: [10.1007/BF00553194](https://doi.org/10.1007/BF00553194)
- [11] De Rosa I. M., Santulli C., Sarasini F., Valente M.: Post-impact damage characterization of hybrid configurations of jute/glass polyester laminates using acoustic emission and IR thermography. *Composites Science and Technology*, **66**, 1142–1150 (2009).
DOI: [10.1016/j.compscitech.2009.02.011](https://doi.org/10.1016/j.compscitech.2009.02.011)
- [12] De Rosa I. M., Santulli C., Sarasini F., Valente M.: Effect of loading-unloading cycles on impact-damaged jute/glass hybrid laminates. *Polymer Composites*, **30**, 1879–1887 (2009).
DOI: [10.1002/pc.20789](https://doi.org/10.1002/pc.20789)
- [13] Meola C., Carlomagno G. M.: Impact damage in GFRP: New insights with infrared thermography. *Composites Part A: Applied Science and Manufacturing*, **41**, 1839–1847 (2010).
DOI: [10.1016/j.compositesa.2010.09.002](https://doi.org/10.1016/j.compositesa.2010.09.002)
- [14] Kowsika M. V., Mantena P. R.: Static and low-velocity impact response characteristics of pultruded hybrid glass-graphite/epoxy composite beams. *Journal of Thermoplastic Composite Materials*, **12**, 121–132 (1999).
DOI: [10.1177/089270579901200203](https://doi.org/10.1177/089270579901200203)
- [15] Artemenko S. E., Kadykova Y. A.: Hybrid composite materials. *Fibre Chemistry*, **40**, 491–492 (2008).
DOI: [10.1007/s10692-009-9091-4](https://doi.org/10.1007/s10692-009-9091-4)

Preparation of microgel composite hydrogels by polymer post-crosslinking method

X. P. Qin, F. Zhao, S. Y. Feng*

School of Chemistry and Chemical Engineering, Shandong University, Jinan, 250100, P. R. China

Received 22 September 2010; accepted in revised form 6 December 2010

Abstract. A novel post-crosslinking method by heating the composite polymer with dispersed reactive microgels was used to prepare microgel composite (MC) hydrogels. This MC hydrogels were crosslinked by reactive microgels instead of traditional crosslinkers. The reactive microgels contained hydroxymethyl groups, which acted as post-crosslinkers. They were prepared by inverse emulsion polymerization. The formed MC hydrogels at appropriate conditions had high equilibrium swelling ratio and excellent mechanical properties. The heating conditions and the polymer water content influenced the hydrogel properties. For MC hydrogels prepared by direct heating the as-prepared composite polymers with 75% water content, their properties were influenced by heating conditions. When the heating conditions were 90°C for 4 h, the MC hydrogel had a tensile strength of 32 kPa and a high elongation of 960%. In addition, for MC hydrogels prepared by heating the partly evaporated composite polymers, their properties can be adjusted by the polymer water content. Appropriate reduction of the polymer water content was beneficial to improve the mechanical strength of the MC hydrogels. The appropriate polymer water content was important to prepare MC hydrogels with excellent mechanical properties. When the composite polymer with 50% water content was heated at 90°C for 3 h, the MC hydrogel had high tensile strength of 130 kPa and high tensile elongation of 503%.

Keywords: mechanical properties, hydrogels, reactive microgels, post-crosslinking

1. Introduction

Polymeric hydrogels have attracted much scientific interest over the past several decades and have found uses in many fields such as superabsorbents, in medicine, hygiene, and in biomedical applications [1]. Given increasing environmental issues, the idea of replacing plastics with hydrogels also seems reasonable [2]. However, the applications of the conventional hydrogels crosslinked by the traditional crosslinkers such as *N,N'*-methylenebisacrylamide are strongly limited by their poor mechanical properties. In recent years, several synthesized hydrogels with excellent mechanical properties have been successfully prepared such as topological hydrogels [3], double-network hydrogels [4, 5], and

composite hydrogels [6–15]. The composite hydrogels include the nanocomposite (NC) hydrogels using inorganic clay as a crosslinker [6, 15], the macromolecular microsphere composite (MMC) hydrogels using hydrophobic macromolecular microsphere as a crosslinker [11, 14], and the hydrophilic reactive microgel (HRM) composite hydrogels using hydrophilic reactive microgels containing C=C double bonds as a multifunctional crosslinker [13]. The HRM composite hydrogels are made from hydrophilic organic monomers only and do not require inorganic or hydrophobic fillers. They have a two-level hierarchic network structure, a primary network inside reactive microgels and a secondary network between microgels similar to NC or MMC

*Corresponding author, e-mail: fsv@sdu.edu.cn
© BME-PT

hydrogels [13]. Reactive microgels have also been used as multifunctional crosslinkers for photopolymerized thin films or thermosets to improve their mechanical properties [16, 17]. In addition to the direct polymerization method by adding the reactive microgels containing C=C double bonds, the crosslinked structure can also be obtained by post-crosslinking of the polymers through irradiation, peroxide, drying, heating, and so on [18–21]. Amide groups of acrylamide can react with other groups [22]. The chemical reactions can occur between the amide groups of acrylamide (AM) and the hydroxymethyl groups of *N*-methylolacrylamide (NMA) at appropriate temperature [13]. Microgel composite (MC) hydrogels can be designed by the post-crosslinking method through heating the composite polymer with dispersed reactive microgels using the reaction between the microgels containing hydroxymethyl groups and the polymer linear chains containing amide groups. High mechanical strength hydrogels were obtained easily by the post-crosslinking method and the crosslinking did not affect the polymerization process. The method might open a new field to manufacture composite hydrogels with novel structures.

In this paper, AM and 2-Acrylamido-2-methylpropane sulfonic acid (AMPS) was used as main monomers. NMA was used as a functional monomer. First, the reactive microgels with hydroxymethyl groups were synthesized by inverse emulsion polymerization. Then, they were dispersed into the monomer solutions to synthesize composite polymers. Finally, the as-prepared composite polymers or partly evaporated composite polymers were heated to prepare MC hydrogels. Effects of the heating temperature, heating time and polymer water content on the swelling and mechanical properties of the MC hydrogels were investigated.

2. Experimental Part

2.1. Materials

AM (chemically pure, Dia-Nitrix. Co., Tokyo, Japan), AMPS (chemically pure, Shandong Lianmeng Chemical Group Co., Shouguang, China) and NMA (chemically pure, Shandong Zibo Xinye Chemical Co., Zibo, China) were used directly. The other reagents were all analytically pure, commercially available and were used without further

purification. Distilled water was used in the whole experiments.

2.2. Preparation of reactive microgels with hydroxymethyl groups

Reactive microgels were prepared by inverse emulsion polymerization. AM solutions (98 ml 43 wt%) and AMPS (5 g) as monomers, NMA (5 g) as a functional monomer, sorbitan monolaurate (9 g) and octylphenol ethoxylate (2.5 g) as emulsifiers and *N,N'*-methylenebisacrylamide (0.003 g) as crosslinking agent were added into a 500 ml round-bottomed three-neck flask with a refluxed condenser, a mechanical stirrer, a vent-plug and a thermometer. The resulting solution was stirred for 20 min, and then cyclohexane (110 ml) was added into the flask. After bubbled by nitrogen for 20 min, the polymerization was initiated at 25°C using redox initiator of ammonium persulfate (0.004 g in 1 ml water) and sodium bisulfite (0.01 g in 1 ml water). Nitrogen atmosphere was maintained throughout the polymerization. The microgel emulsions were obtained after 3 h reaction. First, 13 g of the microgel emulsions were precipitated by enough acetone to obtain microgel powder. Second, the microgel powder was dried at room temperature. Last, the dried powder was dispersed in 87 ml distilled water to obtain dispersed solutions for further use.

2.3. Preparation of composite polymer

The composite polymer was prepared by solution polymerization. The above dispersed solution (13.6 g), distilled water (61.7 ml), AM (20.3 g) and AMPS (4 g) were added into in a beaker. After nitrogen bubbling for 30 min, the solution was initiated by redox initiator of ammonium persulfate (0.004 g in 1 ml water) and sodium bisulfite (0.01 g in 1 ml water) at 20°C. The polymerization was carried out under airproof conditions for 5 h to obtain composite polymers and was cut into appropriate size to be used further. The as-prepared composite polymer has 75% water content. Polymer water content $x\%$ was calculated by the Equation (1):

$$x [\%] = \frac{W - W_{pd}}{W} \quad (1)$$

where W and W_{pd} were the wet polymer weight and the corresponding dry polymer weight, respectively.

2.4. Preparation of MC hydrogels

MC hydrogels were prepared by heating the as-prepared composite polymers or partly evaporated composite polymers with different water content under airproof conditions at 80 to 99°C. When the polymer achieved the designed water content by evaporation, it was wrapped by plastic wrap and tape. It was held at room temperature for two days for uniform diffusion of the water within the whole polymer. Then, it was heated to prepare MC hydrogels. The MC hydrogels were referred to as MC-y-zh and MCx%-y-zh for heating the as-prepared composite polymers and the partly evaporated composite polymers, respectively. Here x , y and z were the partly evaporated polymer water content, heating temperature and the number of hours for heating time, respectively. The schematic illustration of preparing MC hydrogels by post-crosslinking is proposed in Figure 1a.

2.5. Measurements of microgel particle size

The particle size of the reactive microgels was detected by JEM-100CX II transmission electron microscopy (TEM, JEOL Ltd., Tokyo, Japan). TEM samples were prepared by placing a dilute drop of microgel particles onto a sample grid and allowing

them natural drying in air. Dynamic light scattering measurements were performed on a Malvern Zetasizer 3000 instrument (Malvern Instruments Ltd., Malvern, UK) at 25°C and at a scattering angle of 90° to obtain the swollen size of microgel particles in water.

2.6. Measurements of the swelling properties

The swelling experiments were performed by immersing the hydrogels in a large excess of water at room temperature to reach the swelling equilibrium. The swelling ratio was calculated by the Equation (2)

$$Q = \frac{W_e - W_d}{W_d} \quad (2)$$

where W_e is the weight of the equilibrium swollen hydrogel and W_d is the corresponding dried hydrogel, respectively.

2.7. Measurements of the degree of hydrolysis of the MC hydrogels

During the heating process for preparing MC hydrogels, amide groups of acrylamide can hydrolyze at high temperature. The degree of hydrolysis ($z\%$) of the amide groups was determined by the titration

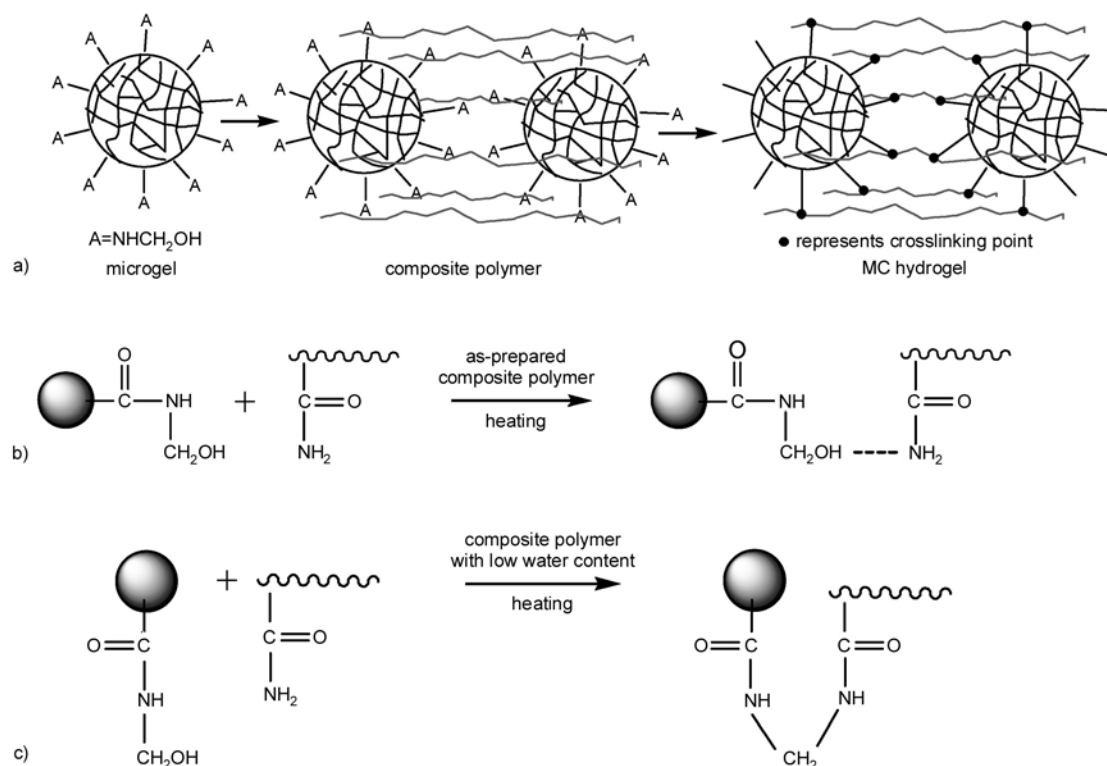


Figure 1. Schematic illustration of a MC hydrogel formation and crosslinking reactions between microgels and polymer matrix. (a) MC hydrogel formation, (b) hydrogen bond formation, (c) covalent bond formation

method. The carboxyl groups produced by hydrolyzing were neutralized by excess 0.1 mol/l standard solutions of sodium hydroxide. The remaining sodium hydroxide was titrated by 0.1 mol/l standard solution of hydrochloric acid. The Equation (3) was used to calculate the degree of hydrolysis of the product:

$$z[\%] = \frac{(V_1 C_1 - V_2 C_2) - (V_{01} C_1 - V_{02} C_2)}{n} \cdot 100 \quad (3)$$

where C_1 and C_2 are the molar concentration of sodium hydroxide and hydrochloric acid standard solution, V_1 and V_2 are the total volume of sodium hydroxide solutions used for neutralization and the consumed volume of hydrochloric acid solution for hydrogels, V_{01} and V_{02} are the total volume of sodium hydroxide solutions used for neutralization and the consumed volume of hydrochloric acid standard solution for polymer without heating, n is the amount of the amide groups [mol], respectively. About 80 g swollen sample was used to measure the degree of hydrolysis. The amount of the amide groups was calculated by the corresponding acrylamide weight of the swollen sample. Three samples were tested and their results were averaged.

2.8. Measurements of the mechanical properties of the MC hydrogels

The mechanical properties of the hydrogels were measured by an electronic pulling tester (LR10KPLUS, 10 kN Universal Materials Testing Machine, Lloyd Instruments, West Sussex, UK). The conditions were as follows: temperature 25°C, sample water content 90%, the sample size 8 mm (thickness) × 15 mm (width) × 60 mm (length), the gauge length 35 mm and crosshead speed 100 mm/min. 90% water content of the sample was prepared as follows. The hydrogel was immersed in water. Its water content was calculated by Equation (1) and controlled according to monitoring its weight. When its weights attained 90% water content, it was removed and put in plastic bags for uniform diffusion of the water within the whole gels. The tensile stress was calculated on the basis of the initial cross section of the specimen and the strain was defined as the change in the length with respect to the initial gauge length. Three samples were tested for each type of hydrogels and the data was averaged.

3. Results and discussion

3.1. Influence of heating conditions on MC hydrogels prepared by heating the as-prepared composite polymers.

The reactive microgels were prepared by inverse emulsion polymerization. The conversion of the monomers in microgel synthesis exceeded 99.5%. It was determined by bromation of the residual double bond according to Liu *et al.* [23]. TEM was used to observe the microgel particle size. The microgel particles have sphere morphology. Their average dry particle size is about 100 nm (Figure 2). The average swollen size of the microgel particles is about 298 nm (Figure 3) and the polydispersity in microgel particle size was 0.449, which was deter-

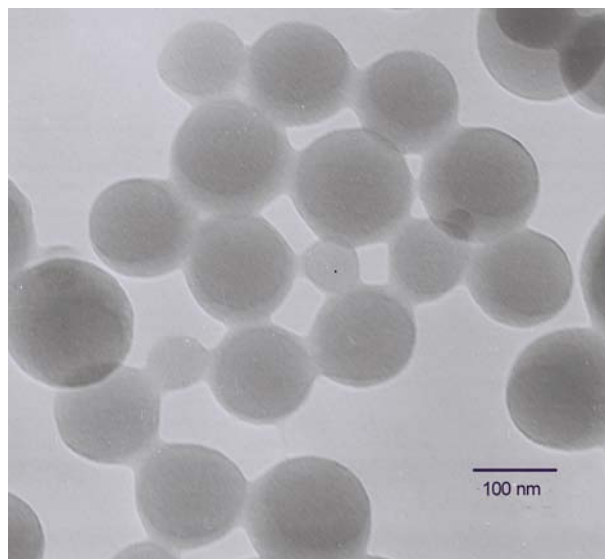


Figure 2. TEM images of the reactive microgel particles

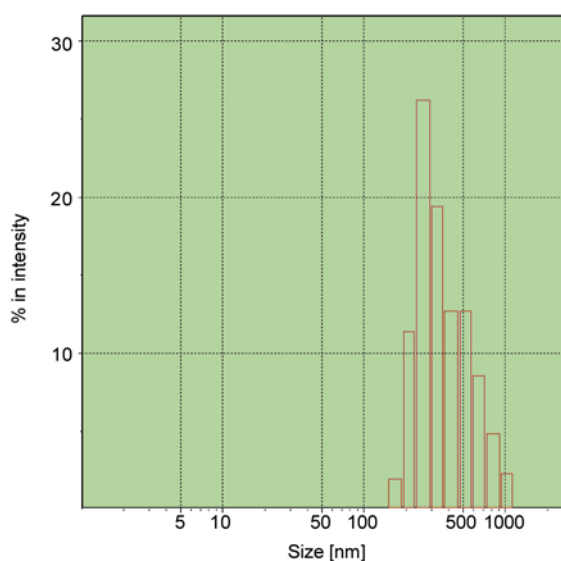


Figure 3. The swollen size of the microgels by dynamic light scattering measurements

mined by dynamic light scattering. The reactive microgels contain hydroxymethyl groups, which were introduced into the microgel particles by using NMA as a functional monomer. The schematic illustration is shown in Figure 1. The hydroxymethyl groups can further react with other active groups such as amide groups and hydroxymethyl groups themselves at suitable temperature [13, 24]. The schematic illustration of preparing MC hydrogels by post-crosslinking is proposed in Figure 1a. The reactive microgels containing hydroxymethyl groups act as potential post-crosslinking agents. The post-crosslinking reaction can occur between the hydroxymethyl groups and the functional groups of the polymer linear chains.

The composite polymer with embedded reactive microgels was prepared by solution polymerization. Reactive microgels containing hydroxymethyl groups were uniformly dispersed in the AM and AMPS solutions before polymerization. As shown in Table 1, the formation of MC hydrogels by direct heating the as-prepared composite polymer strongly depends on the heating temperature and time. The as-prepared composite polymer is still soluble when it is heated at 90°C less than 2 h. When the composite polymer is heated at 90°C for more than 2 h, it cannot dissolve in large excess water but swells in water and shows equilibrium swelling behavior. It suggests that the MC hydrogels are formed. As shown in Table 1, when the heating temperature decreases, it requires a longer heating time such as more than 3 h at 80°C to form hydrogels. It shows that the crosslinking reaction occurred more easily at high temperature for the as-prepared composite polymers.

In order to investigate the action of the reactive microgels, AM and AMPS copolymer without microgels was also prepared by solution polymerization under the same experimental conditions. As shown in Table 1, using the same heating time 5 h and the same temperature 90°C for the as-prepared AM and AMPS copolymer, which is named P-90-5h, the polymer fails to form a hydrogel and is still soluble. Compared with the composite polymer, the AM and AMPS copolymer is lacking of functional hydroxymethyl groups because it does not contain the reactive microgels. It indicates that the reactions of hydroxymethyl groups are the direct cause of the above MC hydrogel formation and the MC hydro-

Table 1. The conditions for MC hydrogel preparation and the properties of MC hydrogels

Polymer and heating conditions for hydrogels	Swelling ratio [g/g]	Degree of hydrolysis [%]	Tensile strength [kPa]	Elongation [%]	Water content for test [%]	Equilibrium water content [%]	0.1 mol/l NaOH
P-90-5h ^a	soluble	–	–	–	–	–	–
MC-90-2h ^b	1200	6.1	20	no precise	90	99.92	soluble
MC-90-3h	1050	6.6	27	790	90	99.90	soluble
MC-90-4h	880	7.3	32	960	90	99.89	soluble
MC-90-5h	1150	13.4	31	970	90	99.91	soluble
MC-99-10min-90-4h	900	–	21 (bubbles)	750	90	99.89	soluble
MC-80-4h	1100	–	16	no precise	90	99.91	soluble
MC58%-90-3h ^c	540	–	107	518	90	99.81	insoluble
MC50%-90-3h	390	–	130	503	90	99.74	insoluble
MC45%-90-3h	260	–	135	347	90	99.62	insoluble
MC40%-90-3h	105	–	105	190	90	99.05	insoluble
MC30%-90-3h	22	–	69	51	90	95.45	insoluble
P30%-90-3h	insoluble	–	brittle	brittle	–	–	insoluble

^aP-90-5h: The AM and AMPS copolymer without microgels is heated at 90°C for 5 h. AM and AMPS copolymer and composite polymer matrix has the same AM/AMPS ratio.

^bMC-90-2h: The as-prepared composite polymer with 75% water content is heated at 90°C for 2 h.

^cMC58%-90-3h: After the composite polymer is evaporated to 58% water content at ambient conditions, it is heated at 90°C for 3 h.

gels are crosslinked by microgel particles. Hydroxymethyl groups can form covalent bonds with amide groups [13] and hydrogen bonds with C=O ester groups of amide (or carboxyl in case of hydrolysis). Either hydrogen bonds or covalent bonds between the hydroxymethyl groups and the amide groups of linear chains in the composite polymer can lead to crosslinking reaction for MC hydrogel formation as illustrated in Figure 1. To determine the hydrogen bonds or the covalent bonds crosslinking for forming the MC hydrogels, the swelling properties of the hydrogels in the 0.1 mol/l sodium hydroxide solution was investigated [11]. As shown in Table 1, no matter how long heating for the as-prepared composite polymers at 90°C, the hydrogels are always soluble in the sodium hydroxide solution. Therefore, it is mainly due to the hydrogen bonds crosslinking rather than the covalent bonds crosslinking for forming the MC hydrogels.

The swelling character of the MC hydrogels from the as-prepared composite polymers were also investigated. As shown in Table 1, the swelling ratio decreases from 1200 to 880 when the heating time increases from 2 to 4 h. Because the crosslinks of MC hydrogels are not points but nanoparticles, the swelling ratio of the MC hydrogels depends on the degree of crosslinks between microgels and the hydrogel matrix. According to the swelling theory [25], the hydrogel swelling ratio is inversely related to the crosslinking density. It indicates that the longer the reaction time, the more crosslinked bonds between the polymer matrix and the microgels are formed. However, when the heating time increases from 4 to 5 h, the swelling ratio has a sudden increase from 880 to 1150. This is inconsistent with the above crosslinking bonds forming character. Ionic carboxyl groups can be formed under high temperature because of the hydrolysis of amide groups. As shown in Table 1, the degree of hydrolysis of the amide groups increases from 7.3 to 13.4% when the heating time increases from 4 to 5 h at 90°C. However, more carboxyl groups in the MC hydrogel hardly can significantly increase the swelling ratio. Increase of swelling ratio can be, probably, due to the self-reaction of methylol groups, as longer times at elevated temperature result in less crosslink degree of MC gels.

Mechanical properties were performed on the MC hydrogels with 90% water content. As shown in Table 1, for the above MC hydrogels from the as-prepared composite polymers, both the heating temperature and heating time influence the mechanical properties. The tensile strength increases as the heating temperature increases from 80 to 90°C. However, the tensile strength decreases as the temperature increases sequentially to 99°C, because large numbers of bubbles generated in the hydrogel. The appropriate heating conditions for high tensile strength are 90°C and 4 h. The tensile stress–strain curve of the MC-90-4h hydrogel is shown in Figure 4. It has a high elongation of 960% and a high tensile strength of 32 kPa, which is much higher than that of the conventional *N*-isopropylacrylamide hydrogels (tensile strength of 8–9 kPa and elongation of 20–50%) [9] or conventional AM hydrogels (tensile strength of 14 kPa and elongation of 35%) [26]. The excellent mechanical properties are attributed to the unique structure that the hydrogels are crosslinked by rubber microgels. However, the tensile strength is lower than that of the MC hydrogels crosslinked by covalent C–C bonds reported by our groups [13]. As described above, the MC hydrogels by heating the as-prepared composite polymers are crosslinked by hydrogen bonds. This is consistent with the fact that hydrogen bonds are weaker than the covalent bonds. It suggests that the covalent bond crosslinking will benefit to improve the mechanical properties of MC hydrogels.

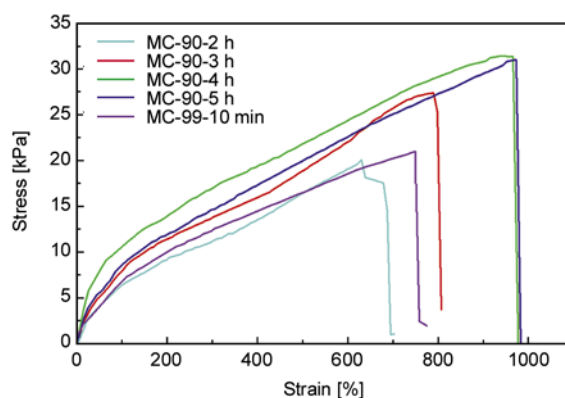


Figure 4. Stress–strain curves of the MC hydrogels at different heating conditions by heating the as-prepared composite polymers. (All hydrogel samples used for test has 90% water content.)

3.2. Effect of polymer water content on the MC hydrogels prepared by partly evaporated composite polymers

When NMA was used as an efficient crosslinking agent, covalent crosslinking bonds could be formed by thermal activation at around 110°C after water was evaporated in the acrylate latex films [27–29]. After water was completely evaporated to form drying films, covalent crosslinking bonds could also be formed under ambient conditions [20]. It is suggested that decreasing the polymer water content is beneficial to the covalent bond formation when NMA is used as a crosslinking agent. When polymer water content decreases, the equilibrium water content decreases as shown in Table 1, which indicates the hydrogel has more crosslinking density. The as-prepared composite polymer has 75% water content. As described above, the hydrogels cannot form covalent crosslinking bonds between the microgels and the polymer matrix by directly heating the as-prepared composite polymer. Considering the influence of the water content on the covalent bond formation, partly evaporated composite polymer was used to prepare MC hydrogels.

First, natural drying polymer with near equilibrium water content (about 30%) in natural environment was used. For MC30%–90–3h hydrogels, after the polymer was evaporated to 30% water content, it was heated at 90°C for 3 h. As shown in Table 1, it is insoluble and has low swelling ratio (about 22). It shows that the hydrogel is formed and has high crosslinking density. However, the hydrogel was very brittle and non-elastic. The tensile strength could not easily be obtained because it was difficult to clamp the hydrogel tightly enough for tensile tests and often broke before obtaining precise mechanical data. As shown in Table 1, although the tensile strength can reach 69 kPa, the elongation at break is only about 51% which is similar to the conventional hydrogel [9] and much lower than that of MC hydrogels prepared by the as-prepared composite polymers. As shown in Table 1, this hydrogel is insoluble in 0.1 mol/l sodium hydroxide solutions. It indicates that covalent crosslinking bonds are formed in the above hydrogels. In order to investigate the reactions between the linear chains in the polymer matrix, the AM/AMPS polymer with the same water content (30%) and heating conditions (90°C and 3 h) as the above composite polymer was

investigated, which is named P30%–90–3h. For P30%–90–3h polymers, it is also insoluble in 0.1 mol/l sodium hydroxide solutions. It suggests that covalent crosslinking bonds occur between the linear poly(AM co AMPS) chains at 90°C and 3 h for polymer with 30% water content. Therefore, for MC30%–90–3h, the hydrogel matrix between microgels also has crosslinking network structure similar to conventional hydrogels rather than linear chains. NC hydrogels with excellent mechanical properties cannot be obtained when the hydrogel matrix has crosslinked structure by adding *N,N'*-methylenebisacrylamide [6]. For MC30%–90–3h, excessive crosslinking of the linear polymer chains also form crosslinked hydrogel matrix causes the weak mechanical properties of the MC hydrogels.

As described above, the hydrogels cannot form covalent crosslinking bonds by heating the as-prepared composite polymer. However, the excessive drying of composite polymer will lead to conventional hydrogels with weak mechanical properties. That is, the polymer water content directly affects the hydrogel properties. For MC58%–90–3h, after the composite polymer was evaporated to 58% water content, it was heated at 90°C for 3 h. As shown in Table 1, the MC hydrogels are formed and their swelling ratio is 540. They also cannot dissolve in 0.1 mol/l sodium hydroxide solution. This MC hydrogels have excellent mechanical properties (Figure 5). It could withstand high levels of deforma-

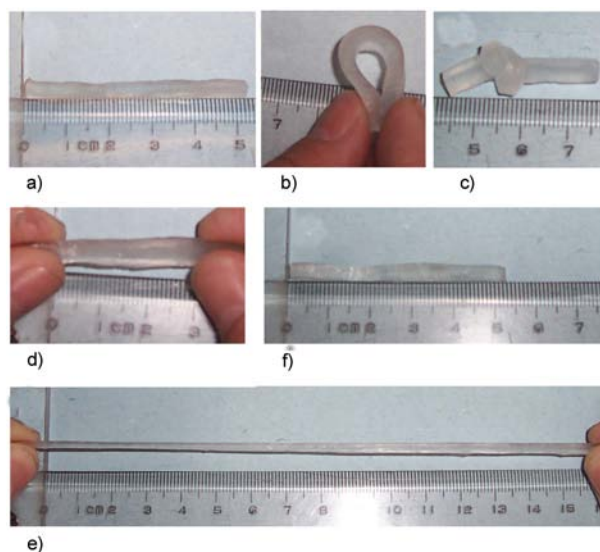


Figure 5. Photographs demonstrated the mechanical properties of MC58%–90–3h hydrogels. (a) and (d) original length, (b) bending, (c) knotting, (e) elongation, (f) recovered after elongation

tion such as bending, torsion, knotting, and elongation. When it was allowed to recover after elongation, it could recover its original length. As shown in Table 1, it has a high elongation of 518%, and high tensile strength of 107 kPa. This tensile strength is close to that of the NC hydrogels [6] and much higher than that of the hydrogels prepared by heating the as-prepared polymers or 30% water content polymers.

As the stress–strain curve shown in Figure 6 and Table 1, the tensile strength increases first and then decreases as polymer water content decreases. At 45% water content, the tensile strength can reach 135 kPa. However, the elongation always decreases as water content decreases. The composite polymer contains microgel and polymer matrix. For MC hydrogels, the crosslinkers are nanoparticles and the hydrogel matrix consists of linear polymer chains. This is different from the reported nanocomposite hydrogels that contain crosslinked hydrogel matrix by *N,N'*-methylenebisacrylamide [30, 31]. Our groups reported that the strength of composite hydrogels with network hydrogel matrix is much lower than that of the MC hydrogels with linear hydrogel matrix [13]. The linear chains for hydrogel matrix between the particles can improve the mechanical properties of the composite hydrogels. For this reason, the mechanical properties of crosslinked hydrogels depend on the matrix, the microgels and the degree of crosslinks between the matrix and microgels. As the polymer water content decreases, the polymer chain length between the microgels decreases because the distances between the microgels decrease [6]. Since the decrease of

distance between microgels during the synthesis is supposed to cause the higher crosslink degree of MC hydrogels, which leads to the decrease of the tensile elongation. As polymer water content decreases, the more covalent bond formation between the microgel and matrix will lead to higher tensile strength. However, with further decrease of polymer water content, the hydrogel matrix is also crosslinked and is similar to traditional hydrogels because of the reaction between the linear chains, which leads to the decreasing of the tensile strength. As described above, the tensile strength and the elongation can easily be adjusted by the composite polymer water content. As shown in Figure 6, for composite polymer with 50% water content, both tensile strength and elongation has high values with 130 kPa of tensile strength and 503% elongation.

4. Conclusions

The MC hydrogels have been successfully prepared by post-crosslinking method by heating the composite polymer. The MC hydrogels prepared at suitable conditions has excellent mechanical properties such as high elasticity, high tensile strength, and high elongation. This post-crosslinking method might open a new convenient method to manufacture soft and wet hydrogels with high mechanical properties.

For MC-90 hydrogels prepared by heating the as-prepared composite polymers with 75% water content, the formation of hydrogels and their properties strongly depend on the heating conditions. More than 2 h is required at 90°C. As temperature decreases, more time are required to form hydrogels. With the heated temperature increasing, the swelling ratio decreases first and then increases. However, it is soluble in 0.1 mol/l NaOH solution. Hydrogen bonds are the main crosslinking bonds. For MC-90-4h, the MC hydrogels have a tensile strength of 32 kPa, which is higher than that of the conventional hydrogels but lower than that of the MC hydrogels crosslinked by covalent bonds.

The mechanical properties and swelling ratio of MC hydrogels are influenced by the polymer water content. When the polymer water content is lower than 58%, the MC hydrogel cannot dissolve in 0.1 mol/l NaOH solutions. For MC hydrogels prepared by heating the partly evaporated composite polymers, as water content decreases, the tensile

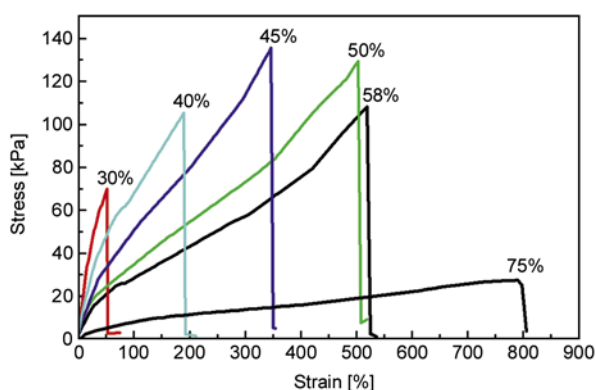


Figure 6. Stress–strain curves of MCx%–90–3h hydrogels. (x% making on the curves is the polymer water content for preparing hydrogels. All hydrogel samples used for test has 90% water content.)

strength increases first and then decreases. However, the elongation always decreases as water content decreases. The tensile strength and the elongation can be adjusted according to the polymer water content. When the composite polymer with 50% water content is heated at 90°C for 3 h, the hydrogels have high tensile strength of 130 kPa and tensile elongation of 503%. When the polymer water content is 30%, the hydrogels have low swelling ratio and weak mechanical properties similar to the conventional hydrogels.

Acknowledgements

This study was supported by Shandong Province Excellent Middle-Aged and Young Scientist Research Incentive Foundation (Grant No. 2008BS04008) and Independent Innovation Foundation of Shandong University (2010TS099).

References

- [1] Bohidar H. B., Dubin P., Osada Y.: Polymer gels: Fundamentals and applications. ACS Symposium Series, San Francisco (2002).
- [2] Wang Q., Mynar J. L., Yoshida M., Lee E., Lee M., Okuro K., Kinbara K., Aida T.: High-water-content mouldable hydrogels by mixing clay and a dendritic molecular binder. *Nature*, **463**, 339–343 (2010). DOI: [10.1038/nature08693](https://doi.org/10.1038/nature08693)
- [3] Okumura Y., Ito K.: The polyrotaxane gel: A topological gel by figure-of-eight cross-links. *Advanced Materials*, **13**, 485–487 (2001). DOI: [10.1002/1521-4095\(200104\)13:7<485::AID-ADMA485>3.0.CO;2-T](https://doi.org/10.1002/1521-4095(200104)13:7<485::AID-ADMA485>3.0.CO;2-T)
- [4] Gong J. P., Katsuyama Y., Kurokawa T., Osada Y.: Double-network hydrogels with extremely high mechanical strength. *Advanced Materials*, **15**, 1155–1158 (2003). DOI: [10.1002/adma.200304907](https://doi.org/10.1002/adma.200304907)
- [5] Webber R. E., Creton C., Brown H. R., Gong J. P.: Large strain hysteresis and mullins effect of tough double-network hydrogels. *Macromolecules*, **40**, 2919–2927 (2007). DOI: [10.1021/ma062924y](https://doi.org/10.1021/ma062924y)
- [6] Haraguchi K., Takehisa T.: Nanocomposite hydrogels: A unique organic–inorganic network structure with extraordinary mechanical, optical, and swelling/deswelling properties. *Advanced Materials*, **14**, 1120–1124 (2002). DOI: [10.1002/1521-4095\(20020816\)14:16<1120::AID-ADMA1120>3.0.CO;2-9](https://doi.org/10.1002/1521-4095(20020816)14:16<1120::AID-ADMA1120>3.0.CO;2-9)
- [7] Haraguchi K., Farnworth R., Ohbayashi A., Takehisa T.: Compositional effects on mechanical properties of nanocomposite hydrogels composed of poly(N,N-dimethylacrylamide) and clay. *Macromolecules*, **36**, 5732–5741 (2003). DOI: [10.1021/ma034366i](https://doi.org/10.1021/ma034366i)
- [8] Haraguchi K., Takehisa T., Fan S.: Effects of clay content on the properties of nanocomposite hydrogels composed of poly(N-isopropylacrylamide) and clay. *Macromolecules*, **35**, 10162–10171 (2002). DOI: [10.1021/ma021301r](https://doi.org/10.1021/ma021301r)
- [9] Haraguchi K., Li H.-J.: Mechanical properties and structure of polymer-clay nanocomposite gels with high clay content. *Macromolecules*, **39**, 1898–1905 (2006). DOI: [10.1021/ma052468y](https://doi.org/10.1021/ma052468y)
- [10] Tanaka Y., Gong J. P., Osada Y.: Novel hydrogels with excellent mechanical performance. *Progress in Polymer Science*, **30**, 1–9 (2005). DOI: [10.1016/j.progpolymsci.2004.11.003](https://doi.org/10.1016/j.progpolymsci.2004.11.003)
- [11] Huang T., Xu H. G., Jiao K. X., Zhu L. P., Brown H. R., Wang H. L.: A novel hydrogel with high mechanical strength: A macromolecular microsphere composite hydrogel. *Advanced Materials*, **19**, 1622–1626 (2007). DOI: [10.1002/adma.200602533](https://doi.org/10.1002/adma.200602533)
- [12] Lu X., Hu Z., Gao J.: Synthesis and light scattering study of hydroxypropyl cellulose microgels. *Macromolecules*, **33**, 8698–8702 (2000). DOI: [10.1021/ma000776k](https://doi.org/10.1021/ma000776k)
- [13] Qin X. P., Zhao F., Liu Y. K., Wang H. Y., Feng S. Y.: High mechanical strength hydrogels preparation using hydrophilic reactive microgels as crosslinking agents. *Colloid and Polymer Science*, **287**, 621–625 (2009). DOI: [10.1007/s00396-009-2018-z](https://doi.org/10.1007/s00396-009-2018-z)
- [14] Wu Y. T., Zhou Z., Fan Q. Q., Chen L., Zhu M. F.: Facile *in-situ* fabrication of novel organic nanoparticle hydrogels with excellent mechanical properties. *Journal of Materials Chemistry*, **19**, 7340–7346 (2009). DOI: [10.1039/b909125d](https://doi.org/10.1039/b909125d)
- [15] Schexnailder P., Schmidt G.: Nanocomposite polymer hydrogels. *Colloid and Polymer Science*, **287**, 1–11 (2009). DOI: [10.1007/s00396-008-1949-0](https://doi.org/10.1007/s00396-008-1949-0)
- [16] Valette L., Pascault J.-P., Magny B.: Use of acrylic functionalized (meth)acrylic cross-linked polymer microparticles in photopolymerized acrylic films. *Macromolecular Materials and Engineering*, **288**, 642–657 (2003). DOI: [10.1002/mame.200300012](https://doi.org/10.1002/mame.200300012)
- [17] Valette L., Pascault J.-P., Magny B.: Use of functional (meth)acrylic cross-linked polymer microparticles as toughening agents for epoxy/diamine thermosets. *Macromolecular Materials and Engineering*, **288**, 867–874 (2003). DOI: [10.1002/mame.200300041](https://doi.org/10.1002/mame.200300041)
- [18] Liu H. Q., Zhen M., Wu R. H.: Ionic-strength- and pH-responsive poly[acrylamide-*co*-(maleic acid)] hydrogel nanofibers. *Macromolecular Chemistry and Physics*, **208**, 874–880 (2007). DOI: [10.1002/macp.200600632](https://doi.org/10.1002/macp.200600632)

- [19] Abbas L., Bouquey M., Flat J. J., Muller R.: New method for post-processing crosslinking reaction. *European Polymer Journal*, **44**, 1238–1246 (2008). DOI: [10.1016/j.eurpolymj.2008.01.018](https://doi.org/10.1016/j.eurpolymj.2008.01.018)
- [20] Zhou J., Wang G., Marquez M., Hu Z.: The formation of crystalline hydrogel films by self-crosslinking microgels. *Soft Matter*, **5**, 820–826 (2009). DOI: [10.1039/b814830a](https://doi.org/10.1039/b814830a)
- [21] Zhang W., Liu Y., Zhu M., Zhang Y., Liu X. L., Jiang Y. M., Chen Y. M., Kuckling D., Adler H.-J. P.: Surprising conversion of nanocomposite hydrogels with high mechanical strength by posttreatment: From a low swelling ratio to an ultrahigh swelling ratio. *Journal of Polymer Science Part A: Polymer Chemistry*, **44**, 6640–6645 (2006). DOI: [10.1002/pola.21749](https://doi.org/10.1002/pola.21749)
- [22] Fong D. W., Kowalski D. J.: An investigation of the crosslinking of polyacrylamide with formaldehyde using ¹³C nuclear magnetic resonance spectroscopy. *Journal of Polymer Science Part A: Polymer Chemistry*, **31**, 1625–1627 (1993). DOI: [10.1002/pola.1993.080310633](https://doi.org/10.1002/pola.1993.080310633)
- [23] Liu X., Xiang S., Yue Y., Su X., Zhang W., Song C., Wang P.: Engineering particle technology preparation of poly(acrylamide-co-acrylic acid) aqueous latex dispersions using anionic polyelectrolyte as stabilizer. *Colloids and Surfaces A: Physicochemical and Engineering Aspects*, **311**, 131–139 (2007). DOI: [10.1016/j.colsurfa.2007.06.007](https://doi.org/10.1016/j.colsurfa.2007.06.007)
- [24] Lu S. J., Yao K., Lin S., Cao D., Chen Y.: Study on preparation and thickening efficiency of an inverse emulsion of anionic starch-graft-polyacrylamide. *Starch/Stärke*, **55**, 518–523 (2003). DOI: [10.1002/star.200300166](https://doi.org/10.1002/star.200300166)
- [25] Flory P. J.: *Principles of polymer chemistry*. Cornell University Press, New York (1953).
- [26] Zhu M. F., Liu Y., Sun B., Zhang W., Liu X. L., Yu H., Zhang Y., Kuckling D., Adler H. J. P.: A novel highly resilient nanocomposite hydrogel with low hysteresis and ultrahigh elongation. *Macromolecular Rapid Communication*, **27**, 1023–1028 (2006). DOI: [10.1002/marc.200600159](https://doi.org/10.1002/marc.200600159)
- [27] Chen Y., Zhang C., Wang Y., Cheng S., Chen P.: Study of self-crosslinking acrylate latex containing fluorine. *Journal of Applied Polymer Science*, **90**, 3609–3616 (2003). DOI: [10.1002/app.13087](https://doi.org/10.1002/app.13087)
- [28] Chen S.-I., Sheu Y.-L., Sheu J.-L., Lee C.-T., Lin J. S.: Morphology of perfluoroalkylacrylate/stearyl methacrylate polymers and their effect on water/oil repellency. *Journal of Applied Polymer Science*, **63**, 903–909 (1997). DOI: [10.1002/\(SICI\)1097-4628\(19970214\)63:7<903::AID-APP10>3.0.CO;2-S](https://doi.org/10.1002/(SICI)1097-4628(19970214)63:7<903::AID-APP10>3.0.CO;2-S)
- [29] Wyss A., Von Stockar U., Marison I. W.: Production and characterization of liquid-core capsules made from cross-linked acrylamide copolymers for biotechnological applications. *Biotechnology and Bioengineering*, **86**, 563–572 (2004). DOI: [10.1002/bit.20050](https://doi.org/10.1002/bit.20050)
- [30] Musch J., Schneider S., Lindner P., Richtering W.: Unperturbed volume transition of thermosensitive poly-(N-isopropylacrylamide) microgel particles embedded in a hydrogel matrix. *Journal of Physical Chemistry B*, **112**, 6309–6314 (2008). DOI: [10.1021/jp711939v](https://doi.org/10.1021/jp711939v)
- [31] Salvati A., Söderman O., Lynch I.: Plum-pudding gels as a platform for drug delivery: Understanding the effects of the different components on the diffusion behavior of solutes. *Journal of Physical Chemistry B*, **111**, 7367–7376 (2007). DOI: [10.1021/jp069051u](https://doi.org/10.1021/jp069051u)

Synthesis and characterization of poly(vinyl alcohol) proton exchange membranes modified with 4,4-diaminodiphenylether-2,2-disulfonic acid

M. S. Boroglu^{1*}, S. Cavus¹, I. Boz¹, A. Ata²

¹Istanbul University, Faculty of Engineering, Chemical Engineering Department, Avcilar, 34320, Istanbul, Turkey

²Gebze Institute of Technology, Materials Science and Engineering, Gebze, Kocaeli, Turkey

Received 24 September 2010; accepted in revised form 10 December 2010

Abstract. A proton-exchange membrane for a direct methanol fuel cell was prepared by modifying the chemical structure of poly(vinyl alcohol) (PVA) by means of sulfonation. We report the synthesis of a new proton-conducting polymer membrane with poly (vinyl alcohol) and diamine-containing organic molecules immobilized to PVA. The sulfonation was carried out by using 4,4-diaminodiphenyl ether-2,2-disulfonic acid (ODADS). A sulfonated diamine monomer, ODADS, was successfully synthesized by direct sulfonation of a commercially available diamine, 4,4-diaminodiphenyl ether (ODA), using fuming sulfuric acid as the sulfonating reagent. The chemical structure and thermal stability of the sulfonated PVA were studied by using FTIR and thermogravimetric analysis techniques, respectively. The proton conductivities of membranes were investigated as a function of ODADS content. The thermal decomposition of PVA-ODADS membranes started at 220°C. Differential scanning calorimetry (DSC) results indicated the homogeneity of the blends. Proton conductivity values of the sulfonated PVA membranes ranged between 8.25 and 16.53 mS/cm and the conductivities of PVA-ODADS membranes increased with the increasing ODADS content.

Keywords: polymer membranes, poly(vinyl alcohol), sulfonation, polymer electrolyte membrane, proton conductivity

1. Introduction

Proton-conducting polymer electrolytes have been given much attention due to their possible applications in electrochemical devices such as fuel cells, humidity and gas sensors, capacitors, and electrochemical displays that work from subambient to moderately high temperatures. Direct methanol fuel cells (DMFCs), in particular, employing polymer electrolyte membranes are one of the most attractive power sources for a variety of applications [1]. The most commonly-used polymer for electrolyte membranes is the perfluorinated ionomer based polymers known by its trade name, Nafion. Nafion developed by DuPont evoked the greatest interest because of its combined chemical, electrochemical,

and mechanical stabilities with high proton conductivity ($\sim 0.1 \text{ S}\cdot\text{cm}^{-1}$) at ambient temperature [2]. However, this still limits the wide applications due to its high cost, high methanol permeability ($\sim 10^{-6} \text{ cm}^2/\text{s}$) and difficulty in synthesis and processing [3, 4]. The high methanol permeability allows the undesired transport of methanol from the anode side of the fuel cell, through the membrane, to the cathode side, a phenomenon known as methanol crossover. As a consequence, excessive methanol permeability of any polymer electrolyte membrane (PEM) leads to an unacceptable decrease in cell performance [4, 5]. To address the problem of methanol crossover, numerous membranes as alternatives to Nafion have been developed and

*Corresponding author, e-mail: mehtap@istanbul.edu.tr

© BME-PT

studied. These studies include Nafion-based composite membranes [6], sulfonated poly (ether ether) ketone [7], sulfonated polyimide [8], polybenzimidazole [9], and sulfonated polyphosphazene [10] and sulfonated poly(vinyl alcohol) (PVA) [4, 11]. Additionally, organic/inorganic hybrid membranes have been investigated, motivated by the potential for inorganic particles which can provide a physical barrier against methanol crossover while simultaneously improving mechanical and thermal stability [12, 13]. Among the materials investigated, poly (vinyl alcohol) (PVA) is on the forefront due to its good mechanical properties, chemical stability, low cost, film forming ability, high hydrophilic behavior [14, 15]. Cussler and co-workers [16] reported that the PVA membranes employed in pervaporation process were much better methanol barriers than Nafion membrane. However, PVA membranes are poor proton conductors as compared with Nafion membrane because the PVA itself does not have any negative charged ions, such as, carboxylic and sulfonic acid groups. Therefore, PVA has to be modified to induce proton conductivity. Shao *et al.* [17] developed a membrane for DMFC by coating Nafion with PVA. Methanol resistance of the membrane increased at the expense of its proton conductivity. In addition, interfacial adhesion between the two polymeric phases has yet to be improved. Here, we have taken the view that the PVA membranes could be used as a PEM in fuel cell applications if the negative ions are held within their structure.

In this work, we report a new proton-conducting polymer membrane with poly (vinyl alcohol) and diamine-containing organic molecules immobilized to PVA to analyze the proton conductivity, methanol permeability, and physical properties. The introduction of sulfonic acid group to polymer structure was achieved by using a sulfonated diamine monomer, 4,4'-diaminodiphenyl ether-2,2'-disulfonic acid (ODADS). Sulfonation degree could be precisely controlled by regulating the weight ratio between PVA and ODADS during polymerization process. It is well-known that the control of sulfonation degree is very important because high sulfonation degree generally leads to high swelling degree or even dissolution of the membranes in water. On the other hand, low sulfonation degree generally results in poor proton conductivity, and therefore it seems that improving membrane stability and enhancing

proton conductivity are contradictory to each other. In this paper, a sulfonated diamine monomer, 4,4'-diaminodiphenyl ether-2,2'-disulfonic acid (ODADS), was synthesized, and a series of polymer blends were prepared. The introduction of negative charged ion group in the PVA membrane was achieved by the immobilization of ODADS. We compared diamine-immobilized PVA with the ones reported in open literature. The resultant membranes are thus capable of possessing all the required properties of a proton exchange membrane, namely, reasonable swelling, good mechanical strength, and low methanol permeability along with the high proton conductivity due to trapped ODADS chains in the PVA network. Physical properties, proton conductivity, and water stability of these membranes were also investigated.

2. Experimental

2.1. Materials

Poly(vinyl alcohol) (PVA, 99.5% hydrolyzed, $M_w = 72\,000$ g/mol) was supplied from Merck Co. Ltd., Hohenbrunn, Germany. 4,4'-diaminodiphenyl ether (ODA) of 98.2% purity was purchased from the Sigma-Aldrich Chemical Co. Ltd., St. Louis, USA and used as received. ODA was converted into 4,4'-diaminodiphenyl ether-2,2'-disulfonic acid (ODADS) using concentrated sulfuric acid (%95, Sigma-Aldrich Chemical Co. Ltd., Seelze, Germany) and fuming sulfuric acid (SO₃, 60%, Sigma-Aldrich Chemical Co. Ltd., Seelze, Germany). For the synthesis of sulfonated polymers, dimethylsulfoxide (DMSO, Merck Co. Ltd., Hohenbrunn, Germany) was used as solvent and used as received. Methanol was an analytical-grade solvent obtained from Sigma-Aldrich Chemical Co. Ltd., Seelze, Germany and the distilled water was also used in this study.

2.2. Synthesis of 4,4'-diaminodiphenyl ether-2,2'-disulfonic acid (ODADS)

A 100 ml three-neck flask equipped with a mechanical stirring device was charged 2.00 g (10.0 mmol) of 4,4'-diaminodiphenyl ether (ODA). The flask was cooled in an ice bath, and then 2.5 ml of concentrated (95–97%) sulfuric acid was slowly added while stirring. After ODA was completely dissolved, 3.5 ml of fuming (SO₃ 60%) sulfuric acid was slowly added to the flask. The reaction mixture was stirred at 0°C for 2 h and then slowly heated to

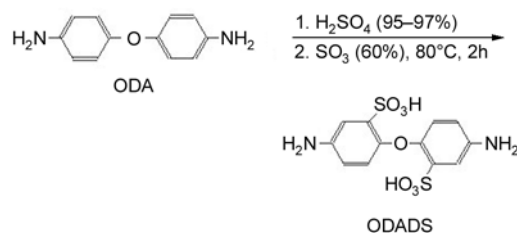


Figure 1. Synthetic pathway of 4,4'-diaminodiphenyl ether-2,2'-disulfonic acid (ODADS)

80°C and kept at this temperature for 2 h. After cooling to room temperature, the slurry was carefully poured into 30 g of crushed ice. The resulting white precipitate was filtered off and then redissolved in a sodium hydroxide solution. The basic solution was filtered, and the filtrate was acidified with concentrated hydrochloric acid. The solid was filtered off, washed with water and methanol successively, and dried at 80°C *in vacuo*. Then 3.05 g of white product was obtained giving a yield of 85%. Figure 1 and 2 show the reaction pathways of ODADS and FTIR spectra of ODADS.

FTIR spectroscopy was used to confirm the presence of the pendant –SO₃H group on the monomer structure. Sulfonation of ODADS is confirmed by the presence of two sharp peaks at 1104 and 1023 cm⁻¹, which are due to the aromatic SO₃H symmetric and asymmetric stretching vibrations,

respectively. The absorption bands at 3540 cm⁻¹ are attributed to the stretching vibration of the hydroxyl –OH group shown in Figures 2b. The presence of the benzene rings in ODA is established by the =C–H stretching vibration at 3050 cm⁻¹ and in the region of 1650–1400 cm⁻¹. There are bands recognized as vibrations in the plane of aromatic ring $\nu_{\text{C}_{\text{Ar}}\text{C}_{\text{Ar}}}$ (1467 cm⁻¹) and antisymmetric and symmetric deformation bands of NH₂ group (1517 cm⁻¹). The C–N stretching vibrations are located at 1365 cm⁻¹. The doublet of ν_{CCN} bands is observed at 914, 830 cm⁻¹, respectively [8, 18, 19].

2.3. Membrane preparation

10 wt% PVA solution was prepared by dissolving the preweighed amount of PVA in DMSO at 90°C for at least 6 h. PVA solutions were mixed with the various amounts of ODADS by the weight ratios of the PVA (5–30%) and then the mixtures were vigorously stirred at 80°C for 24 h. Then, PVA solution was cast onto a teflon sheet. The solvent was removed by evaporation at room temperature for 24 h and then the cast membranes were allowed to dry at 60°C for 24 h. Finally, the dry membranes were subjected to thermal treatment at 120°C. Membrane thickness was measured with probe using magnetic induction principle. Measurements were

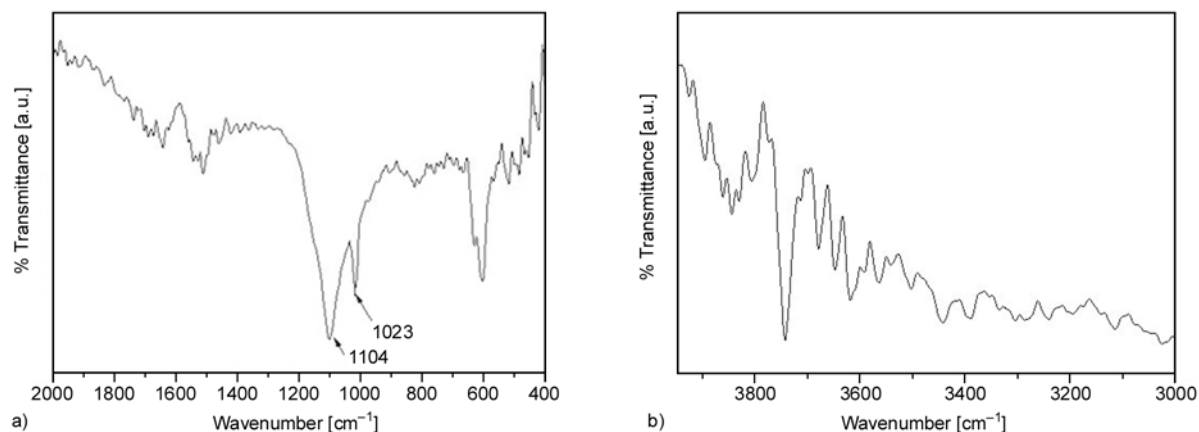


Figure 2. FTIR spectra of ODADS monomer a) at 2000–400 cm⁻¹ region, b) at 4000–3000 cm⁻¹ region

Table 1. Experimental conditions and maximum proton conductivities of polymers

Samples	ODADS/PVA [weight ratio]	% 5 W.L.	Residue % [750°C]	T _g [°C]	Maximum proton conductivity [mS/cm]	Methanol permeability [mol/(cm·s)]	Water uptake [%]
PVA-ODADS (T1)	5	73	3.04	71	4.24	1.27·10 ⁻¹¹	86.39
PVA-ODADS (T2)	10	69	8.15	89	8.25	7.70·10 ⁻¹⁰	98.65
PVA-ODADS (T3)	15	93	8.45	96	15.35	3.45·10 ⁻¹¹	83.77
PVA-ODADS (T4)	20	116	15.15	95	16.53	7.65·10 ⁻¹¹	69.94
PVA-ODADS (T5)	30	123	17.12	93	6.90	8.70·10 ⁻¹¹	45.18
Nafion 117	–	–	–	–	19.78	1.76·10 ⁻⁹	–

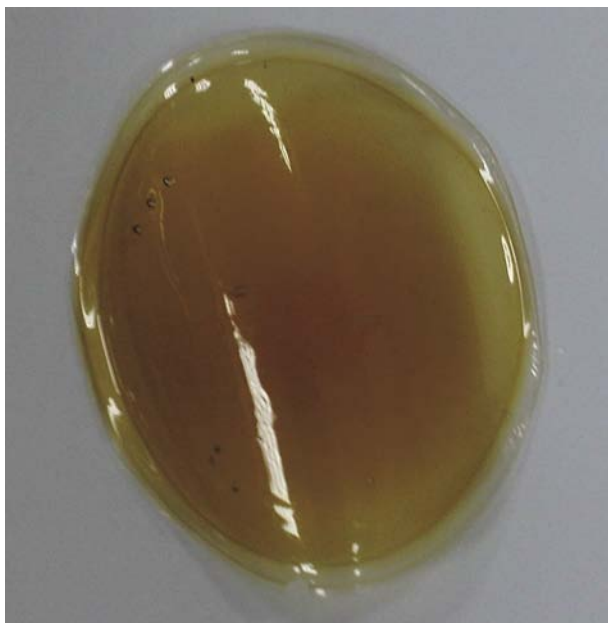


Figure 3. Homogeneous, transparent PVA-ODADS membrane

carried out with a Mega-Check FN coating thickness gauge (0–2000 μm), List Magnetic, Echterdingen, Germany. For each sample, at least 20 measurements were taken from various regions and average membrane thickness of $120 \pm 8 \mu\text{m}$ was obtained. The membranes were stored in deionized water after pretreatment in order to ensure equilibration prior to use in conductivity measurements. The experimental conditions used to prepare the polymer solutions and the nomenclatures used for each sample are shown in Table 1. Transparent, hygroscopic and free standing films (Figure 3) were obtained in all the samples.

2.4. Membrane characterization

To demonstrate the presence of immobilized diamine-containing organic molecules on the PVA membrane, membranes were examined by the Fourier transform infrared (FT-IR) spectra. IR spectra were recorded on a Bruker Alpha-P ATR spectrophotometer with a resolution of 4 cm^{-1} in the range of $400\text{--}4000 \text{ cm}^{-1}$.

Thermal degradation experiments were carried out in Shimadzu TGA-50 Thermogravimetric Analyzer. Thermal analyses were completed on thin films having an average mass of 15 mg. The samples ($\sim 10 \text{ mg}$) were heated from room temperature to 850°C under N_2 atmosphere at a heating rate of $10^\circ\text{C}/\text{min}$.

Glass transition temperatures were determined with Mettler-Toledo DSC 822. Test samples were heated from 25 to 250°C at a rate of $10^\circ\text{C} \cdot \text{min}^{-1}$ under nitrogen atmosphere in the first DSC cycle and then cooled from 250 to 25°C at the rate of $10^\circ\text{C} \cdot \text{min}^{-1}$, and finally subjected to the same procedure in the second cycle. The measurements were made under nitrogen gas with a flow rate of $20 \text{ cm}^3 \cdot \text{min}^{-1}$, up to 250°C . T_g of the sample was determined as the mid-point temperature of the transition region in the second heating cycle.

Methanol permeability was measured using our homemade test cell with a volume of 4 ml [20]. The cell was filled with 2 ml of methanol. Methanol vapor was in equilibrium with the liquid at the bottom of the cell. Methanol vapor diffused through the membrane, which was clamped between the mouth of glass and the cap with a hole on. The cap had a 0.84 cm diameter opening hole through which the methanol diffused into surrounding air. The weight loss caused by the diffusion of methanol through membrane was recorded as a function of time and the data were used for permeability calculations. Molar methanol flux (J) through a PVA-ODADS membranes was calculated using Equation (1). Nafion 112, with known permeability, was used as a reference. The methanol permeability of composite membranes (P) was calculated using molar flux (J) shown in Equation (2) [14]:

$$J = \frac{W \cdot l}{M_w \cdot A \cdot t} \quad (1)$$

$$\frac{J_1}{J_2} \cdot \frac{l_1}{l_2} = \frac{P_1}{P_2} \quad (2)$$

where J = flux, W = weight loss [g], l = thickness [cm], A = area [cm^2], t = time [s].

Thickness of the films does not change after adding with ODADS groups leading the cancellation of the thickness values (l) in Equation (2). Therefore, permeability is directly proportional to the molar flux. Samples dried in vacuum oven at 40°C for 48 h cut into 2 cm^2 squares and then each sample being weighed in the dry state before swelling in water at room temperature (20°C). Afterwards, samples were immersed in deionized water for at least 24 h, dabbed for removal of surface water, and then immediately weighed. Water uptake was calculated by the Equation (3):

$$W [\%] = \frac{W_{\text{wet}} - W_{\text{dry}}}{W_{\text{dry}}} \cdot 100 \quad (3)$$

Proton conductivities of the modified PVA membranes were measured by using a four-point probe technique. The conductivity of the membranes was measured by BT-1005 BekkTech Scanning DC Software. The membrane was cut into a 1 cm × 2 cm strip and immersed in the deionized water for 12 h prior to the measurement. For uniform water content in the membrane, the cell along with the sample was immersed in deionized water.

3. Results and discussion

3.1. FT-IR study

Figure 4 shows FTIR spectra of PVA and PVA modified with ODADS, respectively. From Figure 4, a broad peak at a wavenumber ranging between 3000 and 3400 cm^{-1} , representing the hydroxyl group of PVA, can be observed. In addition, a small sharp peak at 1720 cm^{-1} was noted. This small sharp peak is attributed to the presence of some residual vinyl acetate repeating units in the 99.5% hydrolyzed PVA molecules. After performing the sulfonation, the peaks at 1011–1045 cm^{-1} attributed to symmetric vibration of the sulfonic group [21]. Peaks at 1218–1270 cm^{-1} associate with the symmetric stretching vibration of the $-\text{SO}_3^-$ group. Also C–N stretching vibrations are located at 1320 and 837 cm^{-1} . Membranes have a peak at 1640 cm^{-1} due to amine NH_2 bending vibration. Intensity of the N–H bond

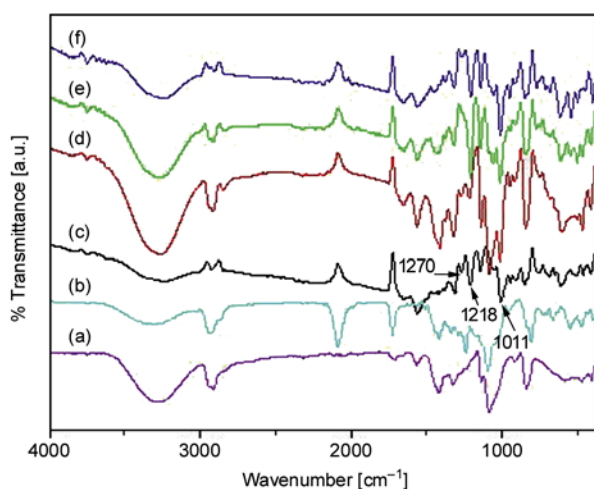


Figure 4. FT-IR spectra of a) PVA monomer, b) PVA-ODADS-5% (T1), c) PVA-ODADS-10% (T2), d) PVA-ODADS-15% (T3), e) PVA-ODADS-20% (T4), and f) PVA-ODADS-30% (T5) series polymers

increased with the ODADS content of the membrane. Additionally, the absorption band at 1640 cm^{-1} indicates the protonated ODADS from the free-nitrogen (unprotonated) side. These results suggest that the $-\text{SO}_3\text{H}$ group deprotonates by doping with ODADS and forms $-\text{SO}_3^-$ group. Our results also demonstrated that the proton conduction occurs by jumping of protons from a protonated ODADS to a non-protonated one, to sulfonic acid functional groups of PVA-ODADS [22]. These spectroscopically specific observations prove that ODADS participated in the PVA network.

3.2. Thermal analysis

Differential Scanning Calorimetry measurements were carried out by a heating-cooling-heating cycle, so-called the H–C–H procedure. The purpose of the first heating cycle was to remove any thermal history of the PVA composite membrane. The glass transition temperatures (T_g) of the PVA/ODADS membranes with various ODADS compositions (5–30 wt%) are listed in Table 1. The glass transition temperature of the pure PVA was reported to be near 85°C [23]. The immobilized membranes exhibited glass transition temperature (T_g) at slightly higher values than the pure PVA. For the samples with different ODADS contents, the glass transition temperature (T_g) appearing around 90°C, slightly shifted to higher temperature for higher ODADS content. The raise in T_g was possibly caused by the hydrogen bonding of the ODADS units which suppressed the segmental mobility of the polymers. Also as it is seen on Table 1, the existence of single T_g for all the samples indicates the homogeneity of the membranes.

In Figure 5, the thermal degradation profiles of PVA–ODADS membranes illustrated changing the ODADS contents and 5 wt% weight loss and the residual ashes at 750°C were also listed in Table 1. Here, it is found that the weight-loss profiles are very similar to each other but the onset temperatures of thermal degradation and the residual weight [%] at 750°C are different in all materials. PVA-ODADS membranes exhibited three weight loss stages at 50–140, 230–320 and 370–460°C followed by the final decomposition of the polymer that began around 460°C. As seen in Figure 5, for the PVA–ODADS membranes the first weight loss region (occurring between temperatures of $T = 50$ –

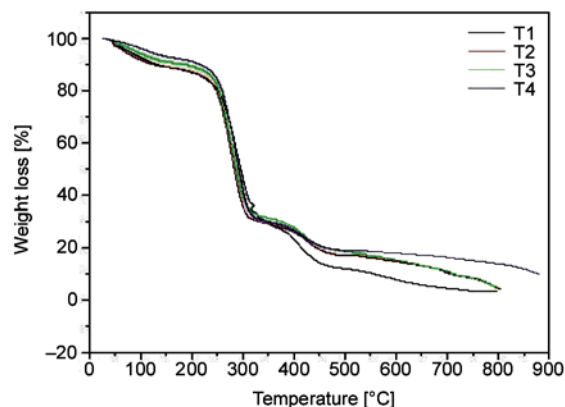


Figure 5. TG thermograms of PVA-ODADS membranes at a heating rate of 10°C/min in inert atmosphere

140°C) corresponds to the loss of water in membranes. The second weight loss region (occurring between temperatures of $T = 230\text{--}320^\circ\text{C}$) corresponds to the loss of sulfonic acid due to the desulfonation of sulfosuccinic acid. In the third weight loss region (at temperatures $> 370^\circ\text{C}$) the polymer residues were further degraded at $T = 370^\circ\text{C}$, which corresponds to the decomposition of the main chains of the PVA. The temperature corresponding to a 5 wt% weight loss in the course of thermoxidative degradation increased with increasing content of ODADS. It was possible to state that ODADS addition increased thermal stability of the structure about 50°C upwards. Additionally, as shown in Figure 5, an increase of the ODADS content leads to an increase of the residual char remaining at the final temperature (750°C). This indicates that the immobilization of PVA by ODADS is partially attributed to the improvement of the thermal stability of the PVA-ODADS membranes and, also in this study, we found that these types of membranes are stable up to 220°C without losing their mechanical strength and functional properties. TGA results did not provide enough information about the microstructure of final membranes. However, we can expect that the relative difference of weight loss observed in Figure 5 may be due to uniform immobilization of ODADS.

3.3. Methanol permeability

Methanol crossover is still an unresolved problem in direct methanol fuel cells, especially for portable applications where the current densities are already relatively low. Fuel crossover at high methanol concentrations from anode side to the cathode side

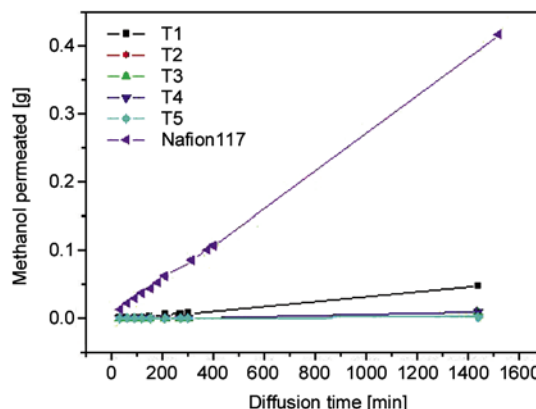


Figure 6. Mass flow of methanol through PVA-ODADS membranes

causes polarization losses. In this study, methanol permeability of the composite membranes was measured by simple homemade test cell similar to the study of Gasa *et al.* [24]. The cell is filled with 2 ml methanol and the mass flow is recorded as a function of time (Figure 6). Figure 6 shows the mass flow of methanol permeated through membranes in the cell, as a function of time. Here, the methanol permeation increased linearly with time. In addition to their attractive proton conductivity values, PVA-ODADS membranes also featured attractive methanol barrier properties. Table 1 showed methanol permeability values of blend membranes. For a comparison, methanol permeability of Nafion 117 was measured under the same experimental conditions, yielding a value of $1.76 \cdot 10^{-9}$ mol/(cm s). The methanol permeation value of blend membranes was appreciably small compared to that of Nafion 117. For PVA-ODADS membranes, the methanol permeability increased with ODADS content, due to an increased number of hydrophilic sulfonic acid groups attached to ODADS. Thus, ODADS content plays a key role in methanol permeability, indicating that the ODADS moieties may interfere with methanol permeation in some manner, while facilitating proton transport through the sulfonic acid groups.

3.4. Water uptake (WU)

Figure 7 presents the WU of the PVA-ODADS membranes plotted as a function of ODADS content in the polymer blend, respectively. Water uptake values of the membranes modified with ODADS are relatively high. This is probably due to the immobilization of ODADS in PVA might lead to more rigid

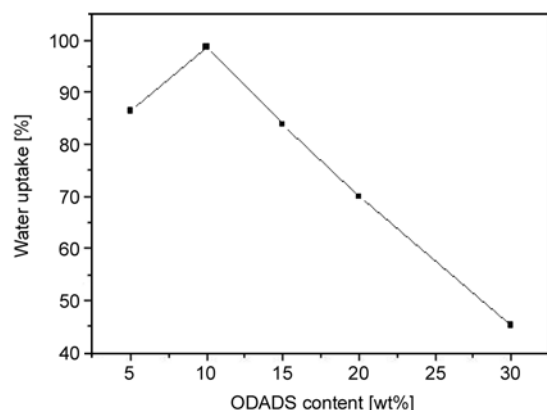


Figure 7. Water uptake versus ODADS content of the PVA/ODADS membrane

and compact polymer structure and resulted in a decrease in the free volume capable of containing water molecules. Also, some water-absorption sites of PVA-ODADS membrane were blocked with $-\text{SO}_3\text{H}$ groups. The blocking effect could also be attributed to the presence of $\text{SO}_3\text{H}/\text{PVA}$ interaction, which reduces the swelling ability of PVA in water.

3.5. Conductivity

The proton conductivity measurements of the membrane were carried out at a 100% RH as a function of ODADS content by using a four-point probe technique and the results are shown in Figure 8. The proton conductivities of the membranes measured at $T = 30^\circ\text{C}$ were in the range 10^{-3} to 10^{-2} S/cm. The conductivity of Nafion 117 measured with our test system is also included for comparison purposes. The membranes made of PVA-ODADS exhibited proton conductivities 4.24 and 16.53 mS/cm. The proton conductivity of blend membranes increased with the increase of ODADS content. The conductivities initially increased with the amount of ODADS,

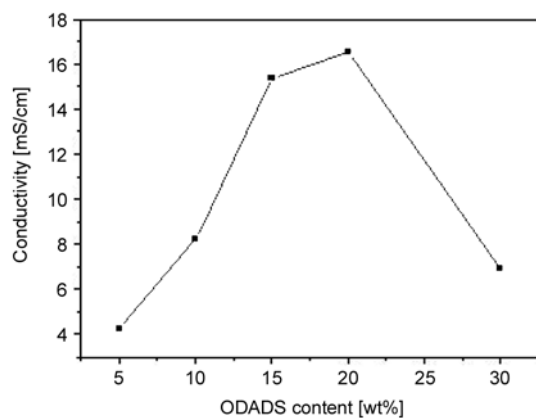


Figure 8. Proton conductivity as a function of ODADS content at 30°C

up to the maximum value of 16.53 mS/cm. After that, the proton conductivity of the PVA membranes decreased again as the amount of ODADS used was above 20%. The maximum proton conductivity value herein is comparable to that of the Nafion 117 membrane measured in this study (19.78 mS/cm). The initial increase in proton conductivity of the membrane can be ascribed to the greater content of sulfonic acid groups in the modified PVA molecules, which is responsible for conducting protons. However, the proton conductivity of a membrane is not only dependent on the degree of sulfonation of the polymer, it also changes with water uptake of the membrane. For example, it was reported [25] that the proton conductivity of the Nafion membrane decreased remarkably when the membrane was operated at a temperature above the boiling point of the water. This is because water molecules serve as the ‘vehicles’ for the transportation of the protons from anode to cathode [26]. In this study, the water uptake values of the sulfonated PVA membranes decreased with the amount of sulfonic acid added (Table 1) and so a decrease in proton conductivity with the amount of ODADS could be expected. Therefore, there should be an optimum value of the amount of ODADS used, in which the effect of the degree of sulfonation and the effect of water uptake on proton conductivities of the sulfonated PVA membranes are compromised. In this study, the optimum value of the amount of the ODADS is found to be 20% by weight. Beyond this value, the water uptake became the predominating factor affecting the proton conductivities of the membrane in negative manner.

Even though the proton conductivity value of the blend membranes was lower than that of Nafion. PVA-ODADS membranes showed quite low values of methanol permeability, it showed the high impact in the application of DMFC.

In general, proton conductive mechanism through these membranes is well known to occur by two routes [26, 27]. The first route is hopping mechanism, also known as the Grotthuss model, wherein a proton is passed down a chain of water molecules. The protons are transferred from one vehicle to the other by hydrogen bonds (proton hopping). The second route is a vehicle mechanism, wherein a proton combines with solvent molecules, producing a complex like H_3O^+ or CH_3OH_2^+ . This complex

then diffuses intact. These two principal mechanisms essentially reflect the difference in nature of the hydrogen bond formed between the protonated species and their environment. In membranes which support strong hydrogen bonding, the Grotthuss mechanism is preferred; the vehicle mechanism is characteristic of species with weaker bonding [26]. The proton conductivity occurs by transport of larger complexes such as H_3O^+ , H_5O_2^+ , H_7O_3^+ or CH_3OH_2^+ or some similar methanol containing complex [27]. In addition, the protons of these complexes are transferred from one vehicle to another. Therefore, the proton conductive mechanism was occurring by two simultaneous routes.

Previously Seepunkai and Wootthikanokkhan [28] prepared sulfonated PVA by reacting the PVA with sulfoacetic acid and poly (acrylic acid). This PVA membrane exhibited a maximum proton conductivity of 6.35 mS/cm at 15% sulfoacetic acid content under hydrous condition. Kim *et al.* [29] prepared PVA/PAA/sulfosuccinic acid/silica hybrid membranes and reported that the maximum conductivity reached was approximately 8.0 mS/cm for PVA/PAA/SSA at 25°C. In this study, maximum proton conductivity of 16.53 mS/cm at 30°C was obtained for PVA-ODADS (T4) which is relatively better than PVA based polymers synthesized in the literature.

4. Conclusions

In the present work, a new proton-conducting polymer membrane with poly(vinyl alcohol) and diamine-containing sulfonic acid group immobilized to PVA was prepared and also evaluated as a potential polymer electrolyte membrane in direct methanol fuel cell applications. Especially, 4,4'-diaminodiphenyl ether-2,2'-disulfonic acid was effectively introduced as an immobilization agent and a donor of negative charged ion ($-\text{SO}_3\text{H}$) in the preparation of the PVA-ODADS membranes. Thermal stabilities of membranes were characterized by TGA and found that PVA-ODADS membranes were thermally stable up to 220°C. From differential scanning calorimetry T_g of the PVA membrane materials were found to have increased with the increasing of ODADS content. The proton conductivity of these materials increased with ODADS content. The PVA-ODADS materials exhibited maximum proton conductivity of 16.53 mS/cm at 30°C. Compared to the other

membranes, the PVA-ODADS containing 20% of ODADS showed high proton conductivity. The membranes made from PVA-ODADS also appeared to be good candidates for direct methanol fuel cells because of their low methanol permeability. The methanol permeability of values of membranes were much lower than that of the Nafion membrane.

References

- [1] Ludvigsson M., Lindgren J., Tegenfeldt J.: Crystallinity in cast Nafion. *Journal of the Electrochemical Society*, **147**, 1303–1305 (2000). DOI: [10.1149/1.1393354](https://doi.org/10.1149/1.1393354)
- [2] Qiao J., Hamaya T., Okada T.: New highly proton-conducting membrane poly(vinylpyrrolidone)(PVP) modified poly(vinyl alcohol)/2-acrylamido-2-methyl-1-propanesulfonic acid (PVA–PAMPS) for low temperature direct methanol fuel cells (DMFCs). *Polymer*, **46**, 10809–10816 (2005). DOI: [10.1016/j.polymer.2005.09.007](https://doi.org/10.1016/j.polymer.2005.09.007)
- [3] Chang Y-W., Wang E., Shin G., Han J-E., Mather P. T.: Poly(vinyl alcohol) (PVA)/sulfonated polyhedral oligosilsesquioxane (sPOSS) hybrid membranes for direct methanol fuel cell applications. *Polymers for Advanced Technologies*, **18**, 535–543 (2007). DOI: [10.1002/pat.913](https://doi.org/10.1002/pat.913)
- [4] Rhim J-W., Park H. B., Lee C-S., Jun J-H., Kim D. S., Lee Y. M.: Crosslinked poly(vinyl alcohol) membranes containing sulfonic acid group: Proton and methanol transport through membranes. *Journal of Membrane Science*, **238**, 143–151 (2004). DOI: [10.1016/j.memsci.2004.03.030](https://doi.org/10.1016/j.memsci.2004.03.030)
- [5] Barragán V. M., Ruiz-Bauzá C., Villaluenga J. P. G., Seoane B.: Transport of methanol and water through Nafion membranes. *Journal of Power Sources*, **130**, 22–29 (2004). DOI: [10.1016/j.jpowsour.2003.12.007](https://doi.org/10.1016/j.jpowsour.2003.12.007)
- [6] Dimitrova P., Friedrich K. A., Stimming U., Vogt V.: Modified Nafion[®]-based membranes for use in direct methanol fuel cells. *Solid State Ionics*, **150**, 115–122 (2002). DOI: [10.1016/S0167-2738\(02\)00267-9](https://doi.org/10.1016/S0167-2738(02)00267-9)
- [7] Li L., Zhang J., Wang Y. : Sulfonated poly(ether ether ketone) membranes for direct methanol fuel cell. *Journal of Membrane Science*, **226**, 159–167 (2003). DOI: [10.1016/j.memsci.2003.08.018](https://doi.org/10.1016/j.memsci.2003.08.018)
- [8] Fang J., Guo X., Harada S., Watari T., Tanaka K., Kita H., Okamoto K-I.: Novel sulfonated polyimides as polyelectrolytes for fuel cell application. 1. Synthesis, proton conductivity, and water stability of polyimides from 4,4'-diaminodiphenyl ether-2,2'-disulfonic acid. *Macromolecules*, **35**, 9022–9028 (2002). DOI: [10.1021/ma020005b](https://doi.org/10.1021/ma020005b)

- [9] Lobato J., Cañizares P., Rodrigo M. A., Linares J. J.: PBI-based polymer electrolyte membranes fuel cells: Temperature effects on cell performance and catalyst stability. *Electrochimica Acta*, **52**, 3910–3920 (2007). DOI: [10.1016/j.electacta.2006.11.014](https://doi.org/10.1016/j.electacta.2006.11.014)
- [10] Guo Q., Pinaturo P. N., Tang H., O'Connor S.: Sulfonated and crosslinked polyphosphazene-based proton-exchange membranes. *Journal of Membrane Science*, **154**, 175–181 (1999). DOI: [10.1016/S0376-7388\(98\)00282-8](https://doi.org/10.1016/S0376-7388(98)00282-8)
- [11] Kim D. S., Park H. B., Rhim J. W., Lee Y. M.: Preparation and characterization of crosslinked PVA/SiO₂ hybrid membranes containing sulfonic acid groups for direct methanol fuel cell applications. *Journal of Membrane Science*, **240**, 37–48 (2004). DOI: [10.1016/j.memsci.2004.04.010](https://doi.org/10.1016/j.memsci.2004.04.010)
- [12] Su Y-H., Liu Y-L., Sun Y-M., Lai J-Y., Guiver M. D., Gao Y.: Using silica nanoparticles for modifying sulfonated poly(phthalazinone ether ketone) membrane for direct methanol fuel cell: A significant improvement on cell performance. *Journal of Power Sources*, **155**, 111–117 (2006). DOI: [10.1016/j.jpowsour.2005.03.233](https://doi.org/10.1016/j.jpowsour.2005.03.233)
- [13] Manea C., Mulder M.: Characterization of polymer blends of polyethersulfone/sulfonated polysulfone and polyethersulfone/sulfonated polyetheretherketone for direct methanol fuel cell applications. *Journal of Membrane Science*, **206**, 443–453 (2002). DOI: [10.1016/S0376-7388\(01\)00787-6](https://doi.org/10.1016/S0376-7388(01)00787-6)
- [14] Lebrun L., Silva A. D., Metayer M.: Elaboration of ion-exchange membranes with semi-interpenetrating polymer networks containing poly(vinyl alcohol) as polymer matrix. *Journal of Applied Polymer Science*, **84**, 1572–1580 (2002). DOI: [10.1002/app.10420](https://doi.org/10.1002/app.10420)
- [15] Hirankumar G., Selvasekarapandian S., Bhuvaneshwari M. S., Baskaran R., Vijayakumar M.: AC impedance studies on proton conducting polymer electrolyte complexes (PVA + CH₃COONH₄). *Ionics*, **10**, 135–138 (2004). DOI: [10.1007/BF02410322](https://doi.org/10.1007/BF02410322)
- [16] Pivovar B. S., Wang Y., Cussler E. L.: Pervaporation membranes in direct methanol fuel cells. *Journal of Membrane Science*, **154**, 155–162 (1999). DOI: [10.1016/S0376-7388\(98\)00264-6](https://doi.org/10.1016/S0376-7388(98)00264-6)
- [17] Shao Z-G., Wang X., Hsing I-M.: Composite Nafion/polyvinyl alcohol membranes for the direct methanol fuel cell. *Journal of Membrane Science*, **210**, 147–153 (2002). DOI: [10.1016/S0376-7388\(02\)00386-1](https://doi.org/10.1016/S0376-7388(02)00386-1)
- [18] Watari T., Fang J., Tanaka K., Kita H., Okamoto K-I., Hirano T.: Synthesis, water stability and proton conductivity of novel sulfonated polyimides from 4,4'-bis(4-aminophenoxy)biphenyl-3,3'-disulfonic acid. *Journal of Membrane Science*, **230**, 111–120 (2004). DOI: [10.1016/j.memsci.2003.10.037](https://doi.org/10.1016/j.memsci.2003.10.037)
- [19] Park H. B., Lee C. H., Sohn J. Y., Lee Y. M., Freeman B. D., Kim H. J.: Effect of crosslinked chain length in sulfonated polyimide membranes on water sorption, proton conduction, and methanol permeation properties. *Journal of Membrane Science*, **285**, 432–443 (2006). DOI: [10.1016/j.memsci.2006.09.026](https://doi.org/10.1016/j.memsci.2006.09.026)
- [20] Sen U., Çelik S. Ü., Ata A., Bozkurt A.: Anhydrous proton conducting membranes for PEM fuel cells based on Nafion/azole composites. *International Journal of Hydrogen Energy*, **33**, 2808–2815 (2008). DOI: [10.1016/j.ijhydene.2008.03.007](https://doi.org/10.1016/j.ijhydene.2008.03.007)
- [21] Gruger A., Régis T., Schmatko P., Colomban P.: Nanostructure of Nafion® membranes at different states of hydration: An IR and Raman study. *Vibrational Spectroscopy*, **26**, 215–225 (2001). DOI: [10.1016/S0924-2031\(01\)00116-3](https://doi.org/10.1016/S0924-2031(01)00116-3)
- [22] Acar O., Sen U., Bozkurt A., Ata A.: Proton conducting membranes based on poly(2,5-benzimidazole) (ABPBI)-poly(vinylphosphonic acid) blends for fuel cells. *International Journal of Hydrogen Energy*, **34**, 2724–2730 (2009). DOI: [10.1016/j.ijhydene.2009.01.073](https://doi.org/10.1016/j.ijhydene.2009.01.073)
- [23] Wilkes C. E., Summers J. W., Daniels C. A., Berard M. T.: *PVC handbook*. Hanser, München (2005).
- [24] Gasa J. V., Weiss R. A., Shaw M. T.: Ionic crosslinking of ionomer polymer electrolyte membranes using barium cations. *Journal of Membrane Science*, **304**, 173–180 (2007). DOI: [10.1016/j.memsci.2007.07.031](https://doi.org/10.1016/j.memsci.2007.07.031)
- [25] Antonucci P. L., Aricó A. S., Creti P., Ramunni E., Antonucci V.: Investigation of a direct methanol fuel cell based on a composite Nafion®-silica electrolyte for high temperature operation. *Solid State Ionics*, **125**, 431–437 (1999). DOI: [10.1016/S0167-2738\(99\)00206-4](https://doi.org/10.1016/S0167-2738(99)00206-4)
- [26] Kreuer K-D.: Proton conductivity: Materials and applications. *Chemistry of Materials*, **8**, 610–641 (1998). DOI: [10.1021/cm950192a](https://doi.org/10.1021/cm950192a)
- [27] Pivovar B. S., Wang Y., Cussler E. L.: Pervaporation membranes in direct methanol fuel cells. *Journal of Membrane Science*, **154**, 155–162 (1999). DOI: [10.1016/S0376-7388\(98\)00264-6](https://doi.org/10.1016/S0376-7388(98)00264-6)
- [28] Seepunkai N., Wootthikanokkhan J.: Proton conductivity and methanol permeability of sulfonated poly(vinyl alcohol) membranes modified by using sulfoacetic acid and poly(acrylic acid). *Journal of Applied Polymer Science*, **105**, 838–845 (2007). DOI: [10.1002/app.26116](https://doi.org/10.1002/app.26116)
- [29] Kim D. S., Park H. B., Rhim J. W., Lee Y. M.: Proton conductivity and methanol transport behavior of cross-linked PVA/PAA/silica hybrid membranes. *Solid State Ionics*, **176**, 117–126 (2005). DOI: [10.1016/j.ssi.2004.07.011](https://doi.org/10.1016/j.ssi.2004.07.011)